

# Long-term durability of bismaleimide composite in marine environments

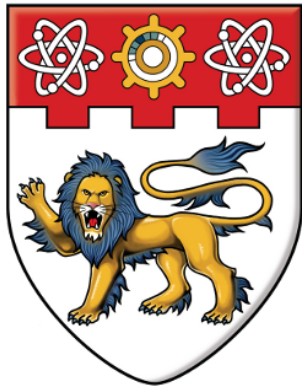
Zhao, Yian

2016

Zhao, Y. (2016). Long-term durability of bismaleimide composite in marine environments.  
Doctoral thesis, Nanyang Technological University, Singapore.

<https://hdl.handle.net/10356/69391>

<https://doi.org/10.32657/10356/69391>



**NANYANG**  
**TECHNOLOGICAL**  
**UNIVERSITY**

**LONG-TERM DURABILITY OF  
BISMALEIMIDE COMPOSITE IN MARINE  
ENVIRONMENTS**

**ZHAO YIAN**

**SCHOOL OF MECHANICAL AND AEROSPACE  
ENGINEERING**

**2016**



# **LONG-TERM DURABILITY OF BISMALEIMIDE COMPOSITE IN MARINE ENVIRONMENTS**

**ZHAO YIAN**

School of Mechanical and Aerospace Engineering

A thesis submitted to the Nanyang Technological University in  
partial fulfilment of the requirements for the degree of Doctor of  
Philosophy in Mechanical Engineering

2016



## **Acknowledgments**

First of all, I would like to express my sincere gratitude to my supervisor Dr. Seah Leong Keey for his continuous support and guidance of my study. Not only through his immense knowledge in this research area, but also his patience, enthusiasm, and inspiration really guided to become a researcher.

My gratitude also goes to Dr. Chai Gin Boay who also offered a lot of inspirational ideas and precious suggestions, which are very helpful to my research. I could not have imagined having better advisors and mentors for my Ph.D. study.

Secondly, I would like to thank Dr. Wang Zhiying ,who has been more of a mentor than a colleague to me, for leading me to start on this project, providing detailed suggestions on research plan and helping me doing experiments with her rich experiences.

Furthermore, I must also acknowledge the support of school of Mechanical and Aerospace engineering, Nanyang Technological University, whose support enabled the completion of these studies. I also want to extend my appreciation to the lab technicians and fellow Ph.D. students who showed remarkable devotion in providing technical assistance and providing helpful ideas to my work.

Last but not least, I would like to thank my beloved family, especially Cathy. Without their love and supports, I would not be able to finish this work.



## Table of Contents

<b>List of Figures</b> .....	vi
<b>List of Tables</b> .....	xii
<b>Abstract</b> .....	xiii
<b>Chapter 1 Introduction</b> .....	1
1.1 Background .....	1
1.2 Objective .....	5
1.3 Scope.....	5
1.4 Report Organization.....	8
<b>Chapter 2 Literature Review</b> .....	9
2.1 Seawater absorption behavior of FRPs .....	9
2.1.1 Review on marine environment .....	9
2.1.2 Water absorption behavior of FRPs .....	11
2.1.3 Diffusion models.....	15
2.1.4 Hygrothermal diffusion behavior in bismaleimide resin and composites.....	18
2.2 Effects of seawater exposure on mechanical properties of FRPs .....	20
2.2.1 Strength and stiffness .....	20
2.2.2 Viscoelastic response of FRPs .....	23
2.3 Prediction of Long-term static and creep strength of FRPs .....	24
2.3.1 Linear viscoelastic models .....	24
2.3.2 Time-Temperature Superposition .....	27
2.3.3 Shifting procedures .....	29
2.3.4 Accelerated testing method and lifetime prediction model .....	32
2.3.4.1 Accelerated testing method .....	32
2.3.4.2 Construction of creep master curve .....	35
2.3.4.3 Probabilistic forms of prediction formulation.....	37



2.3.5 Applicability of prediction methods with water absorption .....	38
2.4 Fatigue behavior of FRPs and the marine environmental effects .....	40
2.4.1 Fatigue of Fiber-Reinforced Composites .....	40
2.4.2 Fatigue life prediction models .....	41
2.4.3 Stiffness degradation.....	46
2.4.4 Seawater exposure effects on fatigue behavior.....	48
2.5 Effects of marine environments on the delamination behavior of FRPs ....	49
2.5.1 Interlaminar fracture toughness of FRPs .....	49
2.5.2 Experimental data reduction method based on Linear Elastic Fracture Mechanics (LEFM).....	50
2.5.3 Experimental data reduction method based on J-integral .....	51
2.5.4 Modeling delamination growth using cohesive element method .....	53
2.5.5 Influence of seawater exposure on the delamination behavior of FRPs.....	56
2.6 Summary of literature review .....	59
<b>Chapter 3 Material and Specimen preparation .....</b>	<b>62</b>
3.1 Material.....	62
3.2 Specimen preparation.....	62
3.2.1 Prepreg processing .....	64
3.2.2 Preparation of artificial seawater .....	68
3.2.3 Desiccation of specimens.....	68
3.3 Summary of the tested specimens.....	68
<b>Chapter 4 Experiments and Prediction Methodologies .....</b>	<b>71</b>
4.1 Moisture diffusion test .....	71
4.2 Mechanical tests.....	72
4.2.1 Tensile test .....	72
4.2.2 Three-point bending test .....	74
4.2.3 Shear test.....	76

4.3 Interlaminar fracture tests .....	79
4.3.1 Static interlaminar fracture tests .....	79
4.3.1.1 Specimen geometry .....	79
4.3.1.2 Experimental setup.....	79
4.3.1.3 Delamination tests method based on ASTM standard .....	82
4.3.1.4 Delamination tests method based on J-integral method .....	84
4.3.2 Fatigue delamination growth under mode II loading.....	88
4.3.2.1 Three-point ENF fatigue analysis .....	88
4.3.2.2 Noise reduction method .....	91
4.3.3 Finite Element Analysis (FEM) using Cohesive zone model (CZM) .....	92
4.4 Dynamic-mechanical analysis .....	95
4.4.1 Introduction.....	95
4.4.2 Test configurations.....	96
4.5 Long-term static strength Prediction.....	97
4.5.1 Introduction.....	97
4.5.2 Master curve model of storage modulus .....	99
4.5.3 Automated shifting program .....	101
4.6 Fatigue test .....	105
4.6.1 Tension-tension fatigue test configuration.....	105
4.6.3 Stiffness degradation model.....	108
<b>Chapter 5 Experimental Results and Discussion .....</b>	<b>110</b>
5.1 Moisture absorption in BMI composite .....	110
5.1.1 Seawater absorption profile .....	110
5.1.2 Diffusion model .....	111
5.1.2.1 Two-stage diffusion model .....	111
5.1.2.2 The Langmuir model.....	113

5.2 Seawater durability of mechanical properties .....	115
5.2.1 Tensile properties .....	115
5.2.2 Shear Properties .....	118
5.2.3 Flexural properties .....	119
5.3 Dynamic-mechanical analysis .....	122
5.4 Long-term static strength prediction .....	124
5.4.1 Construction of master curve by TTS .....	124
5.4.2 Storage modulus model.....	126
5.4.3 Formulation of shift factors and master curves.....	127
5.4.4 Prediction of long-term static and creep behavior .....	132
5.5 Seawater effects on static delamination properties .....	134
5.5.1 Mode I delamination behavior .....	134
5.5.2 Mode II delamination behavior.....	137
5.5.3 Mixed-mode delamination behavior .....	140
5.5.4 Comparison of the methods for characterizing interlaminar fracture toughness .....	142
5.5.5 FEM modeling of delamination behavior .....	145
5.5.5.1 DCB model .....	146
5.5.5.2 ENF model .....	149
5.5.5.3 MMB model.....	151
5.6 Seawater effects on mode II fatigue delamination properties.....	152
5.6.2 Fatigue delamination growth .....	155
5.6.3 Fractography .....	161
5.7 Tension-Tension fatigue tests .....	163
5.7.1 Seawater effects on the S-N relations .....	163
5.7.2 Stiffness degradation curves .....	168
5.7.3 Statistical analysis of S-N curve of fatigue life .....	172

5.7.4 Stiffness degradation model.....	175
5.7.4.1 Statistical analysis of static tests .....	175
5.7.4.2 Relation between failure stiffness with applied stress level .....	175
5.7.4.3 Stiffness degradation model.....	178
<b>Chapter 6 Conclusion and Future work .....</b>	<b>184</b>
6.1 Conclusions.....	184
6.2 Summary of major contributions .....	188
6.3 Future work plan .....	189
6.3.1 Water absorption tests.....	189
6.3.2 Long-term durability prediction.....	190
6.3.3 Fatigue life prediction .....	190
<b>Reference .....</b>	<b>191</b>

## List of Figures

Figure 2.1. Sea surface temperature in Jan 2016 from ESRL database[4] .....	10
Figure 2.2. Typical water uptake trends in composites .....	13
Figure 2.3. Schematics of Berens and Hopfenberg two-stage diffusion model. 18	
Figure 2.4. A typical plot of modulus against temperature for viscoelastic materials .....	24
Figure 2.5. Spring-Dashpot Models .....	26
Figure 2.6. Shifting of storage modulus using time temperature superposition 29	
Figure 2.7. Flow chart of automated shifting program by Tsai .....	30
Figure 2.8. (a) Generation of static strength master curve (b) Generation of creep strength master curve based on LCD .....	33
Figure 2.9. Creep rupture property by constant strain rate master curve shifting .....	36
Figure 2.10. Illustration of fatigue test with constant amplitude loading .....	42
Figure 2.11. Statistics of the S-N diagram .....	43
Figure 2.12. Illustration of CLD diagram .....	46
Figure 2.13. Typical stiffness degradation curve of composite materials .....	48
Figure 2.14. Illustration of fracture modes .....	50
Figure 2.15. Illustration of the integration path and loads and rotation angles for J-intergral .....	53
Figure 2.16. Bilinear traction-separation law of a cohesive element [146] .....	54
Figure 3.1. (a) An illustration of general vacuum bag lay-up (b) A photo of prepreg in preparation .....	63
Figure 3.2. (a) Autoclave (b) Illustration of working principle of autoclave ...	66
Figure 3.3. Cure cycle of autoclave process .....	67
Figure 4.1. Container with specimens in oven set at 50°C .....	72
Figure 4.2. Geometry of the specimen for tensile test .....	73
Figure 4.3. Three-point bending test configurations .....	75
Figure 4.4. Three-point bending test .....	76
Figure 4.5. V-notched rail shear test fixture and specimen geometry .....	77
Figure 4.6. A $[(+45^\circ, -45^\circ)]_8$ off-axis specimen for in-plane shear strength .....	78
Figure 4.7. Test specimen geometry .....	79

Figure 4.8. Microscopic image of the insert and pre-crack on the side view of a specimen .....	80
Figure 4.9. (a) Experimental setup and processed images taken from (b) DCB test (c) ENF test (d) MMB test (red lines indicate the marks detected by the program).....	81
Figure 4.10. Definition of (a) the integration path and the loadings and rotation angles for (b) DCB specimen (c) ENF specimen (d) MMB specimen .....	85
Figure 4.11. Validation test results of the image-processing program .....	88
Figure 4.12. 3-point bend End-notched Flexure (3ENF) test configuration.....	90
Figure 4.13. Mode II fatigue delamination test rig .....	91
Figure 4.14. Typical plot of raw data and noise reduced data vs. fatigue cycles .....	92
Figure 4.15. Schematic of mixed mode softening law.....	94
Figure 4.16. Schematic diagram of typical DMA curves for viscoelastic material .....	96
Figure. 4.18. The Wiechert model .....	99
Figure 4.19. Automated shifting algorithm: (a) storage modulus at different temperatures (b) Shift the storage modulus at next temperature on to the reference curve.....	103
Figure 4.20. Flow chart for automated shift program.....	105
Figure 4.21. Constant amplitude cyclic loading [197].....	106
Figure 5.1. Water absorption curves of BMI composite at different temperatures .....	112
Figure 5.2. (a) Water absorption curves fitted by the two-stage diffusion model (b) diffusivity vs. $1/T$ at various temperatures.....	112
Figure 5.3. Seawater absorption fitted by the Langmuir model .....	114
Figure 5.4. Effect of seawater immersion on tensile strength (a) tested at room temperature (25°C) (b) tested at -20°C .....	115
Figure 5.5. Effect of seawater immersion on tensile modulus (a) tested at room temperature (25°C) (b) tested at -20°C .....	116
Figure 5.6. Statistical distribution of static tensile strength.....	117
Figure 5.7. Effect of seawater immersion on shear strength and modulus .....	118
Figure 5.8. Flexural strength vs. Temperature for dry and wet GF/BMI specimens at 0.5mm/min .....	120

Figure 5.9. Flexural modulus vs. Temperature for dry and wet GF/BMI specimens at 0.5mm/min .....	121
Figure 5.10. Side views of fracture appearances of GF/BMI composites at initial stage (left) and final stage (right) .....	122
Figure 5.11. Effect of seawater exposure on the viscoelastic behavior of the BMI composite.....	123
Figure 5.12. Shift factors of master curves for BMI composites (wet specimen immersed in 50°C seawater up to 3000 hours) .....	125
Figure 5.13. Construction of master curves of storage modulus for BMI composites (wet specimen immersed in 50°C seawater up to 3000 hours).....	125
Figure 5.14. Storage modulus as a function of temperature for dry and wet specimens at 0.1Hz .....	126
Figure 5.15. Modeled shift factors of dry and wet specimens .....	129
Figure 5.16. Modeled master curves for dry and wet specimens.....	130
Figure 5.17. Predicted master curves of dry and wet specimens at 75°C and 200°C .....	130
Figure 5.18. Predicted long-term degradation of modulus at different conditions .....	131
Figure 5.19. Shift factors and construction of CSR master curves for dry and wet50 specimens .....	133
Figure 5.20. Creep master curves for dry and wet50 specimens .....	133
Figure 5.21. (a) Typical load-displacement curves from DCB tests (b) Typical delamination resistance curves. ....	135
Figure 5.22. Mode I fracture toughness measured from insert and pre-crack. ....	136
Figure 5.23. Typical SEM micrographs of mode I delamination surfaces for (a) dry and (b) 80°C immersion specimens ( <i>Direction of delamination from left to right</i> ) .....	136
Figure 5.24. (a) Typical load-displacement curves of ENF tests from pre-cracks (b) Typical delamination resistance curves.....	138
Figure 5.25. Mode II fracture toughness measured from insert and pre-crack. ....	139
Figure 5.26. Typical SEM micrographs of mode II delamination surfaces for (a) dry and (b) 80°C immersion specimens ( <i>Direction of delamination from left to right</i> ) .....	139

Figure 5.27. (a) Typical load-displacement curves from mixed-mode bending tests (b) Typical delamination resistance curves. ....	141
Figure 5.28. Mixed-mode delamination criteria fitted to experimental data ....	141
Figure 5.29. Relative difference between the ASTM standard and the J-integral methods.....	142
Figure 5.30. (a) Load-displacement curves (b) rotation angles vs. crosshead displacement at loading point and (c) Mode I interlaminar fracture toughness results (d) observed and calculated delamination length .....	144
Figure 5.31. Stress distribution of the deformed 2D model of DCB specimen simulation.....	147
Figure 5.32. Effect of cohesive element size on the simulation of DCB load-displacement curve.....	147
Figure 5.33. Effect of interfacial strength on the simulation of DCB load-displacement curve.....	148
Figure 5.34. Stress distribution of the deformed 2D model of ENF specimen simulation.....	149
Figure 5.35. Effect of cohesive element size on the simulation of ENF load-displacement curve.....	150
Figure 5.36. Effect of interfacial strength on the simulation of ENF load-displacement curve.....	150
Figure 5.37. Stress distribution of the deformed 2D model of MMB specimen simulation.....	151
Figure 5.38. Comparison of simulation and experimental results of MMB specimen at mode mixity of 0.51 .....	152
Figure 5.39. Typical loading curves specimens with 30mm crack length in static ENF test .....	154
Figure 5.40. (a) Micro-cracks ahead of crack tip and primary inter-ply crack (b) schematic illustration of primary interplay crack propagation .....	155
Figure 5.41. Typical plots of crack length as a function of fatigue cycles .....	157
Figure 5.42. Fatigue crack growth rates against the $\Delta G_{II}$ .....	158
Figure 5.43. Delamination onset for all specimens and model prediction.....	159
Figure 5.44. Predicted delamination growth behavior for dry and wet specimens; (a) Energy release rate-fatigue growth behavior (b) Normalized energy release rate with corresponding $G_{IIC}$ of dry and wet specimen .....	160



Figure 5.45. Energy release rate vs. delamination length at different loading ratios.....	161
Figure 5.46. Typical SEM micrographs of mode II delamination surfaces from fatigue tests for (a)(b) dry and (c)(d) wet specimens; <i>Direction of delamination from top to bottom</i> .....	162
Figure 5.47. Schematic graph of the crack propagation in woven laminates ..	163
Figure 5.48. Fatigue results of $[(0^\circ, 90^\circ)]_8$ specimens with $R=0.1$ .....	165
Figure 5.49. Fatigue results of $[(0^\circ, 90^\circ)]_8$ specimens with $R=0.5$ .....	166
Figure 5.50. Fatigue results of $\text{dry}^{0/90}$ specimens at $R=0.1$ and $R=0.5$ .....	167
Figure 5.51. Fatigue results of $[(+45^\circ, -45^\circ)]_8$ specimens at $R=0.1$ .....	167
Figure 5.52. Stiffness degradation of the $\text{dry}^{0/90}$ specimens at $R=0.1$ .....	168
Figure 5.53. Stiffness degradation of the $\text{wet}^{50/90}$ specimens at $R=0.1$ .....	169
Figure 5.54. Comparison of stiffness degradation curves of the $\text{dry}^{0/90}$ and the $\text{wet}^{50/90}$ specimens at $R=0.1$ .....	170
Figure 5.55. Stiffness degradation of the $\text{dry}^{\pm 45}$ specimens at $R=0.1$ .....	171
Figure 5.56. Stiffness degradation of the $\text{wet}^{80\pm 45}$ specimens at $R=0.1$ .....	171
Figure 5.57. Weibull distribution of the data set X (a) $\text{dry}^{0/90}$ (b) $\text{wet}^{50/90}$ specimens .....	173
Figure 5.58. Statistical prediction of S-N curve for the $\text{dry}^{0/90}$ specimens .....	174
Figure 5.59. Statistical prediction of S-N curve for the $\text{wet}^{50/90}$ specimens ..	174
Figure 5.60. Failure mode of $\text{dry}^{0/90}$ specimens in different tests .....	176
Figure 5.61. Relationship between stress level and averaged failure stiffness of $\text{dry}^{0/90}$ and $\text{wet}^{0/90}$ specimens .....	176
Figure 5.62. Experimental and predicted failure stiffness for $\text{dry}^{0/90}$ specimen .....	177
Figure 5.63. Experimental and predicted failure stiffness for $\text{wet}^{50/90}$ specimen .....	178
Figure 5.64. Experimental results and predicted curves at 50% stress level for $\text{dry}^{0/90}$ specimen .....	179
Figure 5.65. Experimental results and predicted curves at 70% stress level for $\text{dry}^{0/90}$ specimen .....	179
Figure 5.66. Experimental results and predicted curves at 43% stress level for $\text{wet}^{50/90}$ specimen .....	180

Figure 5.67. Experimental results and predicted curves at 76% stress level for wet50 <sup>0/90</sup> specimen .....	180
Figure 5.68. Statistical predictions by S-N curve and stiffness degradation model for dry <sup>0/90</sup> specimens .....	181
Figure 5.69. Statistical predictions by S-N curve and stiffness degradation model for wet50 <sup>0/90</sup> specimens.....	182
Figure 5.70. Determination of parameters of stiffness degradation model for dry <sup>0/90</sup> and wet50 <sup>0/90</sup> specimens .....	183

## List of Tables

Table 2.1. Temperature vs. depth in the equator region .....	10
Table 2.2. Comparison of property of seawater with pure water[16] .....	12
Table 2.3. Summary of hygrothermal effect on delamination behaviour from different authors .....	58
Table 3.1. Summary of basic composite properties of the specimens and the test conditions .....	69
Table 3.2. Summary of interlaminar properties and the test conditions .....	70
Table 3.3. Summary of Tension-tension fatigue test conditions .....	70
Table 4.1. Tensile tests configurations .....	73
Table 4.2. Three point tests conditions .....	75
Table 4.3. Shear tests configurations .....	78
Table 4.4. Test setup parameters.....	81
Table 4.5. Materials properties of woven E-glass/BMI.....	94
Table 4.6. Fatigue tests conditions.....	107
Table 5.1. Fitting parameters for the two-stage model and the Langmuir model .....	114
Table 5.2. Weibull parameters for the dry and the conditioned specimens .....	117
Table 5.3. Results of V-notched rail shear test and in-plane shear by tensile test of $\pm 45^\circ$ laminates .....	119
Table 5.4. Reduction of flexural strength of dry and wet specimens at different temperatures .....	120
Table 5.5. Fitted parameters of storage modulus model at 0.1Hz .....	127
Table 5.6. Fitted parameters of shift factors model .....	128
Table 5.7. Fitted parameters for delamination criteria.....	142
Table 5.8. Parameters required by the ASTM standard method and the proposed method.....	145
Table 5.9. Specimen geometries .....	146
Table 5.10. Static <i>GIIC</i> test results .....	152
Table 5.11. The values of the fitted parameters at each stress level and data pooling results.....	173
Table 5.12. Fitted parameters for the stiffness degradation model.....	183

## Abstract

Fiber reinforced polymers (FRPs) have been increasingly used for marine and offshore drilling applications for over decades owing to their superior properties such as high strength and stiffness to weight ratio. The FRPs used for marine applications are generally exposed to a combination of long-term seawater exposure and a wide range of servicing temperatures. The life span of those applications is usually expected to be as long as several decades with little maintenance required. However, the uncertainty of the long-term durability due to lack of experimental data and prediction methods has always been a great concern for the design of composite structures. This study investigates the effects of seawater environment and elevated temperature on various mechanical properties of glass fiber reinforced bismaleimide (BMI) composites and estimates the long-term durability of the composite materials in such harsh environmental conditions.

Firstly, the diffusion of seawater in the BMI composite at different temperatures was investigated. The water absorption by BMI composite was found to be a two-stage non-Fickian process. A fast first stage Fickian diffusion was followed by a slow second stage water absorption due to polymer relaxation. Increasing temperature largely accelerates the first stage diffusion but has no clear relationship with the maximum water absorption. A two-stage diffusion model and the Langmuir model were used in this study to describe the water absorption in BMI composite. The mathematic models showed good agreements with the experimental results.

Secondly, the long-term seawater effects on the tensile, flexural and shear properties of the materials were investigated. Those material properties suffered 10-30% of loss after long-term exposure in seawater. Higher seawater temperature generally results in higher degradation of properties. The glass transition temperature ( $T_g$ ) of the BMI composites with seawater absorption is considerably lowered due to the plasticization effect. However, the effect of water absorption below 50 °C was found to be reversible after a re-drying process, which implied no chemical changes taking place at this condition. Furthermore, an accelerated testing method for long-term durability prediction

of FRPs was also reviewed and applied for estimating the viscoelastic, static, creep behaviors based on time-temperature superposition principle (TTSP). An automated shifting program and a formulation for constructing master curve were developed for applying the method on the dynamic tests results. The TTSP was found to be applicable to both dry and wet BMI specimens. For the dry specimen, the shift factors can be clearly expressed by two Arrhenius equations with different activation energies while they became more irregular for the wet specimen. It was obvious that the absorption of water or the chemical degradation affected the activation energies of the material. Based on the prediction, in a period of 50 years, the modulus of BMI material with seawater exposure is expected to degrade by as high as 18.4 % in 50 years compared with 10.9 % for dry condition at 200°C service temperature.

Thirdly, the effect of seawater immersion at different temperatures on the delamination behavior of the composite was studied under mode I, mode II and mixed-mode I/II loadings. The fracture toughness was found to decrease monotonically with seawater exposure and increasing temperature except for pure mode II results, where it surged up nearly 20% over the dry specimen results. However, most specimens with seawater absorption exhibited increasing resistance curves with the delamination growth. This is mainly due to the plasticization of the matrix and higher ductility of the specimen after immersion. The Mode II fatigue delamination growth of the composite was also investigated by end-notched flexure tests. At a given normalized strain energy release rate, the delamination growth was found to be slower in wet specimens than in dry specimens. The experimental results were correlated with existing delamination criteria to determine the parameters for numerical models. In this study, the use of an experimental procedure based on J-integral was explored, and the result was compared with that of well-established ASTM methods. It showed that the J-integral method has wider selection of materials, provides better accuracy. An image-processing program was developed to measure the rotation angles of the specimen automatically, allowing the interlaminar fracture toughness to be monitored with lower requirements for image resolution, light and material surface compared to previous methods.

Finally, fatigue tests were conducted to study stiffness degradation and fatigue life of the material under cyclic loading with the influence of seawater diffusion. Both on-axis and off-axis fatigue tests with various stress ratios were performed with tension-tension loading, and the results were presented in terms of statistical S-N curves. It was found that the fatigue behavior of wet specimens was slightly enhanced at high stress level. However, in general, the fatigue life has been significantly shortened with seawater exposure and elevated immersion temperature. The stiffness degradation curves show that the seawater-aged specimens had higher stiffness reduction in the first stage while slower degradation rate within the linear region (second stage). Overall, the wet specimens tend to have higher final stiffness at failure than the dry specimens. A stiffness degradation model incorporating the strain failure criterion was used to describe the damage accumulation in the BMI composite laminate statistically. The model is capable of predicting the statistical distribution of stiffness degradation curve. The life prediction agreed well with the result of statistical S-N curves and experimental data. The proposed model is attractive as it predicts not only the failure probability but also reflects damage accumulation in the material.

# **Chapter 1 Introduction**

This chapter provides a brief introduction on the background of the study and addresses the problems and motivations of the study. The scope, the research framework and the organization of the report are presented in this chapter as well.

## **1.1 Background**

Composite material is generally defined as a combination of two or more materials, which offers better properties than those of any of its constituents alone. One of the largest and most developed families of composite materials is the fiber-reinforced composites (FRP). Fibrous reinforcements have an obvious advantage of being much stronger and stiffer than their bulk form because fibers are less likely to have surface cracks or defects. Together with matrix materials, which bind fibers and take compressive and transverse load, the fiber reinforcements and matrix form a structural unit. The beauty of this combination is that the materials can be engineered according to the requirements of a particular application, which makes it surpass most traditional materials. Composite materials can be handled by arranging fibers and laminae in different directions and mixing various types of fibers with different matrices, which offers great flexibility in design works [1]. Compared with conventional materials, such as metals and polymers, composite materials have many advantages including very high specific strength and stiffness, low thermal expansion coefficient, high thermal insulation, and good corrosion and fatigue resistance. There are various fabrication processes for composites available. The selection of production method depends largely on the constituent materials of the composite and the quantity and quality of the products as well. The commonly used fabrication methods are open mold, autoclave, RTM (Resin Transform Molding), filament winding, pultrusion, sheet molding compound, etc.

The development of fiber reinforced composite materials has been moving at a much more rapid pace than that of most traditional materials, such as metals

and ceramics, ever since the first real artificial organic fiber was produced in 20th century. The market of composite materials has also been growing at a tremendous speed as well, involving an increasing number of applications and working areas. Until now, composite materials have been widely adopted in almost every area and even replacing traditional materials to become the dominant materials in some industries. Composite materials were first adopted by the aerospace industry and they have become very important to modern aircrafts since the usage of composites has increased significantly in some case to over 50% of their weight. Furthermore, instead of being used originally in the secondary structure, more and more critical parts of the aircrafts are developed using composite materials. In space engineering, advance composite materials are irreplaceable in many applications where the properties of traditional materials cannot fulfill the strict requirements in harsh space environment.

A new frontier where composite material is playing an increasingly important role is the offshore oil drilling industry. The increasing demand in oil resource leads to a rapid depletion of its reserve in land and researchers are obliged to look for resources stored in seabed from coastal regions to even deep sea. The conventional material used in offshore oil drilling industry is steel. However, composite materials with their advantages in properties offer better alternatives and have made a huge impact in this area. As the working depth in the water increases, the self-weight of the risers, pipelines and supporting platform made by conventional materials becomes an important issue. It has been reported that the weight becomes a major problem at a depth over 1500 meters and no conventional materials can be used when the working depth is over 3000 meters. Most fiber reinforced composite materials, on the other hand, have considerably lower density, which largely reduces the weight. A typical carbon fiber epoxy composite can match the same strength with only one third of the weight of steel. Secondly, composite materials usually have good thermal insulation, which is an invaluable property for conducting oil extracted from seabed. Although the temperature of the oil could reach as high as almost 200°C coming out of the seabed, the environmental temperature is around 4°C in the deep sea and could drop to -20°C above the surface of the sea in some areas. During the transportation, the oil cools down and its viscosity increases due to



heat loss. If the viscosity of the oil gets too high, it is very difficult for the oil flowing in the riser or pipeline. Therefore, the good thermal insulation property gives composite material another native advantage in this industry. Finally, the fact that composite materials have better corrosion resistance to seawater and other corrosive substances makes them even more competitive than conventional materials like steel [2].

Despite all those advantages mentioned above, there are still many obstacles hindering further usage of composite materials in offshore oil drilling industry. Aside from relatively complicated manufacture process and high material cost, the most important reason is that composite materials, though fast growing, are still rather new (a few decades). People have much less experience in handling them compared with conventional materials as the experience of using which has been accumulated for over hundreds of years. In addition, the safety issue is so important to offshore oil drilling industry that it is conservative by nature. The FRPs used in these applications are generally exposed to a combination of long-term seawater exposure and a wide range of servicing temperatures. The life span of those applications is normally expected to be as long as several decades with little maintenance required. Therefore, it is very urgent to acquire enough knowledge of the long-term durability of composite materials with environmental effects, especially to predict them with models and experimental methods in a much shorter time comparing with their service lives [3]. The main questions are the seawater absorption behavior of the composite material, environmental damage and degradation of the mechanical properties of composites (e.g. tensile, flexure, shear, delamination and fatigue behaviors) and prediction models of long-term durability. However, the mechanisms controlling the degradation and failure of composite materials are quite dissimilar to that of conventional materials such as ceramics and metals. For example, due to its complex nature, the fatigue damage in composite material can occur in various forms of damages such as fiber fracture, matrix cracking, matrix crazing, fiber buckling, delaminations, etc. The type of damages in those zones could transform from one to another. On top of that, the environmental effect during fatigue would further complicate the problem. It is very difficult to find a general prediction method for the fatigue behaviour of composites.

However, it is feasible to investigate the effect of certain environmental factors on a particular composite, and develop empirical or analytical formulations to reproduce experimental results based on extended testing data.

Bismaleimides are relatively new thermosetting resins based on the polyimide chemistry. They offer excellent physical property retention at elevated temperature and in wet environments. Bismaleimides are nonflammable and have good resistance to chemical agents. They have an operation temperature over 260°C and this unique feature enables them to be used in applications requiring service temperature higher than most resins such as epoxies. In addition, they can be further processed to have higher service temperature with standard autoclave processing. Bismaleimides are suitable for Resin Transfer Molding (RTM) as well, which is an efficient way to make complex composite parts. In fact, the autoclaved BMI composite is able to provide mechanical properties equivalent to some best epoxy based composite at over 177°C and wet environment. In conclusion, bismaleimide is more capable for high temperature use than epoxy, which is the most commonly matrix used, yet only requiring inexpensive epoxy-like processing procedure. Due to the significant advantages, bismaleimide composites have already been adopted in building critical parts of fighter jets, helicopters and formula one racer cars.. Moreover, bismaleimide seems to be an excellent candidate for applications such as risers and pipelines in offshore drilling industry, and an extensive research is needed to understand the long-term durability of the material.

## **1.2 Objective**

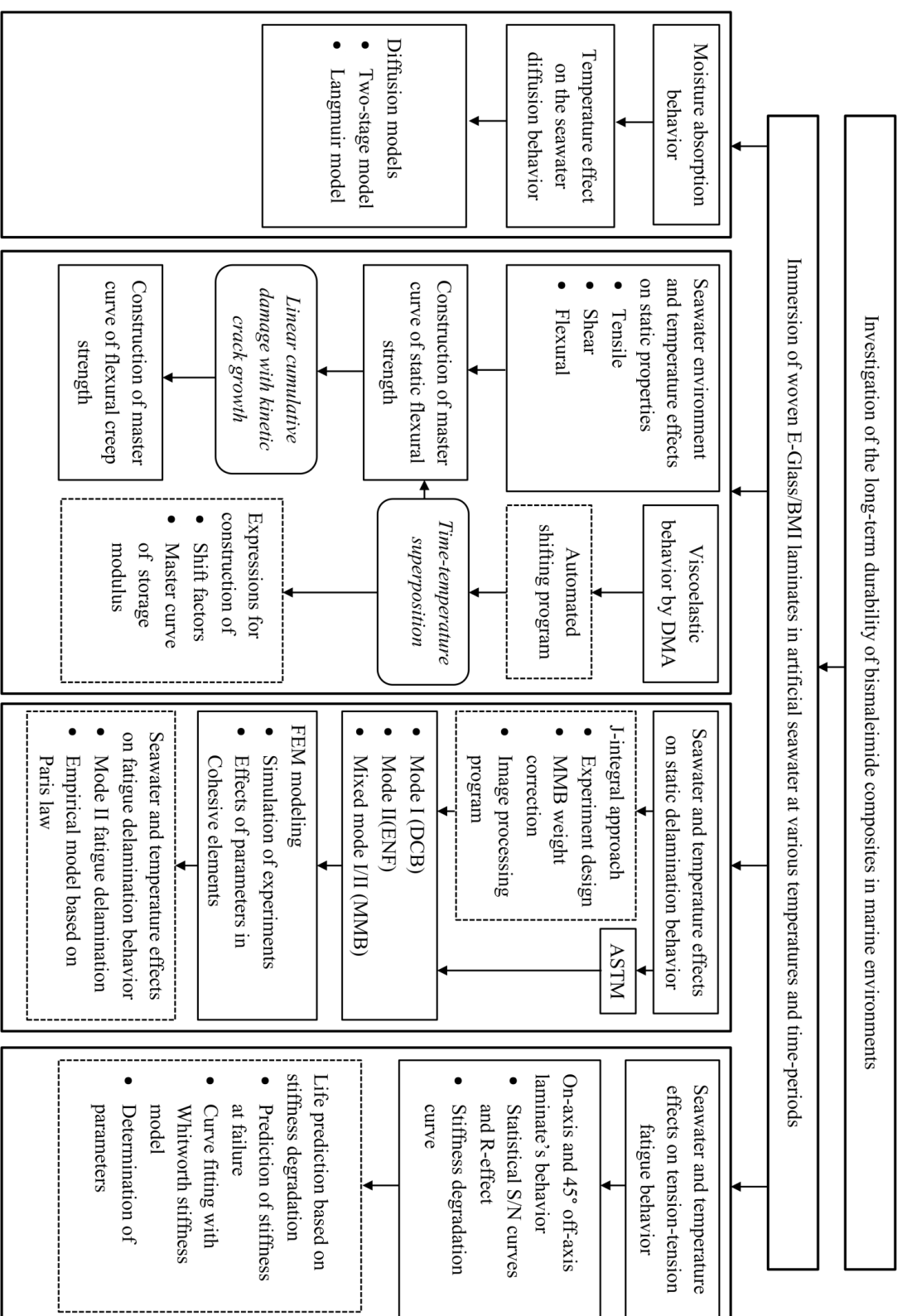
The objective of this research is to investigate the effects of seawater environment and elevated temperature on various mechanical properties of glass fiber reinforced bismaleimide (BMI) composites and estimates the long-term durability of the composite materials in such harsh environmental conditions. Experiments were conducted in order to study the long-term behavior including water absorption, static strength, creep rupture, interlaminar fracture and fatigue failure of the BMI composites. Practical experimental methods and theoretical models were developed and compared for estimating long-term degradations in mechanical properties. Based on the experimental results, various life prediction models were studied and applied on the composite material.

## **1.3 Scope**

In order to achieve the objectives in section 1.2, the following issues were specifically focused in this study:

1. Water absorption behavior and modeling of bismaleimide composites in seawater environment
2. Effects of long-term seawater absorption on the tensile, flexural, creep modulus and strength of bismaleimide composites
3. Dynamic mechanical analysis of bismaleimide material and its composites with the influence of seawater absorption
4. Theoretical life time behavior prediction models of bismaleimide composites under constant load based on Time-temperature superposition principle
5. Experiment methods for measuring static fracture toughness of composite material under different loading modes
6. Seawater effect on the static and fatigue delamination behavior of the composites under different loading modes
7. Fatigue life behavior of bismaleimide composites due to seawater exposure and fatigue life prediction models

The following flowchart is an illustration of the framework of this research. As shown in this figure, the study of temperature and seawater effect on BMI composites can be divided into four parts, namely moisture absorption behavior, the static properties and accelerated testing method, static and fatigue delamination behavior, and the fatigue behavior and life prediction. The solid square box, dash square box and round box represent research topics, major contributions and adopted theories respectively.



☐ Research topics

☐ Major contribution

☐ Adopted theory

## **1.4 Report Organization**

This report is divided into seven chapters. Chapter 2 is the literature review of long-term behaviors of composite materials with environmental effects and the analyzing methods developed in the past. A literature survey on the mechanism of water absorption in composites, the effect of seawater exposure on long-term static, creep behavior, delamination and fatigue life are presented. Theoretical models and experimental prediction methods proposed by other researches are also reviewed and discussed.

Chapter 3 presents a brief introduction on the material used for this study and the preparation procedures of the specimens. The specimens conducted for each experiment and their conditions are summarized at the end of the chapter.

Chapter 4 describes the methodologies used in this work and the experimental configurations and procedures to characterize the behavior of the composites. A brief review of various test methods, the derivations of mechanical properties and prediction approaches used in this study are presented in this chapter. For each test method, there is a general introduction of purpose and experimental configurations, followed by the necessary procedures of conducting the test and calculations of mechanical properties or parameters.

The experimental results are presented, analyzed and discussed in Chapter 5. Prediction models are applied for estimating long-term behavior of composite materials with seawater water effects. In this chapter, the water absorption behavior at different temperatures, seawater immersion effects on tensile, flexural, shear, viscoelastic properties, delamination behaviors and fatigue life are studied. Long-term static and creep behavior of the composite materials in marine environment are predicted.

Chapter 6 draws a conclusion on this report and gives some recommendations on the possible working directions in the future.

## **Chapter 2 Literature Review**

With the increasing usage of composite materials, there has been a great number of research activities focusing on various topics of fiber-reinforced plastics (FRPs). One of the important and complex problems is the long-term durability of the FRPs subjected to different environments. This chapter attempts to summarize the previous published works on the effect of temperature and marine environments of FRPs, including the diffusion behavior, strength degradation, delamination behaviors, fatigue behaviors and developed prediction methodologies.

### **2.1 Seawater absorption behavior of FRPs**

#### 2.1.1 Review on marine environment

Two main parameters of the marine environment, water temperature and salinity, which affect the long-term durability of composites materials, are reviewed in this section. The ocean has a wide range of temperatures from as high as 36°C at shallow coastal waters of the tropical areas to the nearly freezing waters of the poles. The freezing point of seawater is about -2°C, depending on the salinity. The higher the salinity, the lower the freezing point will be. Ocean water generally comprises three layers, i.e. surface layer, thermocline layer and deep ocean layer. The surface layer accepts sun heat and the temperature in this layer varies mainly with latitude, as shown in Figure 2.1. The average temperature of the ocean surface water is about 17°C. However, 90% of the total volume of the ocean is found below the thermocline layer, which begins around 100-400 meters and extends to several hundreds of meters downward. In this layer, the water temperature decreases rapidly with depth and varies in different regions (see Table 2.1). Usually, the temperature of deep ocean water is about 0-4°C.

Besides the seawater temperature, the salinity of the seawater is not uniform throughout the world. The red sea has the highest salinity among open sea

(about 38g/kg) while the salinity is often lower at river mouths or near melting glaciers (about 31g/kg). Despite this, seawater typically has a salinity of about 35g/kg. In addition, the salinity in deep sea is more consistent. The density of surface seawater ranges from about 1020 to 1029 kg/m<sup>3</sup>, depending on the temperature and salinity. Deep in the ocean, under high pressure, seawater can reach a density of 1050 kg/m<sup>3</sup> or higher. Table 2.2 listed some of the properties of the seawater that are quite different from the pure water.

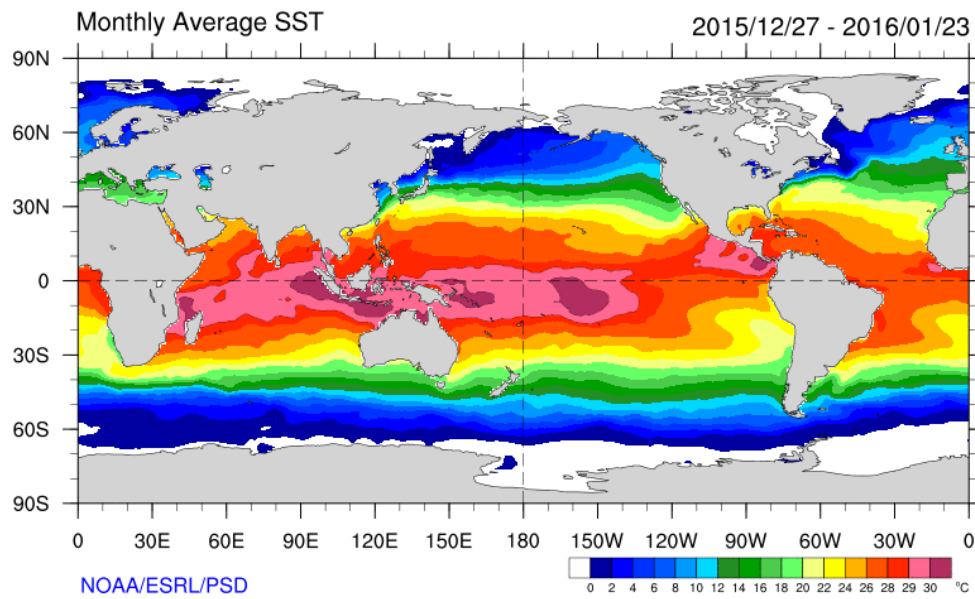


Figure 2.1. Sea surface temperature in Jan 2016 from ESRL database[4]

Table 2.1. Temperature vs. depth in the equator region

Depth (m)	Equatorial Atlantic		Equatorial Indian	
	Low (°C)	High (°C)	Low (°C)	High (°C)
0	5	35	5	35
100	5	30	5	30
250	5	28	3	30
500	3	28	0	28
1000	-0.5	18	0	18
2000	-0.5	13	0	13
3000	-0.5	7	0	7
5000	-0.5	7	-1.5	7



### 2.1.2 Water absorption behavior of FRPs

The water absorption behaviour of FRPs has become more and more important for ever-increasing applications of composites in offshore structures, submersibles and civil infrastructures, as they are generally exposed to a combination of long-term seawater immersion and a wide range of servicing temperatures. The life span of those applications is usually expected to be as long as several decades with little maintenance required. However, the problem of long-term durability prediction of composite materials is often complicated when they are subjected to marine environments. Numerous researches in literature have shown that exposed to moisture or immersed in water have great effect on mechanical properties of composite materials [5-12]. For most composites, those commonly used reinforcements such as glass fibers and carbon fibers are relatively insensitive to water absorption compared with their polymeric matrices. Some reports pointed out that the water molecules would chemically attack the glass fibers causing material leaching, however the effect was rather insignificant compared with the damage to matrices [13, 14]. Therefore, the change of mechanical properties is mainly through matrix phase. Li et.al [15] described the process of water transported into the epoxy resin. Firstly, the water enters the existing free volumes such as voids of the resin, and then bounded to the network sites. As the previous steps of absorption causes swelling of the material, the water finally penetrates to the crosslinked regions.

Table 2.2. Comparison of property of seawater with pure water[16]

Property	Seawater (3.5% salinity)	Pure water
Density (g/cm <sup>3</sup> ), 25 °C	1.02412	1.0029
Specific conductivity, ohm <sup>-1</sup> cm <sup>-1</sup> , 25 °C	0.0532	–
Viscosity, mill poise, 25 °C	9.02	8.90
Vapour pressure, mm Hg, 20 °C	17.4	17.34
Isothermal compressibility, vol/atm, 0 °C	46.4×10 <sup>-6</sup>	50.3×10 <sup>-6</sup>
Temperature of maximum density, 0 °C	-3.25	3.98
Freezing point °C	-1.91	0
Surface tension, dyne cm <sup>-1</sup> , 25 °C	72.74	71.97
Velocity of sound, m/s, 0 °C	1450	1407
Specific heat, J g <sup>-1</sup> °C <sup>-1</sup> , 17.5 °C	3.898	4.182

However, for water diffusion in composite material, the capillary effect or wicking effect plays an important role as well. The absorbed water would flow along the micro-cracks of fiber-matrix interface in liquid form [17]. Kotsikos et. al [18] examined the seawater absorption of a glass reinforced polyester composite at 40°C and 60°C using the nuclear magnetic resonance (NMR) imaging technique. The NMR image showed that the “free” water concentrated at matrix/fiber interface, which leads to the water content in the composite three times higher than that in the bulk resin. It was a strong evidence of water diffusion aided by the wicking effect in composite materials. The most common method of evaluating water absorption in composite material is to use weight gain vs. time. The percent water content of the specimen is measured as a function of time,

$$M(t) = \frac{m(t) - m_{dry}}{m_{dry}} \times 100\% \quad (2.1)$$

where  $m(t)$  is the current weight after immersion and  $m_{dry}$  is the weight of the dry specimen. Weitsman and Elahi [19] did a comprehensive investigation on fluid sorption in composites and summarised several typical weight-gain curves shown in Figure 2.2. The solid line represents the theoretic Fickian diffusion behaviour, which will be further explained in the following sections. Curve A and B are called two-stage diffusion which are most likely associated with reversible or nearly reversible water absorption. The water absorption behaviour similar to curve A and B is considered as benign to the composite material. Curve C and D, on the other hand, are likely associated with extensive interfacial debondings and material leaching and considered as harmful to the composites. However, it is worth noting that the benign absorption curves may switch to harmful curves by changing different combinations of environmental factors, such as temperature, fluids type, exposure time and external pressure. The water uptake curves of epoxy-based composites are found to be curve A and B type in previous studies [6, 8, 17, 20-24], where the diffusion rate was very fast at the first stage, and the water content still increases slowly in the second stage. Vinyl ester composites have superior chemical stability and similar water absorption behaviour of epoxy composites [9, 14, 25, 26]. Studies have shown that the vinyl ester composites absorb even less moisture compared to epoxy-based composites [20, 22].

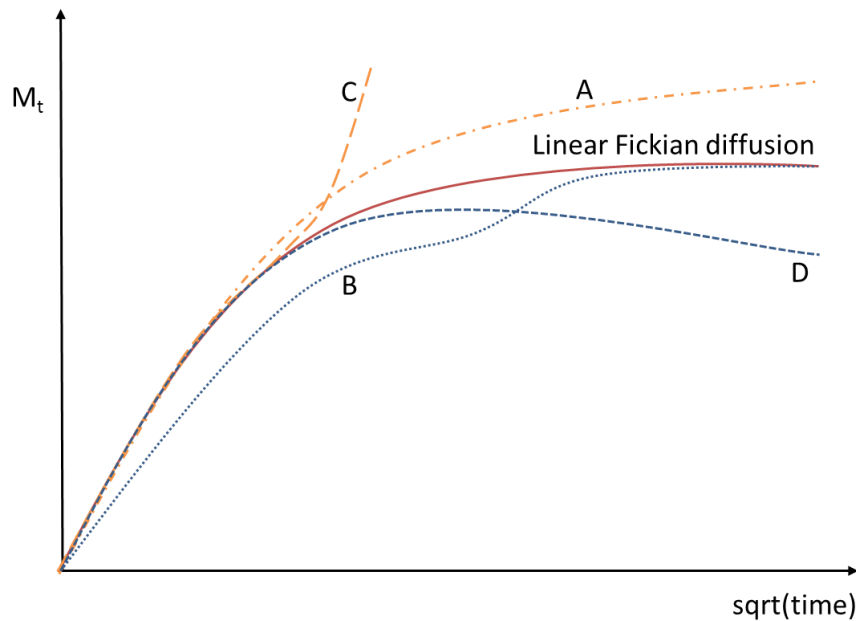


Figure 2.2. Typical water uptake trends in composites

Zhang et al [12] carried out an absorption test by immersing vinyl ester resin and its composites in salt solution with 2.5% of salinity. No saturation was achieved for both the resin and the composite specimens for over 18 months of tests. Another commonly used polymer matrix for marine applications, polyester, is known to be susceptible to water exposure due to the hydrolysis reaction of unsaturated groups within the resin. The hydrolysis of the ester groups results in material leaching when it is immersed in seawater. In the study of Kootsookos et al [14], a significant amount of organic materials were found during the water diffusion test of the polyester composites. The infrared spectra confirmed the low weight organic species were leached out from the polyester matrix. Besides, the polyester-based composites absorb much more water compared to vinyl ester and epoxy-based composites [9, 18, 26], and the absorption curve was similar to the shape of harmful D curve [14]. Several studies have shown that, in general, the diffusion rate would increase with the increase of immersion temperature, as the diffusion is a thermally activated process [3, 8, 18, 23, 27]. Unlike the diffusion rate, the temperature dependence of the amount of final water absorption has not been well understood. Studies have also shown that the absorption behaviour of the material and hence the water uptake curve may change considerably over certain temperatures, where the material goes through some chemical changes [8, 22].

It has been widely reported that the external tensile pressure applied on composite would largely promote the water diffusion rate and maximum water uptake [25, 28]. However, studies [29] have shown that both the water absorption rate and maximum water up-take reduced for specimens under sustained bending when immersed in water. The reason is probably due to the lower free volume fraction of resin matrix. The study of Fahmy and Hurt [30] suggested that one can use the free volume concept to explain and estimate the stress dependent moisture absorption in Epoxy Resin. They modeled the polymer as thick sphere shells with same ratio of inner and outer radii regardless of the difference of polymers in size. Thus, the free volume in the polymer can be written as a function of stress, while the free volume was related with the mobility in polymers. The method was modified by Neumann and Marom [31], who extended the application on composite materials with

arbitrary loading angles, and the volume strain of the composite was calculated based on rule of mixture. The coupling involves considering an evolution of the moisture transport process parameters as a function of the internal mechanical states, especially the volume strain of the organic matrix. The effective diffusion coefficient of the composite material is estimated from the homogenization procedure established by Hashin, accounting for the mechanical state-dependent moisture diffusion coefficient of the constitutive epoxy. In a recent study of Youssef et al. [32], a multi-scale approach was proposed for describing the hygro-mechanical coupling effect of diffusion in composite material. The absorption behaviour of composite materials also varies with types of fluids. Studies have shown higher amount of distilled water absorbed than seawater [11] due to the osmotic pressure effects. The NaCl concentration in the specimen is lower than the outside fluid, which prevents water to be absorbed. However, the degradation effects for both fluids are shown to be similar [33]. Landry et al [21] found no significant difference between soaking carbon/epoxy specimen in deicing fluid and water. However, the material showed negative weight change immersed in hydraulic fluid, which can be related to chemical degradation.

### 2.1.3 Diffusion models

The Fickian diffusion is the most frequently used model to describe the water diffusion in composite materials. The governing equation of the one-dimensional diffusion based on Fick's law is given as

$$\frac{\partial C}{\partial t} = D(t) \frac{\partial^2 C}{\partial x^2} \quad (2.2)$$

where  $C$  is the moisture concentration,  $t$  is time,  $x$  is the distance through the thickness.  $D(t)$  is the time-varying Fickian diffusion coefficient. If the diffusion coefficient is assumed to be constant and the initial water content in a specimen is uniform, the weight change of the specimen due to absorbed water  $M(t)$  is given by [1]

$$M(t) = M_{\infty,F} \left\{ 1 - \frac{8}{\pi^2} \sum_{j=0}^{\infty} \left( \frac{1}{2j+1} \right)^2 \exp \left[ -(2j+1)^2 \pi^2 \frac{Dt}{h^2} \right] \right\} \quad (2.3)$$

where  $t$  and  $h$  are the time and sample thickness respectively, and  $M_{\infty,F}$  is the Fickian equilibrium of water absorption per unit weight. The magnitude of diffusion coefficient  $D$  can be found from the absorption curve as [24],

$$D = \pi \left( \frac{h}{4M_{\infty,F}} \right)^2 \left( \frac{M_1 - M_2}{\sqrt{t_2} - \sqrt{t_1}} \right)^2 \quad (2.4)$$

where  $M_1$  and  $M_2$  are moisture contents at times  $t_1$  and  $t_2$  respectively. A correction is proposed by Shen and Springer [34] for measured apparent diffusion coefficient  $D$  to take unsealed edges and finite size of the specimen into account. The true one dimensional diffusion coefficient  $D_{\infty}$  is given in the equation:

$$D_{\infty} = D \left( 1 + \frac{h}{W} + \frac{h}{L} \right)^{-2} \quad (2.5)$$

where  $L$ ,  $W$  and  $h$  are the length, width and thickness of the specimen respectively. As the diffusion is a thermal activated process, the diffusion coefficient can be related to temperature with an Arrhenius temperature dependence [35, 36]:

$$D = D_0 \exp \left[ -\frac{E_a}{R} \left( \frac{1}{T} - \frac{1}{T_0} \right) \right] \quad (2.6)$$

where  $D_0$  and  $T_0$  are the pre-exponential factor and the reference temperature;  $E_a$  is the activation energy, and  $R$  is the gas constant. The solution given by Eq. (2.3) is often replaced by a simpler approximation [22, 37]

$$M(t) = M_{\infty,F} \left\{ 1 - \exp \left[ -1.73 \left( \frac{Dt}{h^2} \right)^{0.75} \right] \right\} \quad (2.7)$$

However, it was widely reported in previous studies that the Fickian model was not sufficient and tend to over simplify the hygrothermal diffusion behaviour of many polymeric composites. Although most of the actual water absorption curves initially follow the Fickian model, they often deviate from their Fickian equilibrium in the long-term as shown in Figure. 2.2. The diffusion in composites with matrix materials such as epoxy, vinyl ester, polyester and

polyimide often show two-stage diffusion [8, 9, 12, 14, 15, 17-20, 23, 26]. The first stage diffusion is dominated by concentration gradient and the diffusion follows Fickian model. The second stage diffusion, however, is dominated by polymer relaxation as the rearrangement of polymer chains slowly take place that increases the water absorption [38]. In this two-stage diffusion, it is worth noticing that the diffusion rate at first stage is much higher than the second stage since polymer relaxation is a very slow process compared with the Fickian diffusion [35]. Based on the experimental data, it was suggested by Bao et al.[36, 37] that the second stage of water uptake was expressed as a linear function of  $\sqrt{t}$ , while the initial diffusion still obeyed the Fick's law. The entire water uptake can be approximately written as

$$M(t) \approx M_{\infty,F}(1 + k\sqrt{t})G \quad (2.8)$$

and

$$G = 1 - \frac{8}{\pi^2} \sum_{j=0}^{\infty} \left( \frac{1}{2j+1} \right)^2 \exp \left[ -(2j+1)^2 \pi^2 \frac{Dt}{(2h)^2} \right] \quad (2.9)$$

or using the approximation by Eq. (2.7)

$$G = 1 - \exp \left[ -1.73 \left( \frac{Dt}{h^2} \right)^{0.75} \right] \quad (2.10)$$

where  $k$  is the gradient of the second stage line. Berens and Hopfenberg [38] proposed another diffusion model, which is a linear superposition of Fickian diffusion and polymeric relaxations as shown in Figure 2.3. The model was successfully used in the study of [39] to simulate the two-stage water diffusion of adhesives as well.

The Langmuir theory [40] is also commonly used for describing the non-Fickian diffusion behaviour in composites, which is considered as a more accurate model for adhesive or carbon/epoxy conditioned in de-icing fluids [7]. The Langmuir model suggests the existing of both bounded and unbounded water in the system. The absorbed water is bounded with hydroxyl group in the material and becomes unbounded at different probabilities. An approximation [15] for the total water uptake is given as

$$M(t) \cong M_{\infty} \left\{ \frac{\beta}{\gamma + \beta} e^{-\gamma t} \left[ 1 - \frac{8}{\pi^2} \sum_{l=1}^{\infty} (\text{odd}) \frac{e^{-\kappa l^2 t}}{l^2} \right] + \frac{\beta}{\gamma + \beta} (e^{-\beta t} - e^{-\gamma t}) + (1 - e^{-\beta t}) \right\} \quad (2.11)$$

where  $\kappa = \frac{\pi^2}{h^2} D$ . The diffusivity  $D$  is assumed to be both concentration and stress independent, and  $\gamma$  is the bound probability and  $\beta$  is the unbound probability per unit time.

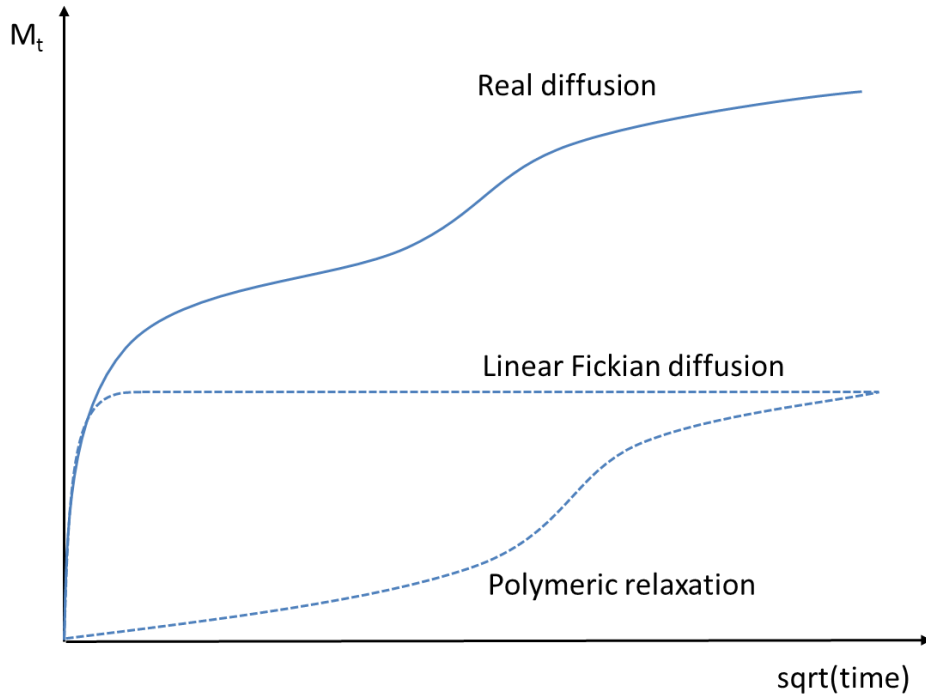


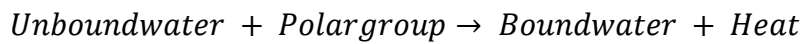
Figure 2.3. Schematics of Berens and Hopfenberg two-stage diffusion model

#### 2.1.4 Hygrothermal diffusion behavior in bismaleimide resin and composites

Past studies showed that the moisture uptake in bismaleimide polymer and its composites was a two-stage non-Fickian diffusion. Bao et al. [37, 41] suggested that the absorption process in bismaleimide composites is self-accelerating. The water absorbed in the polymer, which served as a plasticizer, would lower its glass transition temperature and enhance the relaxation of the network. The relaxed network, in return, accepted more water to be absorbed in the polymer.



They developed a two-stage model based on Eq. (2.8), which showed very good agreement with their experimental results. Li et al [15] also proposed that the non-Fickian diffusion of BMI resin can be fitted with Langmuir model. DMA results showed that moisture absorption would shift the glass transition temperature to a lower value, and the moisture effect is more damaging to samples that are not fully cured or with low post curing temperature. Since samples which had undergone high post curing temperature had higher crosslinking density, and also had higher free volume formation, they were expected to have higher water absorption and the experimental results were consistent with the assumption. The volume change of the specimen was also found to have two stages. At the initial stage, the swelling efficiency was lower than that of latter stage. It could be a sign that the material had less bounded water at the first stage. At higher temperature, the volume change tended to be lower which indicated less bound water, and this can be expressed as,



With additional heat, the reaction shifts to the left hand side. In BMI material, unbound water dominated in the early stages and bound water dominated in the later stage of diffusion process. In the initial stage of water absorption, it was found that elevated temperature would increase the water diffusion rate. The results were consistent with the temperature-dependent diffusivity as expected in the initial absorption, which obeys the Arrhenius temperature dependence. However, lower water diffusion rate on second stage were found in samples at certain high temperature environment. The study of Fourier transform infrared spectroscopy (FTIR) resulted in controversial conclusions showing that there were no obvious chemical reaction, such as hydrolysis, taking place due to the hygrothermal conditioning while studies by Bao et al. [37, 41] pointed out that chemical degradation did have couple with moisture diffusion at 90°C.

## **2.2 Effects of seawater exposure on mechanical properties of FRPs**

### 2.2.1 Strength and stiffness

Composite materials generally exhibit good resistance when they are subjected to environmental attacks during service such as moisture, temperature, radiation and in combination of mechanical loads [11, 42]. However, the lack of experimental data on long-term behaviour and the uncertainty of durability of the composites especially in harsh environment has always been the limiting factor to their applications. Previous studies have shown that the presence of water in the composite can lead to changes in composite materials properties both chemically and physically. The ageing mechanisms can be concluded as follows [42-45]:

- Hydrolysis of the macromolecular chains of resin, which causes leaching out of low-molecular weight chains
- Plasticization effect, which enhances the relaxation of the networks in the matrix
- Interfacial decohesion due to the liquid attack at the fiber/matrix interface
- Swelling of the matrix leads to microcracks and tiny debondings due to the stress between the fibers and the matrix
- Deterioration of fibers

Hydrolysis of the hydrophilic resins often results in a decrease in molecular weight because of migration and leaching of organic groups. This is an irreversible chemical change, and the degree of hydrolysis affects both the stiffness and the strength of the polymer significantly. The absorbed water in the composites also acts as a plasticizer, which promotes the mobility of the molecules and hence relaxes the network. Therefore, the plasticization of matrix softens the material and the glass transition temperature of the composites is often lowered when subjected to water exposure [11, 12, 22, 46]. The mechanism and effect of plasticization is further discussed in the following section. The hydrolysis and plasticization usually take place simultaneously in the composites during the water absorption process. Water also attacks the

interface of fiber and matrix, which weakens the cohesive properties and causes interfacial decohesions. One of the consequences of this effect is the significant decrease in interlaminar shear stress of the composite material with water exposure [9, 42, 47]. In addition, absorbed water can induce a volumetric expansion of the matrix while it has little effect on the fibers. This would cause residual stresses between the matrix and fibers, and combining with the adverse effects of moisture on the interface, result in tiny debondings and microcracks [8, 12, 42, 44, 45]. However, studies have also shown that the swelling of matrix may instead relieve the residual stress in some cases [24].

In general, the matrix is the primary victim of water absorption in the composites and largely responsible for the degradation mechanism of the material. However, studies have shown that moisture also affects fibers to some extent [7, 11, 43]. For example, glass fibers would chemically react with water while aramid fibers tend to absorb water. Nevertheless, carbon fibers are known to be immune to water [14].

The effect of water absorption on the mechanical properties of polymer matrix composites varies considerably with the matrix material, temperature, type and period of exposure. In the past, a great deal of work was published on the degradation of composite material due to humid environments in various conditions. Zafar et al. [11] investigated the long-term effects of moisture on a carbon fiber/epoxy composite material by soaking the specimens in both demineralised water and seawater at ambient temperature for 300 days. The specimens in both conditions showed similar decreasing rate in tensile modulus and strength with immersion. After 300 days specimen in seawater drop 10% and 20% in tensile modulus and strength respectively, which is slightly higher compared to specimens in demineralised water. On the contrary, the study of Kajorncheappunngam et al.[6] showed that glass reinforced epoxy immersion in salt water exhibit the least damage and hence least degradation in mechanical properties among immersion in four different fluids, namely distilled water, salt water, NaOH solution, and HCl solution. Polyester-based composites are generally less resistant to water degradation and absorb more water compared to epoxy and vinyl ester because the polyester chemically reacts with moisture [22, 46, 48]. Visco et al. [26] conducted an investigation on the seawater absorption

and the mechanical performance of glass/polyester and glass/vinyl ester composites. In this case, the specimens were immersed in seawater up to 1440 hours at 17°C and 60°C. For the 17°C seawater immersion group, on one hand, the flexural modulus and strength of the glass/polyester composite decrease with the immerse time and the final reduction was about 13% and 22% respectively. On the other hand, the flexural modulus of the glass/vinyl ester composite showed 20% increase while the strength remained unchanged. This suggests that the vinyl ester matrix used in this study may have not been fully cured and went through a residual cure reaction. Nevertheless, the vinyl ester based composite was very stable in seawater environment. Similar seawater immersion experiments were carried out by Poodts et al. [49] on the glass reinforced vinyl ester and polyester composites at 15°C for about 22 weeks. The three point bending tests on the conditioned specimen showed slight degradation of 6-7% in flexural strength for both materials while the flexural modulus was not affected given the difference in results was small compared with the scattering.

Kootsookos and A. Mouritz [14] also studied the effect of seawater immersion on the several mechanical properties of glass/polyester, carbon/polyester, glass/vinyl ester and carbon/vinyl ester composites. The composite specimens were immersed in natural seawater with a temperature of around 30°C for over two years. The experimental results showed that the polyester-based composites reduced 20-40% of the flexural strength and 10-20% of the flexural modulus upon reaching saturation time. The degradation of the vinylester-based composites was more severe, which was 40-50% in flexural strength and about 30% in flexural modulus. The poor behaviour of vinyl ester based composites was very surprising and the reason was unclear, since the vinylester matrix was normally considered very stable in humid environment. In addition, no obvious correlation of mechanical properties with immersion time was found in the study. In the study of Gellert and D. Turley [9], the mechanical behaviour of polyester, phenolic and vinyl ester GRPs are compared after immersed in seawater for over 800 days. All specimens had about 17%-25% decrease in flexural strength, 20-30% in interlaminar shear strength and less than 10% in flexural modulus. It seems phenolic composite suffered the most but the

difference was not very significant. However, it is worth noting that the phenolic matrix took up the water faster and the degradation reached 25% at very early stage of immersion. In general, it can be concluded that the influence of the moisture absorption is stronger on those properties that depend more on matrix and interface strength such as shear strength and modulus, compressive strength and interlaminar shear strength. Furthermore, drastic degradation in mechanical properties is very likely to happen due to chemical reactions when the composites are subjected to the humid environment with elevated temperature close to or above the glass transition temperature of the matrix [10, 44].

### 2.2.2 Viscoelastic response of FRPs

Most of the composite materials are viscoelastic, which exhibit characters of both viscous fluids and elastic solids. The behavior of the materials are time and temperature dependent and, in the case of being subjected to constant stress, the resulting strain will increase over time adding on the initial elastic strain when loaded. A typical plot of modulus verses temperature for polymers is shown in Figure 2.4. At temperatures well below  $T_g$ , the conformational changes of molecules are restricted and the polymer appears to be glassy in this region and has high modulus (glassy modulus). Conversely, when temperature rises much above  $T_g$ , the modulus drops dramatically due to the high mobility of the main chains. The polymer is rubbery like in this region and the rubbery modulus depends on the crosslink density of the polymer. The glass transition ( $\alpha$ -transition) happens in between the glassy and rubbery region where molecules gradually slide against each other. Besides the primary glass transition, the polymer sometimes shows a secondary transition ( $\beta$ -transition) in glassy region because of the rearrangement of side groups. The energy required for the relaxation of side groups is relatively small which enables it to happen at much lower temperature than  $T_g$ . The mobility of molecules can be enhanced by factors such as water absorption in polymer which leads to lower  $T_g$  [50]. However, it is worth nothing that the plasticization effect, unlike the hydrolysis, is almost reversible, if not fully, after a re-dry process [8, 11]. In the study of Tsai et al. [8] showed that the removal of moisture in a carbon/fiberglass hybrid

epoxy composite can lead to a near full recovery of both glass transition temperature. However, the irreversible damage happens with moisture content exceeds certain level, because of prolonged immersion and high temperature. Taktak et al. [51] tested the mechanical properties of polyamide 6 resin after conditioned in the distilled water at different temperatures. The resin suffered significant deterioration at temperatures of 70°C and 90°C, which is above its glass transition temperature (40°C-54°C). It was found that 60% and 74% of the initial modulus and strength were lost indicating the degradation would be disastrous if the condition temperature is higher than the glass transition temperature of the polymer.

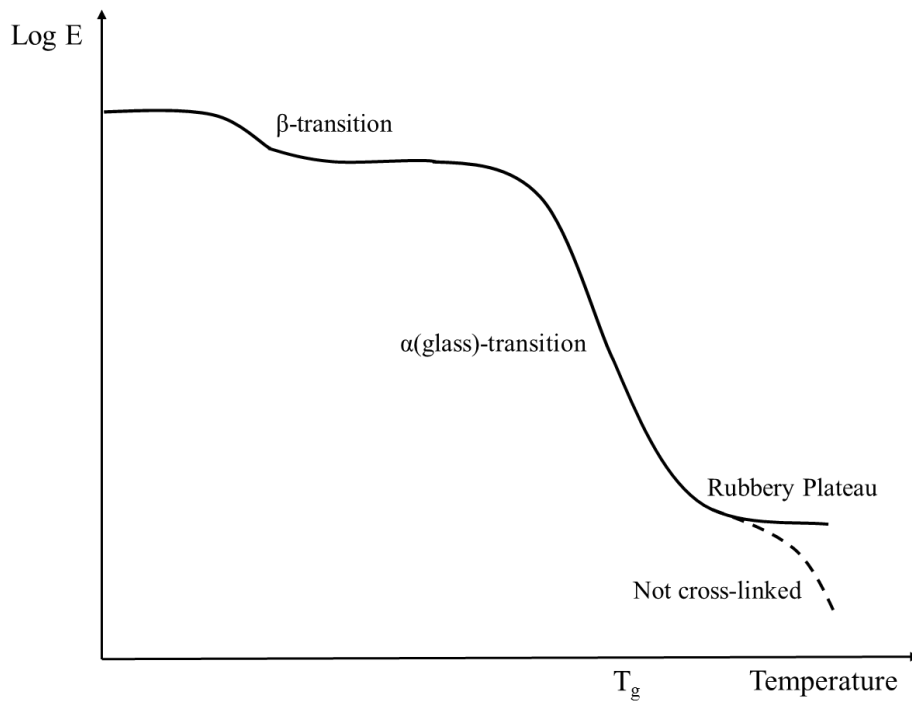


Figure 2.4. A typical plot of modulus against temperature for viscoelastic materials

## 2.3 Prediction of Long-term static and creep strength of FRPs

### 2.3.1 Linear viscoelastic models

The creep behaviour is of great importance to composite applications because creeping may result in structure malfunction due to extra deformation or even catastrophic failure in an extended service time. However, the excessive long

service life of the material has made the direct mechanical testing impracticable. Thus, several prediction theories and testing methods have been developed to evaluate the long-term creep properties of composite materials in an acceptable testing time. Elastic solid stores energy when it is loaded and viscous fluid dissipates energy when it flows. Viscoelastic material, however, has a combination of both characteristics which is capable of energy storage and dissipation under load. Composite materials acquire the viscoelastic behaviour primary from their polymeric constituents. The viscoelastic behaviour of polymeric material becomes stronger as the temperature approaches glass transition temperature at which a transition of polymer from glassy state to rubbery state takes place. As a result, the creep of composite material is both time and temperature dependent deformation and the stress-strain relationship of which can be either linear or non-linear. If the stress-strain curve of a viscoelastic material is always linearly related at each time point, the material is called linear viscoelastic. Most composite materials are considered linear viscoelastic when the stress and time applied are not too high and too long [50, 52]. At certain temperature, the creep compliance  $S(t)$  for a constant stress  $\sigma$  applied is

$$S(t) = \frac{\epsilon(t)}{\sigma} \quad (2.12)$$

where  $\epsilon(t)$  is the strain. According to Boltzmann Superposition Principle, the strain of a non-aging, isotropic, homogeneous linear viscoelastic material with an input at time  $t = \tau$  and the elapsed time  $(t - \tau)$  can be expressed as an integral [1]:

$$\epsilon(t) = S(t - \tau) \int_{-\infty}^t \frac{d\sigma(\tau)}{d(\tau)} \quad (2.13)$$

For composite material, which is anisotropic, the equation is modified as

$$\epsilon_{i,j}(t) = S_{ij}(t - \tau) \int_{-\infty}^t \frac{d\sigma(\tau)}{d(\tau)} \quad (2.14)$$

where  $S_{ij}$  are creep compliances,  $i, j = 1, 2, \dots, 6$ .

Several useful physical models were constructed by elements such as springs ( $\epsilon = \frac{\sigma}{k}$ ,  $k$  is the spring constant) and viscous dashpots ( $\frac{d\epsilon}{dt} = \frac{\sigma}{\mu}$ ,  $\mu$  is the

viscosity). The schematic diagrams of two basic models, the Maxwell model and Kelvin-Voigt model, are displayed in Figure 2.5. Maxwell model shown in Figure 2.5 (a) consists of a spring and a dashpot connected in series while the corresponding elements in Kelvin-Voigt model are connected in parallel shown in Figure 2.5 (b). In Maxwell model, the total strain  $\epsilon$  is the sum of the strains induced in the spring and dashpot:

$$\epsilon(t) = \frac{\sigma_0}{\mu} + \frac{\sigma_0}{k} \quad (2.15)$$

where  $\sigma_0$  is the constant stress applied. The model does not have a good match with the experimental observation on creep behaviour but it could describe relaxation phenomenon adequately. On the contrary, the Kelvin-Voigt model, having same stress on both elements, has a good agreement with experimental observation on creep behaviour but not relaxation. The stress-strain relationship of Kelvin-Voigt model can be written as:

$$\epsilon(t) = \frac{\sigma_0}{k} \left( 1 - e^{-\frac{kt}{\mu}} \right) \quad (2.16)$$

It is obvious that both Maxwell and Kelvin-Voigt are not good enough to describe the creep and relaxation characters in polymeric materials and more elements are needed to modify these models. One way to improve the model is to arrange n Kelvin-Voigt model as elements in series with an elastic string and the corresponding strain can be described as [1]

$$\epsilon(t) = \frac{\sigma_0}{k} + \sum_{i=1}^n \frac{\sigma_0}{k_i} \left( 1 - e^{-\frac{k_i t}{\mu}} \right) \quad (2.17)$$

where  $k_i$  is the spring constant of the  $i^{\text{th}}$  elastic element.

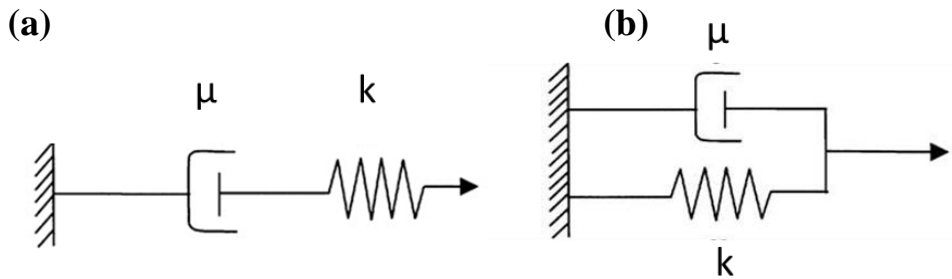


Figure 2.5. Spring-Dashpot Models



### 2.3.2 Time-Temperature Superposition

Due to the viscoelastic behaviour, the deformation of polymer resin under stress is time and temperature dependent. Time-temperature superposition principle (TTSP) can be applied to describe the equivalence of time and temperature effects on linear viscoelastic polymers. By this theory, the elevated temperature has the effect of reducing the relaxation time, which effectively speeds up the real creep responses. The correspondence between time and temperature can be consequently achieved by time-temperature shifting with suitable shift factors and to generate a master curve to predict the polymer behaviour in a much longer time range than testing time under reference temperature. The key idea of using TTSP is to accelerate the polymer resin test by increasing temperature. A general procedure of shifting is demonstrated in Figure 2.6. The time dependent mechanical responses at certain temperature, for example  $T_i$ , can be shifted horizontally onto the reference curve  $T_0$  to generate a smooth curve based on TTSP principle. The final curve, which is called the master curve, shows the mechanical behaviour of the polymer on an extended range of time under reference temperature [1, 53-56]. The shift factor  $a_{T_0}(T_i)$  is defined as:

$$a_{T_0}(T_i) = t_{s,0}/t'_{s,i} \quad (2.18)$$

where  $t_{s,0}$  and  $t'_{s,i}$  are the time to failure before and after shifting to the reference temperature respectively. The static strength and its failure time can be measured when the polymer is under constant strain rate. The Williams-Landel-Ferry Equation (or WLF Equation) [57] is an empirical equation associated to time temperature superposition for almost all amorphous polymers above the glass transition temperature

$$\log a_T = \frac{-C_1(T-T_r)}{C_2+(T-T_r)} \quad (2.19)$$

The two constants,  $C_1$  and  $C_2$ , in this WLF Equation can be determined by fitting the discrete values of shift factors.  $T_r$  is the reference temperature. In fact, two universal values of  $C_1 = 17.4$  and  $C_2 = 51.6$  give us quite good approximation for a variety of polymers when  $T_r$  is set as the glass transition temperature of the material. Unfortunately, most of the applications of polymers and composite materials are used below their glass transition temperatures. Alternatively, the shift factor can be defined by the Arrhenius model, which is

based on the assumption that the polymer obeys the Arrhenius equation for molecular kinematics [50]

$$k = A \exp\left(-\frac{E_a}{RT}\right) \quad (2.20)$$

where  $k$  is the reaction rate of the chemical degradation process under investigation and  $E_a$  is the activation energy which is said to represent the effective activation energy for the overall chemical kinetic expression governing the degradation, and  $R$  is the gas constant. It has been widely acknowledged that Arrhenius equation acquires a good accuracy to determine the shift factor as [58]

$$\log a_{T_0}(T_i) = \frac{E_a}{2.303R} \left( \frac{1}{T} - \frac{1}{T_0} \right) \quad (2.21)$$

If a log plot of the shift factors vs. the difference of inverse absolute temperature between  $\frac{1}{T}$  and  $1/T_0$  is found to be in linear relation, the assumption is considered as valid. Then the activation energy is extrapolated from the equation through linear regression. However, the model is applicable only to relaxation processes showing constant activation energy, examples being those associated with localized motions in the crystalline regions of semi crystalline polymers. Accordingly, the shift factors in this model describe better in glassy region of a polymer [59, 60]. Both WLF and Arrhenius models have their own advantages and draw backs. The WLF model relies on the validity of time-temperature superposition principle while the Arrhenius equation is dependent on the validity of the assumption that temperature merely increases the rate of change or does not introduce new type of change. First, the WLF model is restricted to materials above the glass transition temperatures while Arrhenius equation is more general, especially in glassy state of material. Secondly, if it is believed that all data is relevant and valid then WLF approach is used, on the other hand, if only part of the data is relevant and valid then Arrhenius approach should be taken [57, 61-63]. Ishisaka and M. Kawagoe [27] tried WLF equation in combination with Arrhenius equation for the shift factors of Polyamide 6 and Epoxy resins, and some of the results showed good agreement with the proposed equation.

Based on the molecular theory of viscoelasticity, it is proposed by Ferry and co-workers that the superposition should incorporate a small vertical shift factor. In a modified time-temperature superposition principle for viscoelasticity of

thermosetting resins, small vertical shift factors were also integrated in generating master curves. Creep tests in short term, medium term and long term showed that with help of vertical shifting, results showed better consistency in different testing period [64, 65]. However, the physical meaning of this vertical shift remains controversial among some researches [66].

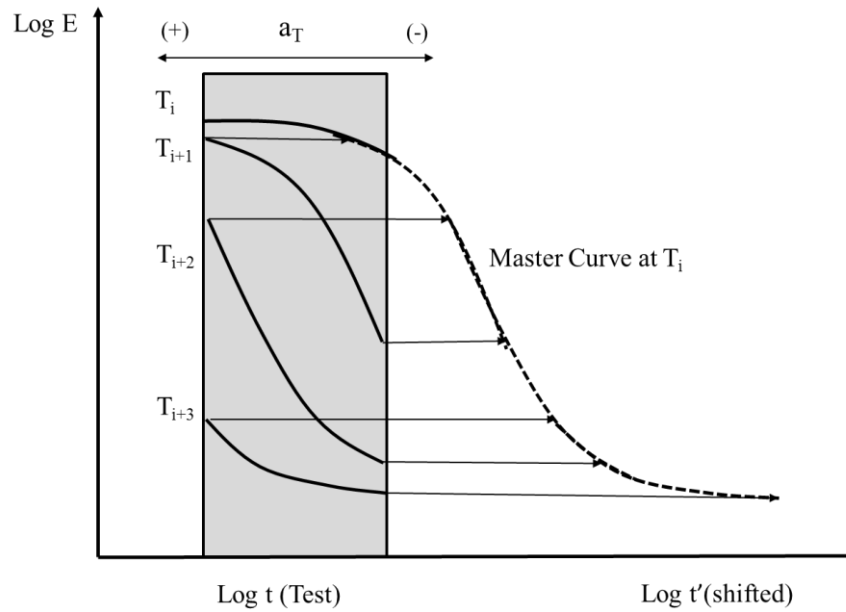


Figure 2.6. Shifting of storage modulus using time temperature superposition

### 2.3.3 Shifting procedures

The shifting process in TTSP is commonly performed manually with requirements of some experience. However, the shift factors obtained often deviates largely from researcher to researcher, and even between two operations by the same person. What is more, even slight change in shift factors would result in decades of difference in master curve generated since the shifting is in log scale. Unfortunately, there are no certain criteria or commonly agreed mathematical procedures that would determine the best or correct shifting given a set of experimental data. Thus, the shifting procedure is one of the important factors that cause errors in the utilization of time-temperature superposition principle. In order to minimize the error induced by hand shifting, there were several other procedures developed for calculating shift factors numerically [56, 67-70]. The automated shift program developed by Tsai [70] was a spreadsheet-based program, which can generate the master curve and corresponding shift

factors at each temperature. The reliability of the shifted data was also discussed in the study. The auto-shift program algorithm employed a general linear least-square method to fit the data at each temperature, and the goodness of the curve fitting was determined by  $R^2$ . With an approximate  $T_g$  of the composite provided, the program can perform the shifting procedure to construct master curves of storage modulus, stiffness, creep compliances or strength properties at certain reference temperature.

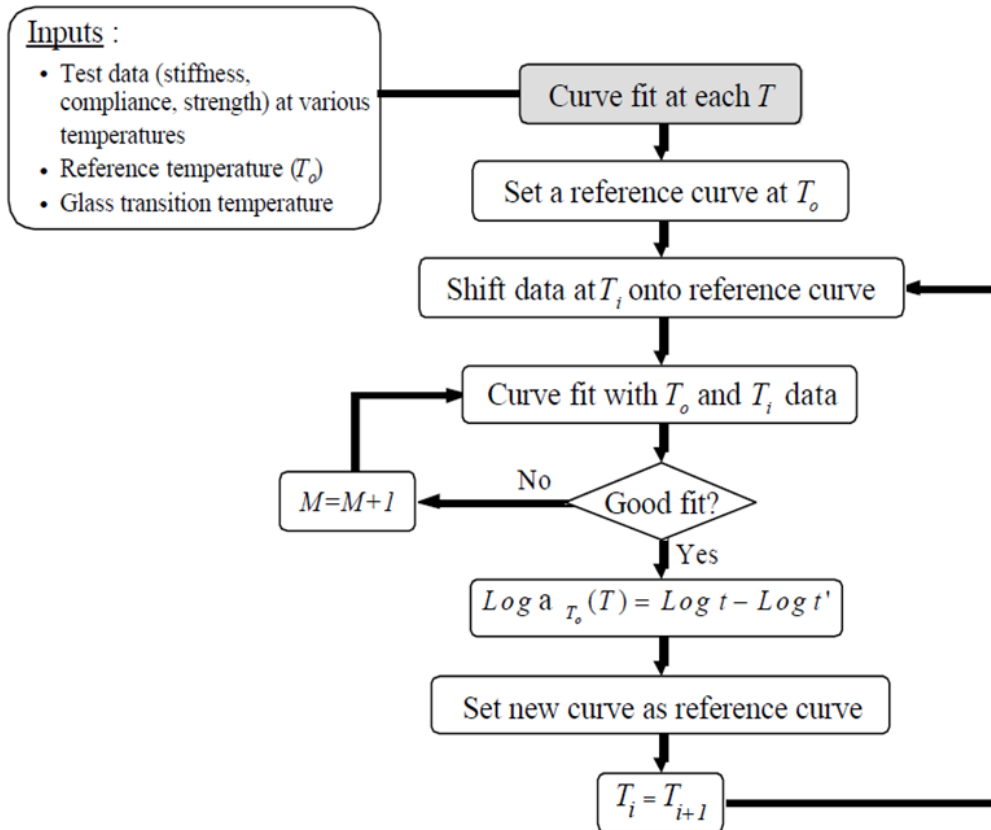


Figure 2.7. Flow chart of automated shifting program by Tsai

The step flow of this method is shown in Figure 2.7. However, the study did not show how the experimental data was mapped to the reference data to construct the master curve. Another method that determines the shift factors mathematically was called closed form shifting algorithm proposed by Gergesova et al. [69], in which the process of generating a fitting curve at each temperature was removed. The principle of the algorithm was to calculate an optimum distance to shift two curves together, by which the net overlapping area in between was zero.

In this algorithm, the following parameters have strong influences on the goodness of the shifting procedure:

- The area of the overlapping window between the reference curve and curve being shifted
- The inclination of the curves
- The error of the experimental data
- The number of data points located in the overlapping area,  $N_t$ .

It is pointed out that the percentage error was around 2 percent where  $\log(N_t)$  was less than 1, which was the usual case for DMA testing. There was a rapid increase in error to around 3-4 percent when overlapping window size was less than 0.1 decade. However, the inclination of segments was actually the main problem with this method. When the segments were getting flattened, the relative error of shift factors increased almost exponentially. Another method [53] was proposed to shift the curves by minimizing the difference in shifted time. Based on this criterion, in log-log scale, the shift factor was calculated as the averaged distance between the reference curve and curves being shifted. However, in some cases, this method may fail to obtain optimum shift factors due to the uneven distribution of experimental data on y-axis. For example, when the density of data points was higher where two segments were close and lower where two segments were more separated, the average distance tends to underestimate the shift factors. The result will be more accurate with more points and the y-axis of data value evenly distributed. With the amount of points keep increasing, the shift factor of this method gradually approaches to that of closed form shifting algorithm. Aside from direct shifting methods mentioned above, Alwis and Burgoyne [71] used a two-stage shifting method. The first stage involved shifting the curves by eye until a relatively smooth match was obtained. Then, a subsequently computer program was adopted to make fine adjustments based on lack of fit minimization. In the second stage, the curves shifted in first stage to form master curve at reference temperature were fitted to a third order polynomial. The shift factor was altered in a region from -2h to 2h, minimizing the sum of square error between the data points and the third order polynomial. After that, the master curve was then fitted to a higher order of polynomial.

### 2.3.4 Accelerated testing method and lifetime prediction model

#### 2.3.4.1 Accelerated testing method

An Accelerated Testing Method (ATM) for estimating long-term properties of polymer composites was proposed by [20, 72-74] based on TTSP. The proposed method can be used for predicting properties including long-term static and creep strength. The methodology is also able to evaluate the fatigue life of the composite under different loading frequency, testing temperature and R ratios. The validity of the method is based on the following four hypotheses,

(A) Same failure mechanism for constant strain rate test, creep rupture and fatigue test

(B) Same time-temperature superposition principle (same set of shift factors) applicable to all types of strengths

(C) Linear cumulative damage (LCD) law is valid for monotonic loading

(D) Linear dependence of fatigue strength on R

Figure 2.8 shows the theoretical background of the accelerated testing procedure. Firstly, as shown in Figure 2.8 (a), a smooth master curve of static strength at reference temperature is obtained by shifting results of constant strain rate tests at different temperatures. The shift factors are generated by this shifting procedure at the same time. Then, according to hypothesis C, the master curve of creep life can be generated by the master curve of static strength. Let  $t_s(\sigma)$  and  $t_c(\sigma)$  stands for the static and creep failure time at the failure stress  $\sigma$ , we have

$$\int_0^{t^*} \frac{dt}{t_c|\sigma(t)|} = 1 \quad (2.22)$$

where  $t^*$  is the failure time under stress history shown as staircase in Figure 2.8 (b). Taking equally spaced increasing sequence of stress as:  $\sigma_i = i\Delta\sigma$ ,  $t_s(i) = t_s(\sigma_i)$  and  $t_c(i) = t_c(\sigma_i)$  are defined as corresponding static and creep failure time respectively. Apply the approximate linear stress loading history by a staircase function, the creep failure time can be estimated based on static failure time as:

$$t_c(2i - 1) = \frac{t_s(2i)t_s(2i-2)}{it_s(2i-2) - (i-1)t_s(2i)} \quad , i = 2, 3, 4 \dots \quad (2.23)$$

where  $t_c(1) = t_s(2)$ . The creep master curve obtained could be used further for fatigue life prediction at arbitrary temperature and frequency, which will be

discussed in other chapters. Various composite materials, especially for marine use, have been tested based on the proposed accelerated testing to predict their long-term durability [20]. In the case of plain woven glass fiber/vinyl-ester laminates, the fracture appearances of GFRP laminates for CSR, creep and fatigue tests were compared and found almost identical for these three types of loading. Because of that, it was considered that the hypothesis A for the ATM holds for this material.

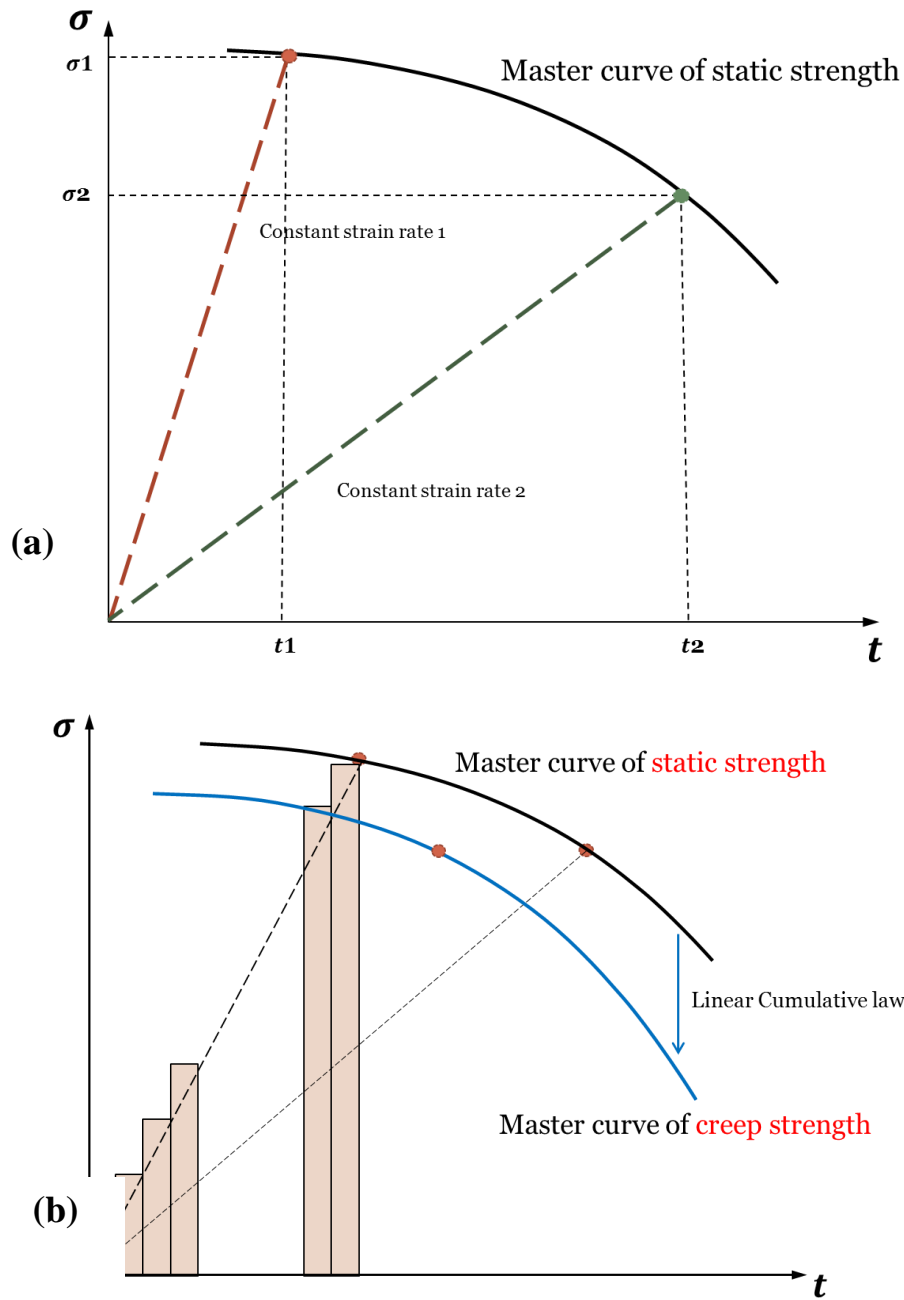


Figure 2.8. (a) Generation of static strength master curve (b) Generation of creep strength master curve based on LCD

The shift factors obtained was found very close to the storage modulus of vinyl-ester resin, which can both be expressed by two Arrhenius equations having different activation energies. As the predicted creep strength roughly agreed with the experimental results, hypothesis C holds for this case. The hypothesis B was proved to be applicable to this case as experiments confirmed that, when the cycles to failure were the same, the failure time is around 100 times for  $f = 0.02\text{Hz}$  to that of  $f = 2\text{Hz}$ . The stress ratio of  $R = 0.5$  is predicted by  $R = 0.05$  (lowest value achievable) and  $R = 1$  (obtained from creep test). The predicted value agreed approximately with experimental results, which proves the applicability of the last hypothesis D in this case [73]. However, for the last hypothesis, the deviation of experimental results and prediction was obvious and considerable larger than that of first three hypothesis [20, 73, 75]. Moreover, the shift factors were found to be identical to the storage modulus of the resin, which is the matrix of laminates. The evidence of failure due to micro buckling of fiber was controlled by the time temperature dependency of matrix resin [75]. The shift factors can be obtained more efficiently and accurately through constructing master curves of storage modulus or creep compliance using dynamic mechanical analysis. The horizontal shift factors  $a_{T_0}(T)$  are often expressed in terms of the following expressions based on Arrhenius equations [76-78]:

$$\log a_{T_0}(T) = \frac{H_1}{2.303R} \left( \frac{1}{T} - \frac{1}{T_0} \right) H(T_g - T) + \left[ \frac{H_1}{2.303R} \left( \frac{1}{T_g} - \frac{1}{T_0} \right) + \frac{H_2}{2.303R} \left( \frac{1}{T} - \frac{1}{T_g} \right) \right] (1 - H(T_g - T)) \quad (2.24)$$

where  $H_1$  and  $H_2$  are the activations below and above the glass transition temperature;  $H$  is the Heaviside step function. The vertical shift  $b_{T_0}(T)$  is also considered in some studies and expressed as

$$\log b_{T_0}(T) = b_1(T - T_0)H(T_g - T) + [b_1(T_g - T_0) + b_2(T - T_g)] (1 - H(T_g - T)) \quad (2.25)$$

where  $\mathbf{b}_1$  and  $\mathbf{b}_2$  are the parameters fitted in vertical shifting below and above  $T_g$ . Noda et al.[79] used another formulation for the shift factors

$$\log a_{T_0}(T) = a_1(T - T_0) + a_2(T - T_0)^2 \quad (2.26)$$

$$\log b_{T_0}(T) = b_1(T - T_0) + b_2(T - T_0)^2 \quad (2.27)$$



where  $a_1, a_2, b_1$  and  $b_2$  are all constants obtained through curve fitting of test data.

#### 2.3.4.2 Construction of creep master curve

The linear cumulative damage with stress controlled kinetic crack growth theory has been developed by Christensen [80] and used in applications to predict the life of polymer materials. A statistical generalization was brought into the theory in the following work [81]. Using a stress intensity factor controlled power law form, Christensen and Miyano [82] followed another approach and further improvements were given in [83, 84]. The theory gave a life prediction based on how long it takes a crack to grow from its initial size to the size that will cause instantaneous failure under certain stress history. The crack kinetic effect was represented by a power law controlled stress intensity factor. The lifetimes under constant stress (creep rupture) and constant strain rate (CSR), which were the two special cases of stress history, can be predicted. Moreover, the theory proved a simple relation between lifetimes of CSR and creep rupture, which provided a theoretical support for ATM. This is important for predicting creep rupture lifetime using master curve of static strength since CSR is easier to obtain experimentally. For an elastic material with idealized initial crack size of  $2a$ , the crack growth rate can be shown as

$$\frac{da}{dt} = \lambda(\sigma\sqrt{a})^r \quad (2.28)$$

where  $r$  is the power law exponent and  $\lambda$  is a material parameter. Separate variables and integrate both sides, from the time when initial crack size is  $a_0$  up to certain point when the crack is not stable, we have

$$\left(\frac{a}{a_0}\right)^{-\frac{r}{2}+1} - 1 = \lambda\left(1 - \frac{r}{2}\right)a_0^{\frac{r}{2}-1} \int_0^t \sigma^r(\tau) d\tau \quad (2.29)$$

Assuming that the critical stress intensity factor remains constant throughout the propagation of the crack, the factor at failure time  $t = t_f$  is equal to which at the initial point, thus

$$\sqrt{a(t_f)}\sigma(t_f) = \sqrt{a_0}\sigma_i \quad (2.30)$$

where  $\sigma_i$  is the stress initially applied on the material. Take the non-dimensional form  $\tilde{\sigma} = \frac{\sigma}{\sigma_i}$  and  $\tilde{t} = \frac{t}{t_1}$  using previous two equations, the equation becomes,

$$1 - \tilde{\sigma}^{r-2}(\tilde{t}_f) = \int_0^{\tilde{t}_f} \tilde{\sigma}^r(\tau) d\tau \quad (2.31)$$

where

$$t_1 = \frac{a_0^{1-\frac{r}{2}} \sigma_i^{-r}}{\lambda(\frac{r}{2}-1)} \quad (2.32)$$

Rearranging the equation, the lifetime  $\tilde{t}$  with a given stress history  $\tilde{\sigma}(\tau)$  is given as

$$\frac{1}{1-\tilde{\sigma}^{r-2}(\tilde{t})} \int_0^{\tilde{t}} \tilde{\sigma}^r(\tau) d\tau = 1 \quad (2.33)$$

Consider the creep rupture condition with constant stress, the lifetime is given as,

$$\tilde{t}_f = \frac{1}{\tilde{\sigma}^r} - \frac{1}{\tilde{\sigma}^2} \quad (2.34)$$

If the material is considered as perfectly elastic, at constant strain rate,

$$\log(\tilde{t}_f) = \log\left(\frac{1}{\tilde{\sigma}^r} - \frac{1}{\tilde{\sigma}^2}\right) + \log(r+1) \quad (2.35)$$

Comparing both equations for creep and constant strain rate, it is obvious that the creep property of the material can be obtained by shifting the constant strain rate result at a constant value of  $\log(r+1)$  along log time scale. At longer time there is a power law behavior controlled by the exponent  $r$  and at shorter time it approaches the static strength asymptote. The exponent  $r$  can be determined by the range of slope power law as shown in Figure 2.9.

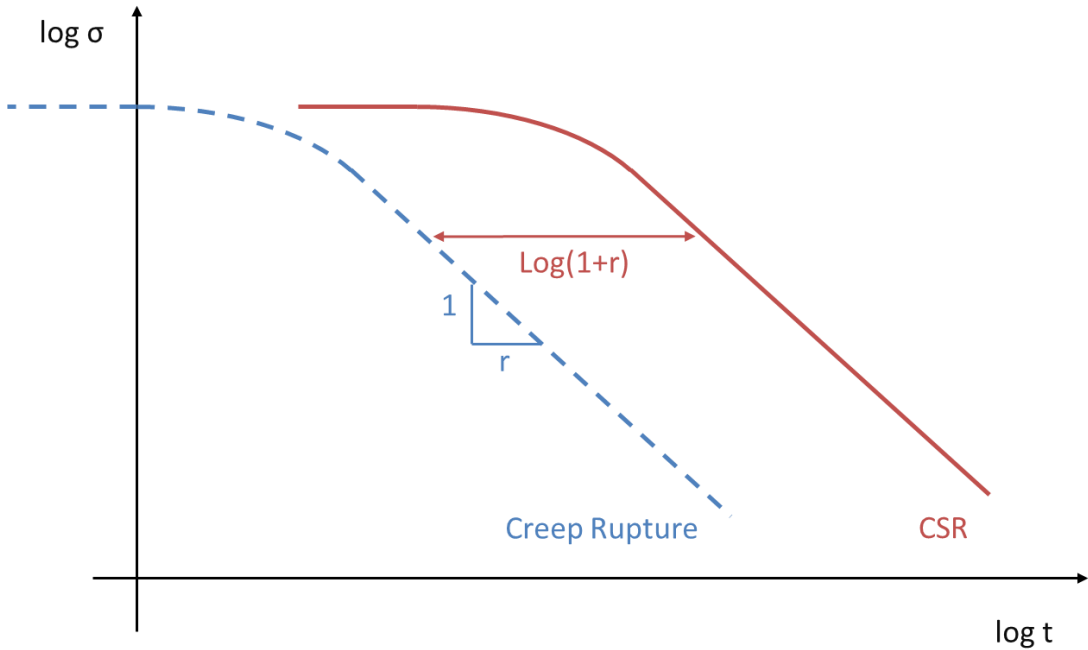


Figure 2.9. Creep rupture property by constant strain rate master curve shifting

### 2.3.4.3 Probabilistic forms of prediction formulation

In real case, the initial flaws resided in origin material vary in size. Especially for fibers, it is impossible to determine the value of strength for a single fiber as it deviates from one to another significantly. Therefore, the large quantity and scatter in strength of fibers require the involvement of statistical analysis. The instantaneous static strength is characterized as a random variable with a specific distribution function. Weibull distribution has been widely adopted in many applications and surprisingly successful when it comes to describe material failure problems. The fundamental idea of using Weibull distribution is that the failure of a solid is like the breaking of a chain in which the weakest link determines the failure strength. This theory is mostly correct in describing behavior of brittle material as the critical defect developed to a crack leading to the failure of the material. The hazard function that defines the instantaneous rate of failure is given as

$$h = \frac{\frac{d}{dt}(CDF)}{1-CDF} \quad (2.36)$$

where CDF is the cumulative distribution function. Assume that the hazards function  $h$  has a power law form

$$h = A\sigma^P \quad (2.37)$$

hence the CDF is given as

$$CDF = 1 - \exp\left[-\left(\frac{\sigma}{\sigma_s}\right)^{(p+1)}\right] \quad (2.38)$$

where

$$\sigma_s = \left(\frac{p+1}{A}\right)^{\frac{1}{p+1}} \quad (2.39)$$

The statistical scatter of constant strain rate tests was successfully used to predict statistical scattering for the creep and fatigue failure and showed good agreement with experimental results [85]. Based on linear cumulative damage with kinetic crack growth theory, considering probabilistic failure, the ATM can be improved and the static strength master curve  $\sigma_s$  was formulated as [74, 86, 87]

$$\log \sigma_s = \log \sigma_{s,0}(t'_0, T_0) + \frac{1}{\sigma_s} \log[1 - \ln(1 - P_f)] - \log\left[1 + \left(\frac{t'}{t'_1}\right)^{n_r}\right] \quad (2.40)$$

and the master curve of creep strength  $\sigma_c$  is given by,

$$\log \sigma_c = \log \sigma_{s,0}(t'_0, T_0) + \frac{1}{\sigma_s} \log[1 - \ln(1 - P_f)] - \log \left[ 1 + \left( \frac{1}{n_r} + 1 \right)^{n_r} \left( \frac{t'}{t'_1} \right)^{n_r} \right] \quad (2.41)$$

where  $\sigma_{s,0}$  is CSR strength at the initial reduced time  $t'_0$  at  $T_0$ ;  $t'_1$  is the transient reduced time at  $T_0$ ;  $t'_1$ ,  $n_r$  and  $\sigma_{s,0}$  are fitted parameters from CSR master curve. It is very important that the prediction given by the accelerated testing method can be verified by actual test results. Although it was impossible to extend the experiment to over decades of time, the predictions can still be partially verified in relatively short term. In a study by Miyano et al [73], the tested creep failure at different stress loadings showed good agreements with the predicted master curve of creep strength. Similar validation results were reported in a recent publication [87]. Additionally, the study showed that estimations from other theories fall within the 90% of the predicted results using probability of ATM methodology.

### 2.3.5 Applicability of prediction methods with water absorption

Many experiments with different combinations of matrices, reinforcements and reinforcement structures under temperature and water environments were conducted to determine the applicability of the prediction methods. In the study of Miyano et al. [73, 75], several types of composite laminates were tested under three different conditions, namely Dry, Wet and Re-dry after wet conditioning. The tested laminates include PAN-based carbon fiber/epoxy, PAN-based carbon fiber/vinylester, PAN-based carbon fiber/PEEK, pitch-based carbon fiber/epoxy, glass-fiber/epoxy and glass fiber/vinylester. After water absorption, the creep compliance of all six types of specimens had been increased. However, after the re-drying process, they all returned to that of dry specimen. The flexural CSR strength of wet E-glass/VE specimen decreased with the water absorption and returned to that of dry specimen after re-drying. The fatigue strength of specimen also decreased with the water absorption and returned to that of dry specimens by re-drying after water absorption except that of E-glass/VE in time and that of T300/EP after long term exposure. It was pointed out that the fatigue strength of Wet+Dry specimen not returning to that

of Dry specimen indicating irreversible chemical change by the process of water absorption happened to the matrix resin. It seemed that the time-temperature superposition principle (TTSP) was applicable to all laminates in different conditions. Another study by Nakada and Miyano [78] also showed the ATM method performs well for CFRP with water absorption. Guedes et al. [88] performed dynamic mechanical analysis (DMA) on both dry and wet samples cut from glass fiber reinforced plastics (GFRP) pipes. Two prediction models, TTSP and power law, were used by applying DMA data for long-term prediction of creep compliance. A creep test of the real pipe was also carried out under wet condition for 4000 hours. The result showed that the TTSP did not perform well for long-term modulus prediction while power law was capable to predict creep behaviour of the specimen better. The experiment also revealed that the moisture effect was almost negligible to the pipe, however this result was very likely due to the protection coating layer, which was not removed from the pipe in the test. Furthermore, there were several major simplifications made in this test that should be noticed. First, it was not the real relaxation modulus calculated for pipe creep test but the reciprocal of creep compliance which is an approximation. Secondly, the experiment approximately took the storage modulus from DMA as relaxation modulus to generate the master curve. DMA tests from 30°C to 75°C were carried out in the study by Goertzen and Kessler [54] to form a master curve of creep compliance using TTSP which predicted material properties over 100 years. At the same time, a tensile creep test using 65% and 77% of ultimate tensile stress were conducted and fitted the curves with power law up to the maximum strain of the material. The power law prediction of tensile tests supported the prediction of TTSP that the material would not fail in 50 years since the material would remain 84% of its ultimate tensile stress.

Ishisaka and M. Kawagoe [27] investigated the effect of moisture on the shift factors of polyamide 6 and epoxy resin and proposed an expression that account for the hygroeffect on shift factors in analogy to the WLF equation:

$$\log a_H = -\frac{D_1(M-M_0)}{D_2+M-M_0} \quad (2.42)$$

where  $M$  is the water content at time  $t$  and  $M_0$  is the reference water content.  $D_1$  and  $D_2$  are the empirical constants. The proposed expression exhibited good

agreement with polyamide 6 resin but the result was poor for epoxy. A moisture-temperature equivalence was proposed by Yao and Ziegmann [89] fitting the creep compliance of composite material at different moisture content and temperature as a linear function. Similarly, an equivalence of moisture and temperature under same aging time was formulated as well. It predicted the aging effect of composite with certain moisture content from dry and isothermal condition. Similar work by Hu and Sun [90] was attempted to establish an interchangeable effects of moisture and temperature on physical aging. However, these moisture-temperature equivalences are purely empirical and deserve further explanations in terms of the underlying mechanism.

## **2.4 Fatigue behavior of FRPs and the marine environmental effects**

### **2.4.1 Fatigue of Fiber-Reinforced Composites**

It is of great importance to understand the fatigue behavior of the composite materials when their applications are designed to take dynamic loading. The properties of the composites would degrade over time under cyclic loadings and finally result in failure even though the applied load is lower than its static strength. Unlike failure due to static loading, fatigue failure happens in a much more complicated way and it is harder to detect and predict. However, the failure of the structure due to fatigue is one of the major causes for accidents. Consequently, it has been one of the greatest concerns in the design of structures. Generally, composite materials are less susceptible to fatigue failure and the fatigue resistance is usually considered as better than conventional materials like steel. However, the downside is that, as composites are relatively new materials, there exist deficiencies in both experiences in fatigue failure and prediction methodologies. Furthermore, fatigue damage in composites is much more complicated than that in conventional isotropic homogeneous materials. Hence, extensive prototype testing and over designed safety factors are usually required and these measures largely increase the cost of using composites in applications consequently.

Composites have different nature of failure accumulation and do not fail by simple crack growth like metals. The damage of fiber reinforced composites starts in the very early stage of fatigue and the damaged zones grow at steady speed. There are various ways in which damage occurs in fatigue of composite material such as fiber fracture, matrix cracking, matrix crazing, fiber bulking, delaminations, etc. The type of damages in those zones could transform from one to another. The stiffness of the material is affected by the damaged zone and decreases gradually over time. The breakage of fibers result in matrix degradation and damage in adjacent areas. A process of redistribution of stress and reduction of stress concentration keeps happening due to the propagation of cracks in fiber matrix interface which leads to further damage to matrix and ultimate failure [2, 91]. There are several parameters summarized by Degrieck and Van Paepegem [92] that can affect the fatigue performances of composites:

- Fiber and matrix types
- Reinforcement architecture (unidirectional forms, fabric forms, etc)
- Stacking sequence of laminate
- Loading conditions (stress ratio, loading pattern, testing frequency, wave form)
- Environmental conditions (temperature and water absorption)

#### 2.4.2 Fatigue life prediction models

Researchers have devoted a lot of efforts to study the fatigue behavior of composite materials and a number of models have been established so far. It is nevertheless difficult to find a general model or prediction method to cover most of the cases due to the complexity of fatigue behaviour in composites. One feasible way is to develop empirical or analytical formulations to reproduce experimental results based on extended testing data. Generally the fatigue damage models can be divided into three categories: fatigue life models [93-96], which do not involve the degradation process; phenomenological models regarding residual stiffness or residual strength of the composites [97-104]; and progressive damage models, where several damage variables are selected to measure the damages of composite materials during fatigue loading [92, 105-109].

The S-N diagram, which was originally adopted for fatigue of metals, is the one of the most widely used and straightforward ways to represent the experimental results. In the diagram, the 'S' can be used to express loads, stresses and strains while the 'N' is normally the numbers of the cycles to failure and expressed in logarithmic form  $\log N$ . The formulation of linear S-N model can be expressed as

$$S_{max} = m \log(N) + b \quad (2.43)$$

where  $S_{max}$  is the maximum applied cyclic stress, as shown in Figure 2.10, where  $m$  and  $b$  are model parameters obtained from experimental results. This linear relationship between maximum stress  $S_{max}$  and  $\log(N)$ , which represents the fatigue life is quite simple yet proved to be accurate within most of the regions in life axis. However, in the real design problem, it is meaningless and impossible to predict the fatigue life of a single specimen. Actually, in composite materials fatigue tests, the scatter of the result on the life axis is up to 2 decades, much higher than that of metallic materials [110]. As a result, a statistical description of fatigue data in the S-N diagram is required to determine the mean fatigue life with certain confidence level as shown in Figure 2.11.

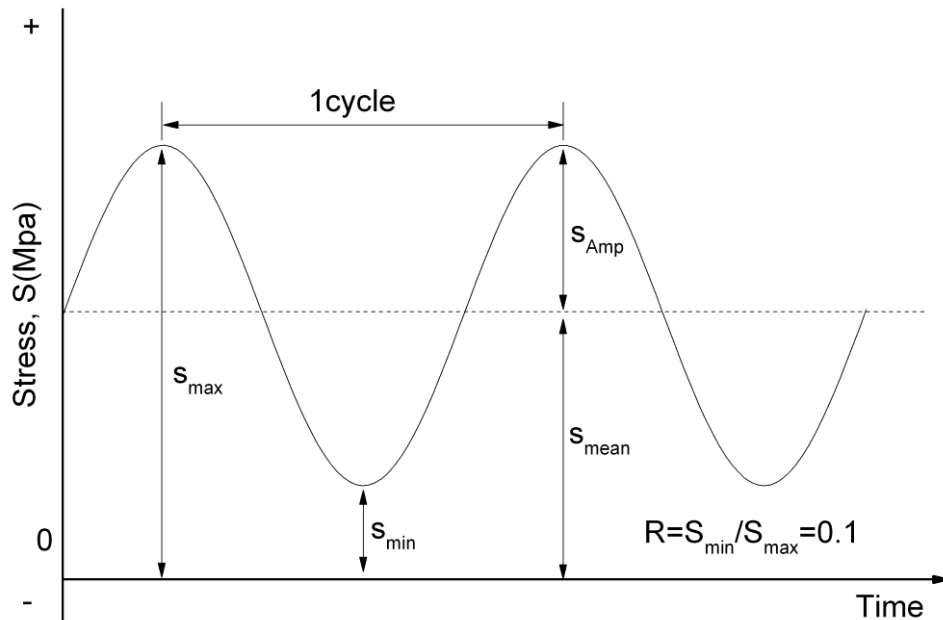


Figure 2.10. Illustration of fatigue test with constant amplitude loading



A two-parameter Weibull distribution is commonly used for characterizing the probability of failure for composite materials. Therefore, at  $i^{\text{th}}$  stress level  $S_i$ , the probability of the sample fails at  $N$  cycles can be described as

$$F_i(N_f) = P_i(N \leq N_f) = 1 - \exp \left[ - \left( \frac{N_f}{N_i} \right)^{\alpha_i} \right], i = 1, 2, \dots n. \quad (2.44)$$

where  $\alpha_i$  and  $N_i$  are scale and shape factors of Weibull distribution for the  $i^{\text{th}}$  stress level. However, a large amount of samples and stress levels are required to determine the Weibull parameters for each  $S_i$  and, subsequently, plot the statistical S-N curves. To overcome this disadvantage, a data pooling procedure is adopted by some researchers, which is discussed in detail in chapter 4 [111, 112].

Although this linear relation appears to be very accurate, it is not wise to blindly extend the prediction too much over the scale of the experimental results. Other than the simple linear relationship, genetic programming has been used to describe the non-linear behaviour of composite material under constant amplitude loading. The key idea of genetic programming is to find out the fittest mathematical expression for S-N curve by cutting out ‘off-springs’, which do not fulfil the criterion in each iteration, and the derived expression does not have to take any assumption which restricts the mathematical form of the expression [105].

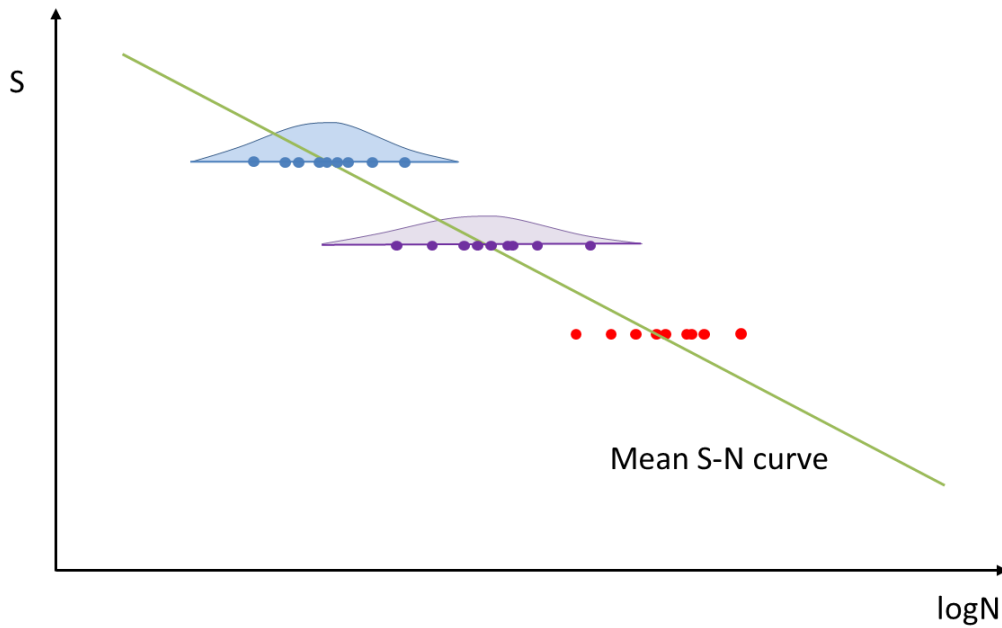


Figure 2.11. Statistics of the S-N diagram

The S-LogN curve can only represent the fatigue behaviour under certain loading type with a particular stress ratio  $R$ . Changing  $R$  value would result in different S-LogN curves. Therefore, it is difficult to understand and describe the full fatigue behaviour for this material using S-LogN curve only. To take stress ratio  $R$  into account, Bond [113] developed the two parameters  $m$  and  $b$  in Eq. (2.43) as fourth-order polynomials in function of ratio range  $R'' = R + 4$ , where  $0 < R < 1$ :

$$\begin{aligned} m &= K(R'')^4 + L(R'')^3 + M(R'')^2 + N(R'') + P \\ b &= Q(R'')^4 + T(R'')^3 + U(R'')^2 + V(R'') + W \end{aligned} \quad (2.45)$$

where the values of  $K, L, M, N, P, Q, T, U, V$  and  $W$  are the parameters derived from fatigue tests. However, the proposed method was entirely empirical, and it was not clear how the relations were established [92].

Constant life diagram (CLD) is often used to describe the full fatigue behaviour of a material as well. As shown in Figure 2.12, the horizontal axis is the mean cyclic stress and vertical axis is the amplitude of the cyclic stress. The diagram is divided into three sectors, which are tension-tension, tension-compression and compression-compression in counter-clockwise direction. Each straight line radiating from the origin represents a certain stress ratio and, for tension-tension fatigue, the  $R$  value starting from zero which is represented by 45 degrees line turns to  $R=1$  on horizontal axis in clockwise direction. The obtained S-N curves are then mapped onto this diagram and points having same failure cycles are connected to form constant lifelines. The constant lifelines converge at the point representing ultimate tensile stress on horizontal axis. Finally, with prediction models, interpolations are made between known available S-N curves to construct unknown S-N curves. Thus, the fatigue life for arbitrary stress level and stress ratio can be predicted using this diagram. There are several CLD models that have been developed in literature [111, 114, 115]. One of the simplest models was the piecewise linear CLD which was derived by linear interpolations between known S-N curves in different sections of the diagram. In the tension-tension sector, when stress ratio  $R'$  is between  $R = 1$  and the first known stress ratio  $R_1$ , then

$$\sigma'_a = \frac{\sigma_s}{\frac{\sigma_s}{\sigma_{a,1}} + r' - r_1} \quad (2.46)$$

where  $\sigma'_a$  and  $\sigma_s$  are stress amplitude and ultimate tensile strength respectively;

$r_i = \frac{1+R_i}{1-R_i}$  and  $r' = \frac{1+R'}{1-R'}$ . When stress ratio  $R_0$  is between  $R_i$  and  $R_{i+1}$ , then

$$\sigma'_a = \frac{\sigma_{a,i}(r_i - r_{i+1})}{\frac{\sigma_{a,i}}{\sigma_{a,i+1}}(r_i - r') + (r' - r_{i+1})} \quad (2.47)$$

Beheshty et al. and Gathercole et al. [116, 117] constructed bell-shape curves CLD using a semi-empirical equation:

$$\frac{\sigma_a}{\sigma_t} = f(1 - \frac{\sigma_m}{\sigma_t})^u (c + \frac{\sigma_m}{\sigma_t})^v \quad (2.48)$$

where  $f, u$  and  $v$  are parameters depend on the logarithm of fatigue life.  $\sigma_a, \sigma_m, \sigma_c$  and  $\sigma_t$  are amplitude, mean stress, compression strength and ultimate tensile stress respectively. Five commonly used CLD models were presented and compared in the work of Vassilopoulos et al. [118], namely piecewise linear CLD, Harris's CLD, Kawai's CLD, Boerstra's CLD and Kassapoglou's CLD. It was found that, for most cases, the piecewise linear CLD gave the most accurate predictions.

The accelerated testing method [74, 87] was developed to predict arbitrary combination of frequency  $f$ , stress ratio  $R$  and temperature  $T$ . The formulation is given as

$$\log \sigma_f(t', N_f) = \log \sigma_{s,0}(t'_0, T_0) + \frac{1}{\alpha_f} \log[1 - \ln(1 - P_f)] - \log \left[ 1 + \left( \frac{t'}{2N_f t'_{11}} \right)^{n_r} (2N_f)^{n_c} \right] - \log[(2N_f)^{n_f}] \quad (2.49)$$

where  $N_f$  is the failure cycles and  $\sigma_{s,0}$  is CSR strength at the initial reduced time  $t'_0$  at  $T_0$ ;  $t'_{11}$  is the transient reduced time at  $T_0$ ;  $t'_1, n_r$  and  $n_f$  are fitted parameters from CSR master curve.  $P_f$  is the probability of failure from static tests. The creep master curve and static master curve were considered as the fatigue strength at stress ratio  $R=1$  and  $R=0$ , and the fatigue life was estimated as a linear interpolation of both curves:

$$\sigma_f(t_f; f, R, T) = \sigma_{f:1}(t_f; f, T)R + \sigma_{f:0}(t_f; f, T)(1 - R) \quad (2.50)$$

where  $\sigma_{f:1}(t_f; f, T)$  and  $\sigma_{f:0}(t_f; f, T)$  represent the creep strength and static strength respectively.

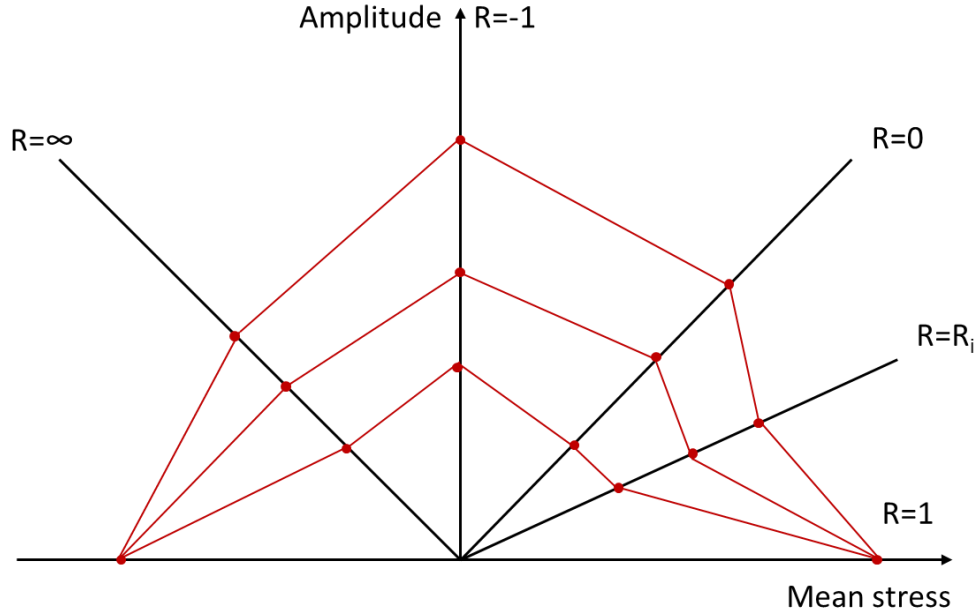


Figure 2.12. Illustration of CLD diagram

### 2.4.3 Stiffness degradation

Although progressive damage models are based on the actual damage mechanisms, it could be very difficult to accurately simulate the fatigue damage due to the complexity of damage modes in composite, especially for woven materials. On the other hand, among these models, the residual stiffness approach has several distinctive advantages. Firstly, stiffness is a straightforward and suitable macroscopic variable to evaluate the damage process of the laminate in fatigue loading. Secondly, the degradation of stiffness with the number of cycles can be easily monitored non-destructively. Lastly, stiffness shows larger changes during the fatigue life than strength which avoids the “sudden death” situation [112]. However, the drawback of the stiffness approach is not directly linked to the final failure [106, 108].

The stiffness  $E$  is calculated as the slope of load-displacement loop at each cyclic loading, and the normalized stiffness degradation at the  $N^{th}$  cycle is defined as  $\bar{E}(N) = E(N)/E_0$ , where  $E_0$  is the initial stiffness at first cycle. Figure 2.13 is an illustration of a typical normalized stiffness degradation curve of a woven composite subjected to cyclic loadings. The damage accumulation

can be clearly divided into three stages. In the first stage, the degradation curve shows a sudden drop of 5-10% in stiffness mainly due to the formation of matrix cracks. Then the stiffness gradually decreases almost linearly in the second stage, which comprises most of the material's life. In this stage, the matrix cracks grow into matrix fiber interface causing delaminations, yarn cracks and longitudinal cracks. Finally, in the third stage, the stiffness of the material starts to reduce rapidly and abrupt failure occurs due to fiber fractures. A lot of efforts were made by previous researchers to develop various empirical or semi-empirical models to describe the stiffness degradation process [97-99, 106, 108, 119]. Mao and Mahadevan [100] proposed a fatigue damage model to describe the fatigue damage:

$$D = q \left( \frac{n}{N} \right)^{m_1} + (1 - q) \left( \frac{n}{N} \right)^{m_2} \quad (2.51)$$

where  $m_1, m_2$  and  $q$  are fitted parameters;  $n$  is the applied loading cycles and  $N$  is the fatigue life at corresponding applied stress level.  $D$  is the accumulated damage

$$D = \frac{E_0 - E_i}{E_0 - E_f} \quad (2.52)$$

where  $E_0$  and  $E_f$  are initial and final dynamic stiffness and  $E_i$  is the stiffness after  $n$  cycles of loading. This model was used in the studies of fatigue with probabilistic analysis by Kang et al.[99] and off-axis fatigue loading of woven laminate by Montesano et al. [120]. Another fatigue damage model by Wu et al. [97] was proposed for the accumulated damage  $D$  as:

$$D = \frac{E_0 - E_i}{E_0 - E_f} = 1 - \left( 1 - \left( \frac{n}{N} \right)^B \right)^A \quad (2.53)$$

where  $A$  and  $B$  are fitted parameters. Both models showed, to some extent, the capability of describing the fatigue damage evolution in the whole fatigue life of the composite materials. However, they are not able to link the applied stress levels with the fatigue life. The stiffness degradation model proposed by Whitworth [119] modeled the fatigue damage and failure prediction for all three stages of the stiffness degradation in fatigue.

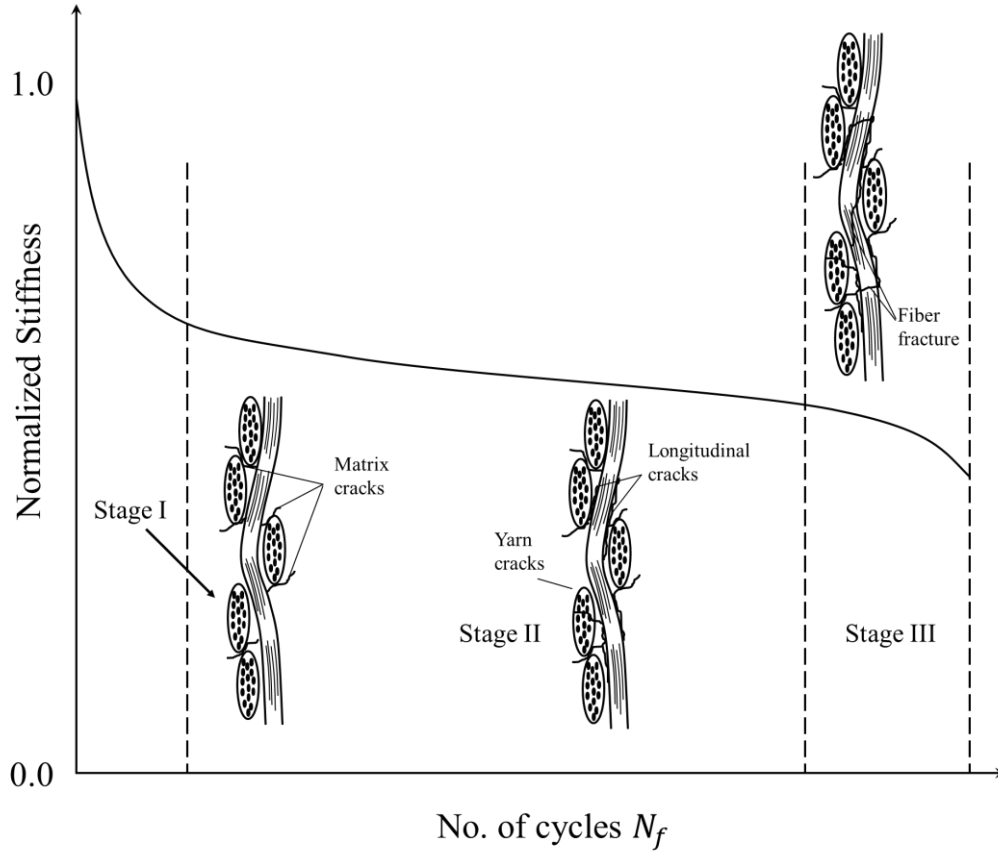


Figure 2.13. Typical stiffness degradation curve of composite materials

The degradation rate of the residual stiffness is assumed to be expressed by [119]

$$\frac{dE^*(N)}{dN} = \frac{-a}{(N+1)E^*(N)^{m-1}} \quad (2.54)$$

$$E^*(N) = \frac{E(N)}{E_n} \quad (2.55)$$

where  $E(N)$  and  $E_n$  are defined as the stiffness at  $N^{th}$  cycle and the failure stiffness respectively. The symbols  $a$  and  $m$  are parameters determined by the applied stress and loading conditions.

#### 2.4.4 Seawater exposure effects on fatigue behavior

In general, water attacks the matrix material and the fiber/matrix interface, facilitating water diffusion of the composite material, which would reduce the fatigue life [19]. However, the presence of water in the composite also softens the material, which tends to improve the fatigue strength and life because of less longitudinal cracks created [43]. The study of Selzer and Friedrich [121]

showed the absorbed moisture caused a largest reduction of 15% for carbon/Epoxy in terms of numbers of cycles to failure while carbon/PEEK was not affected. Another study also found significant reduction of fatigue life for glass/vinyl ester composite with water absorption, but the effect has no different between tap water and seawater immersion [122]. However, Smith and Weitsman [123] reported the cross-ply carbon/epoxy composite saturated in seawater had the longest fatigue life tested in air. Similar results can also be found in other studies [124, 125]. Poodts et al. [49] found that both polyester based and vinyl ester based glass fiber composites showed no appreciable difference in three point bending tests after 22 weeks of immersion in seawater at 15°C. However, a slight improvement in fatigue behavior was found when the specimens were tested in water, which was likely due to the better heat dissipation in water. On the contrary, the study of Shan et al. [126, 127] showed glass fiber reinforced epoxy had shorter fatigue life immersed in water. Microscopic photos revealed more matrix cracking and fiber debondings for the wet specimens than the dry specimens. Similar results were given by the study of [128], in which the seawater conditioned carbon/vinyl ester composites exhibited shorter fatigue life tested in air and the shortest tested in seawater than the dry specimens tested in air. As a result, due to the complex interaction of fatigue damage modes on different composite materials and influence of various other environmental factors, it is not feasible to draw a general conclusion of the effect of seawater on fatigue behavior of composite materials. However, it is still worth to investigate the effects of certain environmental factor on a particular composite, and attempt to develop models that can be extended to more materials and general conditions.

## **2.5 Effects of marine environments on the delamination behavior of FRPs**

### **2.5.1 Interlaminar fracture toughness of FRPs**

Fiber reinforced polymers have been increasingly used in a wide variety of applications owing to the advantages of high specific strength and stiffness, low thermal conductivity, good fatigue resistance, low susceptibility to corrosion,

etc. Woven fabrics are widely used for thick laminates in civil and marine industries because of the easy handling and lay-up during manufacturing [129]. However, polymeric composites generally have low interlaminar strength and the occurrence of delaminations or cracks is one of the major causes for material failure. The initial delaminations are commonly induced by the defects during manufacturing or low velocity impacts in service [129, 130]. As shown in Figure 2.14, the initial delaminations or cracks may then propagate under dynamic loading mainly in mode I (opening mode), mode II (shearing mode) or the combination of both even at much lower value than the critical static energy release rate ( $G_C$ ) [131, 132]. Mode III is usually small for most thin wall structural applications. The growth of delamination would progressively reduce the stiffness and strength of the material resulting in catastrophic failure of the structure. Therefore, delamination is one of the major limiting factors in composite structure design[133].

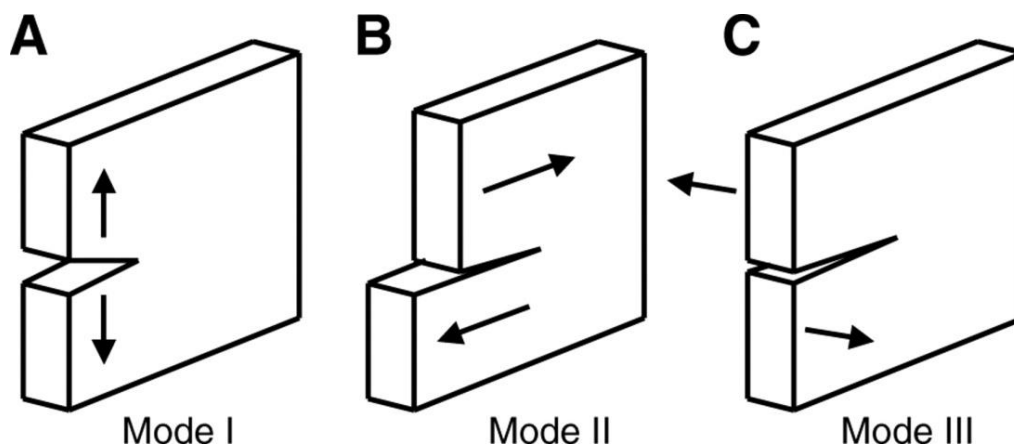


Figure 2.14. Illustration of fracture modes

### 2.5.2 Experimental data reduction method based on Linear Elastic Fracture Mechanics (LEFM)

The accurate measurement of interlaminar fracture toughness is of great importance in the design of composite structures, and it is critical to develop a reliable and practical characterization method. Standard test procedures have been well established for obtaining mode I, mode II and mixed-mode I/II interlaminar fracture toughness using the specimen configurations of double cantilever beam (DCB), end-notched flexure (ENF) and mixed-mode bending



(MMB) respectively [134-136]. The fracture toughness is measured as the critical strain energy release rate ( $G_c$ ) at the crack tip based on the assumptions of linear elastic fracture mechanics (LEFM). The calculations are described with more details in the experimental sections.

### 2.5.3 Experimental data reduction method based on J-integral

Although the LEFM based methods are widely used, they are not applicable to those specimens containing large fracture process zone around the delamination front (e.g. composites with strong fiber bridging, adhesively bonded joints). The fracture toughness measured by the current standard tests is also easily affected by the visual observation of delamination length. The problems involve difficulties in defining crack tip, crack tunneling effect and costly experimental set-up (e.g. travelling microscope) [137]. Alternatively, the J-integral based approaches were proposed for characterizing interlaminar fracture toughness in recent years. The J-integral is a path independent integral proposed by Rice [138] to evaluate the nonlinear strain energy release rate. The original form of J-integral developed by Rice is defined as

$$J = \int_{\Gamma} \left( w dy - \mathbf{T} \cdot \frac{\partial \mathbf{u}}{\partial x} ds \right) \quad (2.56)$$

where  $\Gamma$  is the contour in counter-clockwise direction;  $w$  is the strain energy density;  $\mathbf{T}$  is the stress vector on the contour, and  $\mathbf{u}$  is the displacement vector respectively. For a specimen with an existing delamination and stresses applied in Figure 2.15, the J-integral along the path  $\Gamma_{tip}$  around the crack tip is equal to the integral along the surface of the specimen  $J_{\Gamma}$  ( $\Gamma = \Gamma_1 + \Gamma_2 + \dots + \Gamma_7$ ) due to the path independence of the J-integral. There is no contribution to  $J$  from all the vertical paths ( $\Gamma_1, \Gamma_3$  and  $\Gamma_6$ ) along the edges of the overhangs, as they are in stress free region. Path  $\Gamma_4$  and  $\Gamma_5$  on the free surfaces of the delamination ( $\mathbf{T} = 0$  and  $dy = 0$ ) lead to  $J_{\Gamma_4} = J_{\Gamma_5} = 0$ . The only non-zero components,  $J_{\Gamma_2}$  and  $J_{\Gamma_7}$  are given as

$$J_{\Gamma_2} = \int (T_A(x) + T_c(x)) \frac{\partial v}{\partial x} dx \quad (2.57)$$

$$J_{\Gamma_7} = \int (T_B(x) + T_D(x)) \frac{\partial v}{\partial x} dx \quad (2.58)$$

where  $v$  is the vertical component of the displacement vector. The loads applied on DCB, ENF and MMB specimens can be considered as concentrated forces, and the J-integral can be simply expressed as [139, 140]

$$J_{\Gamma} = (P_A \sin \theta_A + P_B \sin \theta_B + P_C \sin \theta_C + P_D \sin \theta_D) / b \quad (2.59)$$

where  $P_A$  to  $P_D$  are the acting forces at point A to D, and  $\theta_A$  to  $\theta_D$  are the corresponding beam rotation angles with clock-wise as the positive direction;  $b$  is the width of the specimen. As a result, in the J-integral method, the evaluation of interlaminar fracture toughness is directly related to the applied loads and the synchronized angular rotations of the specimen at the loading points. With properly selected integration paths, the fracture toughness of the specimens can be directly related to the load applied and the angular rotations of the beam at the loading points. Therefore, the J-integral methods provide simpler experimental procedure and avoid the ambiguity of visual measurements for delamination length. In addition, they are applicable to a wider selection of materials without the restrictions of small fracture process zones (FPZs) by LEFM. A closed form solution of J-integral for the DCB specimen was derived by Paris and Paris [141] to evaluate the mode I interlaminar fracture toughness. Following this work, Gunderson et al. [137] performed the DCB tests on GFRP specimens using both the J-integral method and the ASTM standard procedure. A video camera and transducers were used to monitor the delamination length and record the beam angles at the loading points respectively. Good agreements were found between the obtained  $G_{IC}$  and  $J_{IC}$ . Bradley et al. [142] and Nilsson [139] derived a more general form of J for the DCB test considering large displacement, mid-plane stretching and additional bending moment generated by the loading point offset from the mid-plane. The use of J-integral method for the mode II ELS (end-load-split) and ENF tests were also investigated analytically and experimentally [133, 142-144]. Stigh et al. [133] designed an integration path for the ENF specimen, and the mode II interlaminar fracture toughness was calculated by the forces and the rotation angles at the loading points. In Stigh's study, an image-processing system was developed to record the rotation angles every five seconds, which were indicated by painted ribs glued to the specimen. Recently, with a similar procedure, the J-integral approach was applied on the MMB configuration by

Sarrado et al [140]. Good agreements were found between the results of ASTM standard and the J-integral method, and the latter showed a significant lower level of uncertainty. They also compared the use of the LEFM-based method and the J-integral method for analyzing adhesive joints under mode I and mode II loadings. The results showed that the LEFM-based method was not suitable for the analysis of adhesive joints fracture, as it depends heavily on the size of the FPZ [145].

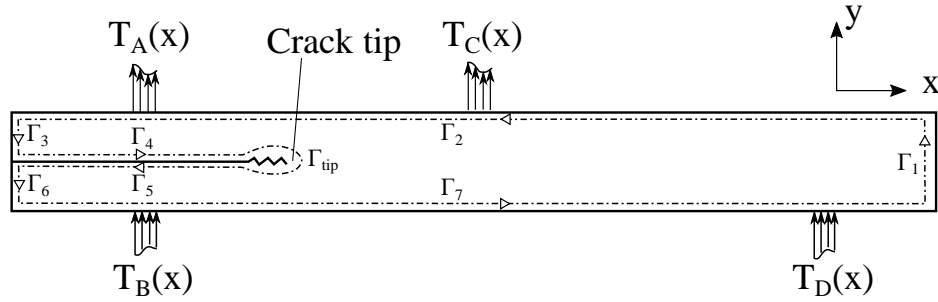


Figure 2.15. Illustration of the integration path and loads and rotation angles for J-intergral

#### 2.5.4 Modeling delamination growth using cohesive element method

The Cohesive zone model is one of the best numerical methods to simulate the delaminations in composite laminates. The commonly used constitutive model of cohesive elements is based on a bilinear traction-separation law shown in Figure 2.16. The cohesive element exhibits initial stiffness without damages if the displacement is less than  $\Delta_0$ . Once the displacement exceeds  $\Delta_0$ , the damage occurs and the stiffness of the element decreases until the propagation criterion is achieved at  $\Delta_f$ , which results in a fully opening of the element. The area under the traction-displacement curve is equal to the fracture toughness of the pure mode. A scalar function  $G$  defines the evolution of the damage value [146]

$$G(\lambda) = \frac{\Delta_f(\lambda - \Delta_0)}{\lambda(\Delta_f - \Delta_0)} \quad (2.60)$$

where  $\lambda$  is the norm of the displacement jump tensor. When the mixed-mode delamination is considered, the  $\lambda$  is given as  $\lambda = \sqrt{(\Delta_3)^2 + (\Delta_{shear})^2}$  and  $\Delta_{shear} = \sqrt{(\Delta_1)^2 + (\Delta_2)^2}$ . A power law criterion [147] is often used to predict

the mixed-mode fracture toughness in terms of the interaction of its mode I and mode II energy release rate

$$\left(\frac{G_I}{G_{IC}}\right)^\alpha + \left(\frac{G_{II}}{G_{IIC}}\right)^\alpha = 1 \quad (2.61)$$

where  $\alpha$  is a material dependent parameter. In most cases,  $\alpha$  is taken as 1 or 2 for prediction. Benzeggagh and Kenane proposed another commonly used mixed-mode criterion (B-K law), and the interlaminar fracture toughness is expressed as [148, 149]

$$G_C = G_{IC} + (G_{IIC} - G_{IC}) \left(\frac{G_{II}}{G_T}\right)^\eta \quad (2.62)$$

where  $\eta$  is a material dependent parameter. A damage initiation criterion is also needed for cohesive zone model in the mixed-mode delamination simulation. Several common damage initiation criteria are maximum stress, maximum strain, quadratic stress, quadratic strain criterion and B-K criteria [150, 151]. The quadratic stress criterion is

$$\left\{\frac{\sigma_I}{\sigma_I^0}\right\}^2 + \left\{\frac{\sigma_{II}}{\sigma_{II}^0}\right\}^2 + \left\{\frac{\sigma_{III}}{\sigma_{III}^0}\right\}^2 = 1 \quad (2.63)$$

where  $\sigma_I^0$ ,  $\sigma_{II}^0$ , and  $\sigma_{III}^0$  are the interfacial strength in each direction. The B-K criteria is given as

$$\sigma^0 = (\sigma_I^0)^2 + [(\sigma_{II}^0)^2 + (\sigma_{III}^0)^2 - (\sigma_I^0)^2] \left(\frac{G_{II}}{G_T}\right)^\eta \quad (2.64)$$

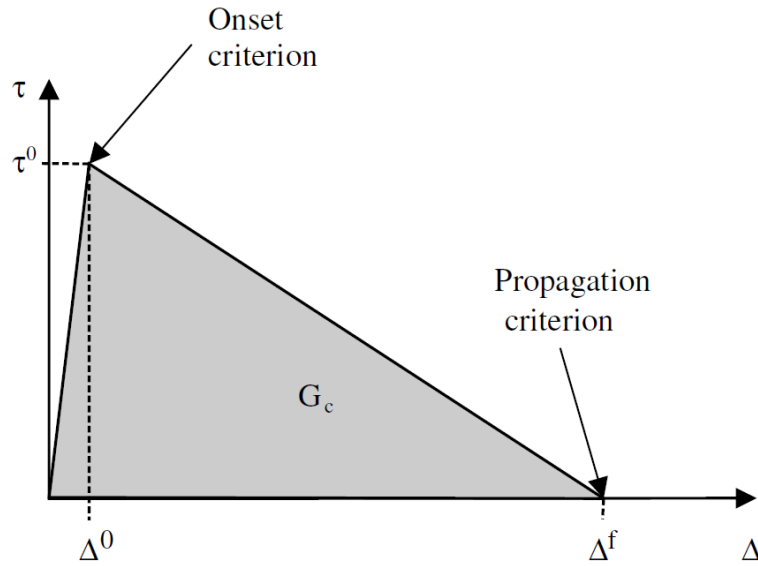


Figure 2.16. Bilinear traction-separation law of a cohesive element [146]

The initial interface stiffness  $k_0$  can be determined by  $k_0 = \frac{\alpha E_3}{t}$  and  $\alpha$  should be larger than 100 [152], where  $E_3$  is the transverse modulus of the material and  $t$  is the thickness of the sublaminates. The cohesive element size is another important factor for accurate prediction using the cohesive zone model. It is required that the cohesive elements to be small enough to capture the accurate stress-strain field. The cohesive zone length  $l_{cz}$  is measured as the distance between the point with maximum traction and the crack tip. The equation  $l_{cz} = ME \frac{G_c}{(\tau^0)^2}$ , where  $M$  varies from 0.21 to 1, is often used for estimating the cohesive length, and for slender substrate,  $l_{cz} = \left[ E \frac{G_c}{(\tau^0)^2} \right]^{\frac{1}{4}} t^{\frac{3}{4}}$  should be used [153-155]. Many researchers recommended that the cohesive length should contain at least 3-5 elements to give a valid simulation [156]. Generally, the simulation results are not sensitive to the change of interfacial strength. However, decreasing the interfacial strength would significantly increase the length of cohesive zone on which a coarse mesh can be used to get a relatively accurate result with much less computational cost. However, if the interfacial strength is too low, significant stiffness loss occurs and the point of crack propagation will be delayed. Zhao et al. [157] proposed a variable fracture toughness model using a USDFLD subroutine in Abaqus to account for the increasing R-curve due to fiber bridging in multidirectional laminates. The fiber bridging zone length was defined as  $l_{bz}$ , and the  $G_{IC}$  can be expressed as a function of crack growth length  $a^*$

$$G_{IC}(a^*) = G_{init} - 2G_{bz} \left( \frac{l_{bz} - a^*}{l_{bz}} \right) - G_{bz} \left( \frac{l_{bz} - a^*}{l_{bz}} - 1 \right)^2 \quad (2.65)$$

where  $G_{init}$  and  $G_{bz}$  are the initial fracture toughness and the toughness caused by the fiber bridging respectively.

### 2.5.5 Influence of seawater exposure on the delamination behavior of FRPs

The FRPs used in marine applications are generally exposed to a combination of long-term seawater exposure and a wide range of servicing temperatures. The life span of those applications is normally expected to be as long as several decades with little maintenance required. Therefore, it is critical to understand the effects of environmental exposure and evaluate the long-term durability of the composite structures in such harsh environmental conditions. Numerous past studies have shown that hygrothermal conditions have significant effects on the interlaminar fracture toughness of composite laminates. However, the results vary considerably with materials, fluids and absorption conditions. The hygrothermal effects are generally more noticeable for the specimens immersed in fluid than exposed in humid air, and the duration and temperature of the exposure affect the fracture toughness results as well. Table 2.1 presents a summary of hygrothermal effect on delamination behaviors from different authors. It appears that many studies found a slight increase in mode I fracture toughness ( $G_{Ic}$ ) with moisture absorption. However, the observed enhancements of  $G_{Ic}$  were generally small, while several studies reported that the effect of moisture was insignificant or even negative. Previous studies also showed inconsistent or even conflicting results of the hygrothermal effects on the mode II delamination. Some authors pointed out that the underlying reason for contradicting results is because that the absorbed water increases fracture toughness through the plasticization of matrix and enhancement of fiber bridging phenomenon, while decreasing the fracture toughness by weakening the matrix and the fiber/matrix interface. In most situations, composite structures are subjected to a mixed-mode I/II loading at various ratios instead of the pure mode I or mode II loadings in service. Finite element analysis using cohesive zone models (CZM) are often used in simulating delamination growth in real applications with complex geometries and loading conditions. However, the accuracy of CZM simulation largely depends on the mixed-mode delamination criterion, where the mixed-mode fracture toughness is expressed in terms of interaction of its mode I and mode II energy release rates. Despite its great importance, very few studies [158-161] were conducted on

characterizing the complete fracture behavior of composite laminates under mode I, mode II and mixed-mode I/II loadings together with the influence of hygrothermal environments.

Table 2.3. Summary of hygrothermal effect on delamination behaviour  
from different authors

Author	Crack	Material	Aging Condition	Mode I	Mode II	Mixed-mode
Sloan et al. [162]	P	Carbon/Epoxy(U D)	RT- 60d (SWI)	Significant increase		
Guedes and Sa [88]	P	Glass/Polyester(R M)	a) RT- 170d (WI) b) 50°C- 170d (WI)	a) Decrease (4.9%) b) Decrease (10.4%)		
Alessi et al. [163]	I	Carbon/Epoxy(U D)	a) 30°C- 56d (WI) b) 70°C- 56d (WI)	a) Slight increase b) Decrease		
Khan et al. [164]	I	Carbon/Epoxy(W)	70°C- 50d (85% RH)	Decrease	Decrease	
Srivastava et al. [165]	I	Glass/Epoxy-Vinyl ester (Quadriaxial)	20°C - 240d (WI)	Increase (36.8%)	Increase (16%)	
Selzer and Friedrich [130]	I	Carbon/Epoxy(U D)	a) 23°C - 300d (WI) b) 70°C - 300d (WI)	a) Increase b) Increase	a) Decrease b) Decrease	
Garg and Ishai [166]	P	Carbon/Epoxy(U D)	a) 70°C- 98d (50% RH) b) 70°C- 62d (WI)	a) No change b) Increase (25.2%)	a) Decrease b) Decrease	
Greenhalgh and Singh [167]	P	a) Carbon/BMI(UD) b) Carbon/Epoxy(U D)	60°C- till saturation (84%RH)	a) Slight decrease b) Slight decrease	a) Decrease b) No change	a)Increase/decrease under Mode I/Mode II dominated loading b)No change
Asp [159]	I	Carbon/Epoxy(U D)	70°C (95% RH)	No change	Decrease (11.1%)	Decrease (7.4%) at $G_{II}/G = 0.54$
Davidson et al. [160]	P	Carbon/Epoxy(U D)	50°C- till saturation (95% RH)	Slight increase	No change	Increase at $G_{II}/G = 0.4$
LeBlanc et al. [161]	P	Carbon/Epoxy(U D)	70°C - 314d (WI)	Increase (14.9%)	Decrease (37.5%)	Significant decrease at all mode ratios except $G_{II}/G = 0$
Meziere et al. [168]	P	Carbon/Epoxy(U D)	95°C- till saturation (80%RH)	Increase (34.1%)	Increase (54.5%)	Increase at all mode ratios
Gong et al. [169]	I	Carbon/Epoxy(W)	72°C - 118d (WI)	Decrease (11.6%)	Decrease (55%)	Decrease (37%) at $G_{II}/G = 0.4$
Hintikka et al. [170]	P	Carbon/Epoxy(U D)	60°C - 8d (95% RH)	Decrease (14.7%)	Increase (13.7%)	
Rusell et al. [158]	I	Carbon/Epoxy(U D)	75°C- till saturation (100%RH)	Slight increase	No change	
Chou [171]	P	a) Carbon/Epoxy(U D) b) Carbon/Epoxy(W)	85°C- 90d (98% RH)	a) No change b) No change	a) No change b) No change	
Todo et al. [172]	I	Carbon/Epoxy(U D)	a) 80°C- 60d (90% RH) b) 80°C- 60d (WI)		a) No change b) Decrease	
Zhao et al. [173]	P	Glass/BMI (W)	50°C - 100d (SWI)		Increase (15.4%)	
Landry et al. [21]	P	Carbon/Epoxy(U D)	70°C - 130d (WI)		Decrease (14.5%)	

P: pre-crack; I: insert; W: woven; UD: uni-directional; d:day; (S)WI: (sea)water immersion; RH: relative humidity



## 2.6 Summary of literature review

This chapter attempts to summarize the past published research on the durability of fiber-reinforced plastics subjected to marine environments. In the present review, attention has been focused on the following topics:

### 1. Water diffusion behavior in fiber-reinforced plastics

Seawater diffusion in composites is usually a complicated process influenced by various mechanisms including concentration-gradient controlled diffusion, relaxation of polymer structure, flow and storage of water in micro-cracks and voids in the matrix. Therefore, the diffusion process often shows non-Fickian behavior and different models have been proposed to describe the observed behavior. However, the diffusion process also varies with different composite materials, fluids and duration of conditioning. As a result, for marine applications using BMI composites, it is important to understand the exact diffusion behavior of the material subjected to different conditions in seawater and find a suitable diffusion model for the process.

### 2. Effects of seawater exposure on mechanical properties of FRPs

Various studies on the effect of moisture and seawater exposure on mechanical properties of composite materials are reviewed. The absorbed moisture influences all components of composites, including fibers, matrix, and fiber/matrix interface. Studies showed that the presence of water in the composite could result in both chemical and physical changes in composite materials. In general, the mechanical properties degrade with moisture environments and elevated temperature in the long term. However, the extent of degradation is a result of a complex interaction of all environmental factors and varies greatly from one composite material to another. Therefore, it deserves further investigation on the behavior of BMI composite for design applications.

### 3. Life prediction method based on time-temperature superposition

The procedures of an Accelerated Testing Method (ATM) and some similar predicting methods and their applicability for different composites with environmental effects are reviewed in this chapter. Properties like static strength,

creep life and fatigue strength under arbitrary frequency, stress ratio and temperature can be predicted based on the methodology. One of the key steps in those methods is to obtaining shift factors through constructing master curve of DMA results. Unfortunately, there is no well-established shifting method or mathematical expression for calculating the shift factors. Thus, the shifting procedure is a major source of error in the utilization of time-temperature superposition principle.

#### 4. Effects of moisture absorption on fatigue behavior of fiber-reinforced plastics

The major damage mechanisms of composites during fatigue loading and several fatigue life prediction models are summarized. Most of the studies showed that water attacks the matrix material and the fiber/matrix interface, facilitating water diffusion of the composite material, which would reduce the fatigue life. However, the absorbed moisture also softens the material, improving the fatigue strength and life with less longitudinal cracks created. Therefore, the effects of marine environments and the use of prediction model for BMI composite need further investigations.

#### 5. Effects of marine environments on the delamination behavior of fiber-reinforced plastics

Numerous past studies have shown that hygrothermal conditions have significant effects on the interlaminar fracture toughness of composite laminates. However, the results vary considerably with materials, fluids and absorption conditions. Some researchers pointed out that this could be the result of the interaction of several competing effects, such as weakening of fiber/matrix interface, softening of matrix material, fiber bridging effects, etc. Experimental data reduction methods for measuring interlaminar fracture toughness of composite materials are also discussed. Finite element analysis using cohesive zone models (CZM) is introduced in this report for simulating delamination growth in composite materials. However, the accuracy of CZM simulation largely depends on the accuracy of fracture toughness at each mode and the mixed-mode delamination criterion. Despite its great importance, very few studies were conducted on characterizing the complete fracture behavior of

composite laminates under mode I, mode II and mixed-mode I/II loadings together with the influence of hygrothermal environments.

## **Chapter 3 Material and Specimen preparation**

This chapter introduces the prepreg material system and the fabrication procedure of the laminates used in this study. The specimens conducted for each experiment and their conditions are summarized at the end of the chapter.

### **3.1 Material**

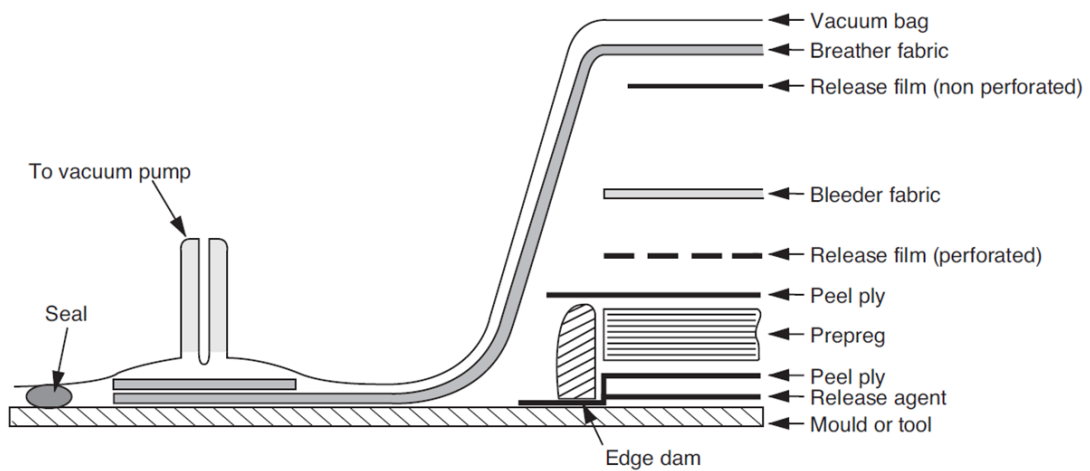
The prepreg used in this study was bismaleimide resin system Hexply F655 with premixed woven fiber glass HexForce 1581. The HexPly F655 resin system is a toughened two-phase thermoset, which cures through an addition reaction and suitable for standard autoclave processing. According to the datasheet [174] provided by the manufacturer, the neat BMI resin has an excellent long-term service life to 204°C and the glass transition temperature is 288°C, obtained by E' peak of DMA test under dry condition with standard curing procedure. The equilibrium moisture absorption of the resin is 4.1%. After proper curing, the resin has excellent property retention at 232°C for dry condition and 177°C for wet condition. Fiberglass HexForce 1581 has a fabric weight of 298g/m<sup>2</sup> and a thickness of 0.22 mm with weave type of eight harnesses satin, which is a very pliable weave and is suitable for forming curved surface. The woven fiberglass fabric also offers balanced strength and stiffness in both longitudinal and transverse directions with very good handling characteristics. It was given that the strength of the fabric is 50.8N/m in the direction of warping and 42.9N/m. The fiber volume content of the prepreg was 67% before curing.

### **3.2 Specimen preparation**

The general process of manufacturing composite material consists of several steps including preparing starting matrix materials, impregnating of fibers by the matrix, preparing the dimensions and shape of composite, processing the composite, curing the resin matrix system and removing the completed composite [2]. There are many production techniques developed for

manufacturing composite material, including contact molding, bag molding, autoclaving, resin transfer molding, vacuum molding, filament winding, etc. Autoclaving is primarily adopted for production of small numbers and able to provide excellent quality for high performance composites. In order to keep the quality of testing specimens from different batches as consistent as possible, autoclave technique was used in this study and the procedures will be elaborated in the following sections.

(a)



(b)

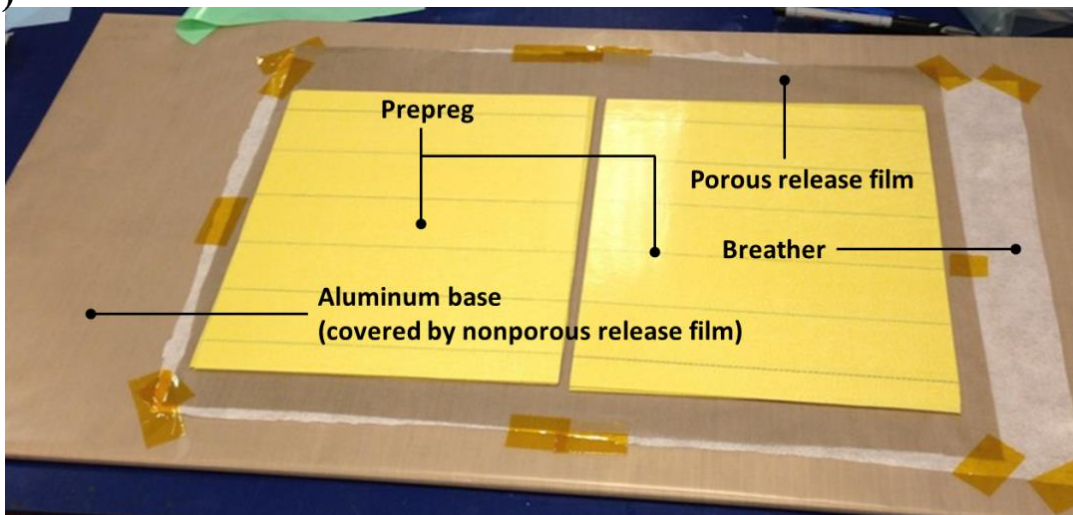


Figure 3.1. (a) An illustration of general vacuum bag lay-up (b) A photo of prepreg in preparation

### 3.2.1 Prepreg processing

Prepreg is a specially formulated resin matrix system with fiber reinforcements impregnated and ready to use in composite manufacturing process. This ensures the accurate and consistent proportion of resin and fibers. However, when thermosetting resin based prepregs are used, they need to be stored in refrigerator to avoid curing before final use. The shelf life of the BMI prepreg is 12 month at -18°C and 6 month at 4°C. In this study, the storage temperature was kept at around -20°C. Before the prepreg can be used for layup of the laminate, it should be kept dry in the room temperature environment at least 10 hours for defrosting.

In this study, the prepreg lay-up was handled manually because the prepregs were required to be cut in various shapes and the quantity for production was small. There are mainly two different ways of processing prepregs, namely vacuum bag oven and autoclave. The key difference between vacuum bag oven and autoclave is that the pressure exerted on the lay-up is only up to one atmosphere for the former while the pressure provided by the latter can be much higher with the pressure vessel. In addition, the autoclave normally has better control on temperature, pressure and vacuum than vacuum bag. Nonetheless, both techniques require a similar vacuum bag, which has a lay-up in general shown in Figure 3.1(a). However, the actual lay-up was specifically modified to achieve optimal quality for this study. Figure 3.1(b) is a photo of an actual vacuum bag in preparation where only the bottom half had been assembled. The components of the vacuum bag lay-up is listed from base to top and a brief introduction of the role of each layer is presented as follows:

1. A smooth flat aluminum plate with a thickness of 8mm served as the base upon which the prepregs were cured.
2. A sheet of nonporous release film is laid above the aluminum plate preventing further flow of excessive resin onto it. This layer of nonporous film kept a clean and smooth base surface, and it can be easily replaced after several productions.
3. Two layers of thin breather fabrics, which would absorb the excessive matrix leaking out of porous release film, were put on top of the

nonporous release film. Another purpose of using the breather fabrics was to regulate the flow of matrix to obtain desired fiber volume.

4. A sheet of porous (perforated) film covered the breather fabrics allowing free flow of matrix to breather fabrics and release of cured product. This film together with breather fabrics controlled the surface roughness of the composite product.
5. Eight or sixteen layers of prepregs were stacked and rolled firmly together after peeling off the polythene protectors and laid on release film. Normally, two pieces of stacked prepregs were placed in parallel with a small gap where a small piece of prepregs attached with thermocouple was placed in between. The thermocouple detected the true curing temperature during the process and gave feedback to the autoclave.
6. A sheet of Porous (perforated) film covered the prepregs allowing free flow of matrix and release of cured product.
7. Two layers of thin breather fabrics were put on the porous release film.
8. A smaller aluminum plate with a thickness of 8mm wrapped with nonporous release film was put on top of the breather fabrics in order to create evenly distributed load and hence achieved at surfaces on both sides of composite component.
9. A vacuum bag, which can withstand high curing temperature, was sealed with sealant tape to remove the air in the bag.

After the preparation of vacuum bag was completed, it was important to check the vacuum bag to be tightly sealed and leak-free before proceeding to the next step. The assembled vacuum bag was then placed in an autoclave. Figure 3.2 (a) shows a photo of autoclave used in this study and Figure 3.2 (b) shows the working principle of autoclave. Autoclave is a pressure vessel in which the vacuum, pressure, heating rate and curing temperature for processing the composite are controlled. The pressure of autoclave is able to reach much higher level than that of vacuum bag. The autoclave is also designed to allow gas circulation evenly distributed the temperature. As a result, the autoclave is able to produce thick and complex composite part with excellent quality.

Nevertheless, the downside of employing this technique is that the procedure is expensive and time consuming.

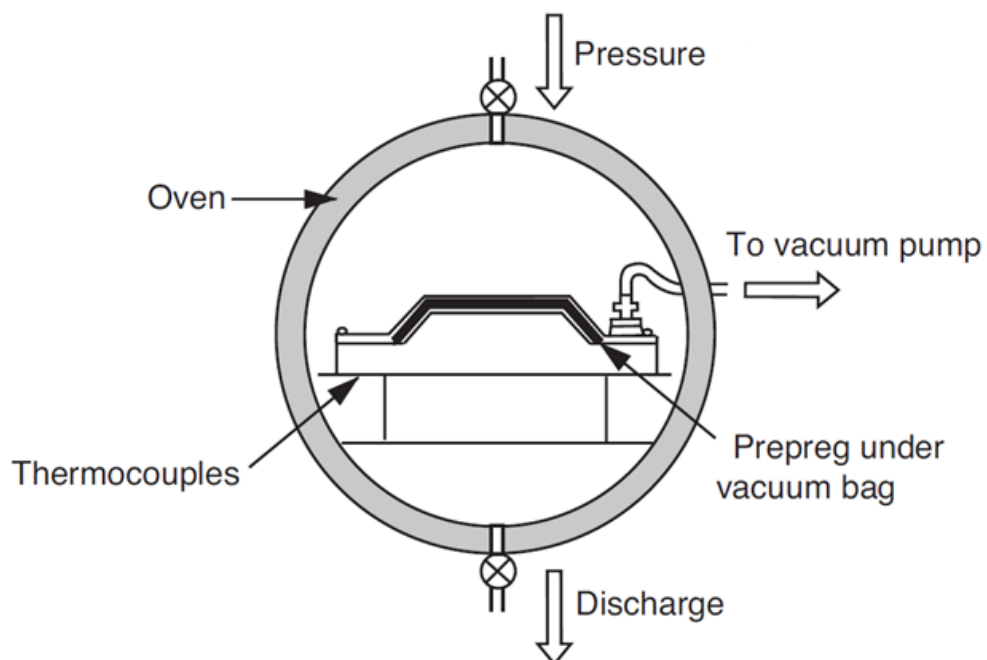


Figure 3.2. (a) Autoclave (b) Illustration of working principle of autoclave



In this study, all the curing process of preregs followed the standard cure cycle recommended by Hexcel shown by Figure 3.3.

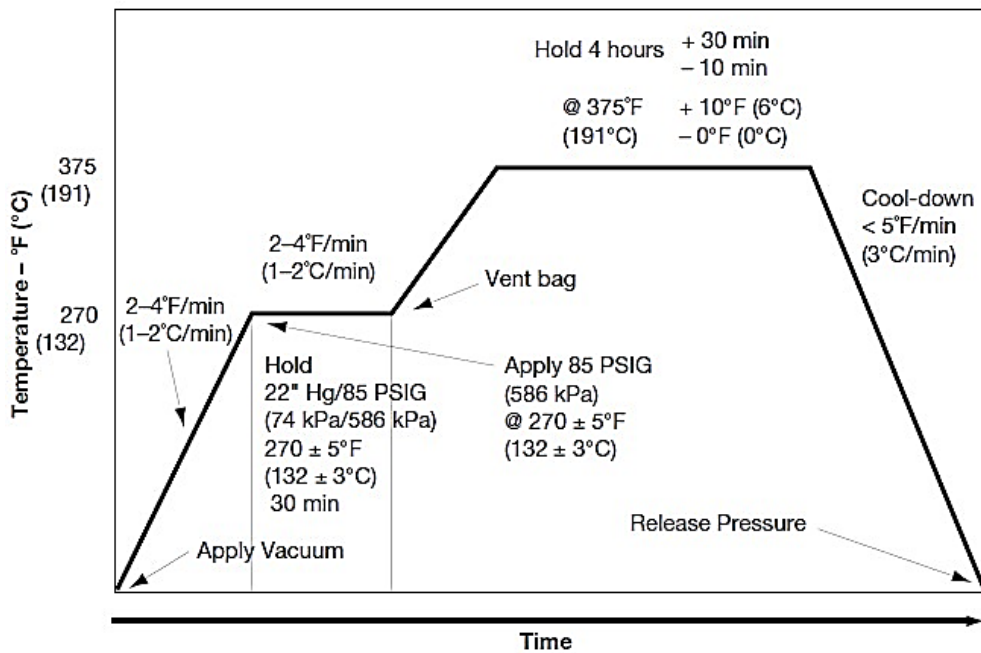


Figure 3.3. Cure cycle of autoclave process

- (A) Apply vacuum -22 inches Hg; increase the temperature at 1.5°C/min from room temperature to 132°C.
- (B) Apply 85 PSI pressure; hold vacuum and temperature at 132°C for 30 minutes.
- (C) Vent the vacuum bag; hold pressure at 85 PSI; increase the temperature at 1.5°C/min from 132°C to 191°C.
- (D) Hold pressure at 85 PSI and temperature at 191°C for 4 hours.
- (E) Hold pressure at 85 PSI and decrease the temperature at 3°C/min from 191°C to 66 °C.
- (F) Release pressure; let the laminate naturally cool down for 12 hours.

The post cure process was carried out by 6 hours of heating at 243°C. The composite laminates after post cure were cut into strips of rectangular specimens by water-jet cutting. The water-jet cutting is less likely to cause damages such as micro cracks and minimizes heat effect to the composite. The

tolerance of cutting was maintained at 0.1mm throughout this research. Specimens with smaller dimensions were then cut from rectangular strips using diamond cutter. For convenience of identification, the specimens cut along weave direction with 8 layers and 16 layers are referred as  $[(0^\circ, 90^\circ)]_8$  and  $[(0^\circ, 90^\circ)]_{16}$  specimens respectively. Some of the specimens with 8 layers were cut and tested in the way that the weave direction of all plies at  $45^\circ$  off the loading axis and they are referred as  $[(+45^\circ, -45^\circ)]_8$  specimens.

### 3.2.2 Preparation of artificial seawater

The artificial seawater, which contains 3.5% salinity, was prepared by dissolving sea salt into water. Specimens were then soaked into the artificial seawater solution in plastic containers and kept in freestanding oven to maintain the required temperature. Thermocouple was attached to the container in order to measure the real water temperature. The temperature variation of the artificial seawater was less than  $2^\circ\text{C}$ . The salt water was changed with fresh solution every 2-3 weeks because the evaporation of water would increase the salinity of the artificial seawater.

### 3.2.3 Desiccation of specimens

Before all the tests, specimens were desiccated in vacuum oven at  $80^\circ\text{C}$  for over 48 hours and taken out to weigh regularly. The specimens were not considered to be “dried” until the averaged weight change of the specimens was less than 0.01% between two consecutive measurements. The “dried” specimens were then stored in dry cabinet to minimize moisture absorption from the ambient environment before any tests.

## **3.3 Summary of the tested specimens**

Table 3.1 to Table 3.3 give brief summaries of the specimens and conditions conducted for each experiment type. The details of specimen geometries and experimental configurations will be described in the next chapter.

Table 3.1. Summary of basic composite properties of the specimens and the test conditions

Test methods	Specimen Lay-up	Immersion condition		Test conditions	No. of specimens
		Temperature	Time		
Diffusion	[(0°, 90°)] <sub>8</sub>	25°C, 50°C, 80°C	0-6000hrs	-20°C, 25°C	15
Tensile	[(0°, 90°)] <sub>8</sub>	50°C, 80°C	0-2700hrs 0-6000hrs	-20°C 25°C	>=120
Flexural	[(0°, 90°)] <sub>8</sub>	50°C	Dry, 1500hrs, 3000hrs	25°C-260°C	>=110
Shear	[(+45°, -45°)] <sub>8</sub>	50°C 80°C	Dry, 2800hrs, 6000hrs	25°C	>=20
DMA	[(0°, 90°)] <sub>8</sub>	50°C 80°C	0-6000hrs	30-250°C	>=40
Tension-Tension fatigue	[(0°, 90°)] <sub>8</sub> [(+45°, -45°)] <sub>8</sub>	50°C, 80°C 50°C, 80°C	Dry, 5000hrs	25°C; R=0.1, R=0.5 25°C; R=0.1	>=170

Table 3.2. Summary of interlaminar properties and the test conditions

Test methods	Specimen Lay-up	Immersion condition		Test conditions	No. of specimens
		Temperature	Time		
Mode I (DCB)	$[(0^\circ, 90^\circ)]_{16}$	50°C 80°C	Dry, 6000hrs	25°C	15
Mode II (ENF)	$[(0^\circ, 90^\circ)]_{16}$	50°C 80°C	Dry, 6000hrs	25°C	15
Mixed-Mode (MMB)	$[(0^\circ, 90^\circ)]_{16}$	50°C 80°C	Dry, 6000hrs	25°C	21
Fatigue Delamination (ENF)	$[(0^\circ, 90^\circ)]_{16}$	50°C	Dry, 2500hrs	25°C, R=0.2	~50

Table 3.3. Summary of Tension-tension fatigue test conditions

Test methods	Specimen Lay-up	Immersion condition		Test conditions	No. of specimens
		Temperature	Time		
Tension-Tension fatigue	$[(0^\circ, 90^\circ)]_8$	50°C 80°C	Dry, 5000hrs	25°C; R=0.1, R=0.5 25°C; R=0.5	~110
Tension-Tension fatigue	$[(+45^\circ, -45^\circ)]_8$	50°C, 80°C	Dry, 5000hrs	25°C; R=0.1 25°C; R=0.1	~60

## **Chapter 4 Experiments and Prediction**

### **Methodologies**

A brief review of various test methods, the derivations of mechanical properties and prediction approaches used in this study are presented in this chapter. For each test method, there is a general introduction of purpose and experimental configurations, followed by the necessary procedures of conducting the test and calculations of mechanical properties or parameters.

#### **4.1 Moisture diffusion test**

Moisture diffusion test is to characterize the rate and amount of liquid absorbed by the material when it is immersed in artificial seawater. The artificial seawater was prepared with salinity of 3.5%, and the  $[(0^\circ, 90^\circ)]_8$  specimens had dimensions of 200 mm by 15 mm. In the moisture absorption test, the dried specimens were soaked in the artificial seawater in plastic containers stored at three different temperatures: 25°C (Room temperature), 50°C and 80°C. Except for the 25°C environmental temperature, the other containers were kept in ovens to maintain the temperature. Immersing samples in water is the worst possible moisture attack, which is also the most likely simulation to real cases for marine applications. The change of mass of the specimens was monitored at various time intervals. Normally, the specimens were weighed more frequently at the beginning of the test when the absorption rate was relatively high. During the weight measuring of the specimen, the specimens were removed from the seawater, wiped clean with tissue papers, and rested for 5 minutes before weighed by an analytical balance with a resolution of 0.0001g. In this study, five specimens with similar weights after desiccation were chosen to get the average value of the water absorption for each immersion temperature. The water absorption is expressed as the percentage change in weight of the samples after immersing in seawater using Eq. (2.1). After the first stable reading was taken, the specimen was put back to the container.



Figure 4.1. Container with specimens in oven set at 50°C

## 4.2 Mechanical tests

### 4.2.1 Tensile test

Laminate ultimate tensile strength, Poisson's ratio and Young's modulus of the specimens were measured using procedures following ASTM D3039/D3039M-14 [175]. In this test, the specimen was clamped by grips of universal testing machine moving at constant speed. The applied tensile force on the specimen increased as the crosshead extended at 1mm/min until failure. The stress-strain response was monitored by the testing software throughout the procedure. The equipment used in this study for tensile test was MTS 810 elastomer test system. The tensile tests were conducted in 25°C and -20°C controlled by a climate chamber. The geometry of the specimen is shown in Figure 4.2. Strain gauges were attached on the specimen measuring the actual strain in the specimen. The tensile strength  $\sigma_f$  is calculated as:

$$\sigma_f = \frac{P_{max}}{bh} \quad (4.1)$$

where  $P_{max}$  is the maximum load applied in the test; b and h are the width and thickness of the tested specimen. The Young's modulus E is measured from the gradient of the linear section of stress-strain curve.

$$E = \frac{\Delta\sigma}{\Delta\varepsilon} = \frac{P}{bh\varepsilon} \quad (4.2)$$

where  $\varepsilon$  is the strain measured by strain gauges.

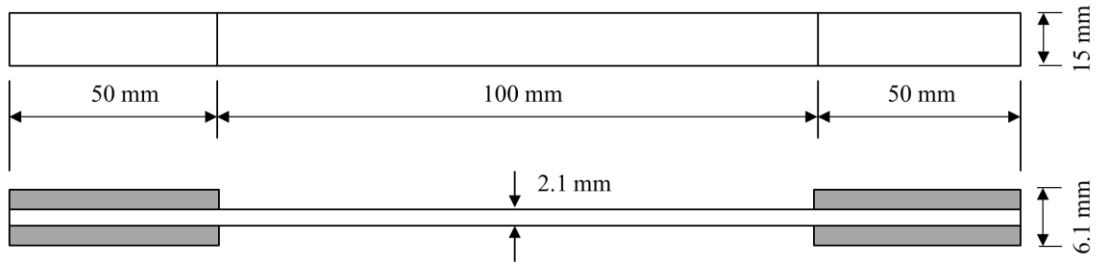


Figure 4.2. Geometry of the specimen for tensile test

Table 4.1 summarizes the testing conditions under which the tensile tests were performed.

Table 4.1. Tensile tests configurations

Immersion Condition		Test temperature	Crosshead speed
Temperature	Time (hrs)		
Dry	0	-20°C	1 mm/min
		25°C	
50°C(Wet )	1000,2800,6000	-20°C	1 mm/min
	200, 1100, 2800,6000	25°C	
80°C(Wet )	1000,2600	-20°C	1 mm/min
	1000, 2800,6000	25°C	

#### 4.2.2 Three-point bending test

The purpose of three-point bending test is to determine the flexural stress-strain response of the composite material. Important mechanical properties including flexural modulus, ultimate flexural strength and flexural failure strain were obtained in this test. The three-point bending tests followed ASTM D790-15e2 [176] and conducted by an Instron 5569 universal testing machine. Figure 4.3 shows the configuration of the test. The span to thickness ratio was roughly 20:1 as the thickness of specimen was about 1.8 mm. The cross head had a round contact shape with a diameter of 4 mm while the support feet had diameter of 2mm. In the test, the cross head went down and pressed onto the middle of the specimen with constant speed. The strain rate is linearly related to cross head speed, which is also constant. The force exerted on the specimen as well as the bending moment increased gradually depending on the speed of cross head. The force increased to certain level until it dropped dramatically which indicated the failure of the material. The highest flexural stress during the test, which occurred at the out most layer of the specimen, was determined as the ultimate flexural strength, and the time when the material started to fail was recorded as the failure time. The failure was determined at 40% drop of the flexural stress in this study since the specimen can no longer be considered as useful in structure with such load reduction. Thermocouple was attached to the base of the fixture to ensure a good control on the actual temperature of the specimen in the environment chamber [177]. Figure 4.4 shows a photo of three-point bending test conducted inside a climate chamber attached to the testing machine. The flexural strength  $\sigma_f$ , which is the maximum stress of the specimen, is calculated as:

$$\sigma_f = \frac{3P_{max}L}{2bh^2} \quad (4.3)$$

where  $P_{max}$  and  $L$  are the maximum applied load and support span respectively. The flexural modulus  $E_f$  is calculated as

$$E_f = \frac{PL^3}{4\Delta bh^3} \quad (4.4)$$

where  $\Delta$  is the vertical deflection of middle point. The flexural strain is give as

$$\varepsilon_f = \frac{6\Delta h}{L^2} \quad (4.5)$$



The tests were conducted under different crosshead speeds and temperatures for both wet and dry specimens. Table 4.2 summarizes the testing conditions under which the three-point tests were performed.

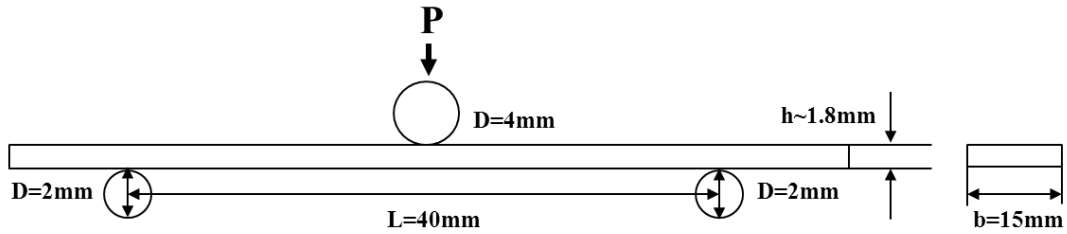


Figure 4.3. Three-point bending test configurations

Table 4.2. Three point tests conditions

Immersion Condition		Crosshead speed (mm/min)	Test temperature ( °C )
Temperature	time		
Dry	0	0.05	60, 105, 150, 195, 215, 230, 260
Dry	0	0.1	105
Dry	0	0.5	30, 60, 105, 150, 195, 215, 230, 245, 260
Dry	0	2	105
50°C(Wet )	1500 hrs	0.5	30, 105, 195, 215, 245, 260
	3000 hrs		30, 105, 150, 195, 210, 230, 245, 260



Figure 4.4. Three-point bending test

#### 4.2.3 Shear test

The shear properties of the material can be determined by clamping the ends of a V-notched specimen between two pairs of loading rails. Due to the anisotropic properties of composite materials, the in-plane shear property needs to be evaluated for material specification, research and development, quality assurance, and structural design and analysis. Factors affecting the shear response include material, methods of material preparation and lay-up, specimen stacking sequence, specimen conditioning, environment of testing, specimen alignment and gripping, speed of testing, temperature, and so on. The test was conducted on MTS 810 machine with an essentially stationary head and a movable head. The shear force is applied by a designed fixture with two fixture halves; each contains a side rail with three bolts applying pressure to secure the specimen during loading in tension. The test fixture and the

geometry of the specimen is shown in Figure 4.5 ( $d=31\text{mm}$  and  $t\sim 2\text{mm}$ ). The ASTM standard D7078/D7078M-12 [178] was adopted for this test.

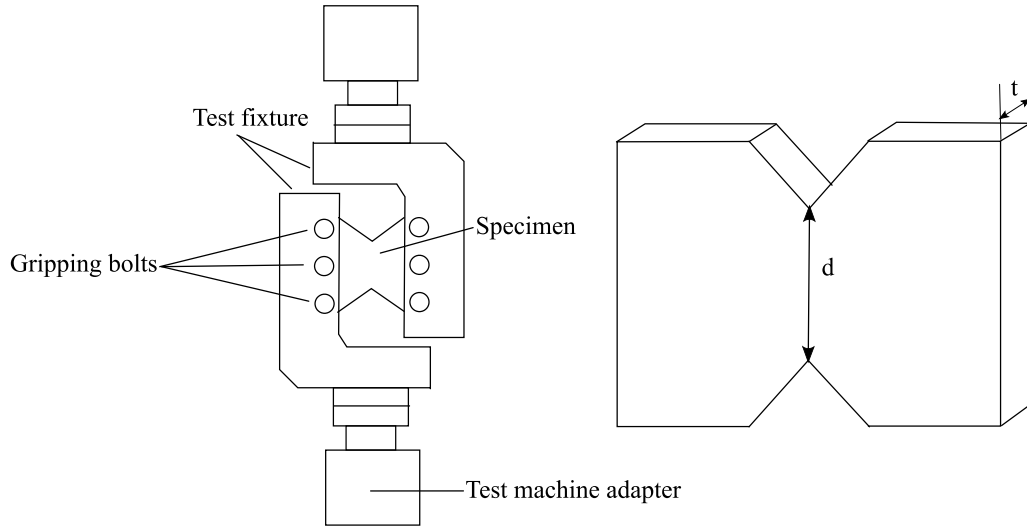


Figure 4.5. V-notched rail shear test fixture and specimen geometry

The ultimate shear strength is given by:

$$\tau_u = P_{max}/td \quad (4.6)$$

where  $\tau_u$  is the ultimate strength and  $P_{max}$  is the force. The engineering shear strain  $\gamma_i$  is expressed as

$$\gamma_i = |\varepsilon_{+45}| + |\varepsilon_{-45}| \quad (4.7)$$

where  $\varepsilon_{+45}$  and  $\varepsilon_{-45}$  are the strain in the  $+45^\circ$  and  $-45^\circ$  directions and the shear modulus is calculated as

$$G = \tau/\gamma_i \quad (4.8)$$

where  $\tau$  is the applied shear stress.

Alternatively, the shear stress can also be determined by conducting tensile tests on the  $\pm 45^\circ$  laminate, which was described in ASTM D3518/D3518M-13 [179]. In this study, some of the specimens were cut and tested in the way that the weave direction of all plies at  $45^\circ$  off the loading axis ( $[(+45^\circ, -45^\circ)]_8$ ), as shown in Figure 4.6. The geometry of the specimen is the same as that of specimen for tensile tests. The shear stress in the laminate along the weave direction is related to on-axis tensile stress  $\sigma_x$  as

$$\tau = \frac{\sigma_x}{2} |\varepsilon_x - \varepsilon_y| \quad (4.9)$$

where  $\varepsilon_x$  and  $\varepsilon_y$  are the strains in the tensile and transverse directions respectively. Table 4.3 summarizes the testing conditions under which the shear tests were performed.

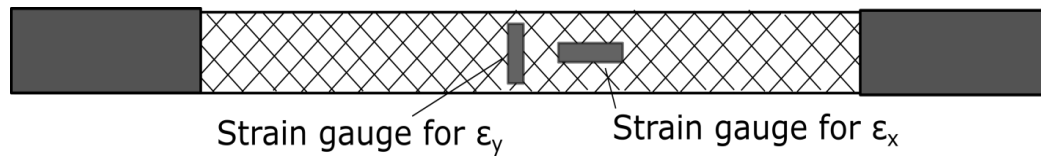


Figure 4.6. A  $[(+45^\circ, -45^\circ)]_8$  off-axis specimen for in-plane shear strength

Table 4.3. Shear tests configurations

Test method	Immersion condition		Test temperature
	Temperature	time	
V-notched rail shear	Dry	0	25°C
$\pm 45^\circ$ laminate tensile test		0	
	Dry	2800hrs,	
	50°C(Wet )	6000hrs	25°C
	80°C(Wet )	2800hrs,	
		6000hrs	

## 4.3 Interlaminar fracture tests

### 4.3.1 Static interlaminar fracture tests

#### 4.3.1.1 Specimen geometry

The fabricated laminate had an average thickness of 4 mm, and it was cut into specimens using a diamond wafer cutter. The dimensions of specimen, as shown in Figure 4.7, are 200mm in length and 20mm in width. During the layup, a thin (25 $\mu$ m) fluoropolymer film was inserted at the mid-plane of the laminate as an artificial crack starter. Each specimen contained a 65mm long insert and the exact location of the insert end was marked on both sides of the specimen with the help of an optical microscope. The insert film was left inside the specimen during the tests in order to reduce friction [21].

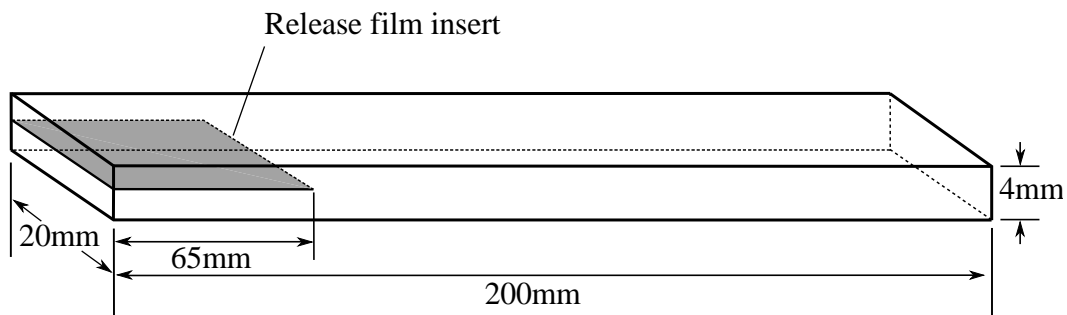


Figure 4.7. Test specimen geometry

#### 4.3.1.2 Experimental setup

The interlaminar fracture toughness of mode I, mode II and mixed-mode I/II were measured using the ASTM standard methods and the J-integral approach simultaneously. The mode I and mixed-mode tests were conducted on a Shimadzu universal testing machine, while the mode II tests were conducted on an Instron universal testing machine. Both machines had a load cell capacity of 10kN. The experimental setups are summarized in Table 4.4. The delamination tips on the specimen were marked using an optical microscope as shown in Figure 4.8. Both sides of the specimen were painted with thin layers of correction fluid from the delamination front as required by the ASTM standards to aid in visual detection of the delamination. A small paper ruler with an accuracy of 1mm was pasted on the specimen below the mid-plane to indicate the delamination length. Rotation marks, made by thin aluminum plates, were

attached on the specimen to indicate the rotation angles of the beams at loading points. A camera with 15 fps was set up to record the delamination length and the rotations of the marks during the test as shown in Figure 4.8. Pictures taken from the camera were able to capture the delamination front on the specimen with an accuracy of at least  $\pm 0.5\text{mm}$ .

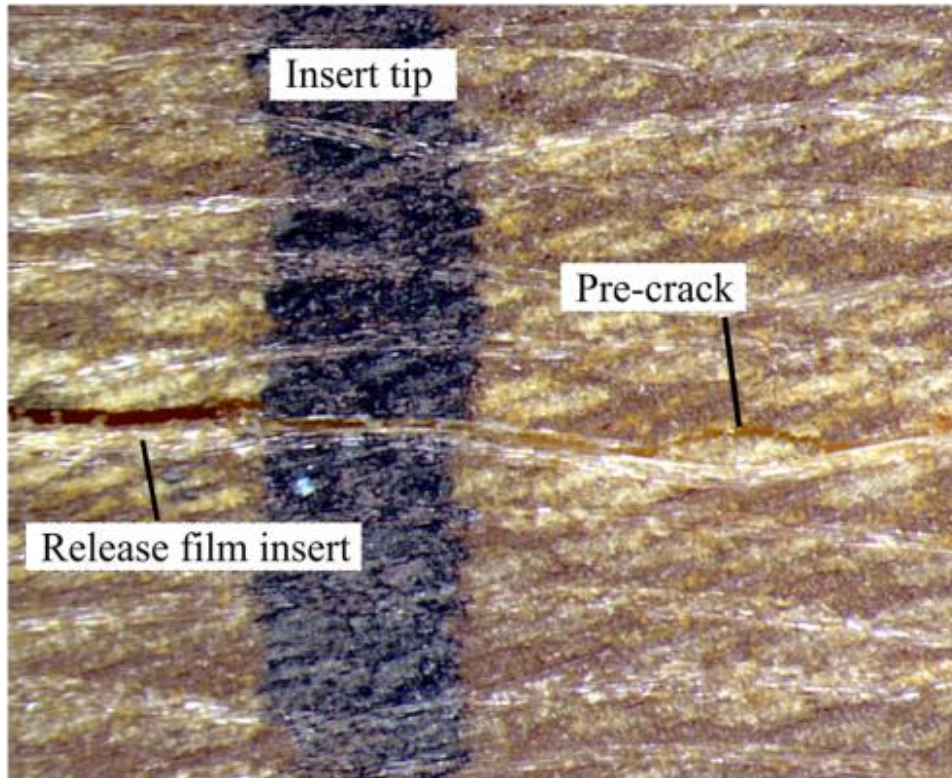


Figure 4.8. Microscopic image of the insert and pre-crack on the side view of a specimen

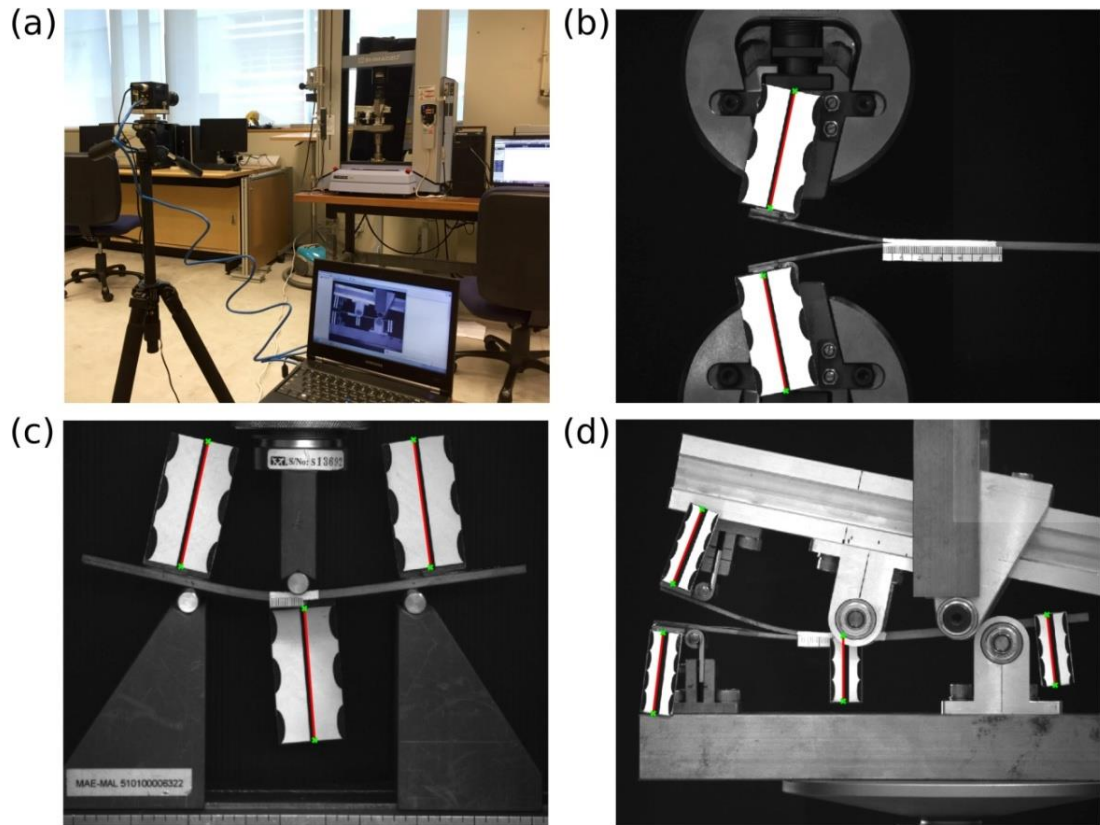


Figure 4.9. (a) Experimental setup and processed images taken from (b) DCB test (c) ENF test (d) MMB test (red lines indicate the marks detected by the program)

Table 4.4. Test setup parameters

Test method	Span (mm)	Initial delamination (mm)	Loading speed (mm/min)	Number of rotation angles	Image acquisition speed	Tab thickness (mm)
DCB	-	50	1.5	2	1frame / 2sec	2
ENF	100	35	0.5	3	1frame / 1sec	-
MMB	140	50	0.5	4	1frame / 2sec	2

#### 4.3.1.3 Delamination tests method based on ASTM standard

##### Mode I DCB test

The mode I energy release rate for DCB ( $G_I$ ) was measured using modified beam theory (MBT) recommended by the ASTM standard 5528-13[135],

$$G_{IC} = \frac{3P\delta}{2b(a+|\Delta|)} F \quad (4.10)$$

where the  $P$  and  $\delta$  are the applied force and load-point displacement;  $a$  and  $b$  are the delamination length and the specimen width respectively. The  $|\Delta|$  is a delamination correction term due to the rotation of DCB arms, which is found as an offset from the origin on horizontal axis by plotting the cube root of compliance as a function of the delamination length of the specimen.  $F$  is the large displacement correction factor

$$F = 1 - \frac{3}{10} \left( \frac{\delta}{a} \right)^2 - \frac{3}{2} \left( \frac{\delta t}{a^2} \right) \quad (4.11)$$

where  $t$  is the sum of the half hinge thickness and the half DCB arm thickness ( $h/2$ ). The delamination length from the artificial insert was 45mm, and the specimen was first loaded at 1.5mm/min to create a pre-crack around 5mm before unloading (see Figure 4.8). Then the specimen was loaded again at the same speed until the delamination propagated for at least 40mm. The values of interlaminar fracture toughness for the DCB specimens to initiate from artificial insert and pre-crack and to propagate were recorded. The calculation of the initiation values was based on the 5%/max criteria described by the ASTM standard, which normally produces the most reproducible results.

##### Mode II ENF test

The static Mode II delamination tests were conducted in accordance with the ASTM D7905/7905M to determine the  $G_{IIC}$  of the specimens and coefficients in the fatigue delamination propagation test [134]. The compliance calibration (CC) method was performed to obtain the  $G_{IIC}$  and pre-crack length. During the test, a specimen was loaded at three different positions, which include 40mm, 20mm and 30mm starter crack lengths respectively, and the bending span was set as 100mm ( $2L$ ). In the first two tests, the specimen was loaded up to around 50% of its failure load at 0.5mm/min so as not to create any



delamination damage. In the third test, the specimen was loaded until failure to create a pre-crack shown in Figure 4.8. The beam compliance is linearly related with  $a^3$ :

$$C = A + ma^3 \quad (4.12)$$

and the crack length can be calculated from compliance as:

$$a = \left( \frac{C-A}{m} \right)^{1/3} \quad (4.13)$$

where  $A$  and  $m$  are CC coefficients. The CC coefficients for each specimen were determined by linear regression analysis of the three starter crack lengths and the corresponding beam compliances by Eq. (4.12). Then, the specimen was reloaded at exactly the same position to 30% of its failure load, and the length of the pre-crack created is estimated using Eq. (4.13). The pre-crack length was also measured using an optical microscope on both sides of the specimen. The same procedure was carried out on specimens after creating the pre-cracks to evaluate the  $G_{IIc}$  of the specimen from pre-crack ( $G_{IIc,pre}$ ) except the starting delamination length was set as 35mm instead of 30mm suggested by the ASTM standard in order to achieve more stable crack propagation. The  $G_{II}$  is given as

$$G_{II} = \frac{3mP^2a^2}{2b} \quad (4.14)$$

where  $b$  is the width of the specimen. Values of  $G_{IIc}$  from the insert ( $G_{IIc,i}$ ) and the pre-crack ( $G_{IIc,pre}$ ) were estimated from the failure load using Eq. (4.14) and Eq. (4.13) respectively.

#### Mixed-mode MMB test

The interlaminar fracture toughness ( $G_T$ ) at different mixed ratios was measured by MMB tests described by ASTM standard D6671/D6671M-13[136]. According to the standard, the  $G_I$ ,  $G_{II}$  and  $G_T$  can be calculated as

$$G_I = \frac{12[P(3c-L)+P_g(3c_g-L)]^2}{16b^2h^3L^2E_{1f}}(a + \chi h)^2 \quad (4.15)$$

$$G_{II} = \frac{9[P(c+L)+P_g(c_g+L)]^2}{16b^2h^3L^2E_{1f}}(a + 0.42\chi h)^2 \quad (4.16)$$

$$G_T = G_I + G_{II} \quad (4.17)$$

where  $P, c, L$  and  $a$  are applied load, loading lever length, half span and delamination length respectively.  $\chi$  is the crack length correction parameter depending on material elastic properties.  $P_g$  and  $c_g$  are the loading apparatus weight and its center of gravity from the center roller, as shown in Figure 4.10(d). The bending modulus  $E_{1f}$  and crack length correction parameter were obtained following the ASTM standard. The mode mixity in the MMB test is defined as

$$\frac{G_{II}}{G_T} = \frac{G_{II}}{G_I + G_{II}} \quad (4.18)$$

The artificial delamination length of the specimen was 45mm, and was extended using DCB test procedure for 5mm prior to the MMB test to achieve a total length of approximately 50mm including the pre-crack (see Figure 4.8).

#### 4.3.1.4 Delamination tests method based on J-integral method

##### **J-integral analysis**

According to the general expression Eq. (2.59) derived in the previous chapter, the J-integrals are evaluated separately for the closed form solutions of DCB, ENF and MMB tests. For the DCB test shown in Figure 4.10 (b), the  $J_{DCB}$  is expressed as [137]

$$J_{DCB} = \frac{P}{b} (\sin\theta_A - \sin\theta_B) \quad (4.19)$$

where  $P$  is the magnitude of the applied load at the crosshead.

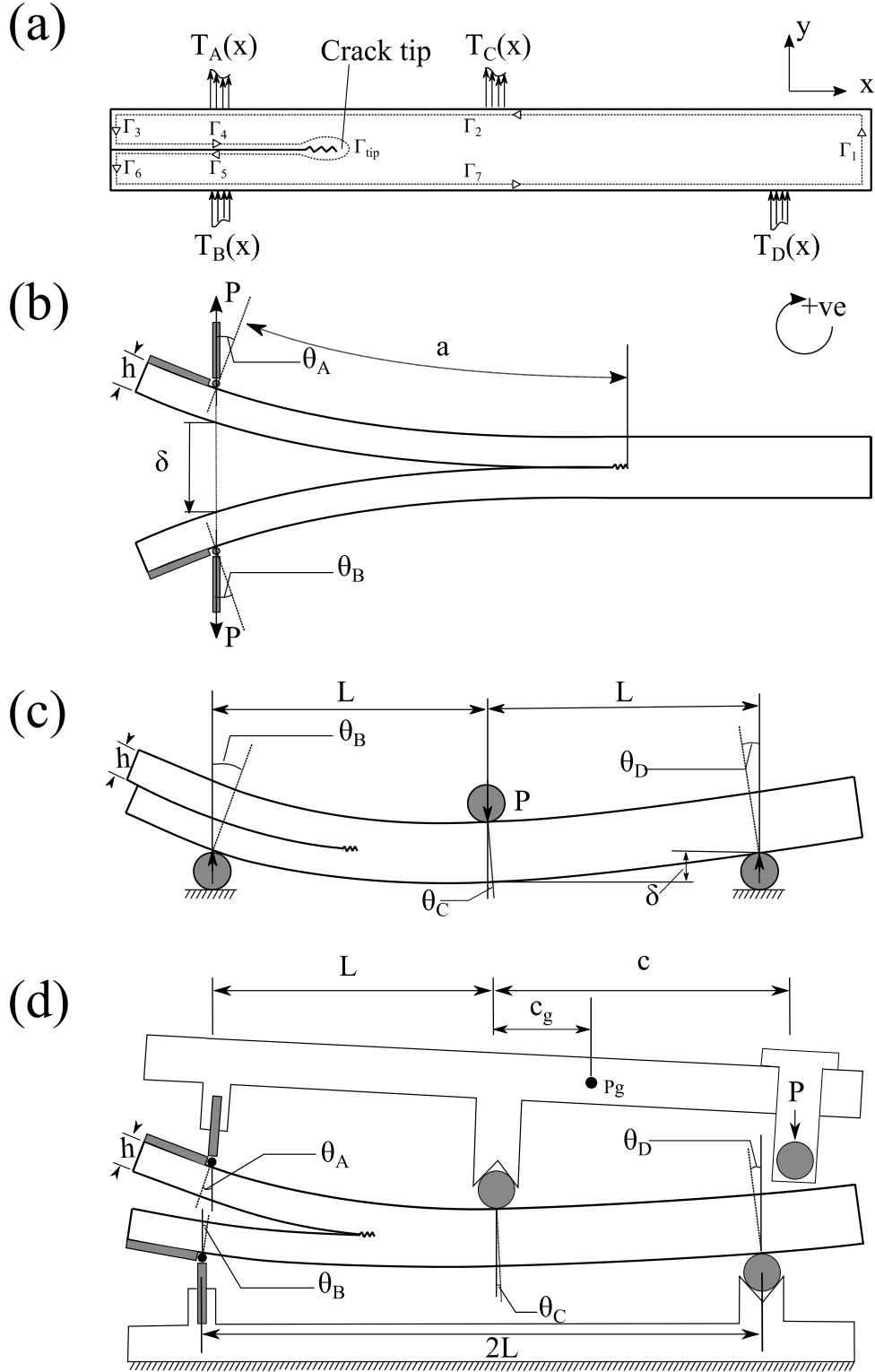


Figure 4.10. Definition of (a) the integration path and the loadings and rotation angles for (b) DCB specimen (c) ENF specimen (d) MMB specimen

For the ENF test shown in Figure 4.10(c), the forces on the specimen can be expressed by the loading  $P$  on crosshead based on the static equilibrium of the experimental setup, and the  $J_{ENF}$  is written as [133]

$$J_{ENF} = \frac{P}{2b} (\sin\theta_B - 2\sin\theta_C + \sin\theta_D) \quad (4.20)$$

Similarly, the  $J_{MMB}$  for mixed-mode bending in Figure 4.10(d) can be written as

$$J_{MMB} = \frac{P}{b} \left[ \frac{c}{L} \sin\theta_A + \left( \frac{1}{2} - \frac{c}{2L} \right) \sin\theta_B - \left( 1 + \frac{c}{L} \right) \sin\theta_C + \left( \frac{1}{2} + \frac{c}{2L} \right) \sin\theta_D \right] \quad (4.21)$$

where  $c$  and  $L$  are the length of level arm and half span respectively. However, when testing low stiffness material, the weight of the loading apparatus needs to be taken into consideration. Therefore, in the present study, a revised expression of Eq. (4.21) is derived to include the lever weight corrections [180]

$$J_{MMB} = \frac{1}{b} \left[ \left( \frac{Pc + P_g c_g}{L} \right) \sin\theta_A + \left( \frac{P + P_g}{2} - \frac{Pc + P_g c_g}{2L} \right) \sin\theta_B - \left( P + P_g + \frac{Pc + P_g c_g}{L} \right) \sin\theta_C + \left( \frac{P + P_g}{2} + \frac{Pc + P_g c_g}{2L} \right) \sin\theta_D \right] \quad (4.22)$$

where the  $P_g$  and  $c_g$  are the loading apparatus weight and its center of gravity from the center roller as shown in Figure 4.10(d). In this case, the weight of the lever contributes to  $J_{MMB}$  about 2-4%, but the effect could be more significant if the fracture toughness of the material is lower. To be consistent with the ASTM standard, the weight correction should be made when the weight of attached loading apparatus ( $P_g$ ) is more than 3% of the maximum applied load in the test, and it should be made for all tests if any test in a series of tests requires the correction.

As a result, the evaluation of interlaminar fracture toughness for mode I, mode II and mix-mode I/II only requires 2, 3 and 4 rotation angles values synchronized with the applied load respectively. In this approach, inputs required by ASTM standards such as material elastic properties, specimen compliance and delamination length are not needed.

## Image-processing algorithm

The image-processing method described in [143] used different colors to distinguish the rotation of ribs glued to the specimen from the white background, which can be easily affected by aliasing and distortion of the image. Moreover, the method took only two mid-points from the ribs to calculate the rotation of the ribs. It also results in relatively long ribs to ensure the accuracy of the measurement. A simpler and more reliable image-processing program was developed using MATLAB in this study. Light rectangular marks printed with the pattern shown in Figure 4.9 (b), (c) and (d) were designed to indicate the rotation of the specimen. The program first captures all the boundaries of a greyscale image taken by the camera through detecting the discontinuities of brightness. All the straight lines of the edges are then extracted using Hough transform. Hough transform is a commonly used technique to find straight lines in a digital image by carrying out a voting procedure in the parameter space. Each point  $(x_i, y_i)$  on the edge image is discretized to a polar representation  $(\rho_i, \theta_i)$  in parameter space, and an accumulator matrix that contains all the possible  $(\rho, \theta)$  values is created. For each edge point in the image, the corresponding element in the accumulator matrix is increased. As all points on the same line would have a common set of parameters  $(\rho, \theta)$ , the straight lines in the image can be obtained by searching for corresponding local maxima of the accumulator with certain threshold. The image is divided into certain bounding boxes, and each of them contains only one mark. Within a box, the printed straight lines on the mark can be easily picked out by the setting limits on the gradients and length of the detected lines. The undulate patterns on the mark were design to avoid the mark edges to be selected instead of the printed lines. The red lines were generated to show the detected lines on the marks by the program, where the rotation angles can be accurately calculated through its polar coordinates. The program was verified by measuring computer generated angle beams ranging from  $-14^\circ$  to  $14^\circ$  with an interval of  $1^\circ$ . Figure 4.11 shows the results obtained from three  $(\rho, \theta)$  resolutions, and the percentage errors are generally below 2%. The setting of  $\rho=1.5$  and  $\theta=\pi/180$  was found to have a good balance between accuracy and computational cost, and hence was used for all the tests. This method is more

accurate compared to the previous method as the angle is obtained through all the points on the line, and it has lower requirements on image resolution, light and material surface.

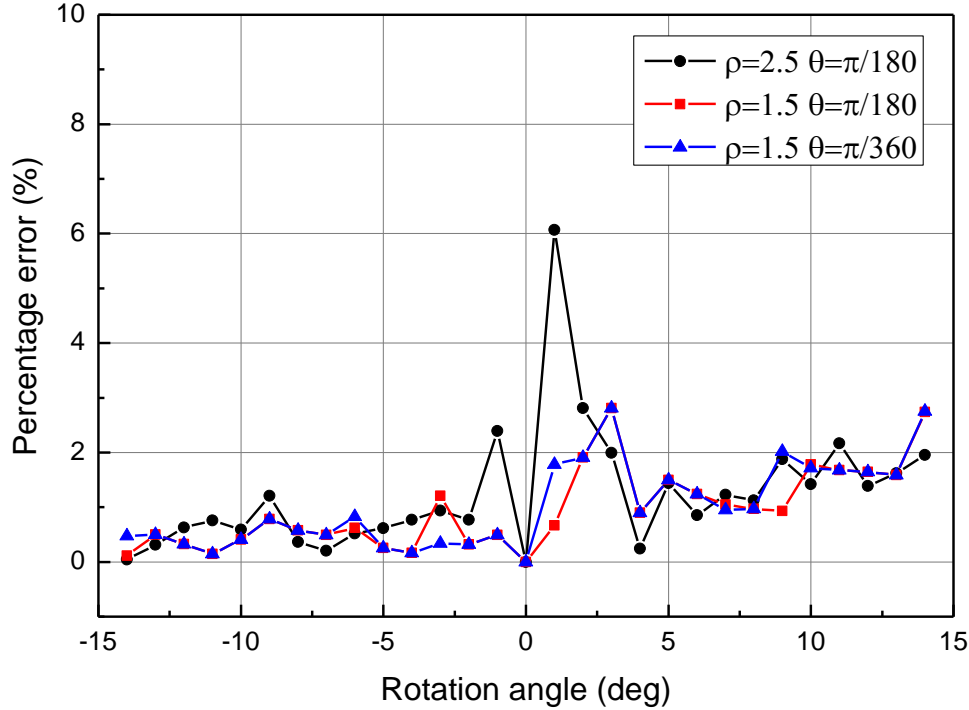


Figure 4.11. Validation test results of the image-processing program

#### 4.3.2 Fatigue delamination growth under mode II loading

##### 4.3.2.1 Three-point ENF fatigue analysis

End-Notched Flexure (ENF) test is a widely used experimental method to evaluate the Mode II strain energy release rate of composite materials. The commonly used ENF configurations are three-point bending (3ENF) and four-point bending (4ENF). Owing to the simple set-up and low interlaminar friction, 3ENF was chosen for static and fixed load fatigue tests in this study [181]. Russell and Street [182] derived an expression for the relation between crack length ( $a$ ) and 3ENF specimen compliance ( $C$ ) using small deflection classical beam theory,

$$C = \frac{2L^3 + 3a^3}{8EBh^3} \quad (4.23)$$

where  $E$  is the Young's modulus, and  $L$ ,  $B$  and  $h$  are the specimen geometries shown in Figure 4.12. The corresponding Mode II energy release rate can be expressed using the following equation:

$$G_{II} = \frac{P^2}{2B} \frac{\partial C}{\partial a} = \frac{9P^2 a^2}{16EB^2 h^3} \quad (4.24)$$

where  $P$  is the applied load on the loading roller. If shear deformation is taken into account, the beam compliance ( $C_{TIM}$ ) can be modified using Timoshenko beam theory as,

$$C_{TIM} = \frac{2L^3 + 3a^3}{8EBh^3} + \frac{3L}{10G_{13}Bh} \quad (4.25)$$

where  $G_{13}$  is the shear modulus on 1-3 plane. However, the energy release rate  $G_{II}$  is found to be independent from shear modulus and the expression remains unchanged as Eq. (4.25) in plane-stress condition [183]. Given the material and specimen geometries of this study, the difference in the compliances calculated by Eq. (4.23) and Eq. (4.25) is less than 3% in the range of  $0 < a/L < 1$ . It is considerably small compared with the intrinsic scatter of experimental ENF results. Therefore, the derivations from classical beam theory are used throughout this study.

No standard test method for fatigue delamination growth has been established. Many researchers in the past used visual observation with a travelling optical microscope to measure the crack length at the side of a specimen. In this manner, the test may need to be interrupted periodically to record the crack lengths. Those tests were laborious and the scatter of crack measurements using high powered optical microscopes was large [131, 184]. Firstly, small delaminations and damages are hard to distinguish under the microscope. Secondly, the delaminations observed on the side of specimens are often not accurate since the crack tip may not be even throughout the width of the specimen. This problem is more significant in woven composites with undulating crack propagation pattern [185, 186]. Lastly, the delamination growth rate is very fast with high cyclic loading, which makes it extremely hard to record the propagation by observation. Moreover, the crack jump mechanism in woven composite makes the matter even worse. To overcome these disadvantages, an experimental compliance calibration (CC) approach is adopted in this study [173], which computes the effective crack length by Eq. (4.13) with specimen compliances obtained by load-deflection curves during fatigue tests [187-189]. A comparison between direct measurements and CC method was reported in a previous study for unidirectional CFRP laminates

revealing a good agreement in both techniques, with a maximum deviation of 10% [188]. The test set-up for this fatigue test is similar to the static test, which is shown in Figure 4.12. A specimen was loaded with a constant 3Hz sinusoidal cyclic force  $P$  using the MTS 810 servo-hydraulic system (see Figure 4.13). The loading ratio  $R$  is set at 0.2 to ensure a good surface contact and the applied load is in linear elastic region. The beam compliance is calculated as a function of cyclic count. The cyclic strain energy release rate  $\Delta G_{II}$  is given as,

$$\Delta G_{II} = G_{II,max} - G_{II,min} = \frac{9P_{max}^2 a^2}{16EB^2h^3} (1 - R)^2 = \frac{3mP_{max}^2 a^2}{2B} (1 - R)^2 \quad (4.26)$$

where  $G_{II,max}$  and  $G_{II,min}$  are strain energy release rates at the maximum force ( $P_{max}$ ) and the minimum force ( $P_{min}$ ) of the cyclic loading respectively;  $m$  is the CC coefficient obtained in previous static tests. The initial crack length  $a_0$  was tentatively set as 25mm in order to keep the influence of friction on strain energy release rate less than 5% [188]. However, the actual initial crack length was corrected by the result after each fatigue test. The maximum length of crack was around 45mm ( $a/L \approx 0.9$ ) to avoid high resistance at loading roller and the sliding effect [190]. A thin cylinder restraint was placed on the specimen to avoid specimens shifting to the notched end with lower stiffness during the tests [181, 191]. Various ratios of  $G_{II,max}/G_{IIC,pre}$  were tested up to 0.6, above which the crack propagation was too fast to record and unstable. Second order polynomials were fitted to the crack length data with crack increment step of 1mm, and the corresponding crack growth rate  $da/dN$  was obtained as the derivative of the middle point of the parabola.

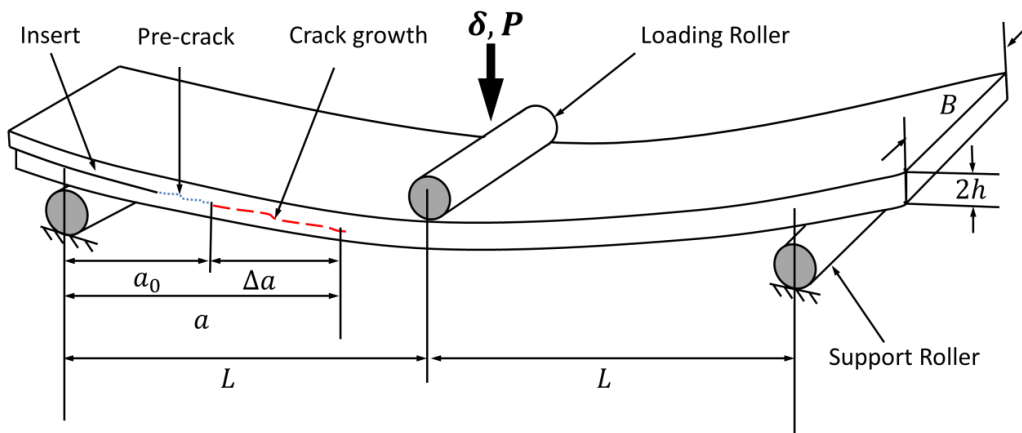


Figure 4.12. 3-point bend End-notched Flexure (3ENF) test configuration



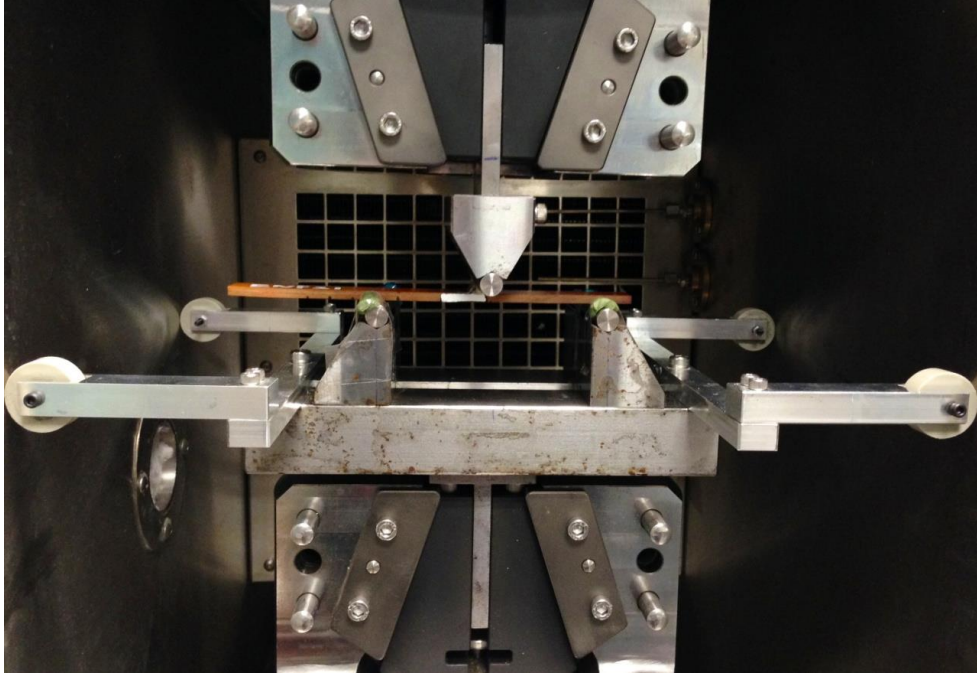


Figure 4.13. Mode II fatigue delamination test rig

#### 4.3.2.2 Noise reduction method

Since the data sets obtained from fatigue experiments were large and contained noise, a data reduction method was performed to reduce the noisy raw data. As mentioned in the past study [189], the crack length data were parsed by filtering any crack growth less than the value of twice of the noise level. However, this technique is sensitive to the selection of the initial point, and usually overestimates the crack length, as the parsed data tend to follow the upper limit of data set. In this study, an un-weighted moving average was used to estimate the crack growth without making parametric assumptions. The filtering algorithm can be expressed as,

$$a_s(i) = \frac{1}{2N+1} \sum_{j=i-N}^{i+N} a(j), \quad i > N \quad (4.27)$$

where  $a_s(i)$  is the smoothed value for the  $i^{th}$  crack length data point,  $a(j)$  is the  $j^{th}$  point from data set and  $2N + 1$  is the span. As shown in Figure 4.14, the method is able to reduce random background noise and catches the crack growth trend without losing necessary details. Approximately, with a span of  $2N + 1$  points, the background noise level can be reduced to  $s/\sqrt{(2N + 1)}$  while  $s$  is the original standard deviation of noise. In this study, the span was set as 15 for low cycle fatigue and 5 for high cycle fatigue.

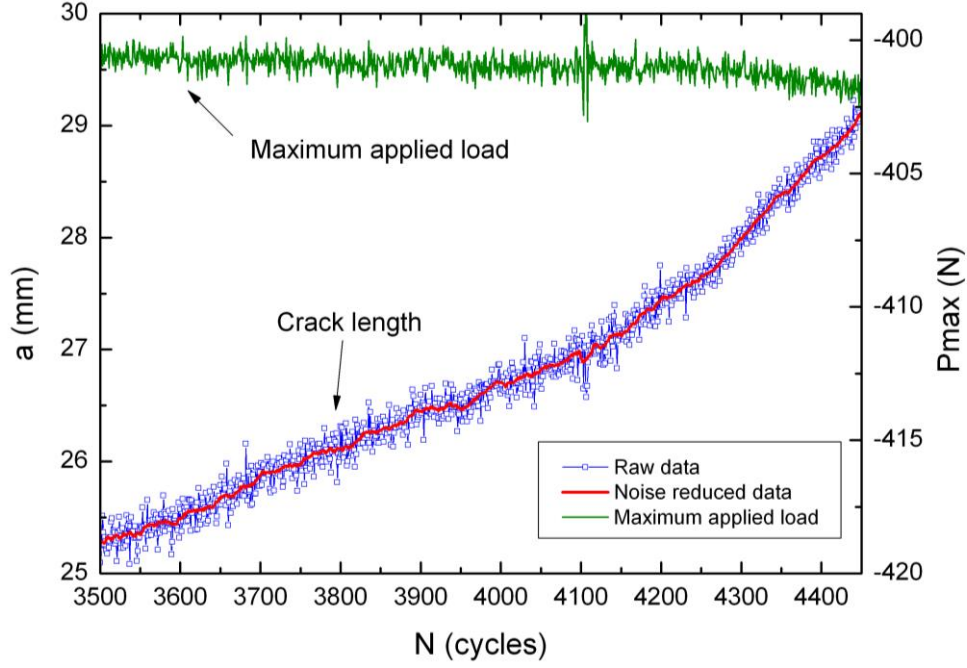


Figure 4.14. Typical plot of raw data and noise reduced data vs. fatigue cycles

#### 4.3.3 Finite Element Analysis (FEM) using Cohesive zone model (CZM)

The fracture behavior obtained from the experimental methods was simulated using the cohesive zone model to validate and evaluate the method. The simulations were performed in ABAQUS finite element code with the implemented cohesive elements. The DCB, ENF and MMB specimens were simulated. This simulation adopted the widely used bilinear softening traction-separation law, which was briefly introduced in Chapter 2 (see Figure 2.16). The 2D models of DCB, ENF and MMB specimens consists of two layers of 4-node plain strain elements CPE4I that are connected together with COH2D4 cohesive elements. The initial delamination of ENF model was set as surface contact. For the MMB specimen, the initial delamination is simulated by placing open cohesive elements along the length corresponding. These elements are capable of dealing with the contact conditions occurring for mixed-mode to avoiding interpenetration of the delamination faces. As shown in Figure 4.15, a quadratic stress failure criterion is used to determine the initiation of failure in the mixed mode loading

$$\left(\frac{\max(\sigma_I, 0)}{\sigma_{I, \max}}\right)^2 + \left(\frac{\sigma_{II}}{\sigma_{II, \max}}\right)^2 = 1 \quad (4.28)$$

where  $\sigma_{I,\max}$  and  $\sigma_{II,\max}$  are the interfacial strength of pure mode I and mode II respectively. Similarly, the displacement of mixed mode initiation is given as

$$\left(\frac{\delta_I}{\delta_{I,0}}\right)^2 + \left(\frac{\delta_{II}}{\delta_{II,0}}\right)^2 = 1 \quad (4.29)$$

where  $\delta_{I,0}$  and  $\delta_{II,0}$  are the damage onset of pure mode I and mode II respectively. Both the power law Eq. (2.61) and the B-K law Eq. (2.62) were used for the crack propagation evaluation, and the parameters were obtained from the experimental results. The parameter K, which governs the initial response of the element before damage ignition, is called the initial stiffness or penalty stiffness. If value of K is too low, it will introduce extra compliance to the bulk material. However, numerical problem may occur such as spurious oscillations of tractions, if it is too high [152]. In this study, a trial and error method was used and the K value was set as  $10^{15} \text{ N/m}^3$ , which was within the commonly used range for composites in literature [157]. The cohesive element size is one of the key factors for accurate simulation using the cohesive element model. A mesh should be refined enough to accurately capture the stress and strain field but increasing elements would result in higher computational cost. It is recommended that the cohesive zone should have at least three cohesive elements. One way to increase the cohesive zone length, which results in less cohesive elements required, is to lower the interfacial strength. Generally, the simulation results are not sensitive to the change of interfacial strength. However, if the interfacial strength is too low, significant stiffness loss occurs and the point of crack propagation will be delayed. It has also been pointed out that the cohesive zone length for mode I is generally very short, hence reducing interfacial strength has strong effect on the accuracy of the analyses. In contrast, the cohesive zone for mode II are generally much longer, thus, a similar reduction in mode II interfacial strength may not cause significant inaccuracies. Besides, larger element size often results in larger oscillation [155]. Therefore, different combinations of interfacial strengths and element size and the accuracy of their simulation results were investigated in this study. The properties and parameters needed for the simulation are listed in Table 4.5.

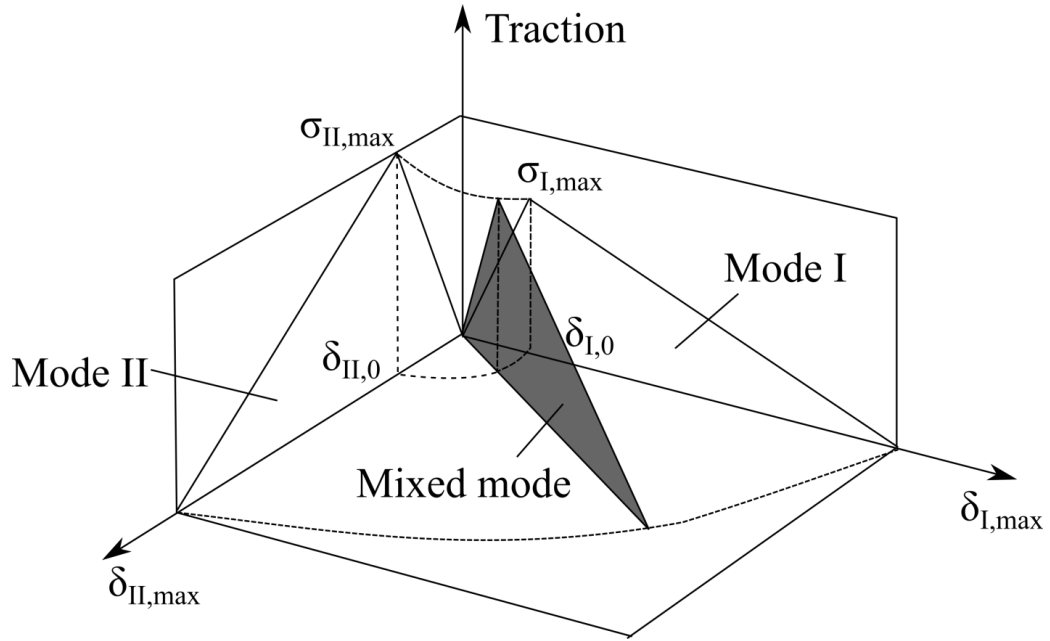


Figure 4.15. Schematic of mixed mode softening law

Table 4.5. Materials properties of woven E-glass/BMI

Laminate properties		Interfacial properties	
$E_{11}(MPa)$	22500	$G_{IC}(J/m^2)$	790
$E_{22}(MPa)$	22500	$G_{IIC}(J/m^2)$	1360
$G_{12}(MPa)$	4500	$\alpha$	1.2
$G_{23} = G_{13}(MPa)$	3800	$\beta$	1.2
$\nu_{12}$	0.13		
$\nu_{23} = \nu_{13}$	0.40		

## 4.4 Dynamic-mechanical analysis

### 4.4.1 Introduction

Dynamic mechanical analysis (DMA) is a technique used to study the viscoelastic behavior of polymers. A small oscillation stress is applied on the material as a function of time and the strain response is measured, allowing one to determine the complex modulus. The variation of the temperature and frequency of the load causes the complex modulus to vary, and the glass transition temperature can be evaluated through this approach. Suppose a sinusoidal force is applied to the test material, the time varying stress ( $\sigma$ ) and strain ( $\varepsilon$ ) are written as [50]

$$\sigma = \sigma_0 \sin(\omega t + \delta) \quad (4.30)$$

$$\varepsilon = \varepsilon_0 \sin(\omega t) \quad (4.31)$$

where  $\omega$  is frequency of strain oscillation,  $t$  is time, and  $\delta$  is phase lag between stress and strain.  $\sigma_0$  and  $\varepsilon_0$  are the maximum amplitude of stress and strain respectively. The complex modulus of the material  $E^* = \sigma/\varepsilon$  is defined as the ratio of stress to the strain of the material. It consists of storage modulus  $E'$  (real part) and loss modulus  $E''$  (imaginary part), which can be expressed as

$$E^* = E' + i E'' \quad (4.32)$$

where  $E' = \frac{\sigma_0}{\varepsilon_0} \cos \delta$  and  $E'' = \frac{\sigma_0}{\varepsilon_0} \sin \delta$ . The phase angle is calculated as

$$\tan \delta = \frac{E''}{E'} \quad (4.33)$$

The storage modulus, which represents the stiffness of a viscoelastic material, is proportional to stored energy. In a single load with reversible deformation, it is approximately equal to the elastic modulus of the material. The loss modulus, on the other hand, represents the energy dissipated during the loading cycle. The resulting strain and the stress are in phase for a perfectly elastic solid while there is a  $90^\circ$  phase lag for a purely viscous fluid. Viscoelastic materials has a phase lag somewhere in between as it exhibits both elastic and viscous characteristics. When the material enters the glass transition range where the change from glass state into rubber state occurs, the storage modulus drops

dramatically while loss modulus and  $\tan \delta$  rise to maximum [52, 192]. This phenomenon shown in Figure 4.16 can be used to determine the glass transition temperature of viscoelastic material.

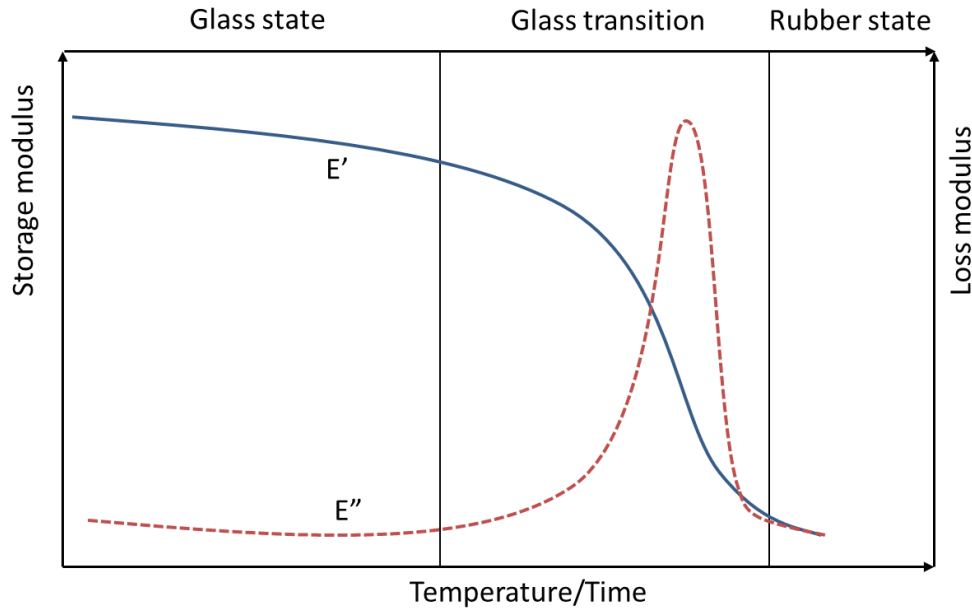


Figure 4.16. Schematic diagram of typical DMA curves for viscoelastic material

#### 4.4.2 Test configurations

In this study, the tests were conducted by Dynamic Mechanical Analyzer Q800. The composite was clamped on the fixture at one end and the load applied at the other end. The geometry deformation was set for single cantilever bending mode in strain control with amplitude of  $20\mu\text{m}$ . The specimen has a dimension of 40mm by 15 mm [193]. In order to minimize the possible error, the sample was tightened on the clamp using a torque wrench set at a constant value of 1.1 N-m (10 in-lb.) throughout all the tests and kept the clamping condition the same for all samples. There were two different testing modes used in this study and their configurations used in DMA were listed here

- Temperature sweep with fixed frequency:

This method was used to obtain the glass transition temperature of the BMI composite. The oscillation frequency was fixed at 1Hz while the

temperature was ramping from 35°C to 345°C at a heating rate of 3°C/min. There are mainly two methods to evaluate the glass transition temperature of a material by DMA spectra. A direct and simple way is to determine the transition temperature at which the peak of  $\tan \delta$  occurs. Another method is called the evaluation of modulus step. In this method, the glass transition temperature is measured as the temperature of the midpoint of inflectional tangent. The  $T_g$  determined by first method using peak  $\tan \delta$  is always higher than that by the modulus step method. In this study, the latter was adopted for evaluating the  $T_g$  of the BMI composites since, in some cases, the peak of  $\tan \delta$  on the DMA spectra was hard to determine.

- Temperature step with frequency sweep:

In this test, the DMA spectrum generated was used to construct the master curves and to determine the corresponding shift factors. The testing temperature increased from 35°C to 315°C with a step of 10°C. The storage modulus ( $E'$ ), loss modulus ( $E''$ ) and  $\tan \delta$  were measured at a series of frequencies (0.1Hz to 10Hz) while the temperature was kept as constant at each temperature step.

## **4.5 Long-term static strength Prediction**

### **4.5.1 Introduction**

Figure 4.17 is a schematic diagram of predicting long term static and creep strengths with effect of seawater absorption respectively. Critical steps of the methodology are presented in round boxes, while theory and assumptions in square boxes. In this study, the accelerated testing method based on time temperature superposition principle (TTSP) was adopted for the predictions of long-term creep strength. The master curve of static flexural strength was constructed by shifting results of three-point bending tests with constant strain rate at different temperatures, and the shift factors of static strength used were obtained by that of storage modulus based on DMA tests. The flexural creep strength was then constructed based on the master curve of static flexural strength using the theory of linear cumulative damage with kinetic crack growth.

The most important assumption of this approach is that the shift factors obtained from storage modulus are applicable for both static strength and creep strength as well. Applicability of the specimen with seawater absorption was also investigated. A prediction model suitable for BMI composites with seawater absorption is proposed in this study.

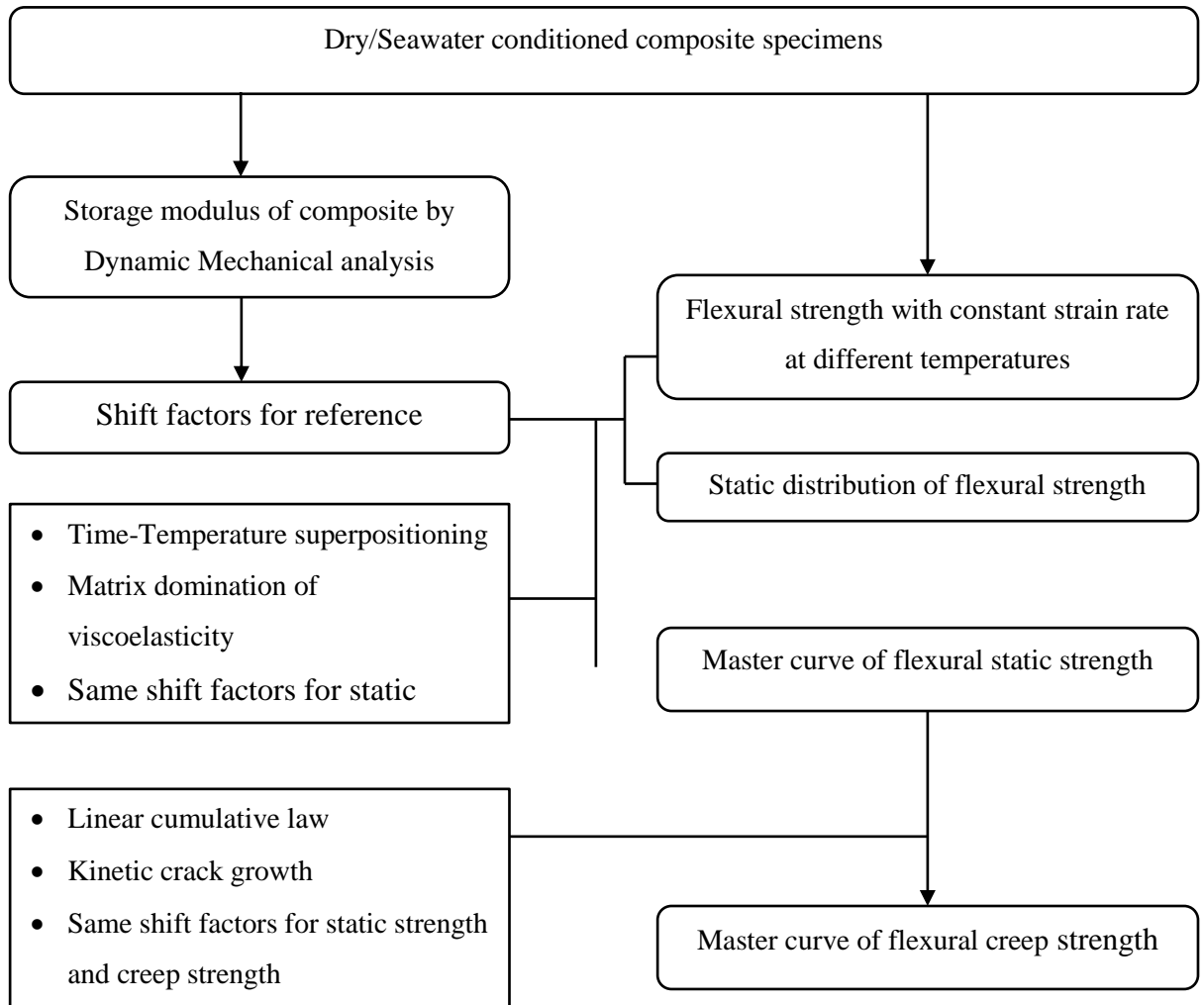


Figure 4.17. Schematic diagram of modeling master curves



#### 4.5.2 Master curve model of storage modulus

The Wiechert model shown in Figure 4.18 is often used to capture the overall response of viscoelastic material with a distribution of relaxation times. The relaxation modulus of the model is given by,

$$C(t) = E_e + \sum_i E_i \exp\left(\frac{-t}{\tau_i}\right) \quad (4.34)$$

where  $C(t)$  is the viscoelastic relaxation modulus and  $E_e$  is the equilibrium modulus.  $E_i$  and  $\tau_i$  are elastic modulus and relaxation time for the  $i^{\text{th}}$  mode. The storage modulus  $E'$  and loss modulus  $E''$  can be derived in terms of the relaxation distribution as,

$$E' = E_e + \sum_i E_i \frac{\omega^2 \tau_i^2}{1 + \omega^2 \tau_i^2}, E'' = \sum_i E_i \frac{\omega \tau_i}{1 + \omega^2 \tau_i^2} \quad (4.35)$$

where  $\omega$  is the applied circular frequency. When the frequency is small enough, the loss modulus is negligible and there is no phase lag between strain and resulting stress. Thus, in the long-term prediction, one can assume the approximation relationship  $E' \approx C(t)$ . Furthermore, the creep compliance  $S(t)$  can be approximately obtained from relaxation modulus as  $S(t) \approx 1/C(t)$  [74]. However, the creep response usually reaches its equilibrium with longer time than relaxation response.

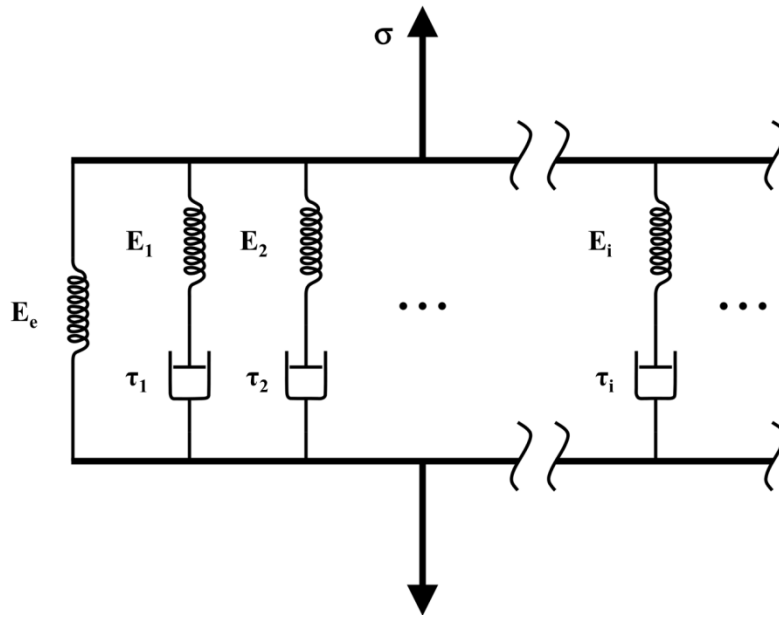


Figure. 4.18. The Wiechert model

For viscoelastic material, increasing the temperature has the same effect on reducing the viscoelastic relaxation time, which effectively accelerates the process. If the material is thermorheologically simple, all relaxation modes of the material scale in the same way with temperature, which can be written as,

$$\tau_i(T) = a_T \tau_i(T_0) \quad (4.36)$$

where  $T_0$  is the reference temperature and  $a_T$  is the temperature-dependent shift factor which defines the time-temperature relation. Therefore the storage modulus at temperature  $T$  can be determined from viscoelastic behavior at reference temperature  $T_0$  by substituting Eq. (4.36) into Eq. (4.35),

$$E'(\omega, T) = E_e(T_0) + \sum_i E_i(T_0) \frac{(a_T \omega)^2 \tau_i^2(T_0)}{1 + (a_T \omega)^2 \tau_i^2(T_0)} \quad (4.37)$$

The expression of storage modulus can be conveniently converted in terms of time variable  $t$  using the relation  $t = 1/\omega$ . As a result, the response curves at different temperatures can be shifted along the logarithmic time axis to construct the superimposed master curve. This is the well-known time-temperature superposition principle of viscoelastic material, and it is the key idea of predicting long-term properties of composite material by short-term tests. Mahieux and Reifsnider [52] developed a statistical model describing the storage modulus as a function of temperature. The idea of the model is based on the fact that the secondary bonds need to be broken and altered in every transition, and Weibull distribution was used to represent such breakages. The general formulation of the model for the materials with three transitions is given as,

$$E(T) = (E_1 - E_2) \exp\left(-\left(\frac{T}{T_1}\right)^{m_1}\right) + (E_2 - E_3) \exp\left(-\left(\frac{T}{T_2}\right)^{m_2}\right) + E_3 \exp\left(-\left(\frac{T}{T_3}\right)^{m_3}\right) \quad (4.38)$$

where  $T_1, T_2$  and  $T_3$  are the characteristic temperatures of each transition.  $E_i$  represents the instantaneous modulus at the beginning of each region and  $m_i$  is the Weibull distribution parameter of the bond breakage for the corresponding transition. This model is derived from the Wiechert model (Figure. 4.18), which offers the consistency for the following works. In dynamic loading, storage

modulus is both temperature and frequency dependent, but the current model can only deal with single frequency condition. Richeton et al. [194] improved the model by taking into account of frequency dependence, however the original model is sufficient for this study. With the instantaneous storage modulus  $E_{\bar{f}}(T)$  modeled as a function of temperature by Eq. (4.37) at fixed frequency  $\bar{f}$ , the storage modulus of the material at an arbitrary time  $t$  and reference temperature  $T_0$  is equal to the fixed frequency storage modulus function  $E_{\bar{f}}(T)$ ,

$$E_{T_0}(T) = E_{\bar{f}}(T) \quad (4.39)$$

The time-temperature shift factors  $a_{T_0}(T)$  at reference temperature  $T_0$  is defined as a function of temperature  $T$ ,

$$a_{T_0}(T) = \bar{t}/t \quad (4.40)$$

or it can be expressed in log form,

$$\log a_{T_0}(T) = \log(\bar{t}) - \log(t) \quad (4.41)$$

where  $\bar{t} = 1/\bar{f}$ . When the temperature is below  $T_g$ , the relaxation time can be correlated with the Arrhenius equation and the shift factors are expressed as Eq. (2.21) [50]. The temperature  $T$  of instantaneous storage modulus  $E_{\bar{f}}(T)$  in Eq. (4.39) can be obtained by inverting Eq. (4.40) to be a function of time  $t$ . As a result, a formulation of master curve of storage modulus at arbitrary temperature is derived here based on the expressions developed for the temperature dependence of shift factors and storage modulus[195].

#### 4.5.3 Automated shifting program

The accelerated testing method (ATM) for predicting long term durability of polymer composites is based on Time-Temperature superposition principle (TTSP). The theory part of TTSP has been discussed in literature review. Properties like static strength, creep rupture life can be predicted based on the methodology. When applying this method, one of the key steps is to obtain the universal shift factors for generating master curve of static strength, and then

predict the creep and fatigue behaviors. Unfortunately, there are no certain criteria or commonly agreed mathematical procedure, which would be able to determine the best or correct shifting given a set of experimental data. Other than shifting manually, there are several other procedures developed for calculating shift factors numerically. Most of them are based on the least-square method where shift factors are determined by minimizing the sum of square errors of horizontal distances between adjacent segments in the overlapping area. However, the disadvantages of those previous developed methods are discussed in section 2.3.3. Here, a two-stage shifting method using computer program for automated shifting is proposed in this study. With curves of creep compliance or storage modulus supplied to the program, the following results will be achieved:

- Master curve of creep compliance or storage modulus obtained at reference temperature after shifting based on TTSP
- Polynomial approximation of master curve
- A curve of time-temperature shift factors as a function of inverse of temperature.
- Time-temperature shift factors at each temperature.
- Reliability of the shift factors obtained.

The procedures of shifting creep compliance and storage modulus are almost the same, so the shifting algorithm is explained in the case of storage modulus as an example here. Before the shifting procedure starts, the storage modulus data at different temperatures are arranged as it is shown in Figure 4.19(a). Each set of the storage modulus data  $C_i$  is obtained at corresponding temperature  $T_i$ . Each point represents the storage modulus measured at certain frequency, which is reflected on horizontal axis as time ( $frequency^{-1}$ ). Then the set of data representing the lowest temperature  $T_0$  (the top set of data) is picked as the reference curve  $C_0$  to which all curves are shifted. Since the purpose of doing this procedure is to predict the long term effect, only right shifting is performed in this program though TTS principle is not restricted to one direction.

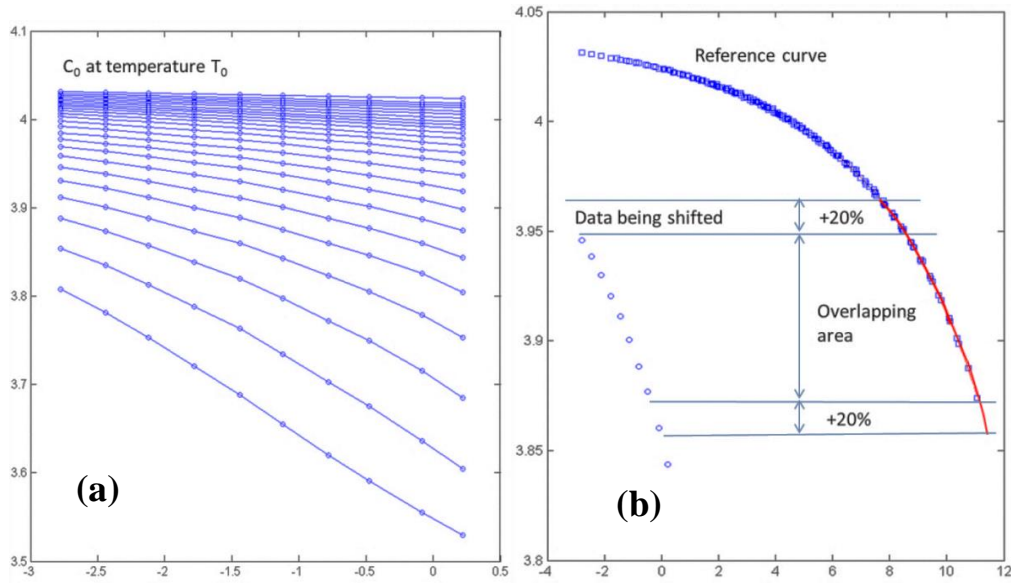


Figure 4.19. Automated shifting algorithm: (a) storage modulus at different temperatures (b) Shift the storage modulus at next temperature on to the reference curve

All the other curves are shifted in temperature increasing sequence to the reference curve. The reference curve is updated every time when a new set of data are mapped on it before the next group of data being shifted. As shown in Figure 4.19(b), the data represented by circles is about to be shifted to the reference data represented by squares. Firstly, the tail part of the master curve would have an overlapping area with the set of data being shifted, and the overlapping area is fitted with a third order polynomial shown by the red solid line in Figure 4.19(b). Only the tail part instead of the whole reference curve is fitted because the previous part of the master curve has little effect on mapping the current set of data to the curve. Moreover, the polynomial fitting with only tail part would give a more accurate result than fitting the whole curve. By experience, the part being fitted with the polynomial is extended by 20% of the overlapping area in order to have a better consistency connecting with previous data points. The manipulation also solves the problem, though it is rare, where the reference curve does not have overlapping area with next curve being shifted. Secondly, the average distance between data points being shifted to the reference curve in the overlapping area was calculated, and this distance was used as a rough shift factor in first stage. The accuracy of shifting at this stage depends on the number of data points and the distribution of horizontal

distances between them. Increasing the data density and arranging them evenly distributed on horizontal axis would enhance the effectiveness of the first stage shifting. The second stage is an adjustment with very small step based on the shift factors obtained in the first stage to find the optimum values. At each step, the Chi-square ( $\chi^2$ ) of the set of data points to the reference curve is calculated as,

$$\chi^2 = \sum \frac{(E'_i - \overline{E'_i})^2}{E'_i} \quad (4.42)$$

where  $E'_i$  and  $\overline{E'_i}$  are  $i^{\text{th}}$  experimental data point and corresponding value by polynomial fitted reference curve. The final shift factor is determined by least Chi-square [196]. A computer program was used to automate the procedure, and Figure 4.20 shows the flow chart of the shifting program.

In this shifting method, the curve fitting was able to use a simple 3<sup>rd</sup> order polynomial, as only the overlapping area instead of the whole master curve was considered for fitting. The first step in this two-stage fitting determines the rough shift factor directly using averaged distance, which largely saves the computational cost. The second stage with fine adjustments ensures the accuracy of the final shift factor results.

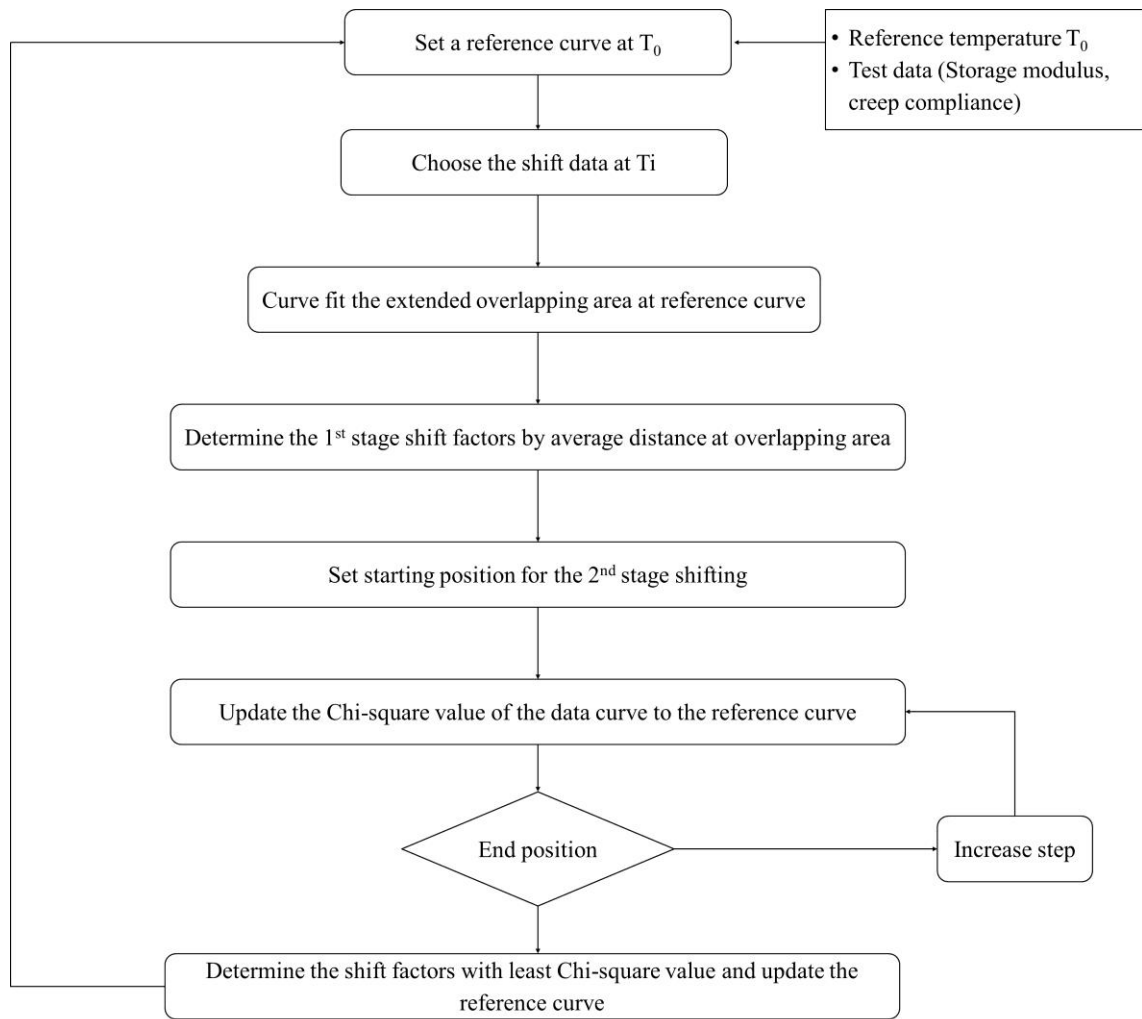


Figure 4.20. Flow chart for automated shift program

## 4.6 Fatigue test

### 4.6.1 Tension-tension fatigue test configuration

Fatigue test were conducted to investigate the damage development and fatigue life of the material under cyclic loading. The tests in this study focused mainly on macroscopic observations such as stiffness degradation, derivation of S-N curves and constant life diagrams (CLD). The equipment and specimen geometry for the fatigue tests, as shown in Figure 4.2 and Figure 4.6, were as same as those for the tensile tests. Specimens with fiber orientations of  $0^\circ$  and  $45^\circ$  were tested, and the off-axis angle ( $\theta$ ) is defined as the angle between the direction of loading and the warp direction of specimen. The tests were performed under tension-tension loading at various constant stress levels and

ratios. There are various factors which would affect the fatigue test results in experimental design such as loading pattern, control mode, stress ratio, testing frequency, wave form, testing temperature, etc. To avoid further complication, the major variables in this study were limited to stress ratio and stress levels. Constant amplitude loading pattern with force control were used throughout the whole research. The testing frequency and waveform were set to be 3-5Hz and tapered sine curve respectively for all the tests. The tapered sine curve allows the amplitude of cyclic loading to increase gradually at the beginning of the test so that the testing specimen would not be damaged due to sudden loading.

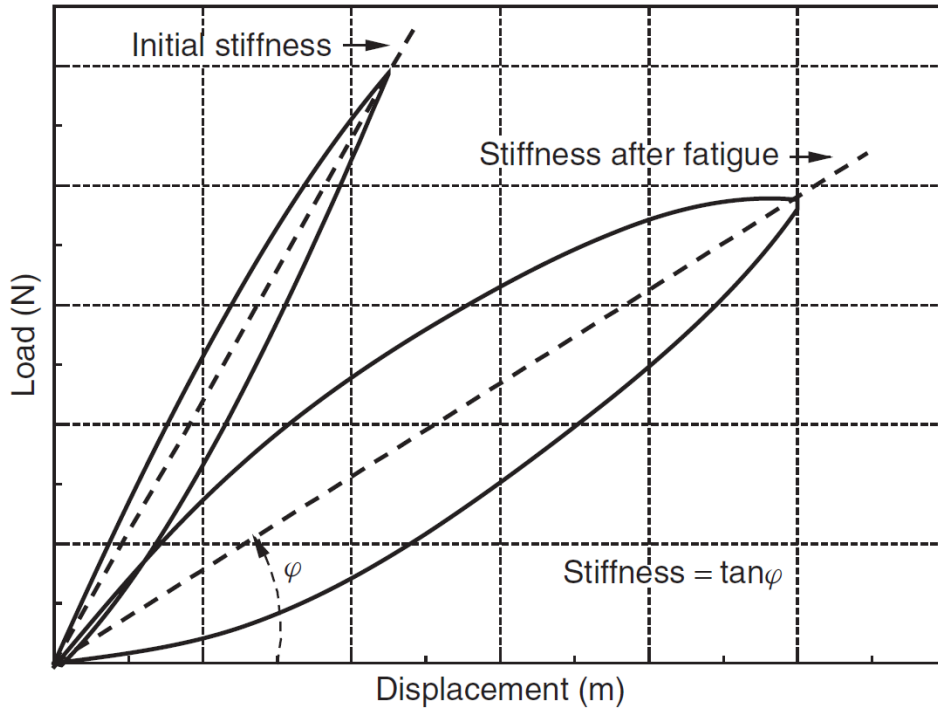


Figure 4.21. Constant amplitude cyclic loading [197]

The stress ratio  $R$  in fatigue test is given by,

$$R = \frac{\text{Minimum stress}}{\text{Maximum stress}} \quad (4.43)$$

As shown in Figure 4.21, the dynamic stiffness  $E$  of the specimen is approximately calculated as the slope of load-displacement curve:

$$E = \frac{F_{max} - F_{min}}{\Delta_{max} - \Delta_{min}} \quad (4.44)$$

where  $F_{max}$ ,  $\Delta_{max}$ ,  $F_{min}$ , and  $\Delta_{min}$  represent maximum applied force, deformation, minimum applied force and deformation of material respectively. The tests would be conducted on dry and wet specimens with different



immersion temperature, and at several stress levels for each stress ratio. The stress level is presented by the percentage of ultimate tensile strength. Table 4.6 summarized the testing conditions under which the fatigue tests were performed in this study:

Table 4.6. Fatigue tests conditions

Specimen Condition	Angle (°)	Immersion temperature (°C)	Stress Ratio	No. of stress levels tested
Dry	0	-	0.1	4
Dry	0	-	0.5	5
Dry	45	-	0.1	5
Wet	0	50	0.1	4
Wet	0	50	0.5	4
Wet	0	80	0.5	4
Wet	45	50	0.1	4
Wet	45	80	0.5	4

#### 4.6.2 Statistical pooling analysis of S-N curve

A two-parameter Weibull distribution is commonly adopted in characterizing the probability of failure for composite materials. Therefore, at  $i^{\text{th}}$  stress level  $S_i$ , the probability of the sample fails at  $N$  cycles can be described as

$$F_i(N_f) = P_i(N \leq N_f) = 1 - \exp \left[ - \left( \frac{N_f}{N_i} \right)^{\alpha_i} \right], i = 1, 2, \dots, n. \quad (4.45)$$

where  $\alpha_i$  and  $N_i$  are scale and shape factors of Weibull distribution for the  $i^{\text{th}}$  stress level. However, a large amount of samples and stress levels are required to determine the Weibull parameters for each  $S_i$  and, subsequently, plot the statistical S-N curves. To overcome this disadvantage, a data pooling procedure is adopted in the following analysis [111, 112]. A data set  $X$  is created by normalizing the number of cycles to failure of each sample  $N_{ij}$  (the  $j^{\text{th}}$  sample tested at the  $i^{\text{th}}$  stress level) with the corresponding shape factor  $N_i$ :

$$X_{ij} = \frac{N_{ij}}{N_i}, i = 1, 2, \dots, n, j = 1, 2, \dots, m_i. \quad (4.46)$$

where  $m_i$  represents the number of samples tested at  $i^{th}$  stress level. Assuming the newly formed data set  $X$  can also be described by a two-parameter Weibull distribution, the cumulative distribution function  $R(X)$  is written as,

$$R(X) = 1 - \exp \left[ 1 - \left( \frac{X}{X_0} \right)^{\alpha_f} \right] \quad (4.47)$$

where  $\alpha_f$  and  $X_0$  are scale and shape factors of Weibull distribution of the data set  $X$ . The value of  $X_0$  is unity in a perfect situation where the Weibull distribution assumptions are satisfied. In real case, to produce  $X_0 = 1$ , the value of characteristic number of cycles at each stress level needs to be adjusted as

$$N_i^* = X_0 N_i \quad (4.48)$$

where  $N_i^*$  is the adjusted characteristic number of cycles at  $i^{th}$  stress level. Fitting the adjusted  $N_i^*$  to an  $S - N_i^*$  relation, the numbers of cycles  $N$  with a failure probability of  $P_f$  at any specific stress level  $S$  can be obtained by Eq. (4.47). In the case of a linear S-Log N equation given in Eq. (2.43), the expression is given as:

$$N = 10^{\frac{S-b}{m}} \left[ -\log(1 - P_f) \right]^{\frac{1}{\alpha_f}} \quad (4.49)$$

#### 4.6.3 Stiffness degradation model

In this section, a stiffness degradation model is used modified from the work of Whitworth [119].

As mentioned in section 2.4.3, the Eq. (2.54) and Eq. (2.55) can be rearranged to express the normalized stiffness with respect to number of cycles  $\bar{E}(N)$  as:

$$\bar{E}(N) = \frac{E(N)}{E_0} = \left[ -h \log(N + 1) \left( \frac{E_n}{E_0} \right)^m + 1 \right]^{\frac{1}{m}} \quad (4.50)$$

where  $h = a \times m$ . The Eq. (4.50) can be used to obtain the stiffness degradation curve. However, it is unable to give a prediction on the failure of the material.

Therefore, a failure strain criterion is introduced here to estimate the probability of the material's fatigue life.

The applied stress level can be approximately related to the averaged failure stiffness  $\bar{E}_n$  as,

$$\frac{S}{S_u} = c_1 \left[ \frac{E_n}{E_0} \right]^{c_2} = c_1 \bar{E}_n^{c_2} \quad (4.51)$$

where  $c_1$  and  $c_2$  are determined experimentally. The ultimate tensile strength  $S_u$  of the material can be statistically expressed by a two-parameter Weibull distribution[198]:

$$P(S_u \leq z) = 1 - \exp \left[ - \left( \frac{z}{\beta_s} \right)^{\alpha_s} \right], z \geq 0 \quad (4.52)$$

where  $\alpha_s$  and  $\beta_s$  are the shape parameters and scale parameters respectively.

By substituting Eq. (4.51) into Eq. (4.52) and rearranging the expression, the statistical distribution of failure stiffness is given by

$$P(\bar{E}_n \leq x) = P \left[ \left( \frac{S}{c_1 S_u} \right)^{\frac{1}{c_2}} \leq x \right] = \exp \left[ - \left( \frac{S}{c_1 \beta_s x^{c_2}} \right)^{\alpha_s} \right] \quad (4.53)$$

The combination of Eq. (4.53) and Eq. (4.50) are used to evaluate the stiffness degradation and survival probability of the material under any stress level applied.

## Chapter 5 Experimental Results and Discussion

In this chapter, the experimental results are presented and analyzed. The water absorption behavior at different temperatures, seawater immersion effects on tensile, flexural, shear, viscoelastic properties, delamination behaviors and fatigue life are studied. Predictions models are also developed and predicted for long-term static and creep behavior of the composite materials in marine environment.

### 5.1 Moisture absorption in BMI composite

#### 5.1.1 Seawater absorption profile

Figure 5.1 presents the percentage weight change of the BMI composite immersed in seawater at 25°C (room temperature), 50°C and 80°C. Each data point represents the averaged value of four specimens weighed, and the error bars shows  $\pm 1$  standard deviations. The seawater absorption curves at different temperatures are quite similar. The water content increased rapidly in the initial stage following the Fickian diffusion behavior, and continued to grow slowly over the Fickian equilibrium. There is a relatively slow but clear second stage water absorption. At 6000 hours of immersion, the water contents in the room temperature and 50°C immersion specimens are still slowly increasing. Saturation was only achieved for 80°C immersion specimens. The maximum water absorption value was around 1.2% for 80°C immersion specimens. As a result, the classic Fickian's model is considered insufficient for describing this phenomenon. The water absorption behavior by BMI composite is a non-Fickian diffusion process. The test results showed that increasing immersion temperature accelerates the initial water diffusion rate. However, there is no clear relationship between the immersion temperature and the amount of final water absorption.

### 5.1.2 Diffusion model

#### 5.1.2.1 Two-stage diffusion model

The test results showed the initial absorption rate of the BMI composites increased with temperature, indicating the initial water absorption process was thermal activated. The water absorption curves are in good agreement with Fickian's law at initial stage, however they deviate from their equilibrium water contents with time later. Therefore, the water absorption of BMI composite can be described by a two-stage model (see Figure 2.3). The absorption behavior is assumed to be a combined effect of concentration gradient controlled diffusion and polymer relaxation. The initial water absorption is dominated by the Fickian diffusion, as it is a more rapid process than the polymer relaxation. The second stage is much slower driven by the first order of concentration difference. The original two-stage diffusion model is given as [38]

$$M(t) = M_{\infty,F}G + \sum_i M_{\infty,i}[1 - \exp(-k_i t)]$$

with

$$G = 1 - \frac{8}{\pi^2} \sum_{j=0}^{\infty} \left( \frac{1}{2j+1} \right)^2 \exp \left[ -(2j+1)^2 \pi^2 \frac{Dt}{(2h)^2} \right] \quad (5.1)$$

where  $t$  and  $h$  are the soaking time and specimen half thickness respectively;  $M_{\infty,F}$  is the Fickian equilibrium,  $M_{\infty,i}$  and  $k_i$  are  $i^{th}$  mode of the equilibrium absorption and the relaxation rate constant respectively. However, in this study, an approximation by using the first three terms of  $G$  and one relaxation mode was found sufficient to describe the water diffusion behavior [199]. Figure 5.2(a) depicts a good agreement between the fitted model and the experimental data. As shown in Figure 5.2(b), the obtained  $\log(D)$  is in linear relationship with  $1/T$ , which is consistent with the Arrhenius equations (Eq. (2.6)). It confirms the assumption that the diffusion is thermally activated, and the diffusion rate is very sensitive to temperature. The diffusion rate at 80°C is nearly 20 times higher than that at room temperature. Another observation is that the specimen immersed at lower temperature tends to have slightly higher water content in long term. The non-Fickian diffusion behavior indicates the plasticization of the matrix and possible fiber-matrix debonding in the long-term.

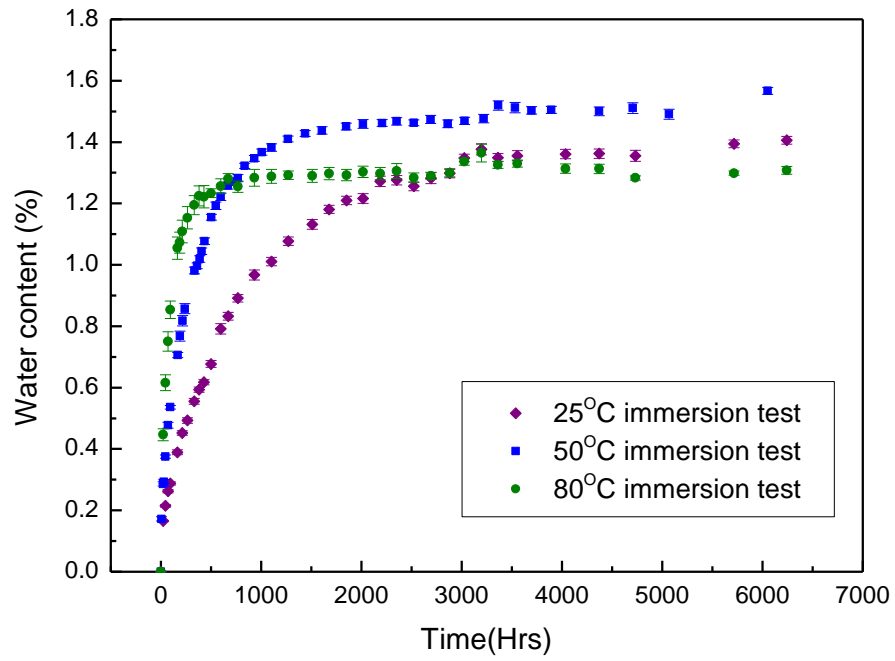


Figure 5.1. Water absorption curves of BMI composite at different temperatures

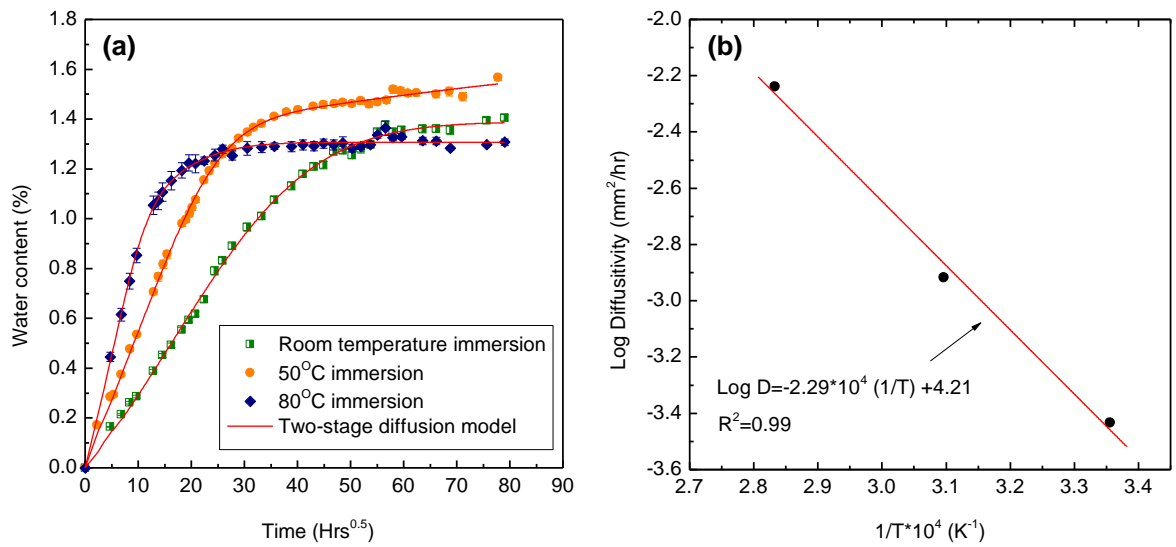


Figure 5.2. (a) Water absorption curves fitted by the two-stage diffusion model  
(b) diffusivity vs.  $1/T$  at various temperatures

### 5.1.2.2 The Langmuir model

The Langmuir model is another commonly used non-Fickian diffusion model for the moisture absorption of polymer and polymer based composites. In this model, the water entered the composite is assumed in two different forms. On one hand, a number of water molecules are bonded with the BMI resin by forming hydrogen bonds with the hydroxyl groups or trapped within the polymer chains. On the other hand, the rest of the water molecules, which are considered as unbounded, are able to enter and leave the composite freely. An approximation of the total water absorption is given by Eq. (2.11),

$$M(t) \cong M_{\infty} \left\{ \frac{\beta}{\gamma + \beta} e^{-\gamma t} \left[ 1 - \frac{8}{\pi^2} \sum_{l=1}^{\infty (odd)} \frac{e^{-\kappa l^2 t}}{l^2} \right] + \frac{\beta}{\gamma + \beta} (e^{-\beta t} - e^{-\gamma t}) + (1 - e^{-\beta t}) \right\}$$

in which  $\gamma$  is the probability of water being bounded and  $\beta$  is the probability of water being unbounded per unit time. The amount of bounded and unbounded water molecules varies over time until equilibrium is reached. In this study, the diffusion rates at different temperature were determined by those from the Fickian diffusion in the previous two-stage model. In fact, the Langmuir model is equivalent to Fickian diffusion model if the amount of bounded water is negligible. Figure 5.3 shows that the experimental result is in good agreement with the fitted Langmuir curves. This indicates that the concept of bound and free water molecules can be used to describe the seawater diffusion behavior of BMI composites as well. The fitted parameters for the two-stage model and the Langmuir model is given in Table 5.1

Table 5.1. Fitting parameters for the two-stage model and the Langmuir model

Immersion Temperature	The two stage model				The Langmuir model		
	$M_{\infty,F}$ (%)	$M_{\infty,1}$ (%)	$D$ ( $10^{-4}mm^2$ /hr)	$k_1$ ( $10^{-4}hr^{-1}$ )	$\beta$ ( $10^{-4}/hr$ )	$\gamma$ ( $10^{-4}/hr$ )	$M_{\infty}$ (%)
25°C	1.16	0.22 7	3.69	19.4	11.50	1.14	1.38
50°C	1.38	0.24 4	12.10	1.76	2.25	0.37	1.60
80°C	0.99 9	0.30 8	57.80	30.8	35.50	14.10	1.31

The  $\gamma$  is much smaller than  $\beta$  at all temperatures implying that the absorption behavior is dominated by the unbounded water. However, the  $\beta$  to  $\gamma$  ratio drops from around 10 to 2.5 as the temperature increases from room temperature to 80°C. This indicates that more water is bounded with the increasing immersion temperature.

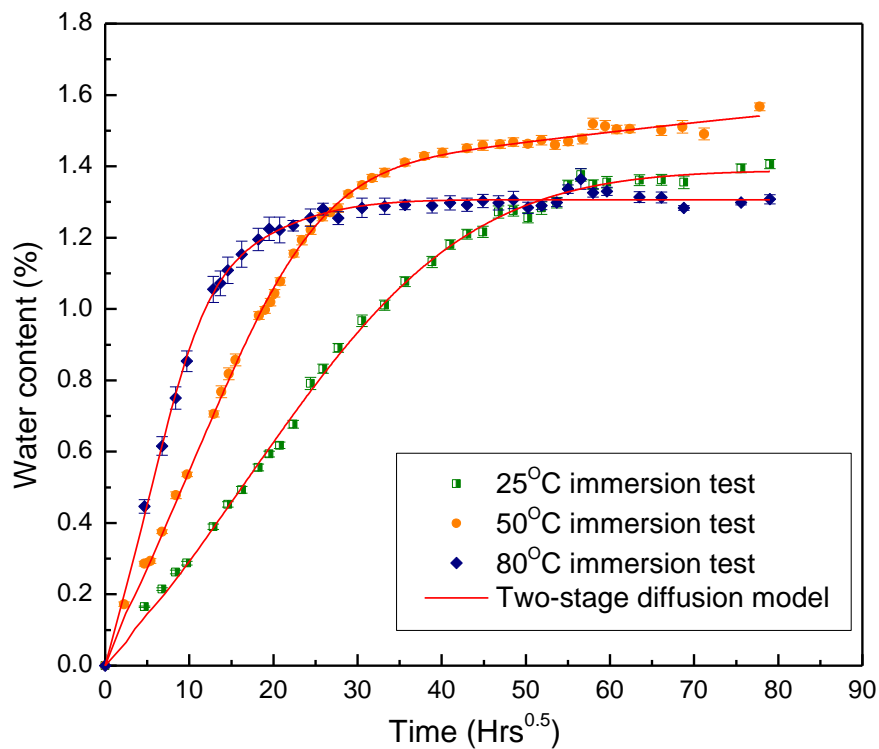


Figure 5.3. Seawater absorption fitted by the Langmuir model



## 5.2 Seawater durability of mechanical properties

### 5.2.1 Tensile properties

The tensile strength and modulus of the BMI composite with respect to immersion time are presented in Figure 5.4 and Figure 5.5 respectively. The tensile tests were conducted at both room temperature (25°C) and -20°C. The specimens were immersed in seawater at 50°C and 80°C up to 6000 hours. Each data point shown in those figures was the averaged value of 3-5 tests results, and the error bar indicates the standard deviation. At 6000 hours of immersion, Figure 5.4 shows that the ultimate tensile strength tested in room temperature decreased by slightly 8.8% with 50°C immersion and a more significant drop by 21.2% with 80°C immersion. The test results at -20°C environment showed similar trends as those at room temperature, however, the strength of the material was enhanced by around 15%. The modulus behavior at different conditions (see Figure 5.5) resembles the trend of strength change: The modulus decreased with immersion time and increasing temperature; Lower testing temperature resulted in higher modulus. In general, the BMI composite seems to have a good retention of its tensile properties while working in wet environment, which is apparently an advantage for marine use.

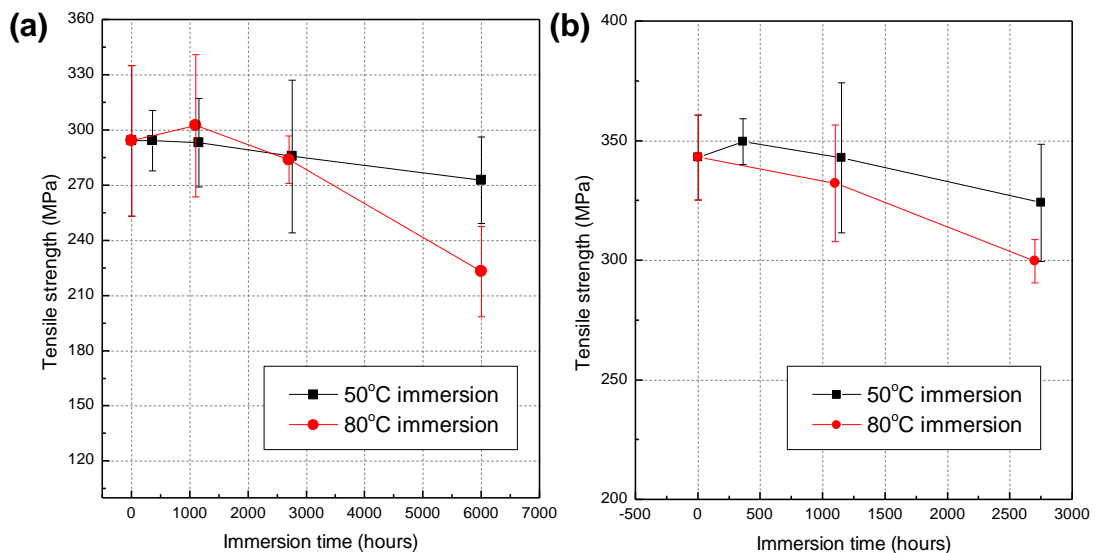


Figure 5.4. Effect of seawater immersion on tensile strength (a) tested at room temperature (25°C) (b) tested at -20°C

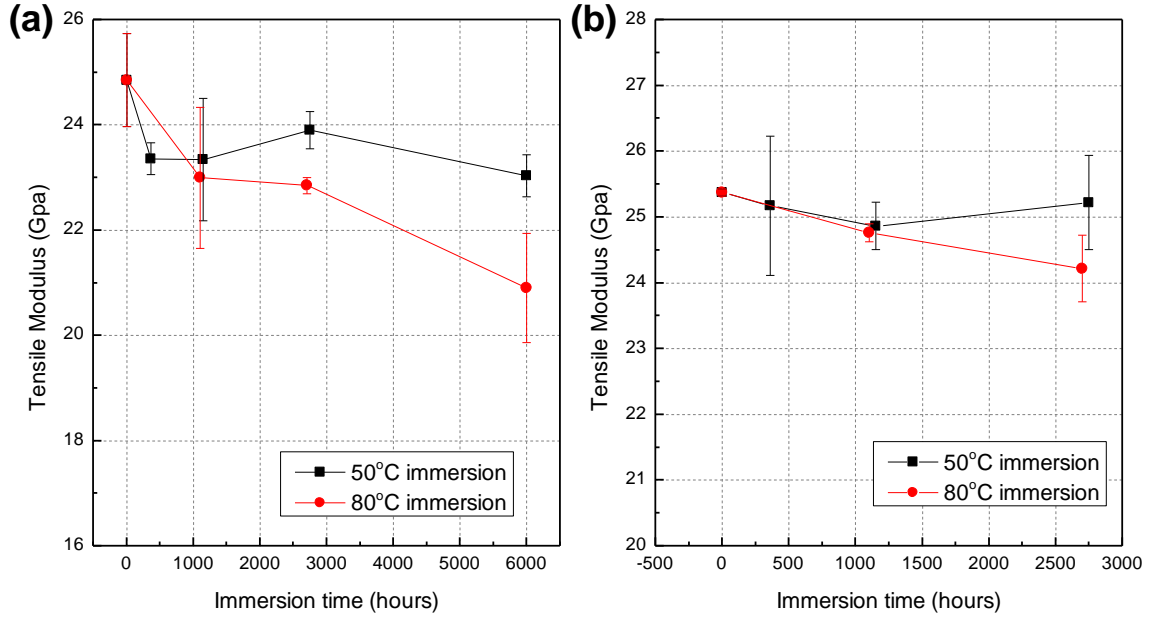


Figure 5.5. Effect of seawater immersion on tensile modulus (a) tested at room temperature (25°C) (b) tested at -20°C

The experimental results of the dry and wet specimens are fitted with two-parameter Weibull distribution as described by Eq. (4.52):

$$P(S_u \leq z) = 1 - \exp \left[ - \left( \frac{z}{\beta_s} \right)^{\alpha_s} \right], z \geq 0$$

The wet50 and wet80 specimens refer to the specimens after 6000 hours of immersion in seawater at 50°C and 80°C respectively. The estimated Weibull parameters for the dry and the conditioned specimens are listed in Table 5.2. The Weibull distribution curve is plotted as the solid line and the experimental results as cycles in Figure 5.6. The cumulative probability of failure for the  $i^{th}$  of  $n$  specimens tested  $F(i, n)$  is approximated by [200],

$$F(i, n) = \frac{i-0.3}{n+0.4} \quad (5.2)$$

As shown in the figure, the experimental data are in good agreement with the Weibull distribution. The results imply the material went through a brittle failure under fatigue loading, which can be described by the “weakest link theory”. The wet specimens had similar variance of results compared with that of dry specimens.

Table 5.2. Weibull parameters for the dry and the conditioned specimens

Condition	$\alpha_s$	$\beta_s$	No. of specimen
Dry	8.32	311.86	25
Wet50 (6000hours)	15.96	282.52	21
Wet80 (6000hours)	11.45	233.50	10

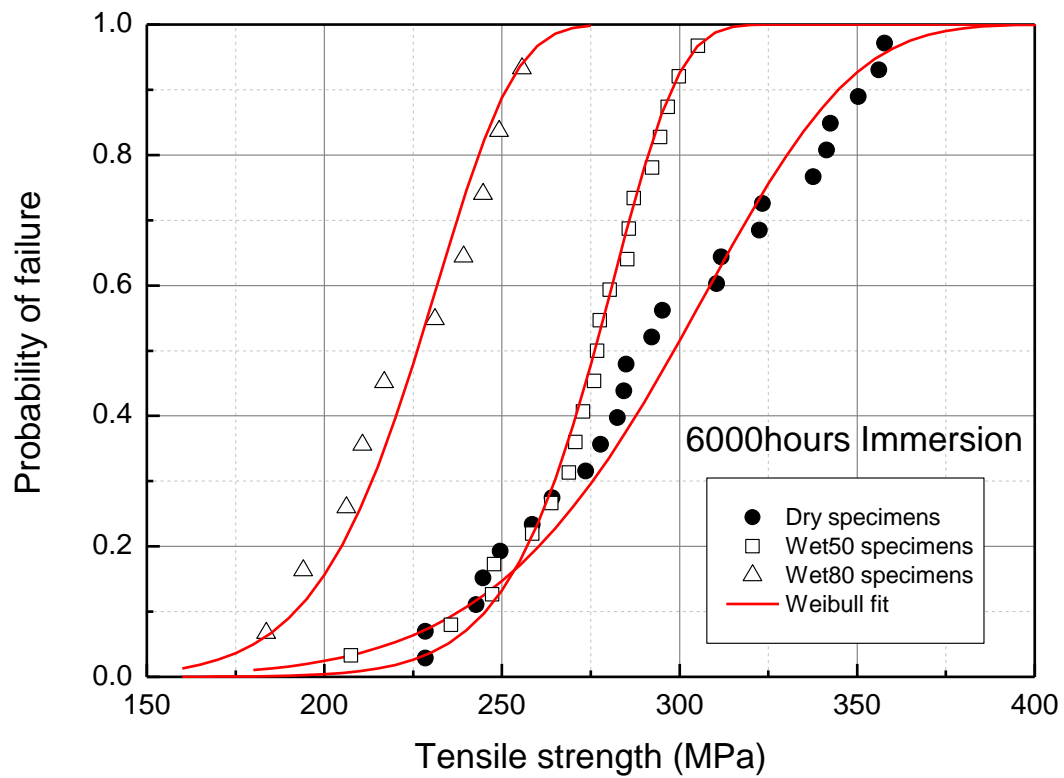


Figure 5.6. Statistical distribution of static tensile strength

### 5.2.2 Shear Properties

The shear properties of the dry specimen were tested using both the V-notched rail shear tests and in-plane shear by tensile test of a  $\pm 45^\circ$  laminate specimens. The results of these two methods are presented in Table 5.3. The measured shear modulus and shear strength of both methods were in good agreement with comparable variations. The V-notched specimens gave slightly higher results as some of the fracture surfaces were inclined, which led to larger shear fracture area than the expected cross-section area. Therefore, the in-plane shear by tensile test of a  $\pm 45^\circ$  laminate specimen was selected to determine the shear properties of the BMI composite in this study. Figure 5.7 presents the comparison of shear strength and modulus with different seawater immersion conditions. The shear properties showed similar trends as tensile properties. Both shear modulus and strength drop with increasing immersion time and temperature. After 6000 hours of immersion, shear modulus and strength of the specimen decreased by over 15%. This outcome was most likely caused by the degradation of the BMI matrix and the weakening the interfacial bonding between fiber and matrix due to the seawater absorption.

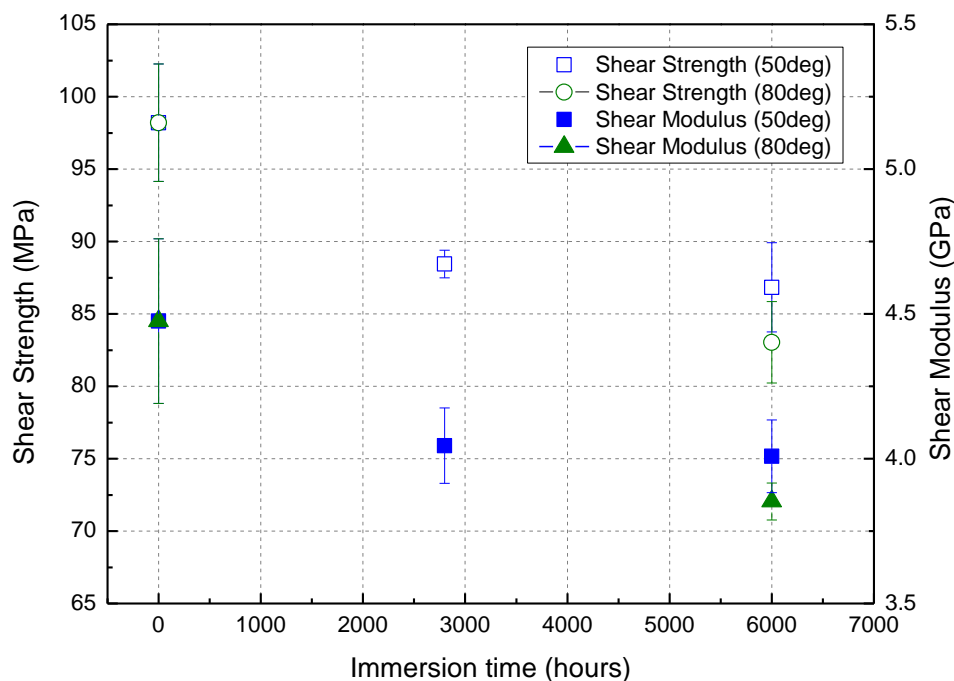


Figure 5.7. Effect of seawater immersion on shear strength and modulus

Table 5.3. Results of V-notched rail shear test and in-plane shear by tensile test of  $\pm 45^\circ$  laminates

Test method	Immersion time (hrs)	Immersion temperature	Shear modulus (GPa)	Ultimate shear strength (MPa)
V-notched rail shear	0	/	$4.72 \pm 0.18$	$104.07 \pm 8.12$
$\pm 45^\circ$ laminate tensile test	0	/	$4.47 \pm 0.28$	$98.20 \pm 4.06$
$\pm 45^\circ$ laminate tensile test	2800	50°C	$4.05 \pm 0.13$	$88.44 \pm 0.95$
$\pm 45^\circ$ laminate tensile test	6000	50°C	$4.01 \pm 0.13$	$86.83 \pm 3.08$
$\pm 45^\circ$ laminate tensile test	6000	80°C	$3.85 \pm 0.66$	$83.04 \pm 2.81$

### 5.2.3 Flexural properties

The three-point bending tests at different strain rates did not show significant difference in ultimate tensile strength. Therefore, the test results presented here were all obtained from flexural tests with a cross-head speed of 0.5mm/min. As shown in Figure 5.8, the failure strength of dry GF/BMI composite specimen do not have much difference when testing temperature increases from room temperature up to 195°C, and even have a trend of increasing with elevated temperature. This interesting phenomenon was also reported by [201], where the strengths of BMI composite increased along with temperature from 55°C to 200°C measured by four-point bending tests. It was probably due to the extra curing process during the bending test at elevated temperature. Nevertheless, the measured flexural strength reduced by 23.6% as temperature rose from 195°C to 260°C. It is worth noting that 195°C is very close to the onset temperature of the composite material. After 1500 hours immersion in 50°C seawater, the failure strength of wet specimens have been significantly reduced by 23% at testing temperature below 195°C. However, it seems that the flexural strength of the wet specimens becomes less susceptible with elevated temperature. The flexural strength of the specimens further reduced to around 60% of the dry specimens with an immersion time of 3000 hours. Similar to the

behavior of the dry specimen, the degradation of flexural strength accelerated at around 195°C testing temperature. Table 5.4 presents the reduction of flexural strength of the wet specimens to that of the dry specimens at several testing temperatures.

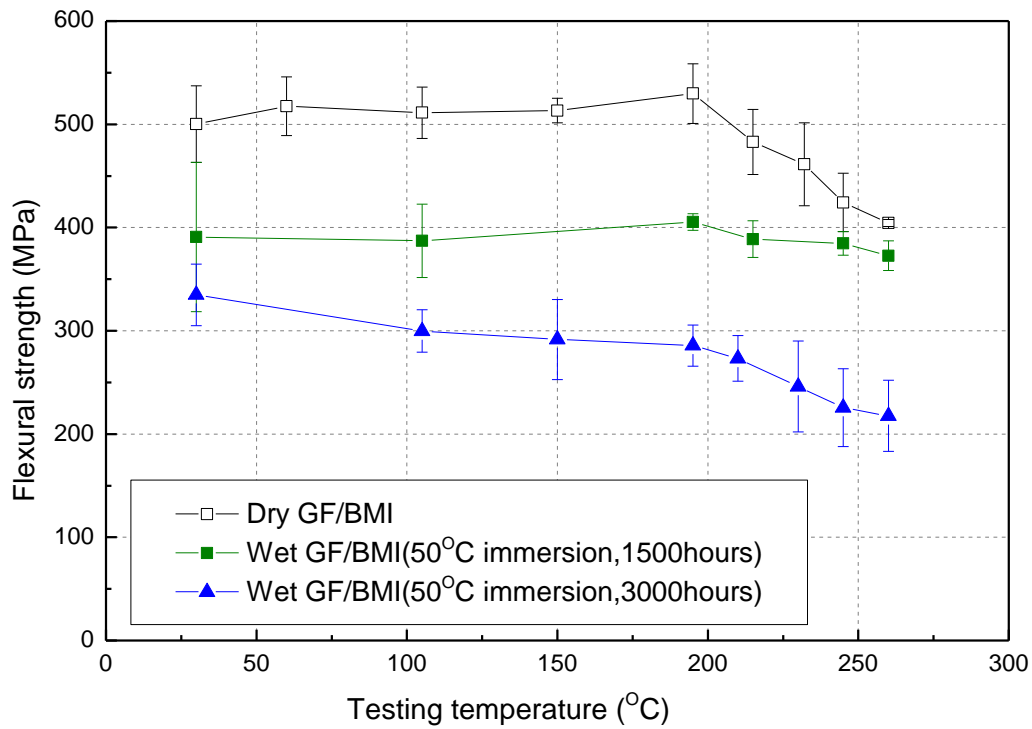


Figure 5.8. Flexural strength vs. Temperature for dry and wet GF/BMI specimens at 0.5mm/min

Table 5.4. Reduction of flexural strength of dry and wet specimens at different temperatures

Test temperature		Flexural strength (MPa)		
		Dry	wet (1500hrs)	wet (3000hrs)
25°C	Mean	500	390	334
	(diff.)	(/)	(-22.0%)	(-33.2%)
195°C	Mean	529	405	285
	(diff.)	(/)	(-23.4%)	(-46.1%)
260°C	Mean	404	372	217
	(diff.)	(/)	(-7.9%)	(-46.2%)

Figure 5.9 presents the temperature dependence of the flexural modulus for both the dry specimens and the wet specimens immersed in 50°C seawater for 3000 hours. The flexural modulus for both dry and wet specimens showed similar trends with increasing testing temperature as the flexural strength. The flexural modulus decreased slightly with increasing temperature but dropped significantly when tested near or above the onset temperature. The wet specimens, after 3000 hours of seawater exposure, were softened considerably due to the plasticization effect of water. The flexural modulus of the wet specimen reduced about 20% compared to that of dry specimens at all testing temperatures. The reduction was slightly smaller at high temperatures, and it is possibly because that the specimens were partially dried during the bending tests at those temperatures.

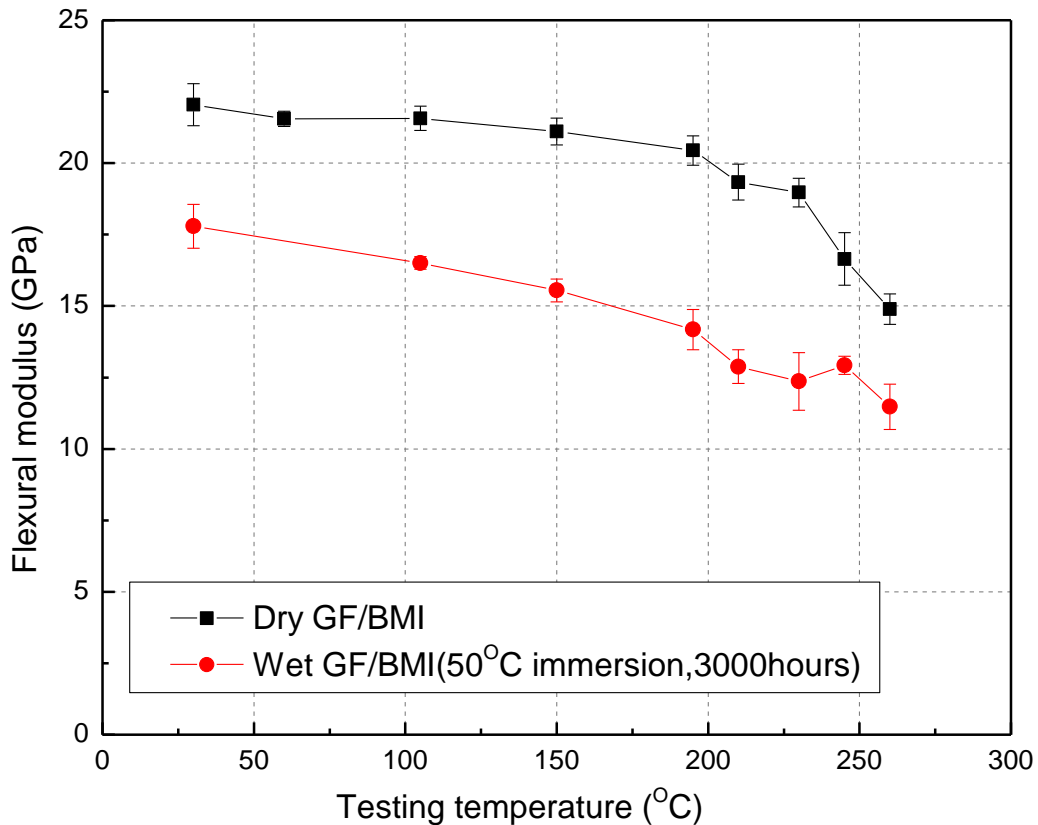


Figure 5.9. Flexural modulus vs. Temperature for dry and wet GF/BMI specimens at 0.5mm/min

A typical flexural failure process of GF/BMI composite was captured by a high-speed camera. The fracture appearances at the initial stage of matrix failure and crack propagation of the specimen are displayed in Figure 5.10. The photo on

the left shows that, at initial stage, a visible sign of failure occurred at the lower surface of the specimen on the tensile side where the stress is the highest. Then, with the deflection increased, the initiated cracks propagated from edge into the middle of the thickness accompanying with matrix failure, warp fiber buckling, pullout and breakage. Finally, an obvious delamination occurred all the way to the middle plane as shown in the photo on the right, which led to the failure of the specimen. The upper surface suffered with highest compressive force remained almost intact throughout the entire failure process. The failure modes and processes were found similar in all three-point bending tests at various temperatures and strain rates. This indicates that all failures of flexural tests in this study were actually tensile failures with similar fracture process. Therefore, the master curve of flexural strength can be constructed using the same set of shift factors obtained by DMA.

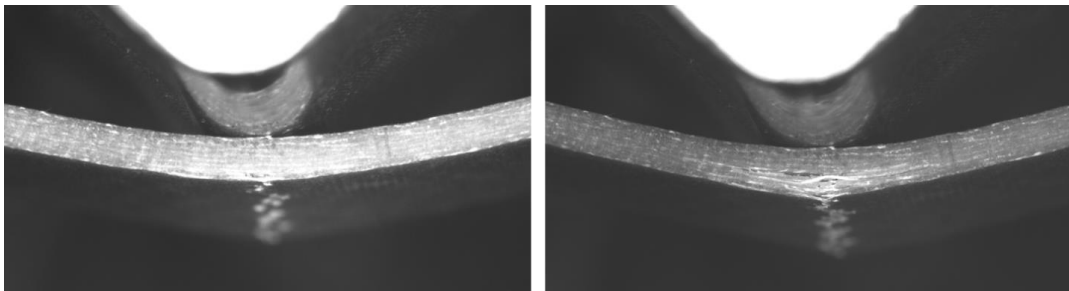


Figure 5.10. Side views of fracture appearances of GF/BMI composites at initial stage (left) and final stage (right)

### 5.3 Dynamic-mechanical analysis

The effect of seawater immersion on the viscoelastic behavior of the composite was investigated by dynamic mechanical analysis. Figure 5.11 presents the change of the onset temperature and the glass transition temperature ( $T_g$ ) for specimens immersed at 50°C and 80°C. The absorbed water, acting as a plasticizer, significantly lowered the onset and glass transition temperatures of the material. At the initial stage of absorption, both temperatures dropped sharply as the water content in the specimen increased at a very fast rate. When the diffusion rate slowed down, the temperatures remain nearly constant. After 6000 hours of immersion, the glass transition temperature reduced about 60°C



and 70°C for the wet50 and wet80 specimens respectively, and the gap between onset temperature and glass transition temperature was 15°C-20°C. Bao et al. [37, 41] suggested that the absorption process in bismaleimide composites is self-accelerating. The water absorbed in the polymer enhances the relaxation of the network. The relaxed network, in return, accepted more water to be absorbed in the polymer. That explains the two-stage absorption behavior observed in the diffusion test. The DMA results showed an evidence of strong plasticization effect of seawater absorption into the matrix. However, the storage modulus curve of re-dried specimens, which were immersed in 50°C seawater up to 3000 hours returns to the similar shape of dry specimen with only 2.4% reduction, and the  $T_g$  is back to the original value as well. This suggests that the effect of water absorption of the BMI composite up to this temperature is reversible and no obvious chemical reaction has taken place. Similar conclusion was given by Li et al. [15] using FTIR analysis.

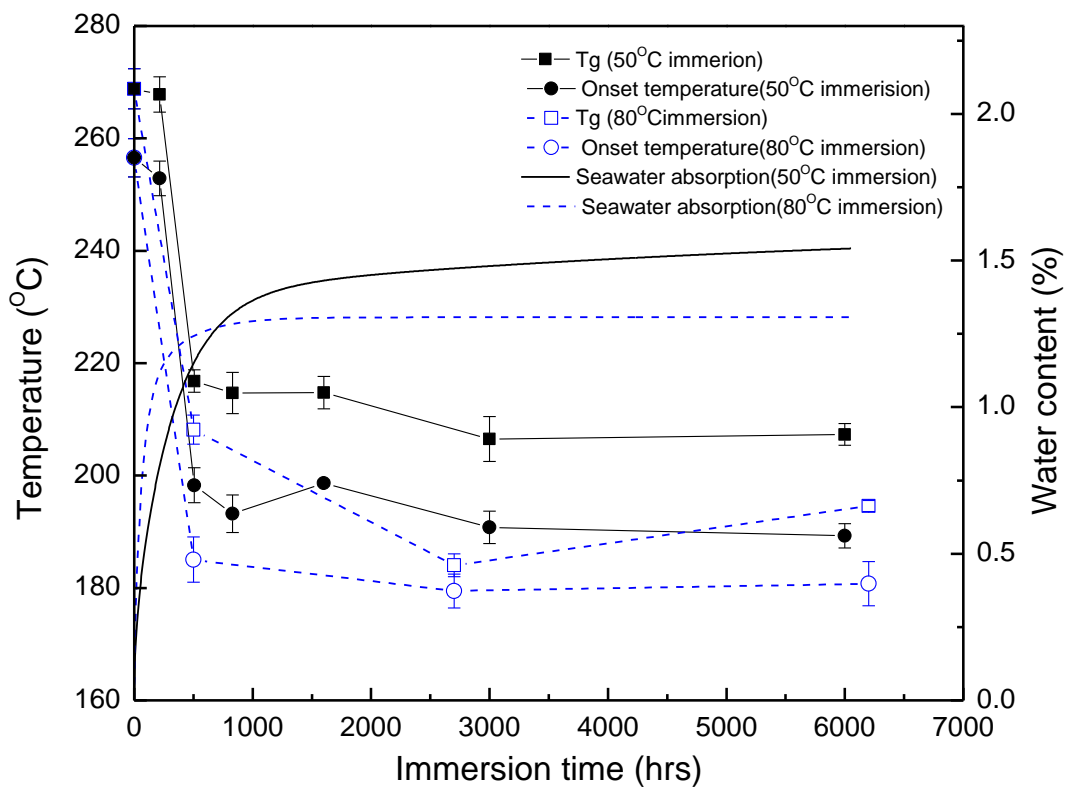


Figure 5.11. Effect of seawater exposure on the viscoelastic behavior of the BMI composite.

## 5.4 Long-term static strength prediction

### 5.4.1 Construction of master curve by TTS

All the “wet” specimens in this section 5.4 refer to BMI composites with 5000 hours of immersion in 50°C seawater. The master curves of storage modulus  $\log E'$  verses reduced time  $t'$  were constructed by shifting storage modulus curve at temperatures from 35°C to 315°C along time axis in log scale. The shifting procedures were automatically done using the developed computer program mentioned in section 4.5.3. Figure 5.12 presents the shift factors in log scale against  $T^{-1}$  derived from the master curves at reference temperature 35°C. Five specimens were tested for both dry and wet conditions and only one re-dried specimen was tested since the test for re-dried specimen is just for confirmation purpose and the result is in good agreement with dry specimens. Figure 5.13 is a demonstration of constructing master curve for one dry specimen. As shown in the figure, storage modulus at various temperatures superimposed perfectly generating a smooth master curve for BMI composite. The obtained master curves for wet and re-dried specimens are also presented as solid and dash lines respectively. Therefore, the material is considered thermorheologically simple and time-temperature superposition principle (TTSP) is applicable for both dry and wet specimens.

At low testing temperatures, the shift factors of wet specimens are almost coincident with that of dry specimens. However, the water absorption altered the shift factors curve to a more irregular shape as temperature increases to near  $T_g$  region, where the master curve has been shortened and the degradation of wet specimens accelerates. Miyano et al. [202] tested neat vinylester and epoxy resin and did not find an obvious difference of shift factors between dry and wet specimens, because their testing temperature was only up to around 90°C, which is not high enough to reveal the divergence. However, in a recent study of Nakada, M. and Y. Miyano [78] on wet unidirectional Carbon Fiber/Epoxy composites, the shift factors of wet specimen clearly deviates from that of dry specimen around its  $T_g$ . In addition, we suspect that the temperature at which the shift factors of dry and wet specimens start to diverge is water content dependent. The water absorption effect up to 50°C is found to be reversible, as

the glass transition temperature and shift factors are the same for both dry and re-dried specimens.

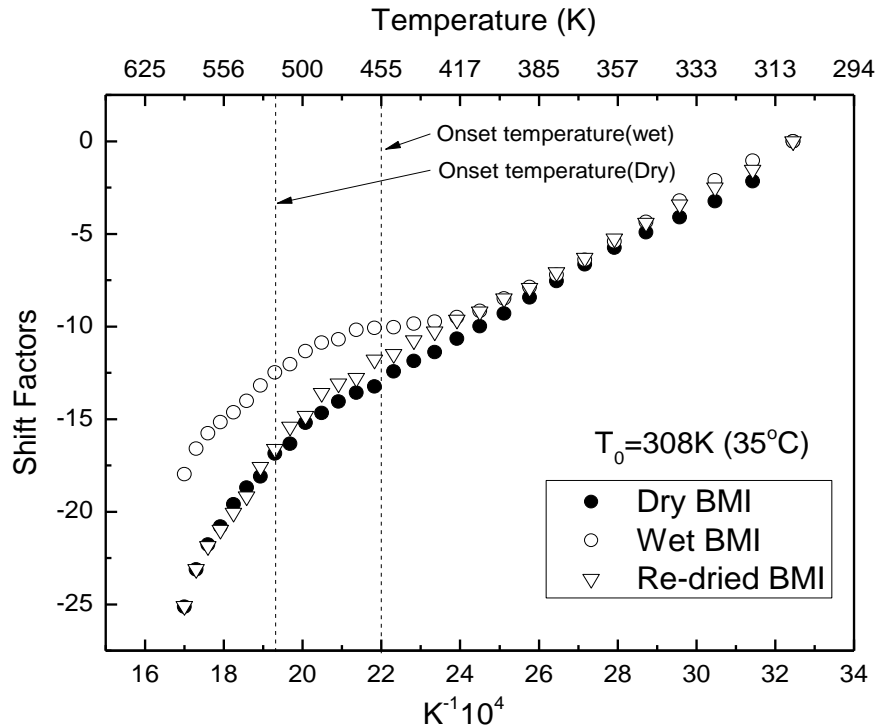


Figure 5.12. Shift factors of master curves for BMI composites (wet specimen immersed in 50°C seawater up to 3000 hours)

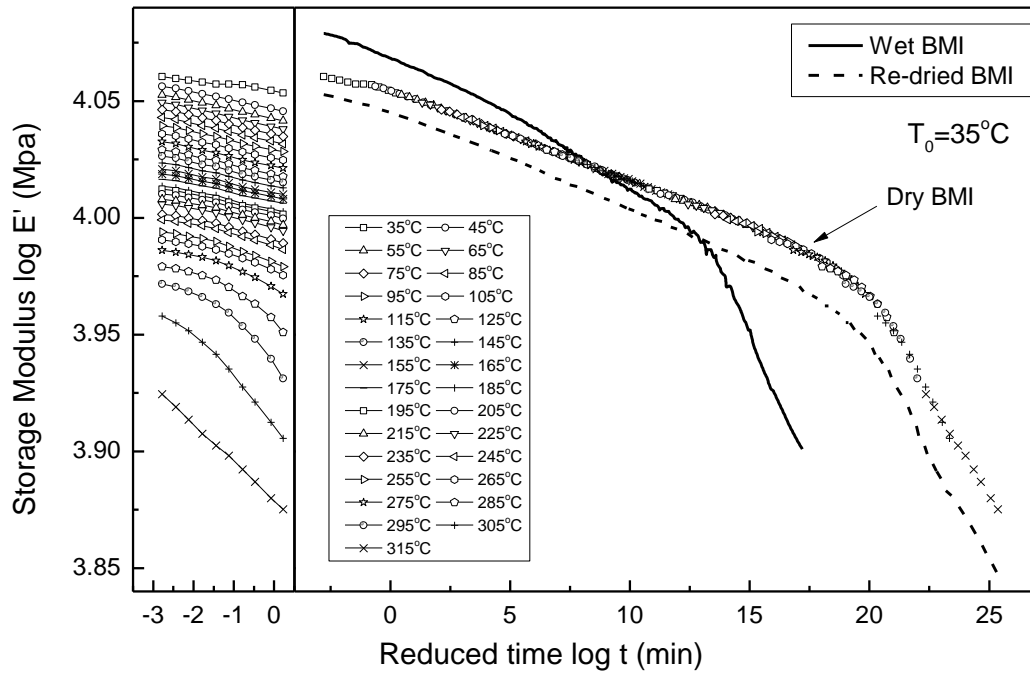


Figure 5.13. Construction of master curves of storage modulus for BMI composites (wet specimen immersed in 50°C seawater up to 3000 hours)

### 5.4.2 Storage modulus model

Storage modulus  $\log E'$  as a function of temperature  $T$  at fixed frequency of 0.1Hz extracted from temperature step mode tests in Figure 5.13 are displayed in Figure 5.14 for dry, wet and re-dried specimens. Since the specimens only exhibit the presence of  $\beta$ -transition and glass transition ( $\alpha$ -transition), Eq. (4.38) is modified as follows,

$$E(T) = (E_1 - E_2) \exp\left(-\left(\frac{T}{T_1}\right)^{m_1}\right) + (E_2 - E_3) \exp\left(-\left(\frac{T}{T_2}\right)^{m_2}\right) \quad (5.3)$$

The experimental results shown in Figure 5.14 are also modeled and presented as solid lines using the modified equation (Eq. (5.3)) above and the fitted parameters are listed in Table 5.5. The Weibull distribution coefficient  $m_2$  associated with glass transition is lower for wet specimen implying that the exposure of seawater has broadened the glass transition region. The storage modulus of wet specimen is slightly lower compared to that of dry specimen owing to the softening of matrix with seawater absorption, which was also reflected by the static tests results of the wet specimens. The result of  $m_1$  and  $m_2$  is also in agreement with the study of Mahieux and Reifsnider [52], which stated that  $m_1$  and  $m_2$  are normally around 5 and 20 respectively.

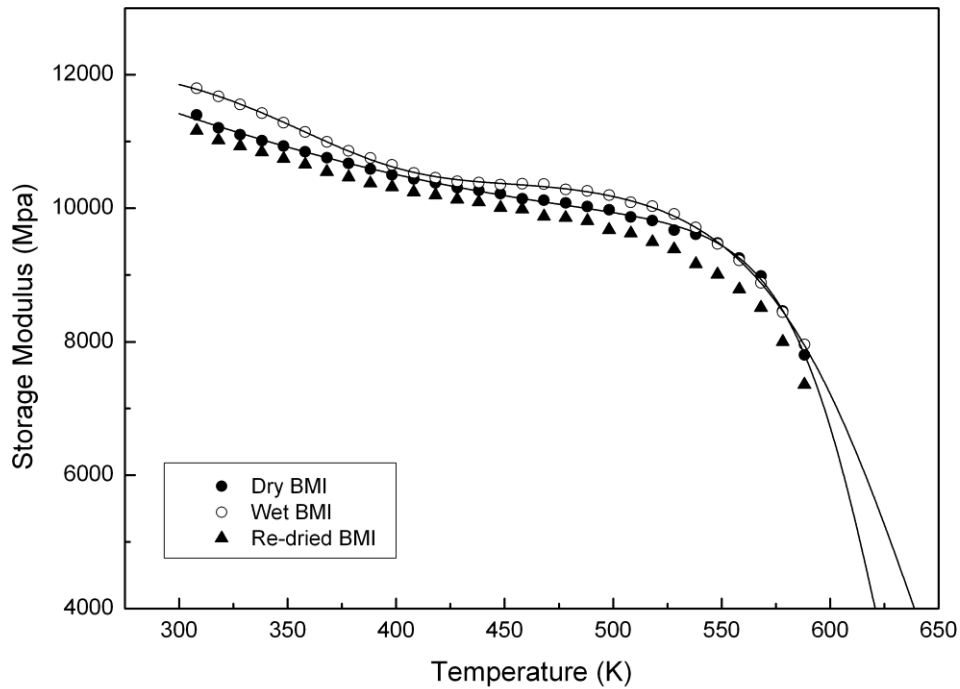


Figure 5.14. Storage modulus as a function of temperature for dry and wet specimens at 0.1Hz

Table 5.5. Fitted parameters of storage modulus model at 0.1Hz

Conditions	$E_1$ (MPa)	$E_2$ (MPa)	$E_3$ (MPa)	$T_1$ (K)	$T_2$ (K)	$m_1$	$m_2$
Dry	14943.2	10783.4	1160.1	325.7	623.3	2.10	25.70
Wet	12941.4	11150.0	740.3	363.3	640.7	8.04	15.28

#### 5.4.3 Formulation of shift factors and master curves

The shift factors of the master curves for dry and wet specimens in Figure 5.12 are modeled and presented in Figure 5.15. The shift factors of dry and wet specimens exhibit linear relationship with  $T^{-1}$  at relatively low temperature region, which can be correlated with temperature by Arrhenius equations. It implies that the process is thermally activated, and follows the kinetic rate theory in this temperature region. However, the shift factors deviate from Arrhenius behavior as temperature increases towards the glass transition region. Arrhenius relation sometimes is not applicable to the primary transitions (i.e.  $\alpha$ -transition), hence an alternative treatment by Vogel-Fulcher-Tammann (VFT) equation is proposed to represent the temperature dependence of shift factors in the neighborhood of glass transition temperature. The VFT like behavior of viscoelastic material in the temperature range of  $T_g$  to  $T_g + 100$  has been studied in detail by Rault [203] and many modified models were developed. In VFT equation, the temperature dependence of relaxation time  $\tau$  of viscoelastic material is expressed as follows,

$$\tau = \tau_0 \exp\left(\frac{A}{T-T^*}\right) \quad (5.4)$$

where  $T^*$  is a temperature below  $T_g$  and  $A$  is a constant which relates to activation energy of  $\beta$ -transition motion [203]. Therefore, based on the VFT form equation, the shift factor in log scale can be proposed as,

$$\log a_{T_0}(T) = \frac{A}{T-T^*} \quad (5.5)$$

Combining the two segments, the logarithmic shift factors of temperature  $T$  to the reference temperature  $T_0$  can be formulated as follows,

$$\text{Log } a_{T_0}(T) = \left[ \frac{A}{T-T^*} - \frac{A}{T-T^*} H(T_0 - T_c) - \frac{E_a}{2.303R} \left( \frac{1}{T_0} \right) H(T_0 - T_c) \right] H(T_0 - T_c) + \frac{E_a}{2.303R} \left( \frac{1}{T} - \frac{1}{T_0} \right) H(T_0 - T_c) \quad (5.6)$$

where  $R$  is gas constant,  $E_a$  is the activation energy for Arrhenius equation and  $H$  is the Heaviside step function respectively.  $T_0$  and  $T_c$  are the reference temperature and temperature where two segments intersect respectively. This formulation is able to represent shift factors of BMI materials with different water content. However, it is not wise to blindly extend the modeled shift factors to temperature above  $T_g + 100$  where the validity of VFT equation is questionable. The parameters of modeled shift factors of storage modulus curves are listed in Table 5.6. At temperatures below  $T_c$ , the relationship between shift factors and temperature is governed by Arrhenius equation and surprisingly the calculated activation energy is the same for dry and wet specimen but the  $T_c$  for wet specimen is 76K lower than dry specimen.

Table 5.6. Fitted parameters of shift factors model

Conditions	$E_a$ (KJ/mol)	A	$T^*$ (K)	$T_0$ (K)	$T_c$ (K)
Dry	225.73	3629.90	733.4	308.2	473.5
Wet	222.02	3070.00	761.1	308.2	397.0

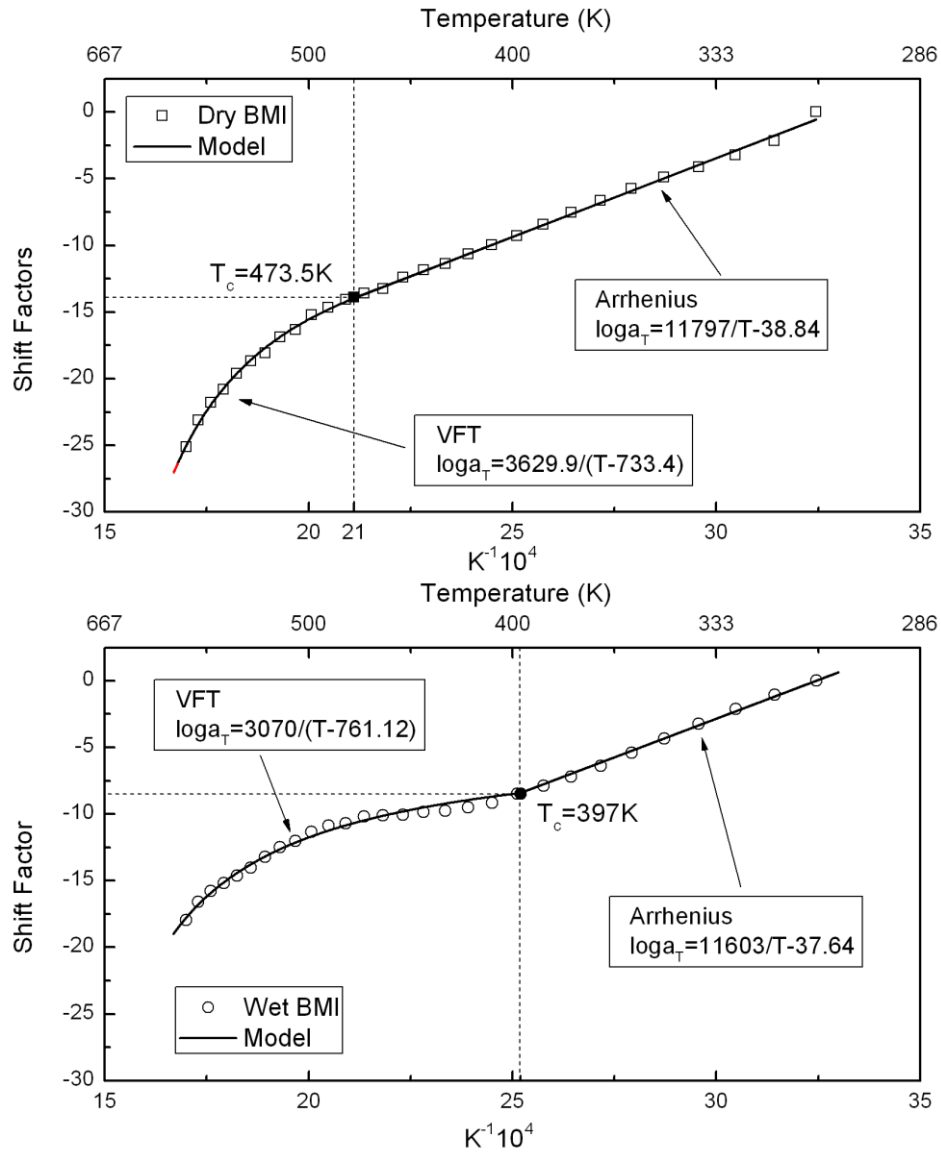


Figure 5.15. Modeled shift factors of dry and wet specimens

Now that the shift factor can be expressed as an implicit function of temperature by taking the inverse of Eq. (5.6), the storage modulus of equivalent time  $t$  at reference temperature  $T_c$  are related to instantaneous storage modulus of a fixed frequency (e.g. 0.1Hz) at corresponding temperature  $T$ ,

$$\text{Log}(t) = -\text{Log } a_{T_0}(T) - 0.788 \quad (5.7)$$

The master curves of storage modulus of dry and wet specimens are constructed at reference temperature of 35°C. As shown in Figure 5.16, the master curves generated showed good agreement with the experimental results. The master curves of demonstrated dry and wet specimens at elevated temperatures of 75°C

and 200°C can be predicted by the model and their long-term viscoelastic behaviors are presented in Figure 5.17.

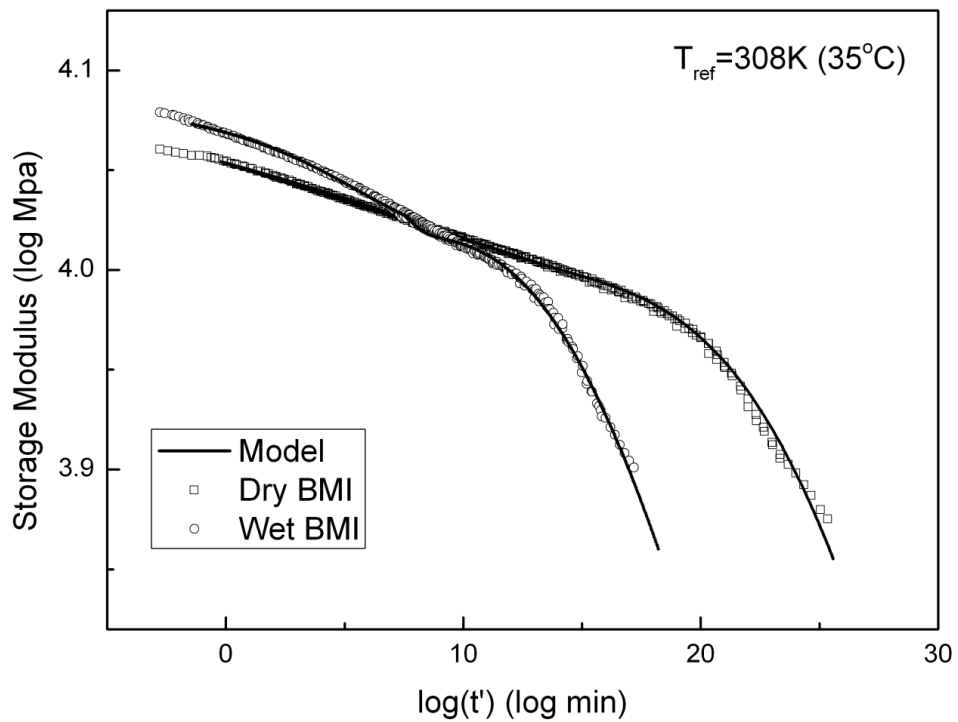


Figure 5.16. Modeled master curves for dry and wet specimens

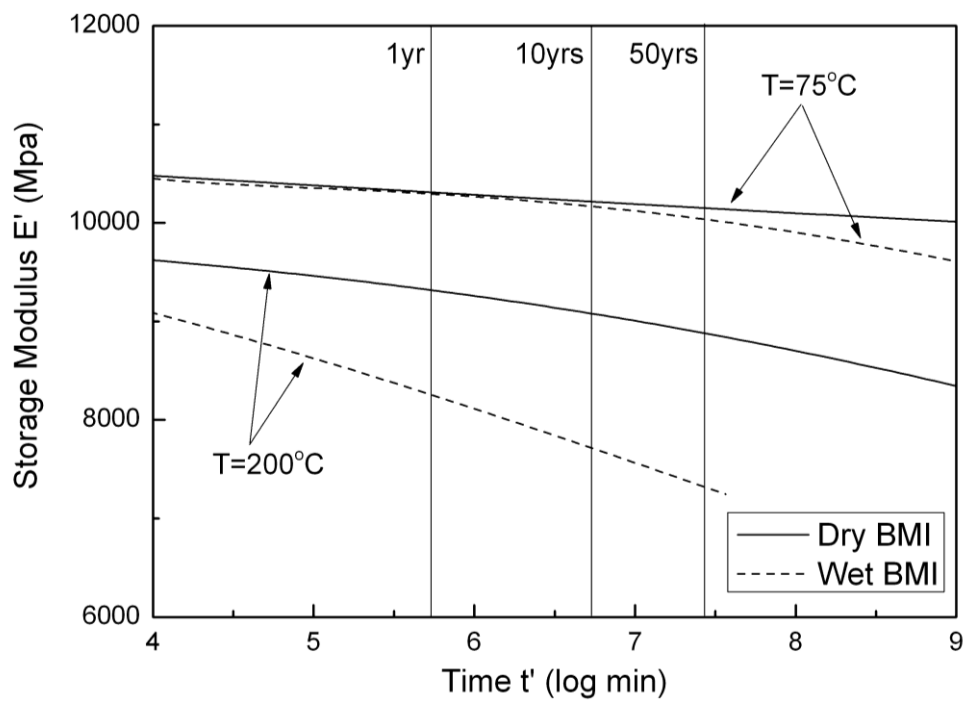


Figure 5.17. Predicted master curves of dry and wet specimens at 75°C and 200°C



The reduction in modulus with respect to time for all dry and wet specimens predicted using the model described in this report is presented in Figure 5.18. It shows that exposure to seawater environment would accelerate the degradation process of BMI composites. In a period of 50 years, which is normally the maximum service life of pipelines, the specimen immersed in seawater is estimated to have 9.1% reduction in modulus while dry specimen only decreases by 6.5% at reference temperature at 75°C. The degradation due to water absorption appears even faster at higher temperature. At 200°C environmental temperature, the modulus of BMI material with seawater exposure is expected to degrade by as high as 18.4% in 50 years compared with 10.9% for dry condition. The purpose of choosing 75°C and 200°C is to give a demonstration of the predicted results in moderate and relatively high temperature. At the reference temperature of 35°C, the difference was too small to show in 50 years time. Generally, the uncertainty of prediction increases with longer prediction period and higher temperature. However, the results revealed not much difference between dry and wet specimens in terms of uncertainty, as the standard deviation ranges from 0.77% to 2.12% for dry specimens and 0.32% to 3.35% for wet specimens.

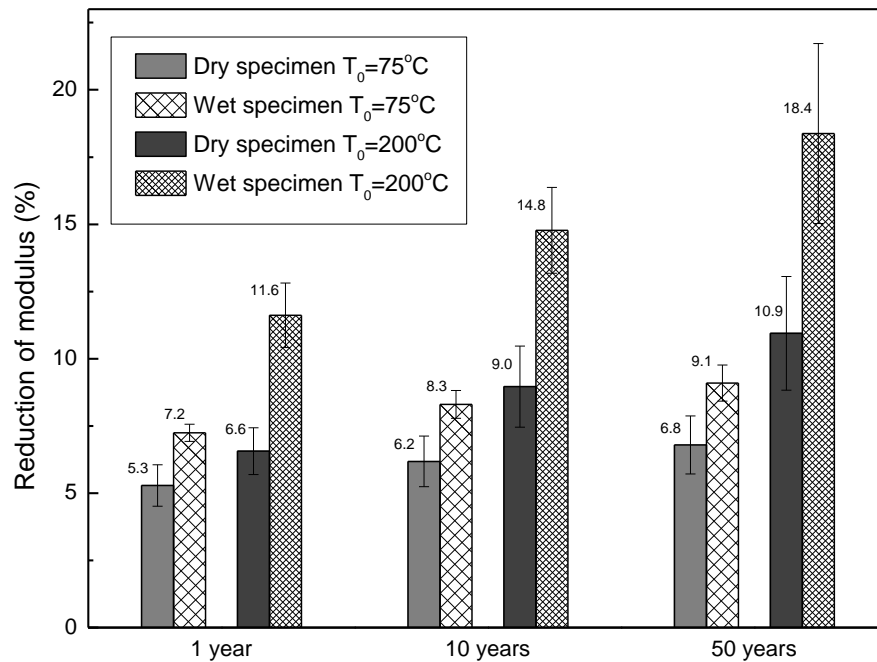


Figure 5.18. Predicted long-term degradation of modulus at different conditions

#### 5.4.4 Prediction of long-term static and creep behavior

The predicted master curves of constant strain rate (CSR) strengths of both dry and wet specimens (50°C immersion for 3000hrs) are presented in Figure 5.19 based on the TTS principle. The reference temperature was set to be 35°C and all the points representing static strength at various temperatures were shifted horizontally to the right on time axis in log scale by corresponding shift factors. Accordingly, the degradation of flexural strength by increasing of time at arbitrary reference temperature can be predicted from this master curve and shift factors as well. In this case, the shift factors for storage modulus were used for creating the master curve of constant strain rate strengths (CSR), as in the previous study of Miyano [73], it was shown that the shift factors for CSR strength are almost identical to those for the storage modulus. It is quite clear that the CSR strength of the material decreases with the increase of the time. Increasing temperature and exposing to seawater environment would reduce the strength and accelerate the degradation of the composites. The flexural creep master curve is constructed in Figure 5.20 using the linear accumulative damage law described in section 2.3.4. The creep master curve is obtained by shifting the CSR master curve by a constant value of  $\log(r+1)$  along log time scale (see Figure 2.9). The reference temperature of this figure was set as 105°C so that the prediction period falls in a range of a few hours to less than 50 years. It can be seen that the shifting constant is larger for the wet specimen than the dry specimen, which means the wet specimen has lower creep strength and it decreases much faster with time. The construction of the creep master curve is based on the presumption that the static and creep behavior are governed by the same time-temperature superposition principle.

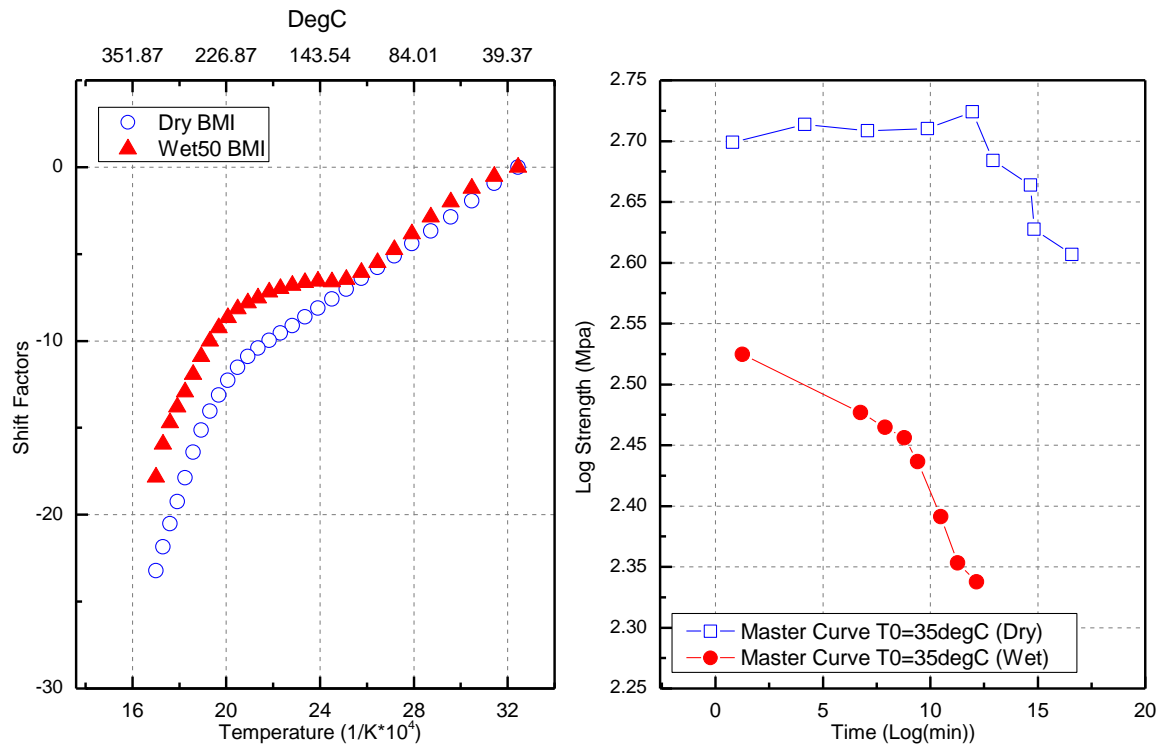


Figure 5.19. Shift factors and construction of CSR master curves for dry and wet50 specimens

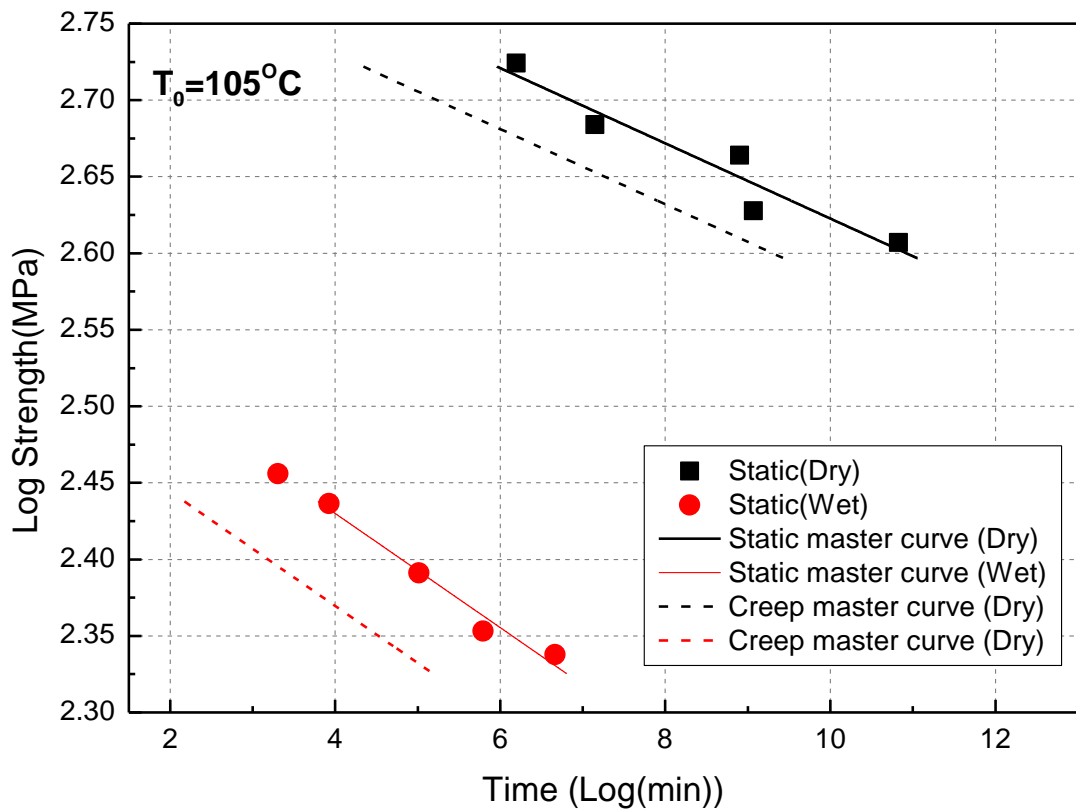


Figure 5.20. Creep master curves for dry and wet50 specimens

## 5.5 Seawater effects on static delamination properties

### 5.5.1 Mode I delamination behavior

Four DCB specimens were tested for each condition. The Figure 5.21(a) shows typical applied load vs. load-point displacement curves of the dry DCB specimen and the specimens after immersion in different temperatures. The experimental results showed that specimens immersed in seawater generally had lower peak forces and higher compliances. In particular, an approximate of 25% reduction in peak force was found for the 80°C immersion case compared with that for the dry specimen. The softening of the specimen after immersion was a result of plasticization effect, which was shown by the DMA tests. However, different immersion temperatures seem to have little effect on the ductility of the specimens. Besides, no obvious fiber-bridging phenomenon was observed in all DCB specimens. Figure 5.21(b) shows the  $G_I$  and  $J_I$  vs. load-point displacement of the specimens in Figure 5.21(a). It can be seen that both methods provided comparable results, and the variations were very small. For the dry specimen, the obtained delamination resistance curve (R-curve) showed consistent mode I interlaminar fracture toughness for both initiation and propagation. The 50°C immersion specimens had a similar initiation value of interlaminar fracture toughness, while the resistance curve increased significantly with delamination growth. The resistance increased from around 800J/m<sup>2</sup> to around 1000J/m<sup>2</sup> before it stabilized. However, the 80°C seawater immersion caused a significant drop in fracture toughness but the resistance for delamination growth remains stable. The mode I interlaminar fracture toughness obtained by J-integral method for both insert and pre-crack is summarized in Figure 5.22. The interlaminar fracture toughness measured from the insert was lower than that from pre-crack for all conditions. Besides, the fracture toughness from the insert appears to be insensitive to seawater immersion or elevated temperature. Owing to the resin rich area at the insert tip, the delamination initiation of the insert is dominated by resin fracture. The plasticization of the matrix due to the presence of moisture slightly increased the fracture toughness of the insert, but the effect was negligible given the scattering of the experimental results. The dry and 50°C immersion specimens

showed similar fracture toughness of  $800 \text{ J/m}^2$  from the inserts, while the value for  $80^\circ\text{C}$  immersion specimens reduced to less than  $600 \text{ J/m}^2$ , which is about 25% lower. The delamination of the pre-crack under mode I loading is associate to the matrix fracture and the failure of fiber/matrix interface. The weakening of the interface is likely to be a more significant effect during seawater immersion especially at elevated temperature, which is responsible for the lower fracture toughness for the specimens at  $80^\circ\text{C}$  immersion temperature. Figure 5.23 shows the scanning electron micrographs (SEMs) of the typical fracture surfaces of the DCB specimens. The dry and wet specimens had similar fracture surfaces. However, the wet specimen seems to have clearer surface with fiber debonding, which is an evidence of the matrix degradation and the weakening of fiber/matrix interface due to seawater absorption. Many authors reported that the increase of Mode I fracture toughness after immersion is mainly due to the enhanced fiber-bridging effect of unidirectional composites, which was not found in the woven laminate used in this study. Therefore, the decrease of mode I fracture toughness for  $80^\circ\text{C}$  immersion specimens is a direct result of fiber/matrix interface weakening.

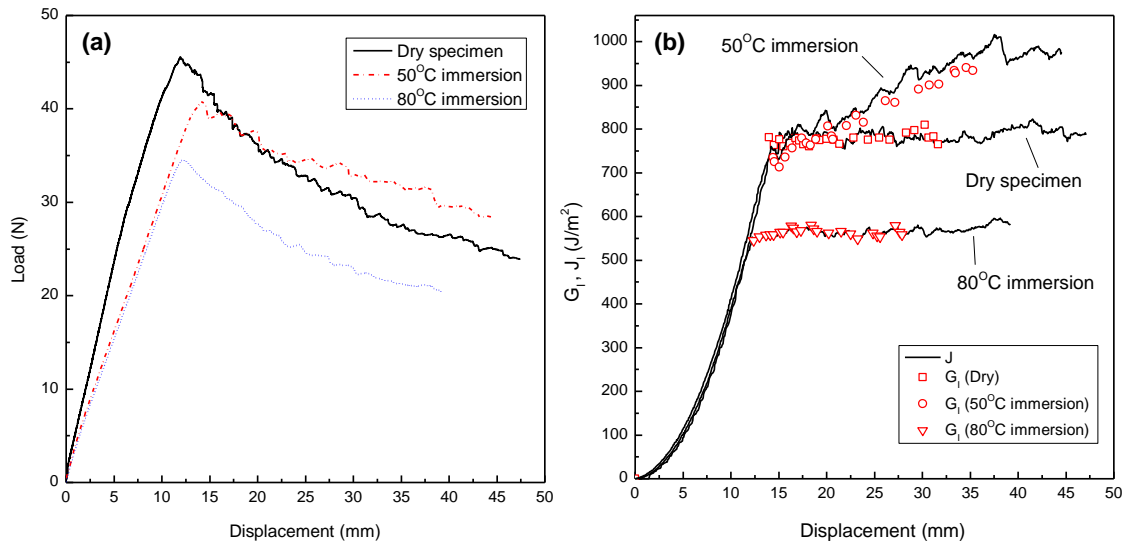


Figure 5.21. (a) Typical load-displacement curves from DCB tests (b) Typical delamination resistance curves.

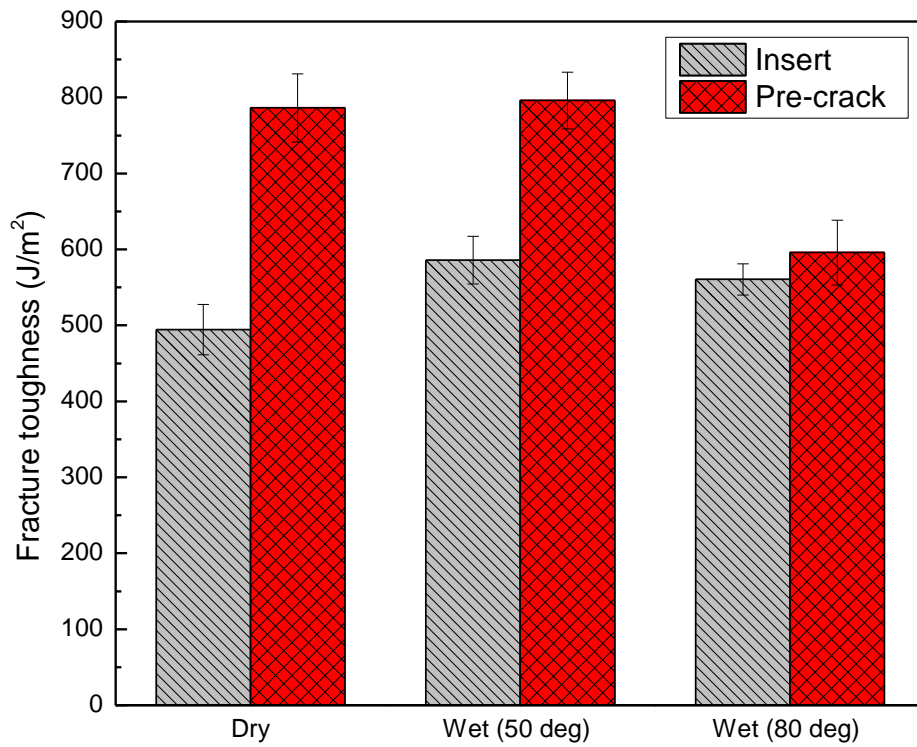


Figure 5.22. Mode I fracture toughness measured from insert and pre-crack.

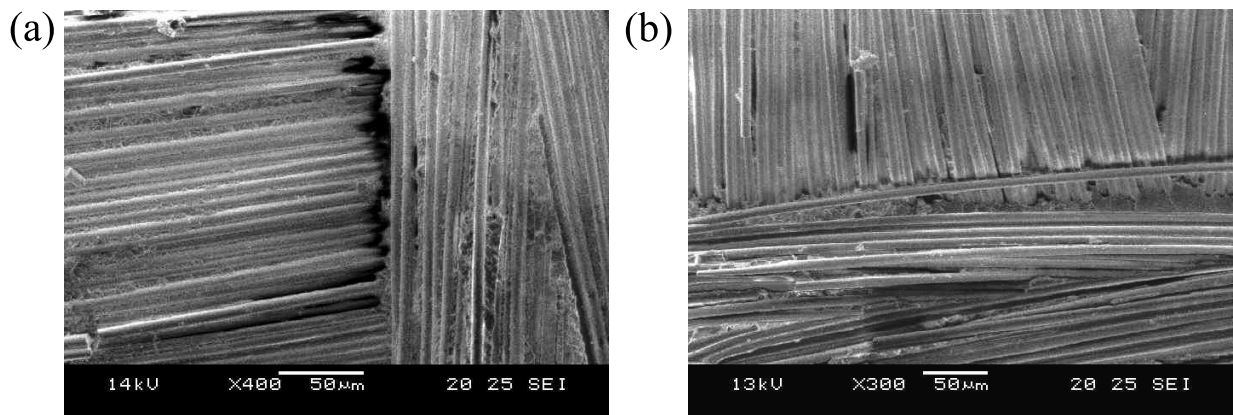


Figure 5.23. Typical SEM micrographs of mode I delamination surfaces for (a) dry and (b) 80°C immersion specimens (*Direction of delamination from left to right*)

### 5.5.2 Mode II delamination behavior

Typical loading curves at delamination front of pre-cracks for dry and wet specimens immersed in 50°C and 80°C seawater are presented in Figure 5.24 (a). The test results showed similar stiffness for dry and 50°C immersion specimens, whereas the stiffness reduced considerably for the specimens immersion in 80°C seawater. The delamination growth for mode II ENF tests was unstable compared to mode I DCB tests, and the loading curves of wet specimens showed strong non-linear behavior. The  $G_{II}$  and  $J_{II}$  vs. load-point displacement of the specimens are shown in Figure 5.24(b). The variation of the ENF test results was significantly higher than that of the DCB test due to the unstable propagation. It was also very hard to determine the delamination tips visually, and only a few points were obtained using the ASTM standard procedure. On the other hand, the J-integral was able to record the resistance with delamination growth in real-time, as it has no requirements on knowing delamination length and specimen properties except for specimen width. It is also more appropriate to take the J-integral results over the ASTM results for the wet specimens, as the LEFM was not applicable to the wet specimens with the enlarged fracture process zone. The initiation fracture toughness obtained from both inserts and pre-cracks was presented in Figure 5.25. The fracture toughness from inserts decreased monotonically with the seawater immersion and increasing temperature due to the degradation of the matrix material. The pre-crack results were quite similar to insert results for dry specimens and 50°C immersion specimens given the level of intrinsic scattering of ENF experiments, except for the 80°C immersion specimens showing much higher fracture toughness from the pre-crack. Comparing to the result of dry specimen, the fracture toughness from pre-crack had a reduction of 17.7% and an increase of 19.7% after immersion at 50°C and 80°C respectively. The delamination under mode II loading is dominated by matrix shear cracking and interface fracture. The presence of water, on one hand, increases the fracture toughness by softening the material and extending the fracture process zone. On the other hand, it weakens the matrix and damages the bonding between the fiber and matrix, which was shown in 5.2.2, and results in lower fracture toughness. Therefore, the influence of seawater on the mode II delamination behavior is a

combination of these two competing effects. The increasing resistance of the immersed specimen is an evidence of strong plasticization effect. Therefore, the significant increase of  $G_{IIC}$  at 80°C immersion can be related to the dominant effect of enlarged fracture process zone with viscoelastic deformation near the tip area.

This explanation is supported by examining the SEMs of the fracture surfaces in Figure 5.26. The fracture surface of the dry specimens exhibited brittle fracture with typical matrix hackles. The morphology showed no sign of plastic deformation. On the contrary, no distinguishable hackles were observed on the fracture surfaces of the wet specimens. Many matrix residues were found on the fibers due to matrix plasticization and ductile fracture. The difference of fracture mechanisms between dry and aged specimens were also observed in previous studies [160, 168]. However, it has also been shown that the improvement could be only temporary and reversible as the damaging effect prevails in the longer term [162, 204, 205]. Moreover, the dry specimens had stable delamination resistance curves, while wet specimens under both conditions had increasing resistance with delamination growth. The resistance was even higher for 80°C immersion specimens than 50°C immersion specimens.

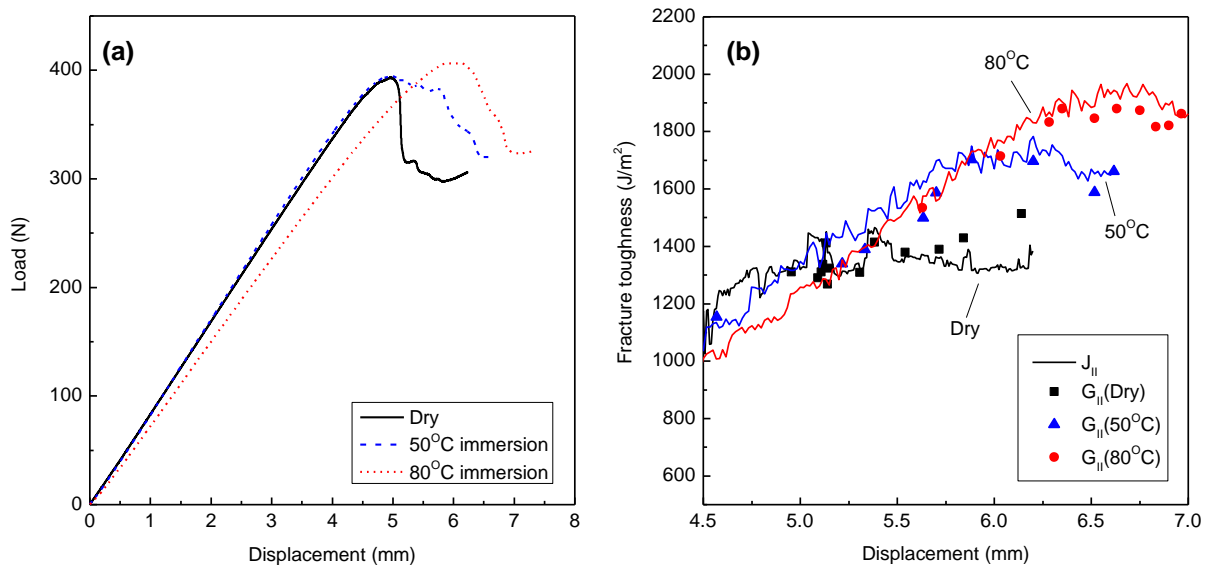


Figure 5.24. (a) Typical load-displacement curves of ENF tests from pre-cracks  
(b) Typical delamination resistance curves.



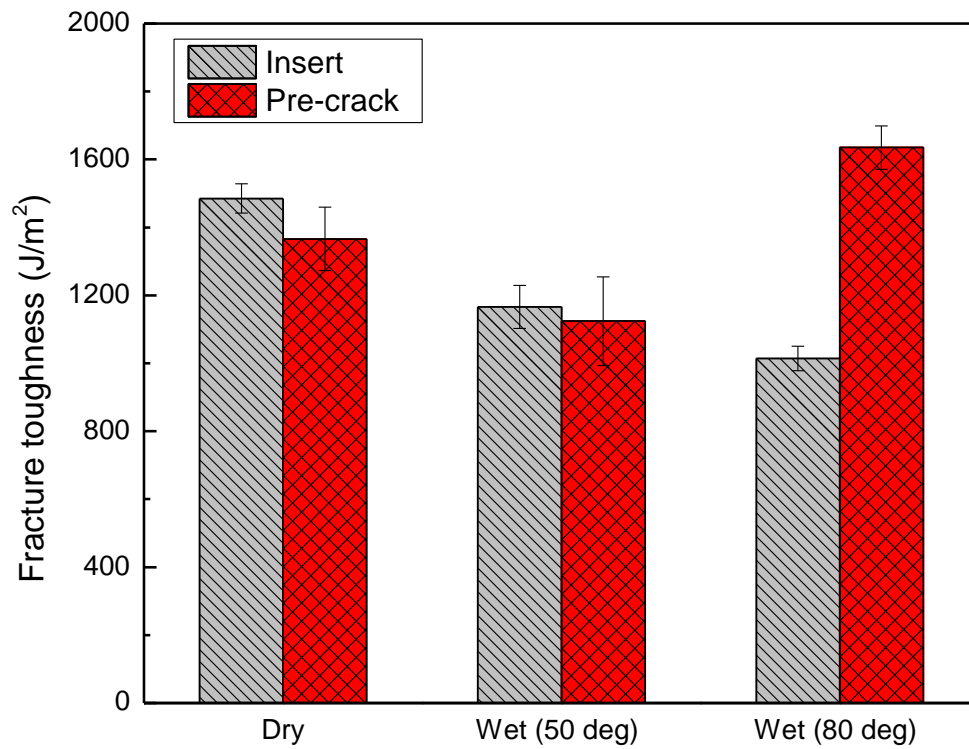


Figure 5.25. Mode II fracture toughness measured from insert and pre-crack.

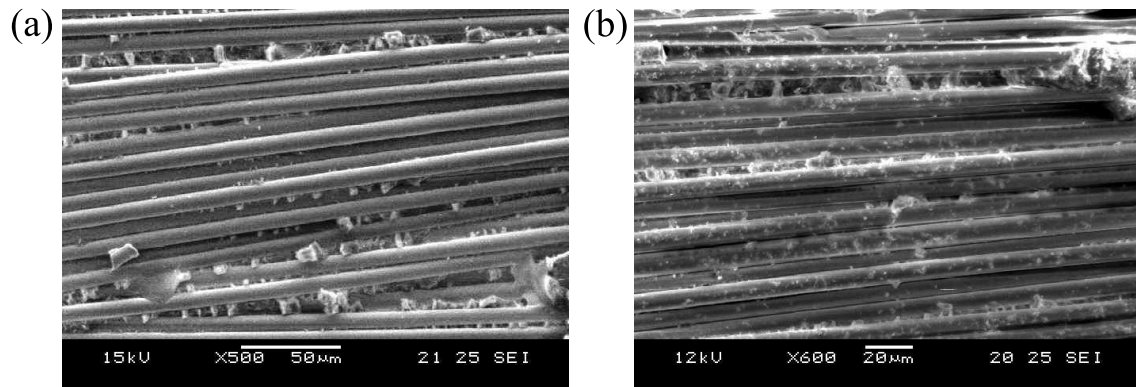


Figure 5.26. Typical SEM micrographs of mode II delamination surfaces for (a) dry and (b) 80°C immersion specimens (*Direction of delamination from left to right*)

### 5.5.3 Mixed-mode delamination behavior

Mixed-mode bending tests were conducted for both dry and wet specimens subjected to mode mixity ranging from 0.33 to 0.81. Typical applied load vs. crosshead displacement curves for 80°C immersion specimens at five mode mixities are presented in Figure 5.27(a). All the conditioned wet specimens showed stable delamination propagations, whereas no stable delamination growth was achieved for all the dry specimens. The test results of two mixed-mode specimens with 80°C immersion are presented in Figure 5.27(b). In general, the fracture toughness measured by the J-integral method and the ASTM method is in good agreement for dry and wet specimens at all mode mixities. Figure 5.28 presents the fracture toughness of initiation as a function of the mixed mode ratio,  $\frac{G_{II}}{G_T}$ , for the dry and wet specimens, where  $G_T = G_I + G_{II}$ . The fracture toughness was found to decrease monotonically with seawater exposure and increasing temperature except for pure mode II results, where it surged up nearly 20% over the dry specimen results. In addition, the wet specimens all exhibit slight increasing resistance curves at all mode mixities.

In the cohesive zone FEM model, delamination criterion needs to be selected to simulate the delamination growth. A power law criterion [147] is often used to predict the mixed-mode fracture toughness in terms of the interaction of its mode I and mode II energy release rate

$$\left(\frac{G_I}{G_{IC}}\right)^\alpha + \left(\frac{G_{II}}{G_{IIC}}\right)^\alpha = 1 \quad (5.8)$$

where  $\alpha$  is a material dependent parameter. In most cases,  $\alpha$  is taken as 1 or 2 for prediction. Another commonly used mixed-mode criterion (B-K law) was proposed by Benzeggagh and Kenane, which can be expressed as [149]

$$G_C = G_{IC} + (G_{IIC} - G_{IC}) \left(\frac{G_{II}}{G_T}\right)^\eta \quad (5.9)$$

where  $\eta$  is a material dependent parameter. These two criteria were fitted to the experimental data in Figure 5.28, and the fitted material dependent parameters and  $R^2$  are presented in Table 5.7. In general, both criteria are able to provide

reasonable predictions while the Power law gives a better overall result for the dry and 50°C immersion specimens. The results of 80°C specimens significantly deviated from the others due to the sudden increase at pure mode II loading. This is an implication that the failure mechanism has been altered due to the possible chemical reaction which occurs during seawater immersion at elevated temperature.

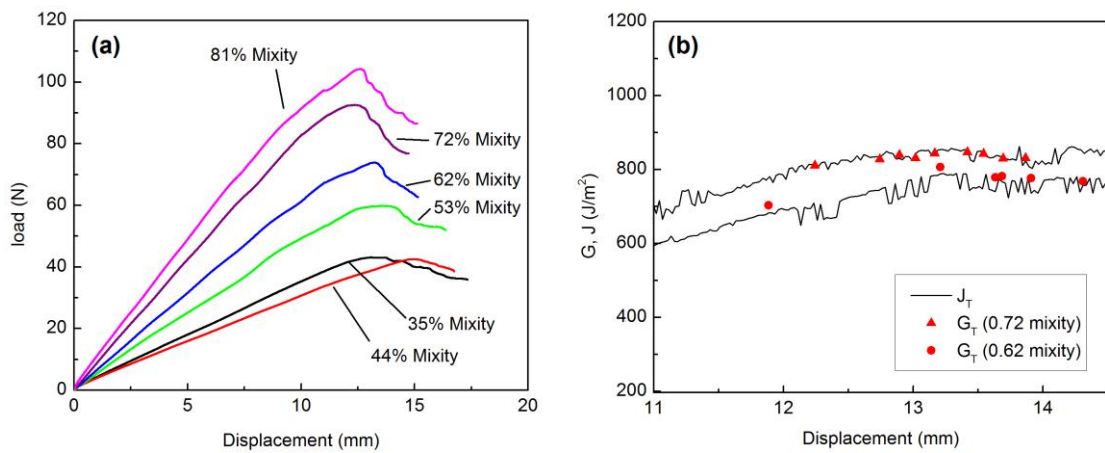


Figure 5.27. (a) Typical load-displacement curves from mixed-mode bending tests (b) Typical delamination resistance curves.

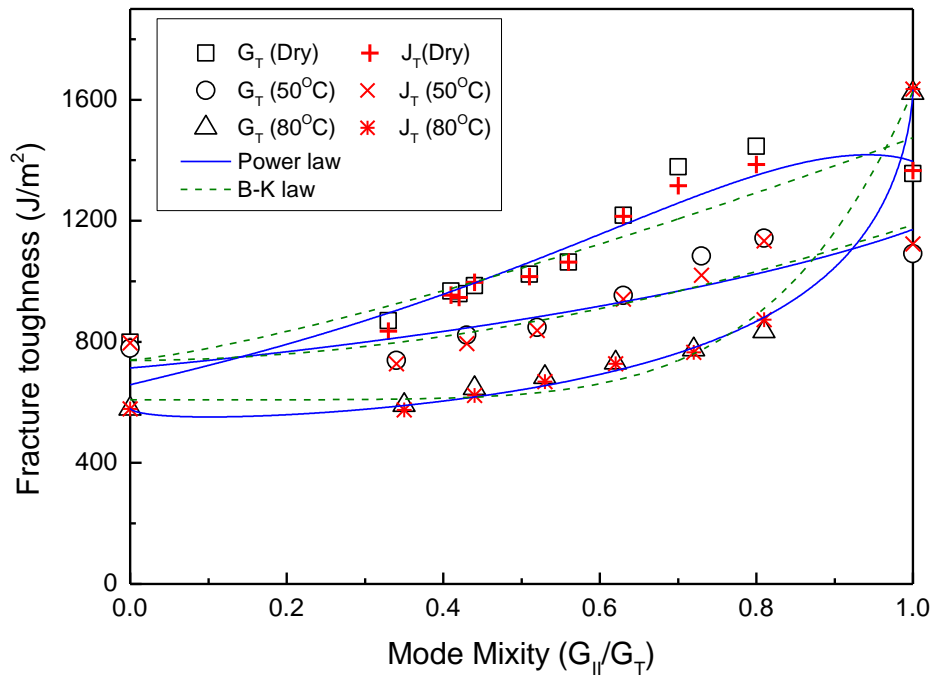


Figure 5.28. Mixed-mode delamination criteria fitted to experimental data

Table 5.7. Fitted parameters for delamination criteria

Condition	B-K law		Power law	
	$\eta$	$R^2$	$\alpha$	$R^2$
Dry	1.27	0.89	1.37	0.93
Wet (50°C)	1.88	0.86	0.89	0.89
Wet (80°C)	5.79	0.99	0.67	1.00

#### 5.5.4 Comparison of the methods for characterizing interlaminar fracture toughness

In this section, the fracture toughness results were obtained using the well-established ASTM methods and the proposed J-integral method simultaneously, and the results are compared in Figure 5.29. Good agreement was found between the results of the two methods for the dry specimens due to the small fracture process zone of the specimens.

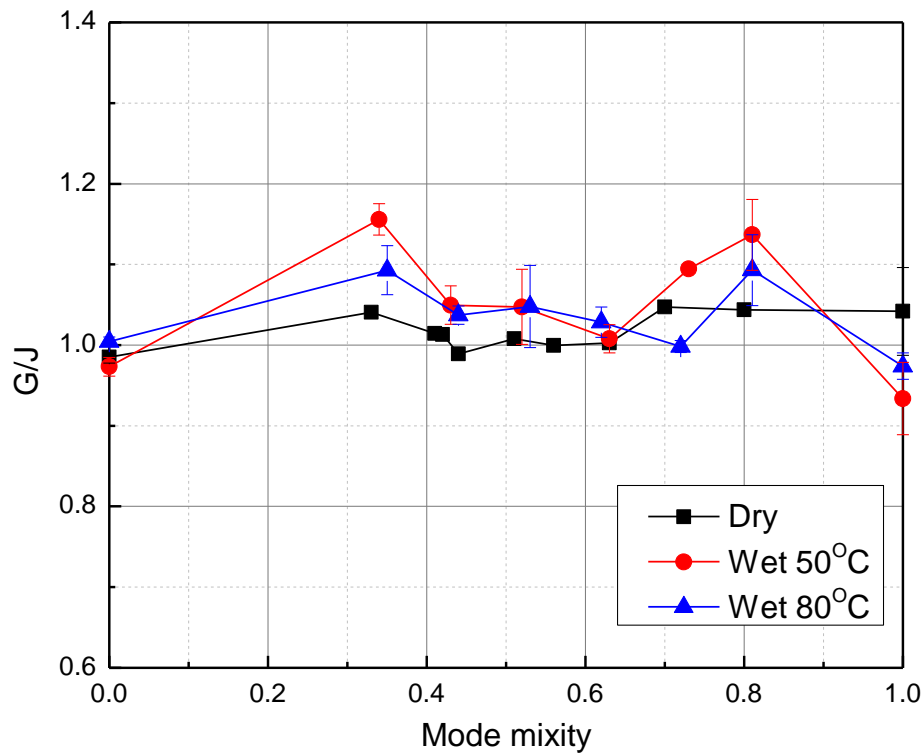


Figure 5.29. Relative difference between the ASTM standard and the J-integral methods

For example, Figure 5.30(a) shows a typical applied load vs. load-point displacement curve of a specimen from the DCB tests. The analytical solution of the DCB test based on LEFM is given by [206]

$$P = \sqrt{\frac{8}{\delta}} b \left( \frac{G_{IC}}{12} \right)^{\frac{3}{4}} (h^3 E_{1f})^{\frac{1}{4}} \quad (5.10)$$

where the  $G_{IC}$  was taken as the averaged value of all the DCB specimen results, and  $E_{1f}$  was determined based on the modified beam theory. In Figure 5.30(a), good agreement was found between the experimental results, the analytical solution, as no fiber bridging was observed in all DCB specimens, and the FPZ was small. The rotations at two loading points were continuously monitored by the proposed image-processing program, described in section 4.3.1.4, and presented in Figure 5.30(b) with respect to the corresponding displacement. The  $G_I$  and  $J_I$  vs. load-point displacement were calculated and shown in Figure 5.30(c). The  $G_{I,NL}$  and  $G_{IC}$  are the mode I critical energy release rate obtained by non-linear and 5% offset/Maximum criteria described in the ASTM standard. The obtained delamination resistance curves (R-curve) showed consistent mode I interlaminar fracture toughness for initiation and propagation. As shown in Figure 5.30(c), both methods provided comparable results and the variations were very small. However, J-integral approach is able to take continuously accurate readings and avoid the needs for visually determining the delamination length. In fact, J is interchangeable with G in the cases where the LEFM holds, and the delamination length is given as [137]

$$a = \frac{3\delta}{2(\sin\theta_A - \sin\theta_B)} \quad (5.11)$$

In Figure 5.30(d), the calculated delamination length is compared with that from visual observation and the results are in excellent agreement. It is worth noting that the visually obtained delamination was corrected with  $|\Delta|$  in Figure 5.30(d).

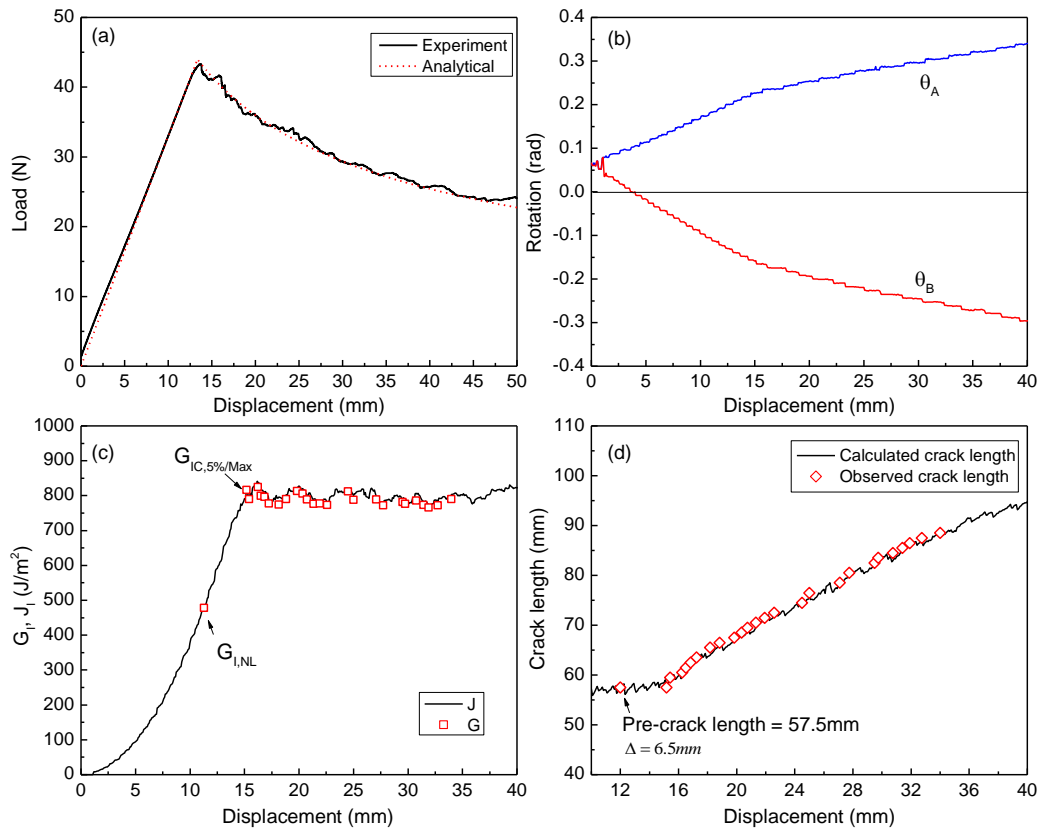


Figure 5.30. (a) Load-displacement curves (b) rotation angles vs. crosshead displacement at loading point and (c) Mode I interlaminar fracture toughness results (d) observed and calculated delamination length

However, larger deviations were observed in the measurements for the wet specimens, especially for propagation values. Similar results were also reported and discussed in a recent study of Sarrado et al. [145]. They argued that the LEFM-based data reduction method depends heavily on the size of the fracture process zone and is not suitable for characterizing the fracture toughness of adhesive joints. Likewise, the LEFM assumption of small FPZ may not be valid for the wet specimens with strong plasticization as well. However, the J-integral method is still applicable to the materials without the restrictions of LEFM assumption, especially for those with large FPZ and significant fiber bridging phenomenon. The discrepancy between two methods is higher for the mode II ENF test than the mode I DCB test. That is mainly because the delamination growth in the ENF tests was unstable and difficult to measure for the standard methods. The J-integral method exhibited significant lower variances because the visual determination of delamination length was avoided in the proposed process. The inputs required by the ASTM standard method and the proposed

method are listed in Table 5.8. The sources of uncertainty are reduced in the proposed method, as no delamination length, elastic properties and system compliance need to be measured.

The proposed experimental method obtains the fracture toughness by measuring the applied loads and the angular rotations of the specimens at the loading points. Therefore, the method reduces the complexity of using three different procedures to measure the fracture toughness under mode I, mode II and mixed-mode I/II loading. In addition, the resistance curve can be easily monitored in real-time using an image processing program.

Table 5.8. Parameters required by the ASTM standard method and the proposed method

Specimen	ASTM standard method	Proposed method
DCB	$b, h, P, \delta, a$	$b, P, \theta_A, \theta_B$
ENF	$b, h, P, \delta, a$	$b, P, \theta_A, \theta_B, \theta_C$
MMB	$b, c, c_g, L, h, P, P_g, \delta, E_{11}, E_{22}, G_{13}, a$	$b, c, c_g, L, P, P_g, \theta_A, \theta_B, \theta_C, \theta_D$

### 5.5.5 FEM modeling of delamination behavior

A 2D plane strain FEM model was used to simulate the delamination behavior of the dry specimens. The dimensions of the model for DCB, ENF and MMB specimens are given in Table 5.9. The selection of several important parameters, such as the cohesive element size, the length of cohesive zone and interfacial strength, has strong influence on the accuracy of the cohesive zone model. In this section, the effects of these parameters are examined for the simulations, while the composite substrates are meshed with two dimensional plane strain element CPS4I with a size of 0.5mm\*0.5mm.

Table 5.9. Specimen geometries

Test method	Span (mm)	Initial delamination (mm)	Thickness (mm)	Width(mm)
DCB	200	55	4	20
ENF	100	35	4	20
MMB	140	50	4	20

#### 5.5.5.1 DCB model

A typical simulation of mode I delamination is presented in Figure 5.31. As reviewed in section 2.5.4 the cohesive length of a DCB model, with a fixed normal interfacial strength  $\tau^0$ , can be estimated by

$$l_{cz} = \left[ E \frac{G_c}{(\tau^0)^2} \right]^{\frac{1}{4}} t^{\frac{3}{4}} \quad (5.12)$$

where  $E$  is the young's modulus,  $G_c$  is the fracture toughness and  $t$  is half thickness of the specimen. As a result, the number of elements ( $N_e$ ) in one cohesive length is given as

$$N_e = \frac{l_{cz}}{l_e} \quad (5.13)$$

where  $l_e$  is the cohesive element length used in the model. Numerical load-displacement curves for different cohesive element size with fixed normal interfacial strength are compared with the actual experimental results in Figure 5.32. In this case, the length of the cohesive zone is 2.4mm calculated by Eq. (5.12), and the corresponding number of elements was around 10, 5 and 3 for  $l_e = 0.25\text{mm}, 0.5\text{mm}$  and  $1\text{mm}$  respectively. It is obvious that at least five cohesive elements in one cohesive length are needed for the simulation to accurately predicts the DCB delamination behavior. When only three cohesive elements were used, the load was significantly over estimated by the simulation and the oscillation of the results was very strong.



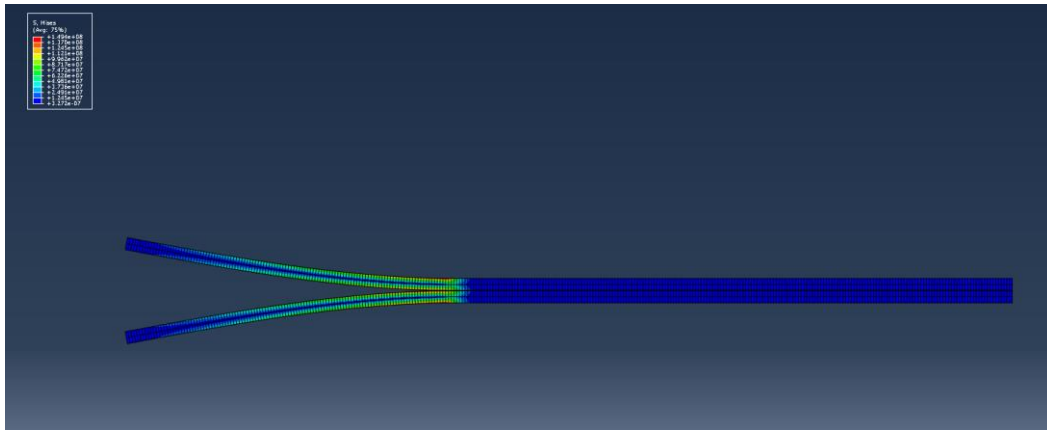


Figure 5.31. Stress distribution of the deformed 2D model of DCB specimen simulation

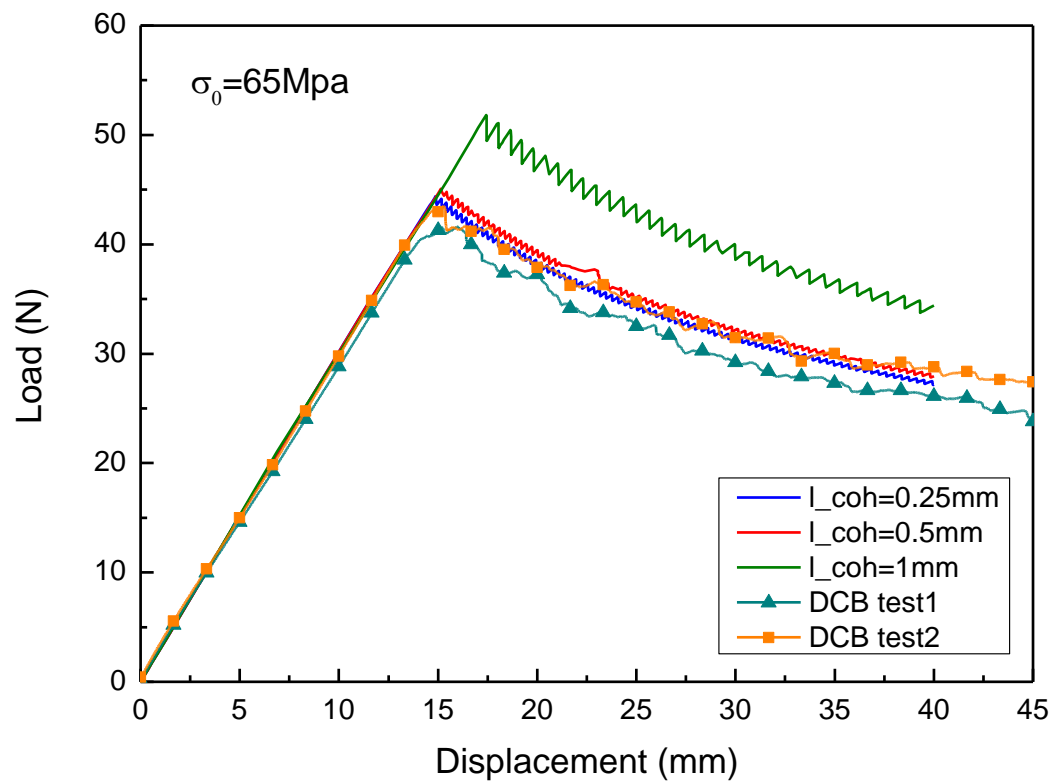


Figure 5.32. Effect of cohesive element size on the simulation of DCB load-displacement curve

The results of  $l_e = 0.25mm$  only showed limited improvement from that of  $l_e = 0.5mm$ , though the number of elements were doubled. Both simulation results of  $l_e = 0.25mm$  and  $l_e = 0.5mm$  are in very good agreement with the experimental result. Based on Eq. (5.12), reducing the interfacial strength will increase the length of the cohesive zone. Thus, if properly used, fewer elements can be used to give an accurate simulation, which reduces the computational cost considerably. However, the parameter needs to be adjusted with great care. A comparison in Figure 5.33 is made for several simulations with different interfacial strengths. It can be seen that low interfacial strength might cause significant increase of the specimen compliance and delay of crack propagation. Higher interfacial strength will reduce the cohesive zone length and affect the stability of the result. The solution tends to diverge during the analysis and higher viscous regularization is needed.

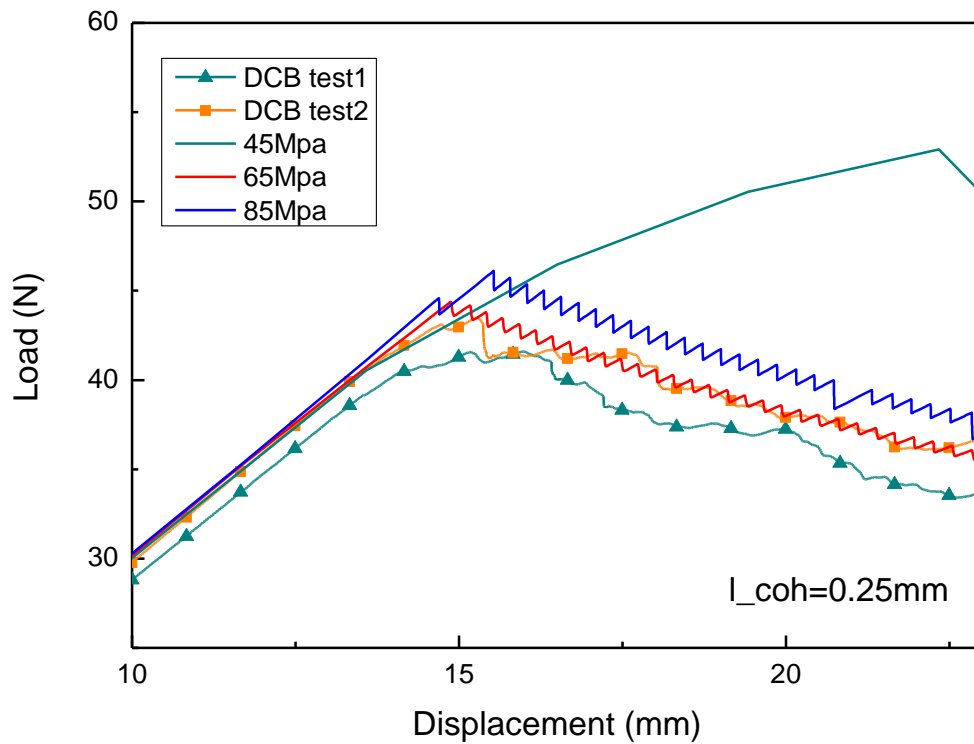


Figure 5.33. Effect of interfacial strength on the simulation of DCB load-displacement curve

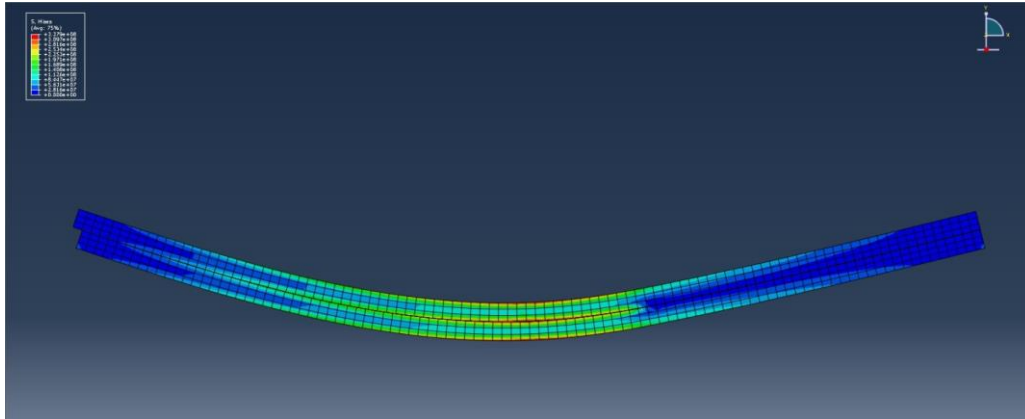


Figure 5.34. Stress distribution of the deformed 2D model of ENF specimen simulation

#### 5.5.5.2 ENF model

Similar analyses were carried out on the simulation of ENF specimens. Figure 5.34 gives an example of a typical 2D ENF simulation result. In this case, contact surfaces were defined at the initial cracks to avoid crack face overlap. The ENF simulations were carried out on three different cohesive elements size and presented together with experimental results in Figure 5.35. The simulation of ENF results are in good agreement with the experimental results. However, the simulations failed to catch the nonlinear behavior prior to delamination. The propagation simulation deviates from the actual test results because the propagations in ENF tests were not very stable. Unlike DCB model, ENF simulations with three element sizes all give similar results in peak force and propagation but the refined mesh shows less oscillation. The effect of interfacial strength is shown in Figure 5.36. Higher interfacial strength results in slightly higher maximum load and higher oscillation in the solution. Lower interfacial strength would show some nonlinear behavior prior to the delamination. However, in general, it can be seen that the ENF simulation is quite insensitive to the change of interfacial strength as well. The finding indicates that reducing interfacial strength in ENF simulation can be an effective way to reduce the mesh density and hence the computational cost.

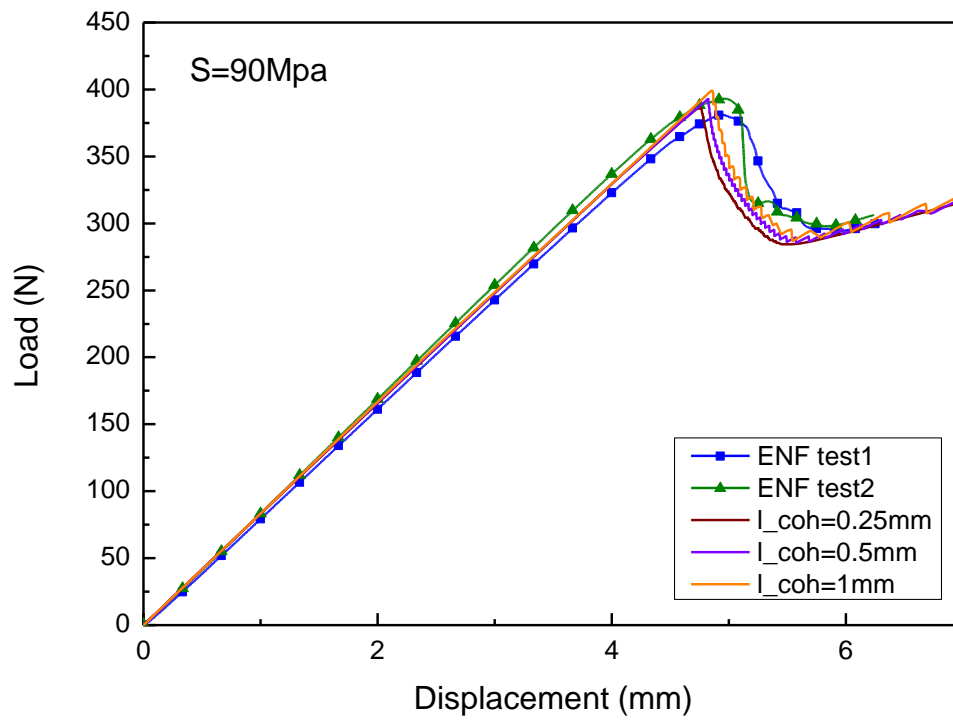


Figure 5.35. Effect of cohesive element size on the simulation of ENF load-displacement curve

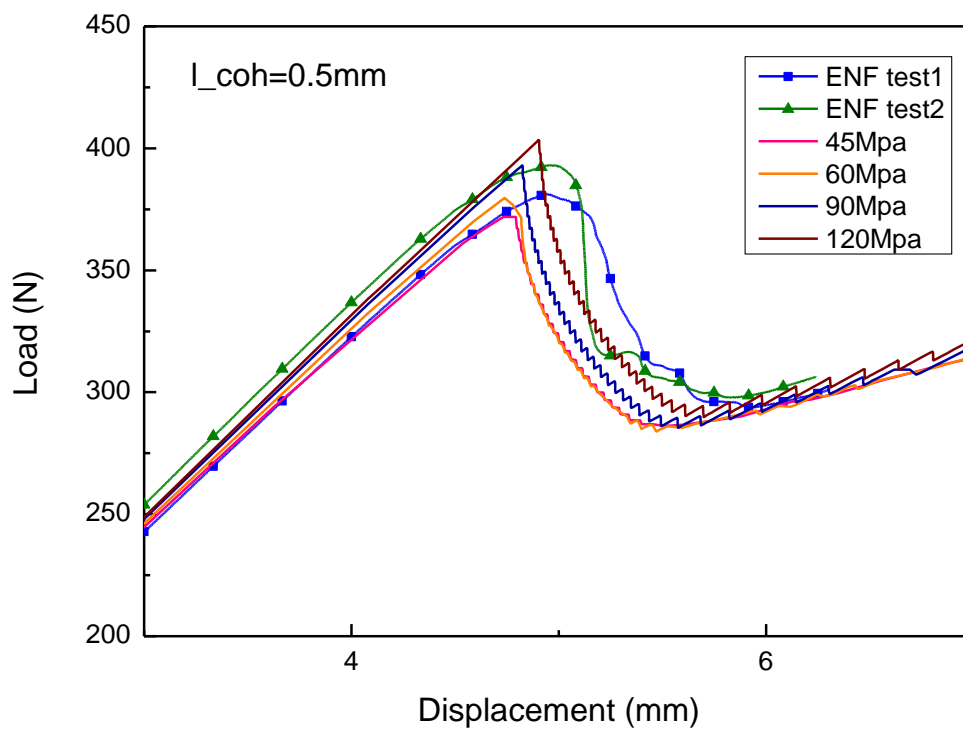


Figure 5.36. Effect of interfacial strength on the simulation of ENF load-displacement curve

### 5.5.5.3 MMB model

In the FEM model of the MMB specimen, the initial cracks were placed with already opened cohesive elements to avoid interpenetration during compression. The penalty stiffness for the opened cohesive elements was set as  $1\text{E}15\text{Pa/m}$ . The length of level arm was set to be  $65.8\text{mm}$ , which was the same as the experimental configuration of the MMB test with a mode mixity of  $0.51$ . The size of the cohesive element used in the MMB model was  $0.25\text{mm}$ . The quadratic maximum stress for delamination initiation and the B-K law for predicting the propagation. The parameter was obtained from experimental data in section 5.5.3. Figure 5.37 shows an example of a 2D MMB simulation result, and the corresponding load-displacement curve is given in Figure 5.38 with the experimental result. The FEM model accurately captured the load and displacement at the initiation of the delamination. However, the actual test results showed a sudden fracture without a stable delamination propagation, which was predicted by the FEM model. Besides, the simulation slightly underestimated the stiffness of the actual load-displacement curve of the MMB specimen.

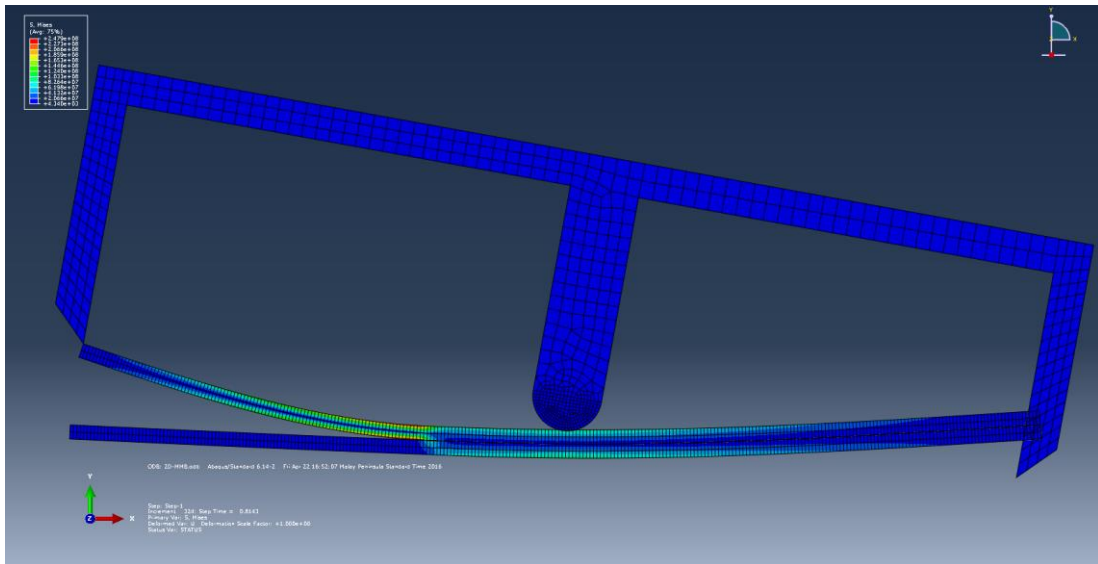


Figure 5.37. Stress distribution of the deformed 2D model of MMB specimen simulation

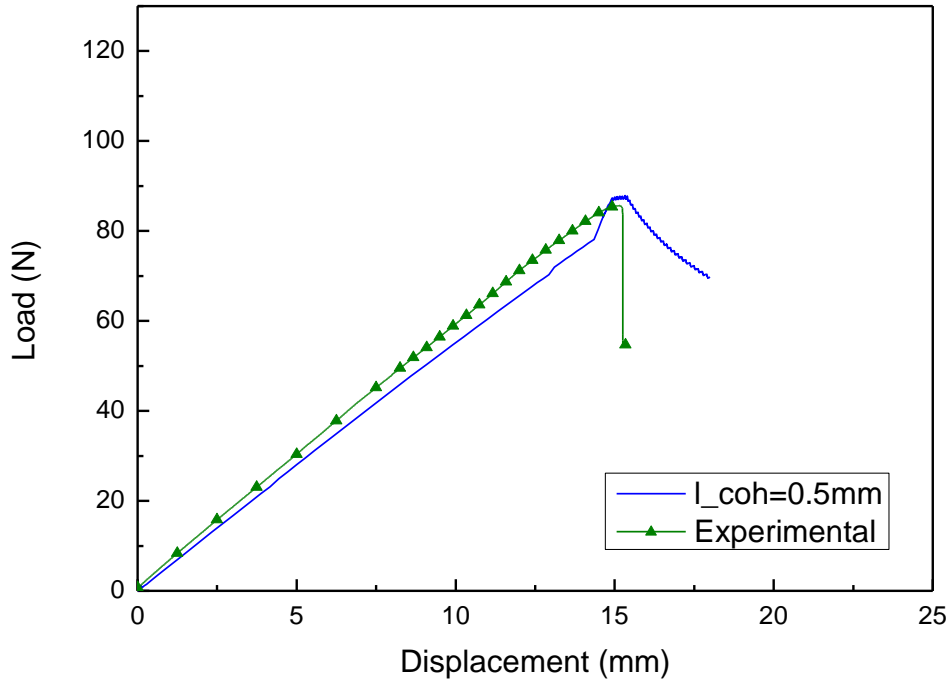


Figure 5.38. Comparison of simulation and experimental results of MMB specimen at mode mixity of 0.51

## 5.6 Seawater effects on mode II fatigue delamination properties

The ENF specimens used for the mode II fatigue delamination had the same dimension and curing process as the specimens for static tests used in the previous chapters. However, they were manufactured from different batches and had slightly different properties. On top of that, the specimens were tested at 2500 hours of immersion in 50°C artificial seawater. Therefore, the static delamination properties were performed prior to the fatigue tests. In this chapter, the strain energy release rate ( $G$ ) were used so that the evaluation methods were consistent for both static and fatigue tests.

### 5.6.1 Static Mode II strain energy release rate

Table 5.10. Static  $G_{IIC}$  test results

Condition	No. of Specimens	$G_{IIC,i}$ ( $J/m^2$ )	Diff.	$G_{IIC,pre}$ ( $J/m^2$ )	Diff.
Dry	15	$1789.1 \pm 93.0$	-	$1359.3 \pm 25.1$	-
Wet	15	$1762.6 \pm 79.2$	1.48%	$1568.4 \pm 37.2$	15.4%

The averaged static test results of  $G_{IIC}$  with one standard deviation for dry and wet specimens are summarized in Table 5.10. After the pre-crack was created, the crack lengths on both sides were examined using optical microscope and an average deviation of 1.3 mm was found. In order to validate the crack length obtained by CC method, same ENF tests were carried out on pre-cracked specimen with 30mm crack length based on the calculated value. The compliance obtained using calculated crack length is compared with that obtained from the original 30mm crack-starter, and the result indicates the method to be quite accurate with only an averaged difference of 2.21%. The critical strain energy release rates are calculated based on the maximum loads applied to the specimen from the insert ( $G_{IIC,i}$ ) and the pre-crack ( $G_{IIC,pre}$ ). Typical loading curves at delamination front of insert and pre-crack for dry and wet specimens are presented in Figure 5.39. The  $G_{IIC}$  obtained from pre-crack is about 76% of that from insert for dry specimens and 89% from wet specimens. Similar results have been also reported by other researchers [21, 189, 207] on different kinds of carbon fiber epoxy laminates. The lower value of  $G_{IIC,pre}$  to  $G_{IIC,i}$  is mainly owing to an area of micro-tension cracks zone ahead of the delamination front which takes less energy for the main crack to propagate. However, the delamination growth from insert requires the zone to be created before it can propagate resulting in higher  $G_{IIC}$  (Figure 5.40 (a) (left)) [189]. Therefore, the  $G_{IIC,pre}$  is considered as the actual  $G_{IIC}$  of the specimen and used in the following fatigue tests. Nevertheless, the CC coefficients were found to be consistent for ENF tests from insert and pre-crack in both dry and wet conditions. The crack on the side of the specimens was examined by optical microscope, and a typical view is shown in Figure 5.40(a) (right). Figure 5.40(b) is a schematic illustration of the propagation of primary inter-ply crack, which follows the weave structure confined in the ply interface [21]. However, a few secondary cracks including crack bifurcation and inter-yarn cracks were also observed along the primary cracks. It is also worth noting that the  $G_{IIC}$  of wet specimen turns out to be 15.4% higher than that of dry specimens. This is mainly because the plasticization effect of water enhances the ductility of the matrix, extends the damage zone and increases the delamination area, which leads to a higher  $G_{IIC}$  of the composites [208]. In fact, the compliance of the

specimen is measured to be 13.2% higher after water absorption. As the plasticization effect of seawater is relatively strong for BMI composites, the  $G_{IIC}$  is improved after 2500 hours of exposure to seawater at 50°C. However, it has also been well acknowledged that the water absorption would weaken and damage the fiber/matrix interface in the long-term. Therefore, the interaction of these two competing effects may be the reason of the conflicting results reported in previous studies [208, 209]. However, this effect of enhancing  $G_{IIC}$  is more important in a relatively short-term and almost reversible while the deterioration effect of water prevails in the long run.

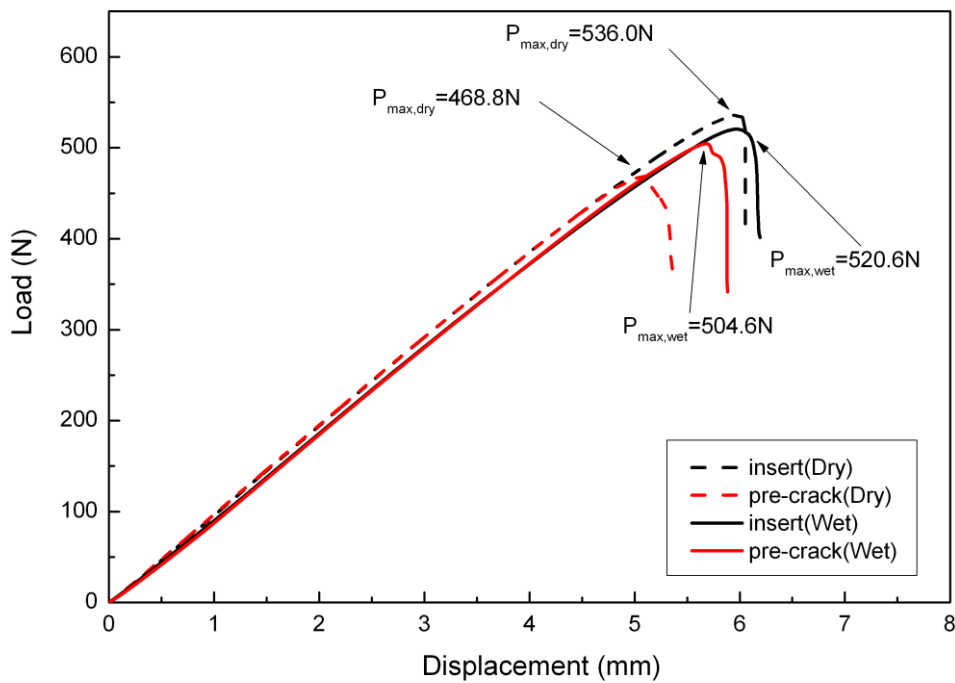


Figure 5.39. Typical loading curves specimens with 30mm crack length in static ENF test



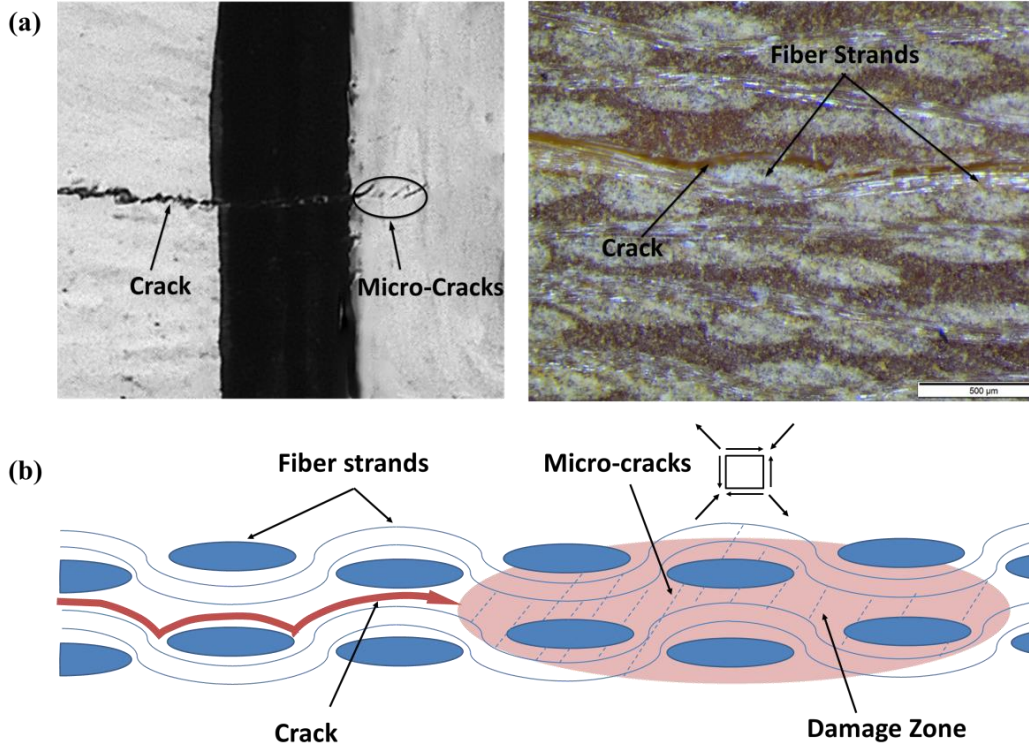


Figure 5.40. (a) Micro-cracks ahead of crack tip and primary inter-ply crack (b) schematic illustration of primary interplay crack propagation

### 5.6.2 Fatigue delamination growth

Generally, the stable fatigue crack growth follows the Paris law, and the relation between crack growth rates and  $\Delta G_{II}$  can be written as:

$$\frac{da}{dN} = D(\Delta G_{II})^q \quad (5.14)$$

where  $D$  and  $q$  are constants dependent on laminate properties and loading conditions. The relation between cycle count  $N$  and crack length  $a$  can be obtained by substituting Eq. (4.24) into Eq. (5.14) and integrating, which yields:

$$N = \frac{A(P)^{-q}}{D(1-2q)} (a^{1-2q} - a_0^{1-2q}) \quad (5.15)$$

or in the form suggested by [181]

$$a = H(N^* - N)^s \quad (5.16)$$

with

$$H = [D(2q - 1)A(P)^q]^s \quad \text{and} \quad N^* = \frac{a_0^{1-2q}}{D(2q-1)A(P)^q} \quad (5.17)$$

where

$$A(P) = \frac{3m(1 - R^2)}{2B} P^2$$

and

$$s = \frac{1}{1 - 2q}$$

$a_0$  and  $N^*$  are initial crack length and the cycle where the crack tends to propagate to infinite length. It is worth noticing that generally the equation derived from Paris law is valid under stable crack growth, which is  $a/L \approx 0.5$  to 0.9 in this case. The typical plot of crack length as a function of fatigue cycles for the specimens is shown in Figure 5.41. It can be seen from the fitted curve that the Paris law is able to model the delamination growth accurately. With the established model Eq. (5.16), the initial crack  $a_0$  is determined at  $N=0$ , and the corresponding normalized strain energy release rate,  $G_{max}/G_{IIC,pre}$ , is recalculated based on the initial crack length. The averaged initial crack lengths are  $a = 23.60$  mm for dry specimens and 24.41 mm for wet specimens. The averaged initial crack lengths are slightly lower than 25mm mainly because of the slippage of specimens on the fixture. The onset of the stable crack propagation is determined when the crack length has propagated to  $a = 0.05$ mm.

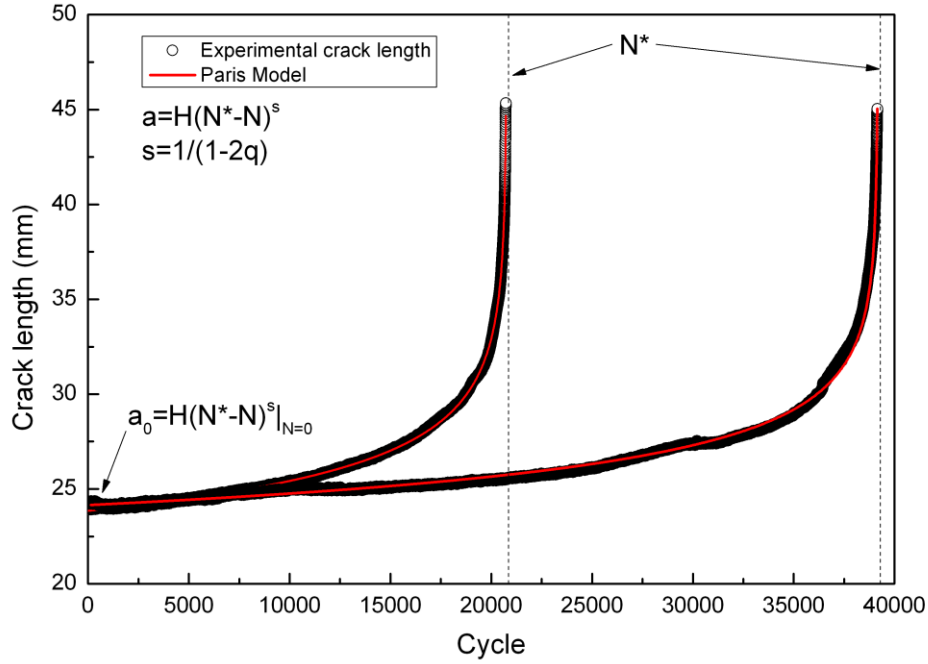


Figure 5.41. Typical plots of crack length as a function of fatigue cycles

Figure 5.42 shows the crack growth rates  $\frac{da}{dN}$  against  $\Delta G_{II}$  with a crack length increment ( $\Delta a$ ) of 1mm for dry and wet specimens. Based on the constants obtained from linear regression of the results and averaged initial crack length, the crack propagation of the specimen can be modeled as a function of fatigue cycles and applied force using Equation (5.16). Figure 5.43 presents a comparison between the cycles of delamination onset for each specimen and the prediction using the established model for dry and wet specimens. The  $G_{IIC,pre}$  value obtained in static test is also plotted as 100% normalized strain energy release rate at  $N = 0.5$  (half cycle). It can be seen that the predicted model is in a very good agreement with the experimental results for both dry and wet specimens. The predicted numbers of cycles for the delamination to propagate to 0.05mm and 10mm at all normalized strain energy release rates are presented in the Figure 5.44. Figure 5.44(a) shows that, at same energy release rate, the wet specimen shows slower delamination growth rates than dry specimen. The delamination growth rate normalized with corresponding critical energy release rates for dry and wet specimens are presented in Figure 5.44(b). It can be seen that the crack growth is slower for dry specimen at higher normalized strain energy release rates but the crack propagates much faster in wet specimen than

dry specimen at lower normalized strain energy release rates. The result of Figure 5.44 shows that the seawater exposure has significant effects on the Mode II fatigue delamination behavior of the material.

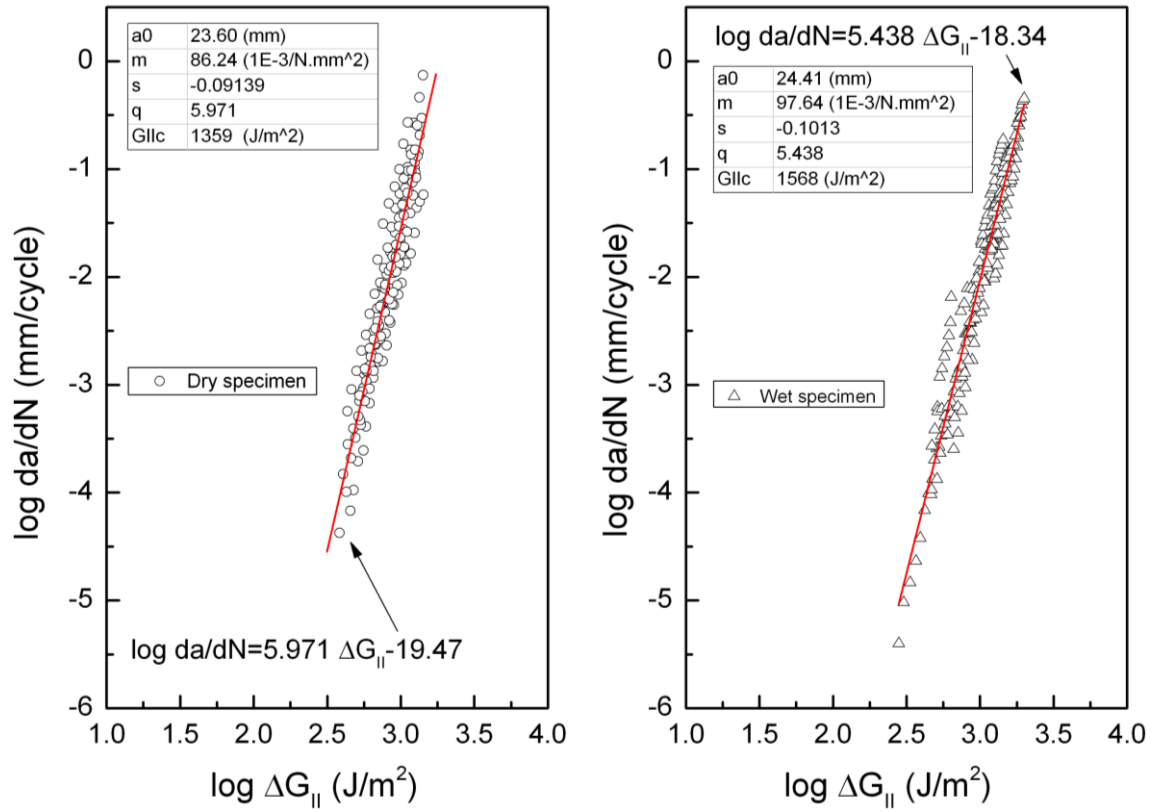


Figure 5.42. Fatigue crack growth rates against the  $\Delta G_{II}$

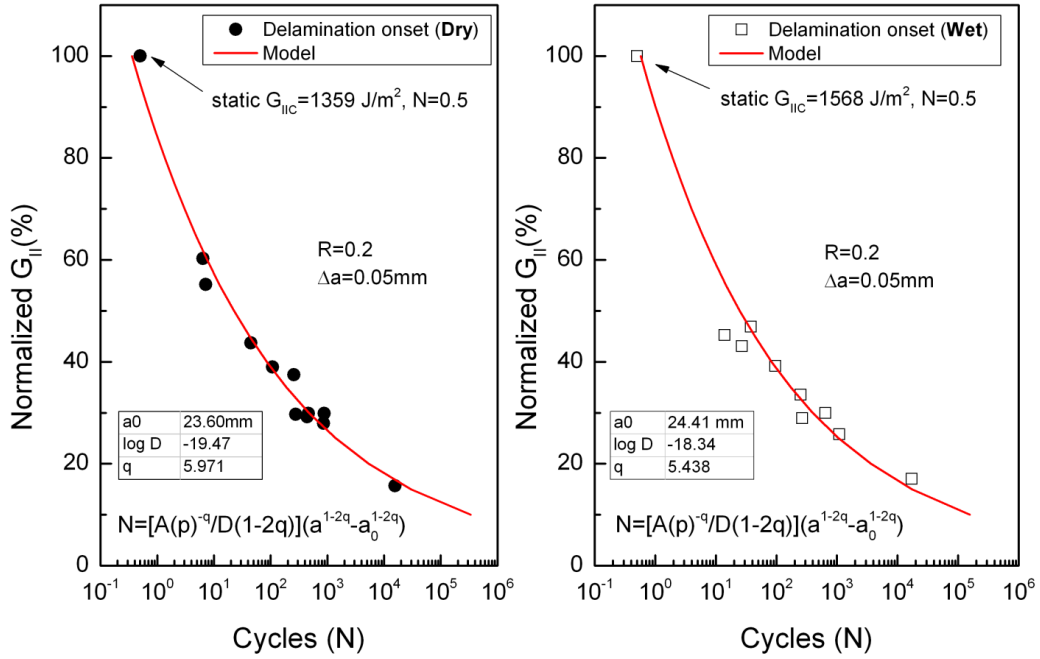


Figure 5.43. Delamination onset for all specimens and model prediction

The energy release rate vs. delamination length of dry and wet specimens at different constant loading are presented in Figure 5.45.  $P_{50}$ ,  $P_{35}$ , and  $P_{20}$  represent constant loadings applied on the specimen which generate 50%, 35% and 20% critical energy release rate at  $\Delta a = 0$  respectively. With constant loading, the energy release rate increases with the growth of crack length. The delamination growth is considered to be stable with the strain energy release rate ( $G_{II}$  line) lower than  $G_{IIC}$  (horizontal line in Figure 5.45), and become unstable once the  $G_{II}$  line passes  $G_{IIC}$ . As shown in Figure 5.45, the crack growth would remain stable with constant fatigue load at  $P_{20}$  throughout the whole fatigue test. In the case of  $P_{35}$ , the crack growth would only be unstable at the end portion of the test ( $\Delta a \approx 16 \text{ mm}$ ). It is calculated that 15 specimens (i.e. 8 dry specimens and 7 wet specimens) out of a total number of 20 have at least 70% stable crack growth region in the fatigue tests. Therefore, most of the test results are within stable growth region where the use of Paris law is valid.

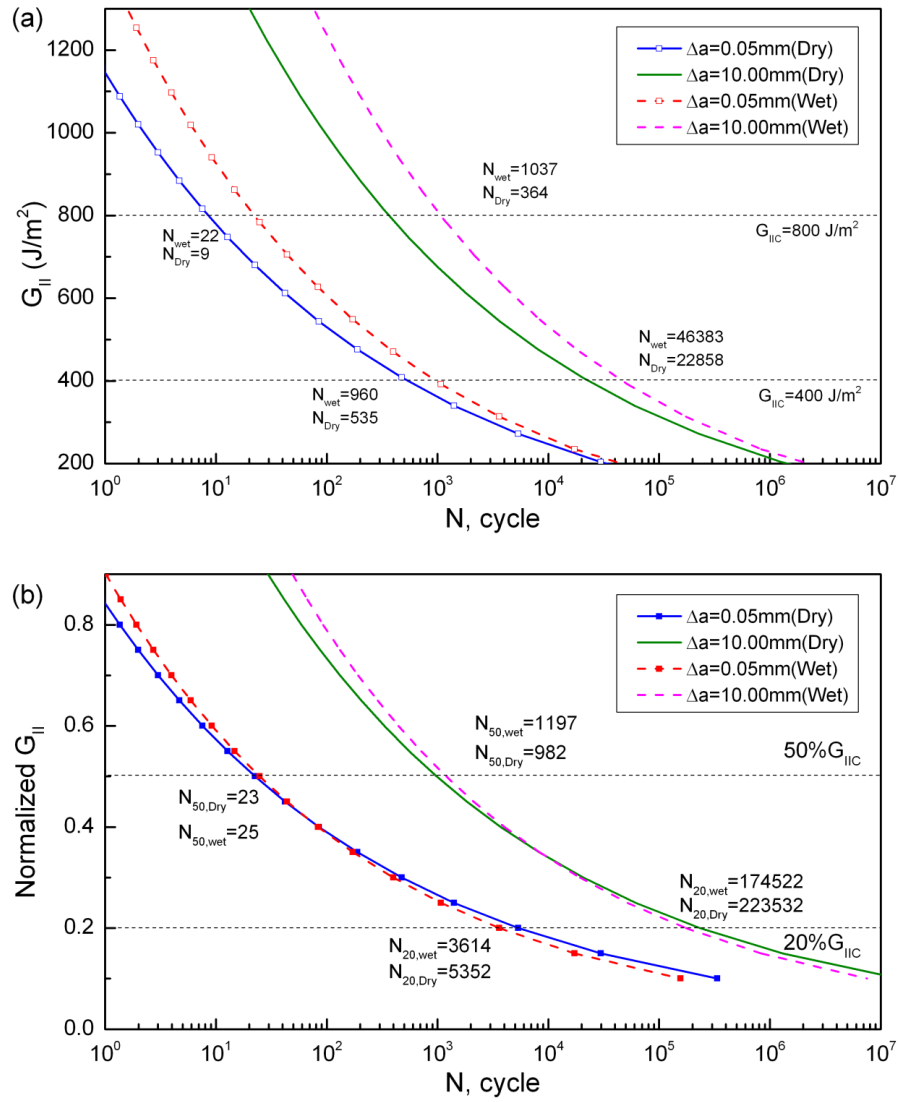


Figure 5.44. Predicted delamination growth behavior for dry and wet specimens;  
 (a) Energy release rate-fatigue growth behavior (b) Normalized energy release  
 rate with corresponding  $G_{IIC}$  of dry and wet specimen

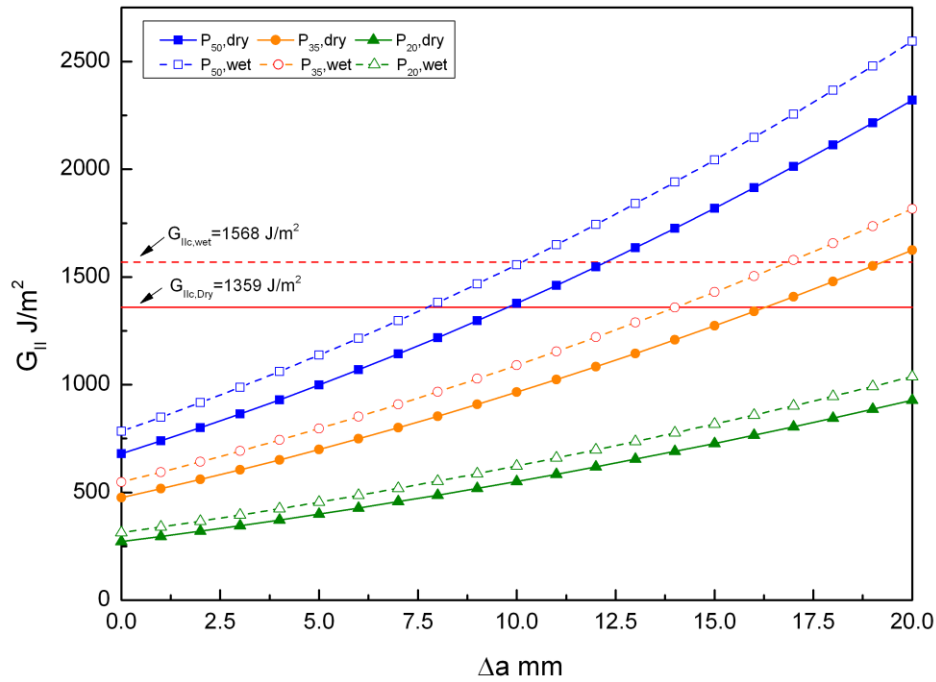


Figure 5.45. Energy release rate vs. delamination length at different loading ratios

### 5.6.3 Fractography

The delamination surfaces were examined by scanning electron microscope (SEM) to understand their different behaviors. Typical fracture surfaces of dry specimen and the wet specimen after fatigue tests are presented in Figure 5.46(a)(b) and (c)(d) respectively. The yarns, which are parallel and perpendicular to crack propagation direction, exhibit two distinctly different fracture surfaces. Smooth bare fibers are shown in yarns aligned in crack direction, whereas rougher surfaces with more remaining matrix and random fiber breakages can be noticed in transverse yarns. The surface topography also illustrates the discontinuous crack front in woven laminate where the crack front is more advanced on parallel yarns and lagged on perpendicular yarns (See Figure 5.47)[186].

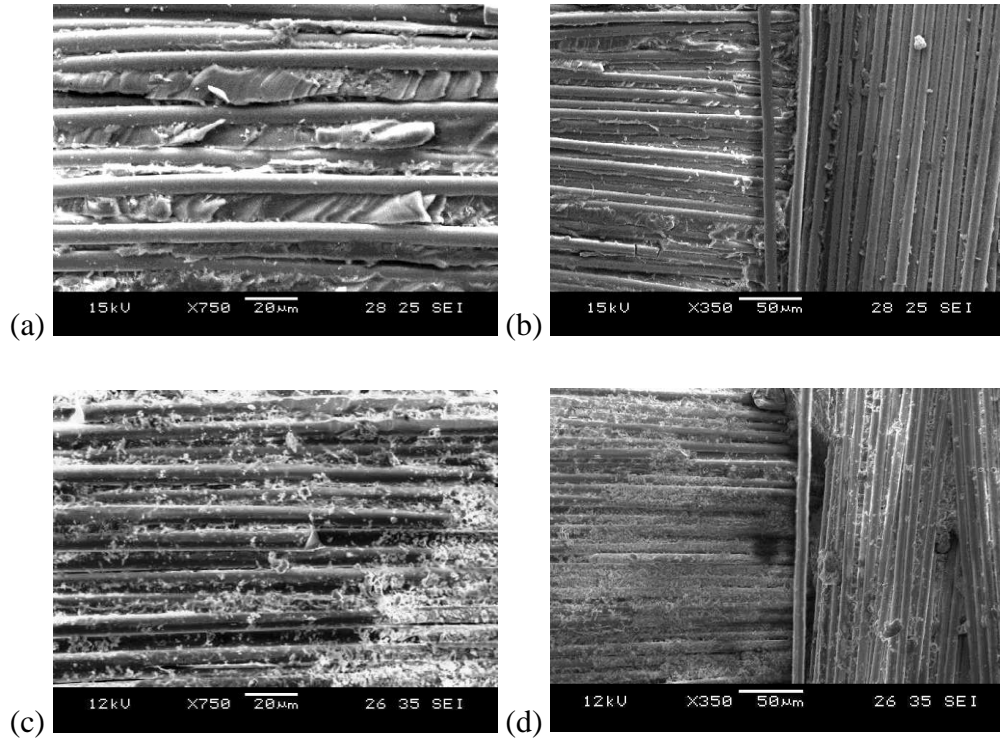


Figure 5.46. Typical SEM micrographs of mode II delamination surfaces from fatigue tests for (a)(b) dry and (c)(d) wet specimens; *Direction of delamination from top to bottom*

Soaking in seawater also induces different fracture surfaces to the specimens. As shown in Figure 5.46, distinguished matrix hackles observed in transverse yarns of dry specimen almost disappear from the wet specimen. The formation of hackle pattern in mode II delamination is mainly because of the coalescence of micro-cracks which are limited to matrix between fibers in the propagation of crack tip. The hackles appear to be more distinct for brittle matrix than ductile matrix, as the plastic deformation is more likely suppressed and localized in the former case [210]. After 2500 hours immersion in 50°C seawater, the ductility of the BMI matrix has been enhanced due to the strong plasticization effect. Therefore, matrix yielding and ductile fracture may occur before the formation and coalescence of micro-cracks, leaving no distinguish hackle marks on the wet specimen[208, 211, 212].



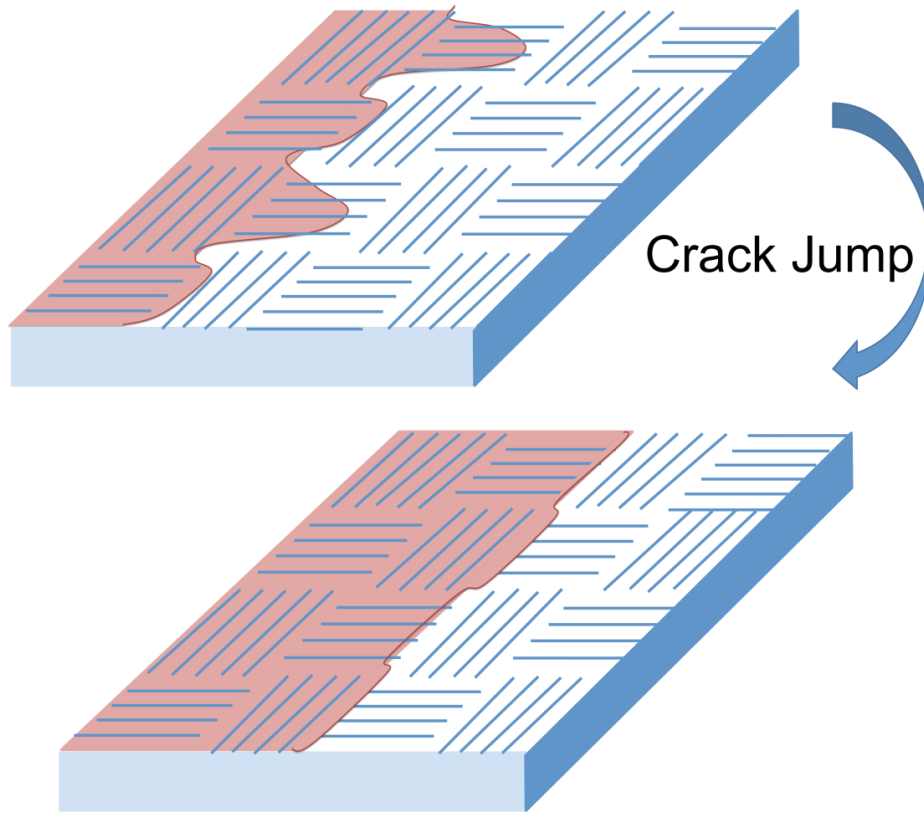


Figure 5.47. Schematic graph of the crack propagation in woven laminates

## 5.7 Tension-Tension fatigue tests

### 5.7.1 Seawater effects on the S-N relations

Fatigue tests were conducted to study the behavior of the dry and aged specimens under cyclic loading. Tension-tension loading at various constant stress levels and ratios were performed and presented in terms of S-N curves. For convenience of identification, the desiccated dry specimen consisting  $[(0^\circ, 90^\circ)]_8$  is referred as  $\text{dry}^{0/90}$  specimen whereas the dry specimen with weave direction of all plies at  $45^\circ$  off the loading axis  $[(+45^\circ, -45^\circ)]_8$  is referred as  $\text{dry}^{\pm 45}$  specimen. The  $[(0^\circ, 90^\circ)]_8$  specimens immersed in seawater at  $50^\circ\text{C}$  and  $80^\circ\text{C}$  for around 5000 hours are referred as  $\text{wet}50^{0/90}$  and  $\text{wet}80^{0/90}$  specimens respectively. Similarly, the  $[(+45^\circ, -45^\circ)]_8$  specimens immersed in seawater at  $50^\circ\text{C}$  and  $80^\circ\text{C}$  for around 5000 hours are referred to as  $\text{wet}50^{\pm 45}$  and  $\text{wet}80^{\pm 45}$  respectively. The stress ratio  $R$  is defined as the ratio of the minimum applied stress over the maximum applied stress in the cyclic loading.

Figure 5.48 and Figure 5.49 show the testing results for the dry and seawater aged  $[(0^\circ, 90^\circ)]_8$  specimens with stress ratio  $R=0.1$  and  $R=0.5$ . The diagrams demonstrate the relationship between the maximum tensile stresses applied on the specimens against their fatigue life in terms of failure cycles (in log scale). The results showed the fatigue life of composite materials could scatter more than 1 decade, and it is impossible to predict individual fatigue failure. Therefore, a statistical description is required to determine the mean fatigue life with certain confidence level. Weibull distribution is commonly adopted in characterizing the probability of failure for composite materials. Here, the median failure cycles were obtained at each stress level through Weibull distribution and the semi-log linear relationship between applied cyclic stress and the number of cycles to failure is written as:

$$S_{max} = m \log(N) + b ,$$

where  $N$  and  $S$  are fatigue life in terms of failure cycles and maximum tensile stress respectively. The parameters  $m$  and  $b$  are determined by curve fitting. The experimental results revealed the linear semi-logarithmic formulation to be quite accurate in describing the relationship between statistical cyclic stress and cycles to failure of this laminate. However, it is not wise to blindly extend the prediction over the scale of the experiment results.

As shown in Figure 5.48 and Figure 5.49, the seawater immersion at different temperatures has significant influence on the fatigue life of the specimens. Compared to dry<sup>0/90</sup> specimen, the specimens immersed in 50°C seawater showed a better performance tested with relatively high stress level but the slope of the S-N curve is steeper for wet50<sup>0/90</sup> specimens than for dry specimens. Figure 5.48 indicates that the fatigue life of wet50<sup>0/90</sup> specimen is shorter for those tests with lower stress levels. In the case of  $R=0.1$ , the fatigue life of wet50<sup>0/90</sup> specimens with maximum stress at 207MPa was almost three times higher than that of dry<sup>0/90</sup> specimens. However, the gap was getting smaller with decreasing stress level, and there was no difference in terms of fatigue life for both specimens with maximum stress as low as 118MPa. The trend was similar for the case of  $R=0.5$ , where the S-log N curve of wet50<sup>0/90</sup> specimens had steeper gradient. However, the S-Log N curves of dry<sup>0/90</sup> and wet50<sup>0/90</sup>

crossover was at 181MPa for R=0.5 and 118 for R=0.1. The immersion in 80°C seawater further degraded the fatigue behavior of the specimens as shown in Figure 5.49. Although the slope of the S-N curve for wet80<sup>0/90</sup> specimens was the flattest, it is very likely due to the scattering of the fatigue data. Compared to the dry<sup>0/90</sup> specimens, the fatigue lives of most wet80<sup>0/90</sup> specimens were at least a decade shorter. Figure 5.50 shows the comparison of fatigue life for dry<sup>0/90</sup> specimens at R=0.1 and R=0.5. Considering the scatter of fatigue test results, no appreciable difference in fatigue life between R=0.1 and R=0.5. This indicates that the maximum applied stress is the dominant factor of the fatigue life for the [(0°, 90°)]<sub>8</sub> specimen.

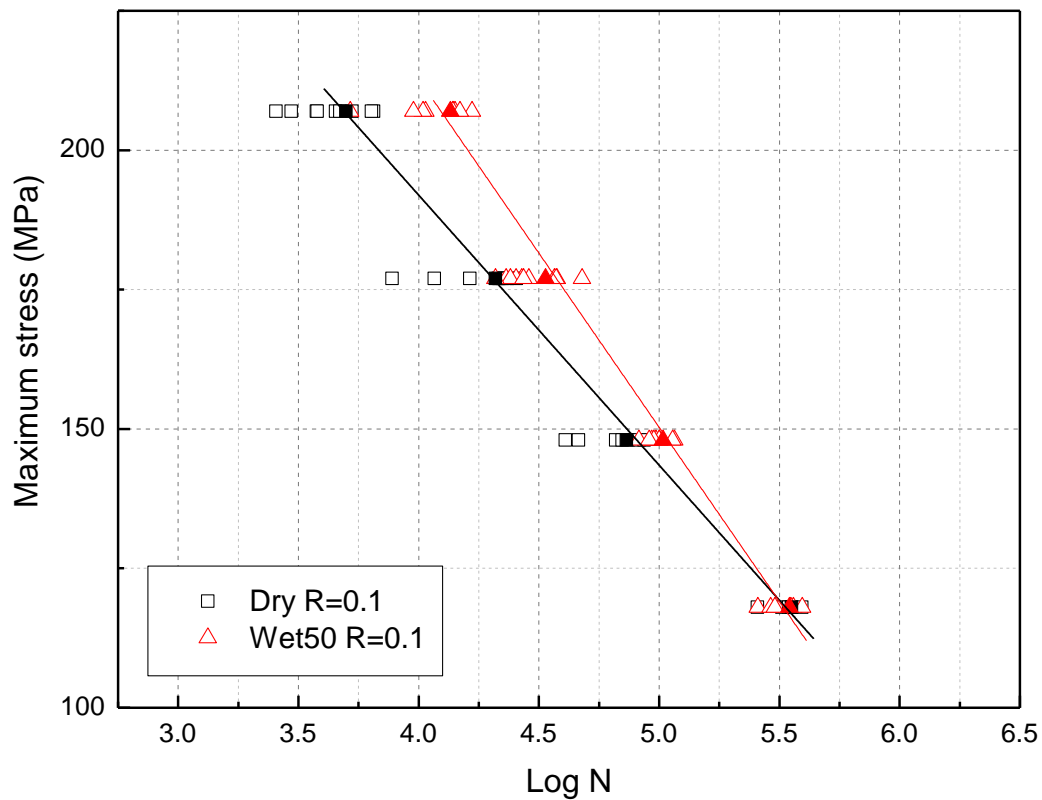


Figure 5.48. Fatigue results of [(0°, 90°)]<sub>8</sub> specimens with R=0.1

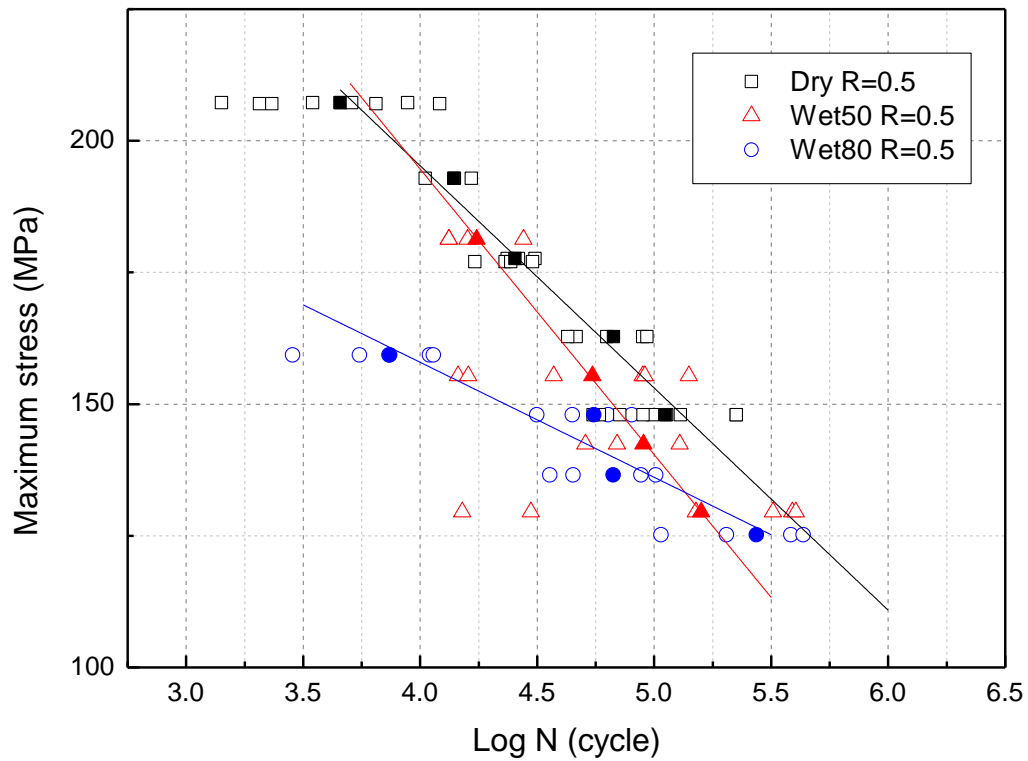


Figure 5.49. Fatigue results of  $[(0^\circ, 90^\circ)]_8$  specimens with  $R=0.5$

The fatigue test results for the  $[(+45^\circ, -45^\circ)]_8$  specimens are presented in Figure 5.51. The dry<sup>+45</sup> specimens and the aged specimens with 50°C and 80°C seawater immersion were tested at stress ratio  $R=0.1$ . In contrast to  $[(0^\circ, 90^\circ)]_8$  specimens, no enhancing effect in fatigue life was found for wet specimens at high stress levels. The fatigue life has been significantly shortened with seawater exposure and elevated immersion temperature. The seawater effect was stronger for the  $[(+45^\circ, -45^\circ)]_8$  specimens than for the  $[(0^\circ, 90^\circ)]_8$  specimens. It can be explained that the shear failure of the former specimen is matrix dominated, which is susceptible to water exposure. Moreover, it seems that the seawater aged specimens showed more variations in fatigue test results.

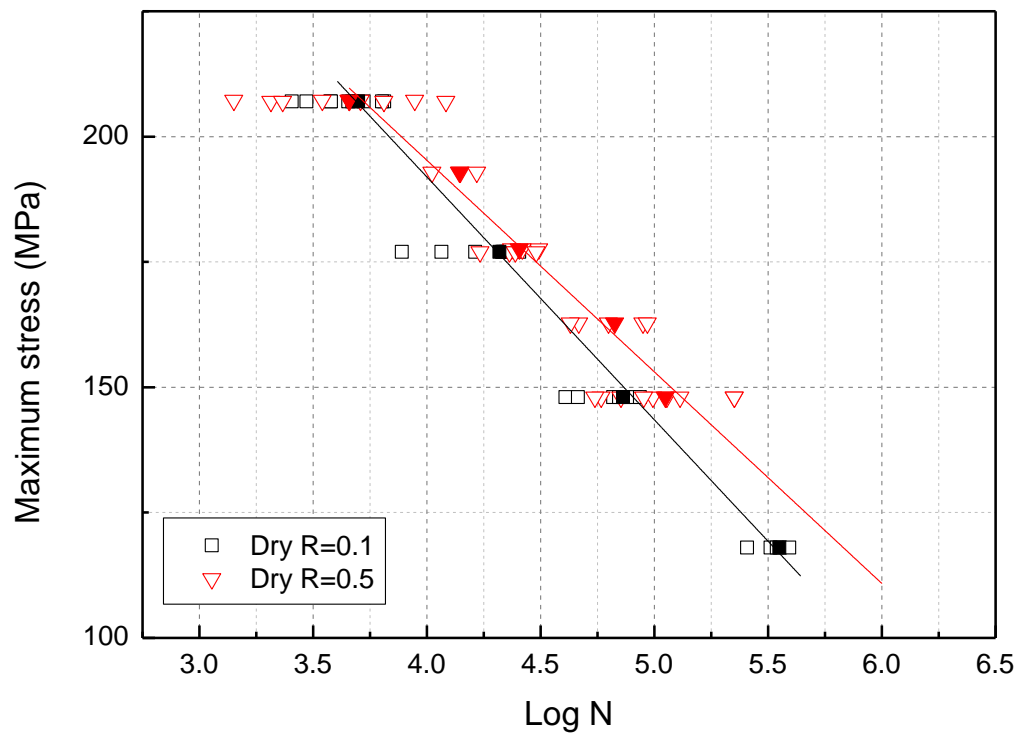


Figure 5.50. Fatigue results of dry<sup>0/90</sup>specimens at R=0.1 and R=0.5

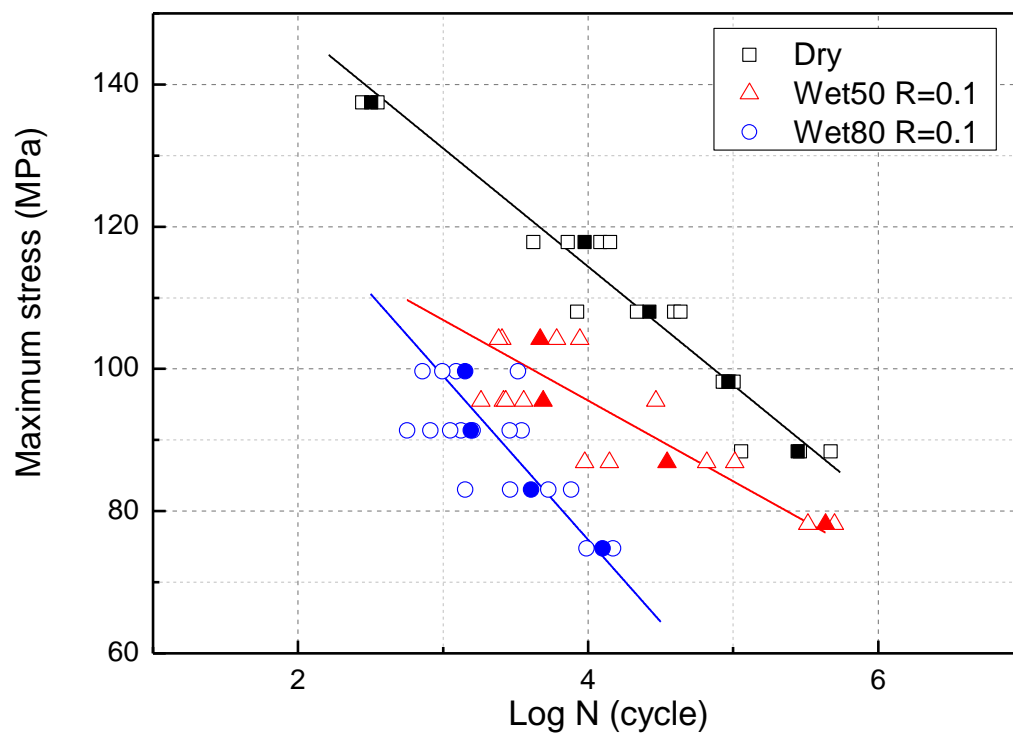


Figure 5.51. Fatigue results of  $[(+45^\circ, -45^\circ)]_8$  specimens at R=0.1

### 5.7.2 Stiffness degradation curves

The dynamic stiffness has been commonly used in the literature for evaluating the accumulative damage process of the specimen during cyclic loading. The change of dynamic stiffness, which is an indicator of specimen state, is often presented as the stiffness degradation curve. The calculation of dynamic stiffness is given in the previous chapter in Eq. (4.44). The normalized stiffness degradation curves at different stress levels for the dry<sup>0/90</sup> specimens and the wet50<sup>0/90</sup> specimens with R=0.1 are shown in Figure 5.52 and Figure 5.53 respectively. In these figures, the applied cycles are presented in a normalized form. The stiffness degradation curves from various stress levels showed similar curves, which can be divided into three stages. In the first stage, the curves exhibit a quick drop of stiffness within first 5% to 10% of life. The stiffness reduction in this stage is dominated by the formation of transverse matrix cracks. In the second stage, where the stiffness degradation curve decreases linearly in most of the specimens' life, the damage is mainly due to the interfacial delaminations along the longitudinal fibers and small cracks on the fibers. Finally, in the third stage, the stiffness drops abruptly and the specimen fails due to fiber breakage. In some cases, especially with high stress level, the last stage was too short to be observed in a brittle fracture.

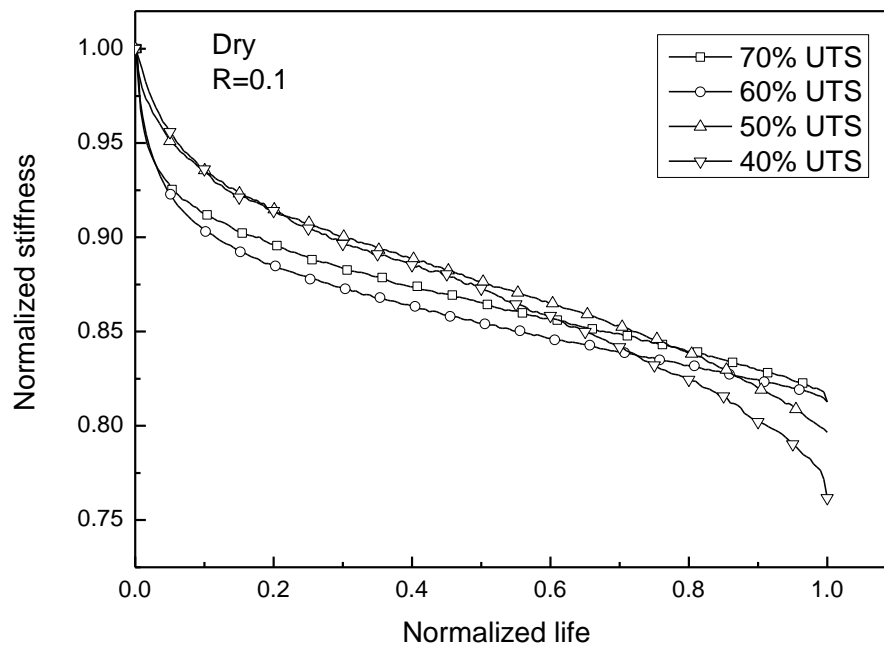


Figure 5.52. Stiffness degradation of the dry<sup>0/90</sup> specimens at R=0.1

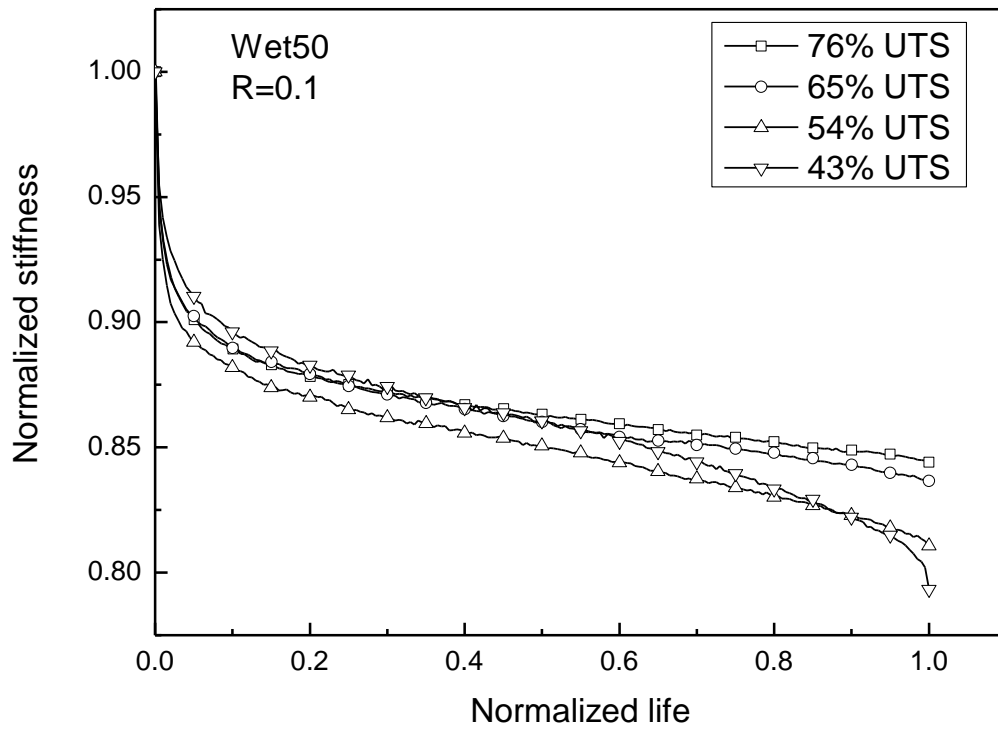


Figure 5.53. Stiffness degradation of the wet50<sup>0/90</sup> specimens at R=0.1

Higher applied stress generally results in larger reduction of stiffness in the first stage but higher final stiffness. The stiffness degradation curves of wet50<sup>0/90</sup> specimens resemble those of dry<sup>0/90</sup> specimens, indicating that the damage mechanism has not changed by seawater immersion. However, as shown in Figure 5.54, the seawater aged specimens had higher stiffness reduction in the first stage while slower degradation rate within the linear region (second stage). Overall, the wet50<sup>0/90</sup> specimens tend to have higher final stiffness at failure than the dry<sup>0/90</sup> specimens.

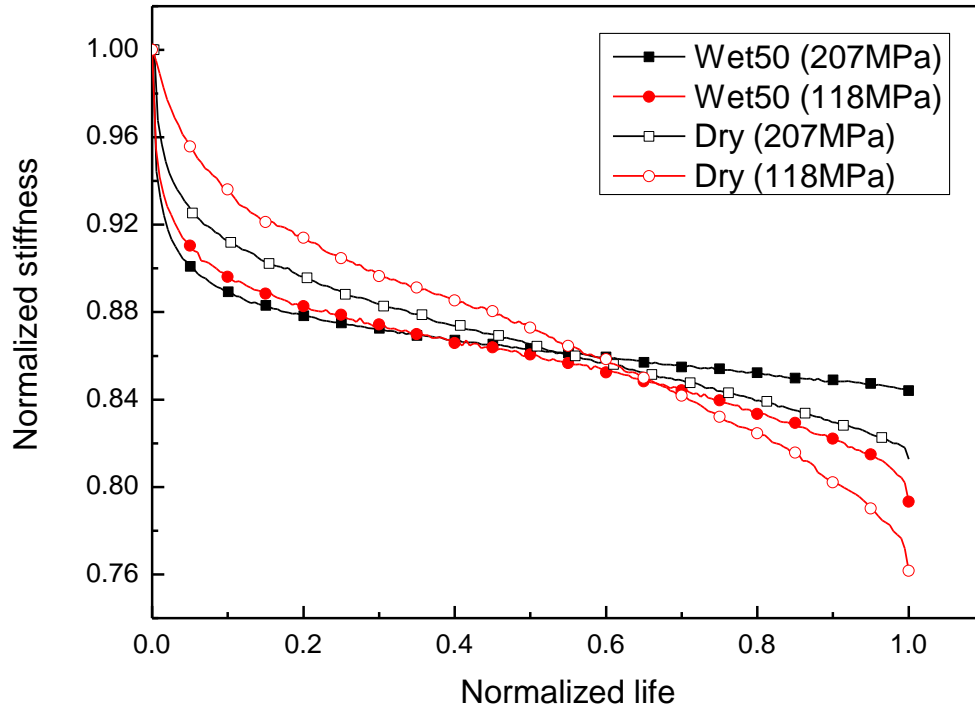


Figure 5.54. Comparison of stiffness degradation curves of the dry<sup>0/90</sup> and the wet50<sup>0/90</sup> specimens at R=0.1

Figure 5.55 and Figure 5.56 show the behaviors of fatigue stiffness degradation for the dry<sup>±45</sup> and wet80<sup>±45</sup> specimens. In contrast to the fiber-failure mode of the on-axis specimen, the fatigue failure of the off-axis specimen is dominated by the accumulation of matrix cracks and delaminations. As a result, the stiffness at failure for the off-axis specimen is often decreased to less than 0.5 compared to 0.75-0.9 for on-axis specimen. However, despite larger stiffness degradation, the curves still show three distinct stages. Compared to the dry<sup>±45</sup> specimen, the seawater aged off-axis specimen has even larger reduction in stiffness, which indicates more damage accumulation in the matrix. However, the stiffness degradation curves of the wet80<sup>±45</sup> specimens showed rather abrupt failure without the final stage.



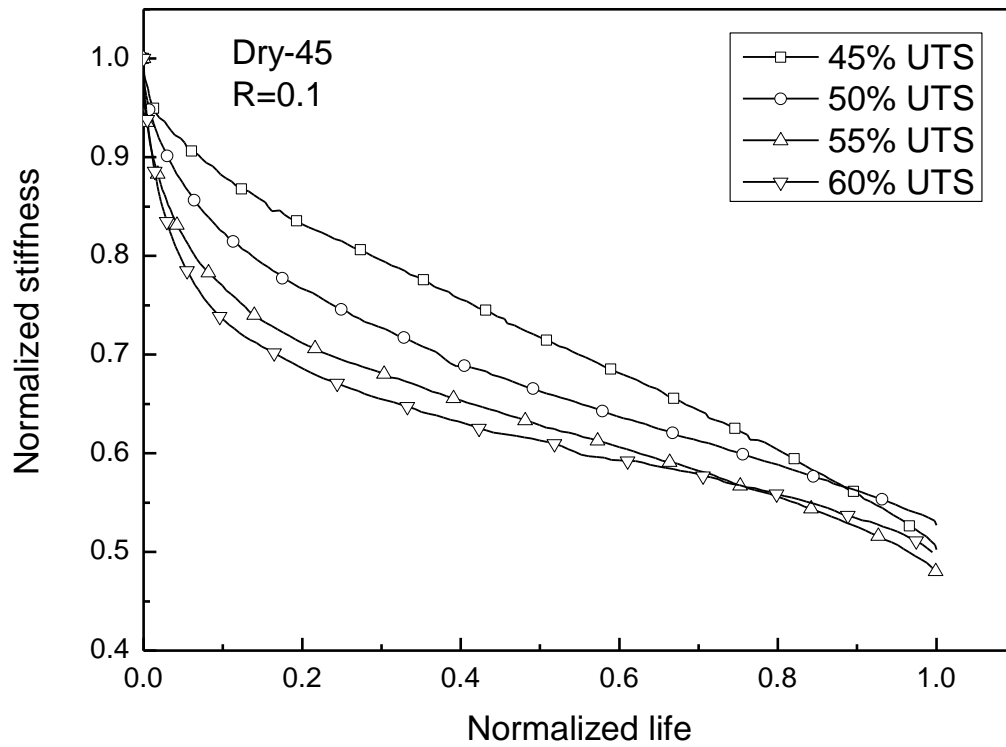


Figure 5.55. Stiffness degradation of the dry<sup>+45</sup> specimens at R=0.1

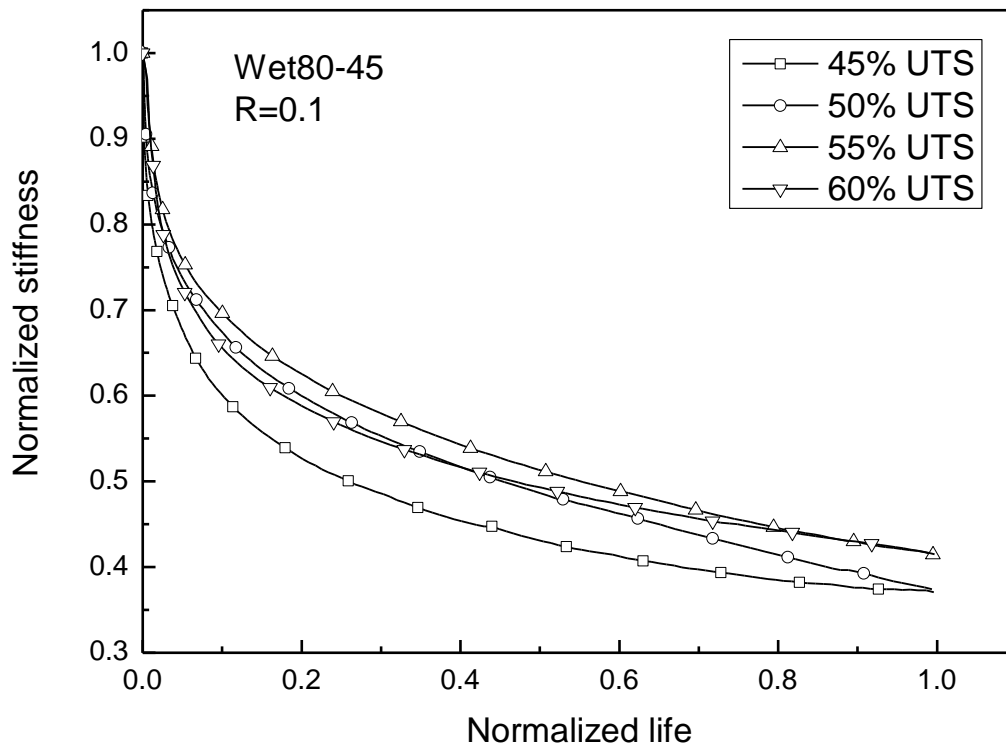


Figure 5.56. Stiffness degradation of the wet80<sup>+45</sup> specimens at R=0.1

### 5.7.3 Statistical analysis of S-N curve of fatigue life

A two-parameter Weibull distribution is commonly adopted in characterizing the probability of failure for composite materials. With an applied stress level  $S_i$ , the probability of the specimen fails at  $N$  cycles can be described by Eq. (2.44), and the corresponding scale and shape factors are obtained as  $\alpha_i$  and  $N_i$ . The S-N curves determined by linear regression of the median cycles obtained are displayed in Figure 5.48-Figure 5.51. However, using this method, a large amount of specimens and stress levels are required to determine the Weibull parameters for each  $S_i$  and, subsequently, plot the statistical S-N curves. To overcome this disadvantage, a data pooling procedure is adopted in this study. The methodology is based on the assumptions that the normalized set of data also follows the two-parameter Weibull distribution and the fatigue results can be represented by a semi-log linear S-N curve. The failure cycles of specimens tested at each stress level were individually fitted with the two-parameter Weibull distribution. Then, the data pooling procedure described in the previous section was carried out on the dry<sup>0/90</sup> and wet50<sup>0/90</sup> specimens. The estimated Weibull distribution of the data set X is plotted in Figure 5.57. The value of  $X_0$  is obtained as 1.0024 for the dry<sup>0/90</sup> specimens and 1.0048 for the wet50<sup>0/90</sup> specimens, which are very close to the theoretical value of 1. The fitted universal Weibull shape parameter  $\alpha_f$  and adjusted characteristic number of cycles at each stress level are given in Table 5.11. The statistical S-N curves plotted based on the predetermined parameters in Table 5.10 and the prediction model using Eq. (4.45) and Eq. (4.48), are shown in Figure 5.58 and Figure 5.59 for the dry<sup>0/90</sup> and the wet50<sup>0/90</sup> specimens respectively. Compared with the experimental results, it can be seen that the S-N model is able to offer a good prediction of the materials probabilistic fatigue life at arbitrary stress levels. However, as shown in the figures, it tends to overestimate the variation of fatigue life in high cycle situations. Another drawback of this method is that the damage accumulation process cannot be reflected by this approach.

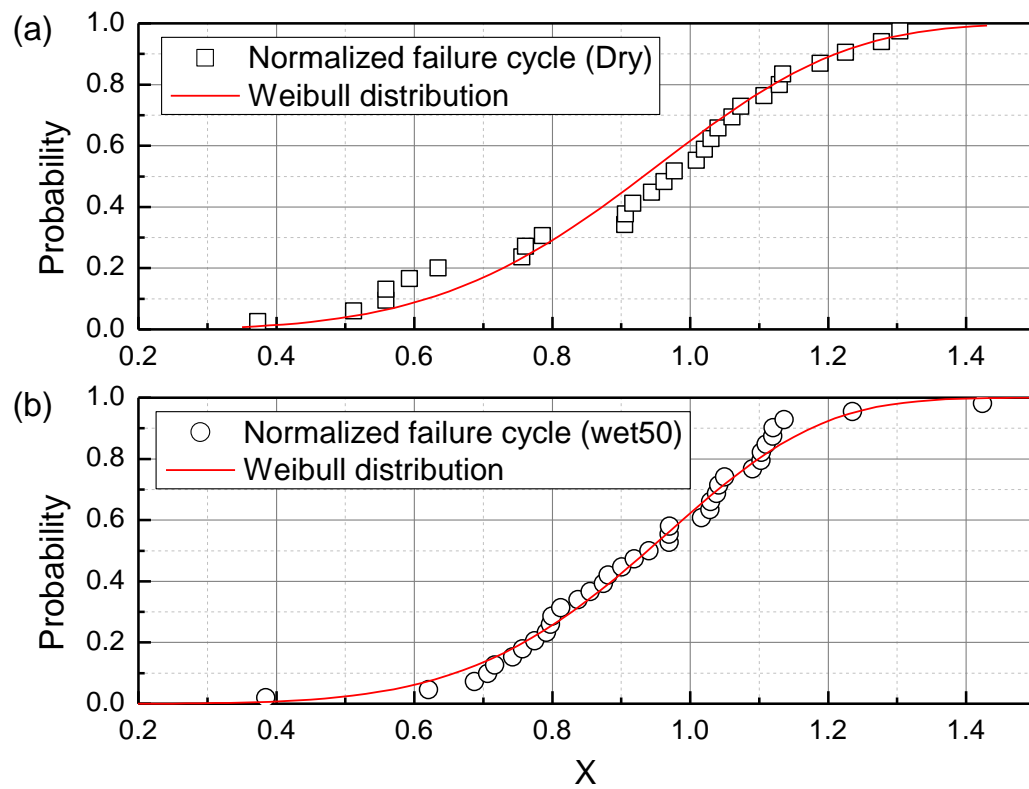


Figure 5.57. Weibull distribution of the data set X (a)  $\text{dry}^{0/90}$  (b)  $\text{wet50}^{0/90}$ specimens

Table 5.11. The values of the fitted parameters at each stress level and data pooling results

Maximum stress (MPa)	$\text{dry}^{0/90}$ specimen					$\text{wet50}^{0/90}$ specimen				
	Stress level	$N_i$ (cycles)	$N_i^*$ (cycles)	$\alpha_i$	$\alpha_f$	Stress level	$N_i$ (cycles)	$N_i^*$ (cycles)	$\alpha_i$	$\alpha_f$
207	70%	4980	4992	4.06	4.62	76%	13476	13540.95	4.90	5.34
177	60%	20794	20844	3.99	4.62	65%	33583	33744.87	4.03	5.34
148	50%	72861	73036	5.12	4.62	54%	103259	103756.7	10.74	5.34
118	40%	354104	354954	9.48	4.62	43%	346814	348485.6	8.07	5.34

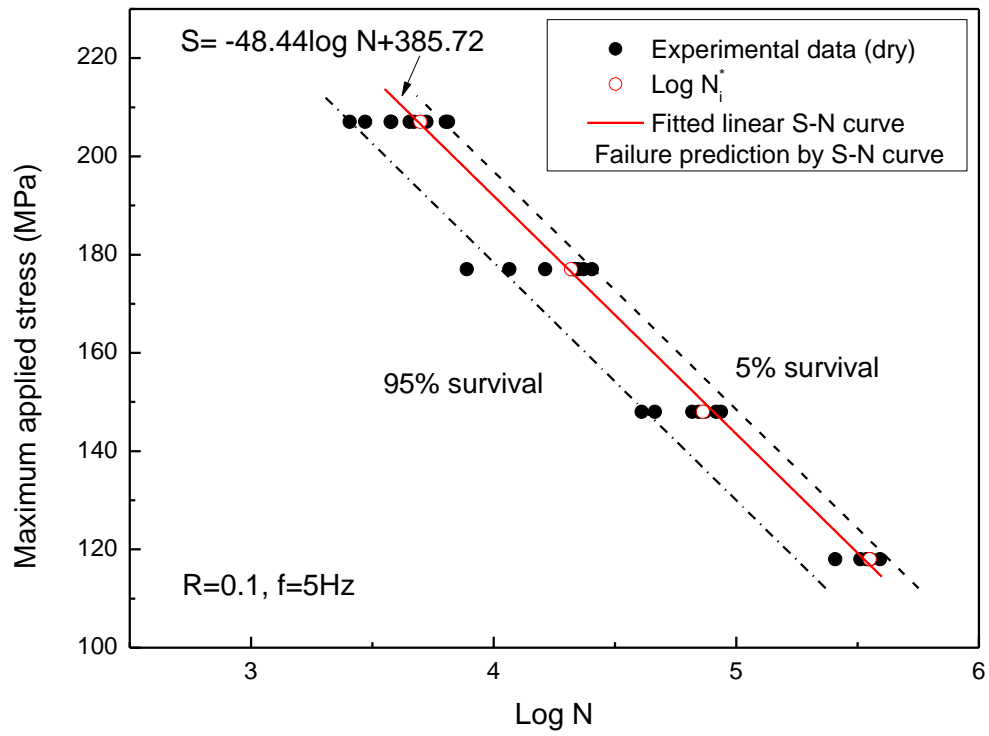


Figure 5.58. Statistical prediction of S-N curve for the dry<sup>0/90</sup> specimens

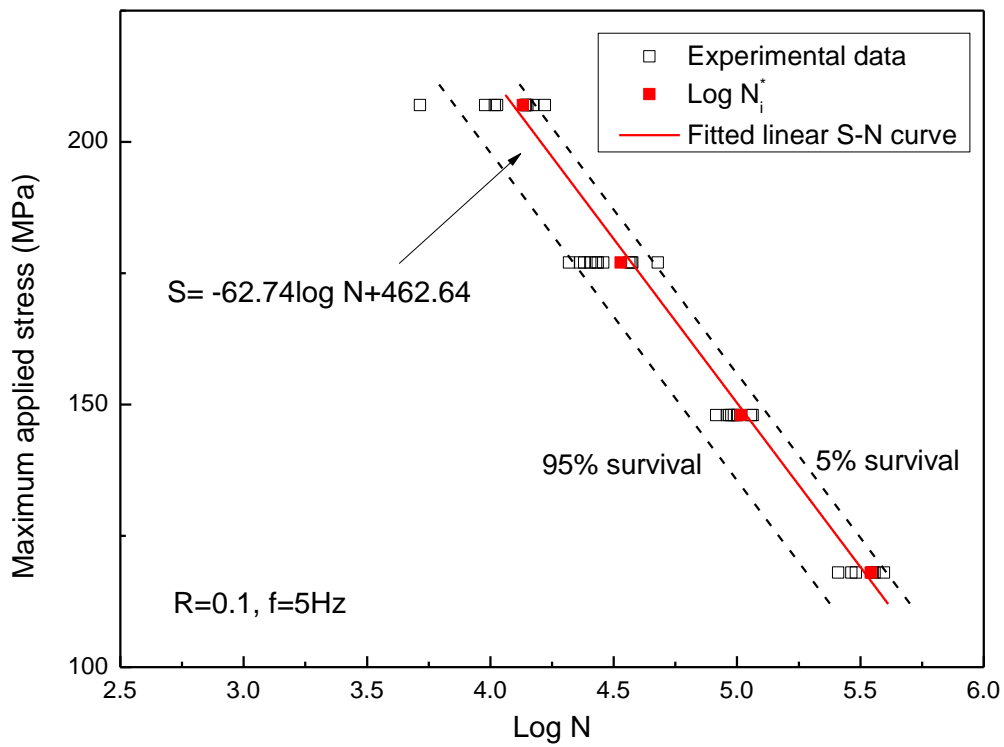


Figure 5.59. Statistical prediction of S-N curve for the wet50<sup>0/90</sup> specimens

#### 5.7.4 Stiffness degradation model

##### 5.7.4.1 Statistical analysis of static tests

In order to measure the ultimate tensile strength of the material, specimens were loaded with tensile force up to failure at a constant displacement rate of  $1\text{mm}/\text{min}$ . The mean value of ultimate tensile strength is obtained as  $S_u = 295\text{Mpa}$  for dry<sup>0/90</sup> specimens and  $S_u = 272\text{Mpa}$  for wet50<sup>0/90</sup> specimens. The experimental results are then fitted with a two-parameter Weibull distribution, and the estimated Weibull parameters for static tensile strength of dry<sup>0/90</sup> specimen are  $\alpha_s = 8.32$  and  $\beta_s = 311.86\text{Mpa}$ . Similarly, the corresponding Weibull parameter for wet50<sup>0/90</sup> specimen are  $\alpha_s = 15.96$  and  $\beta_s = 282.52\text{Mpa}$  (see Table 5.2).

##### 5.7.4.2 Relation between failure stiffness with applied stress level

The typical failure surfaces of specimens failed in static tensile tests, and fatigue tests at 70% and 40% of ultimate tensile stress (UTS) are presented in Figure 5.60. It is shown that the brittle fracture surfaces and failure mode are very similar. No significant delamination was found in experiments, which is a completely different failure mode. Therefore, due to the similarity in failure mode, the stiffness degradation and failure of the laminate at any desired stress levels were fitted with the stiffness degradation model proposed by Whitworth [119] (see section 4.6.3). In the stiffness degradation model, the failure of the specimen is assumed to follow a failure strain criterion, which means the specimen will fail when the fatigue strain reaches the ultimate tensile strain. As a result, the stress level can be related to the corresponding averaged normalized failure stiffness by Eq. (4.51). The experimental data are presented in Figure 5.61 and it can be seen that the Eq. (4.51) fits the test results quite well. Then the probabilistic failure strain at arbitrary stress levels can be obtained using Eq. (4.53), as the statistical distribution of static strength has already been determined.

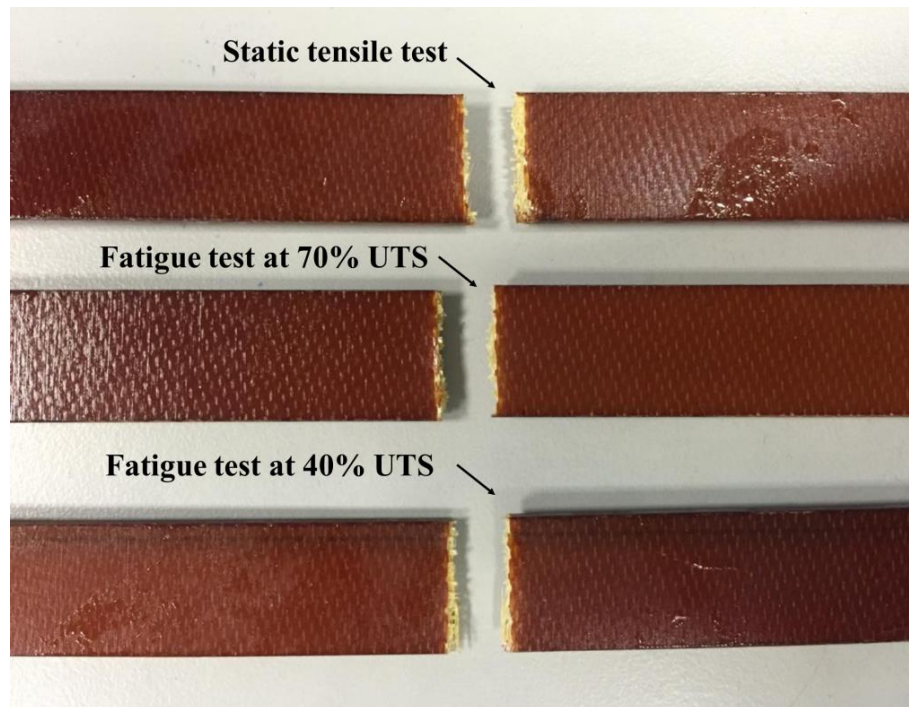


Figure 5.60. Failure mode of dry<sup>0/90</sup> specimens in different tests

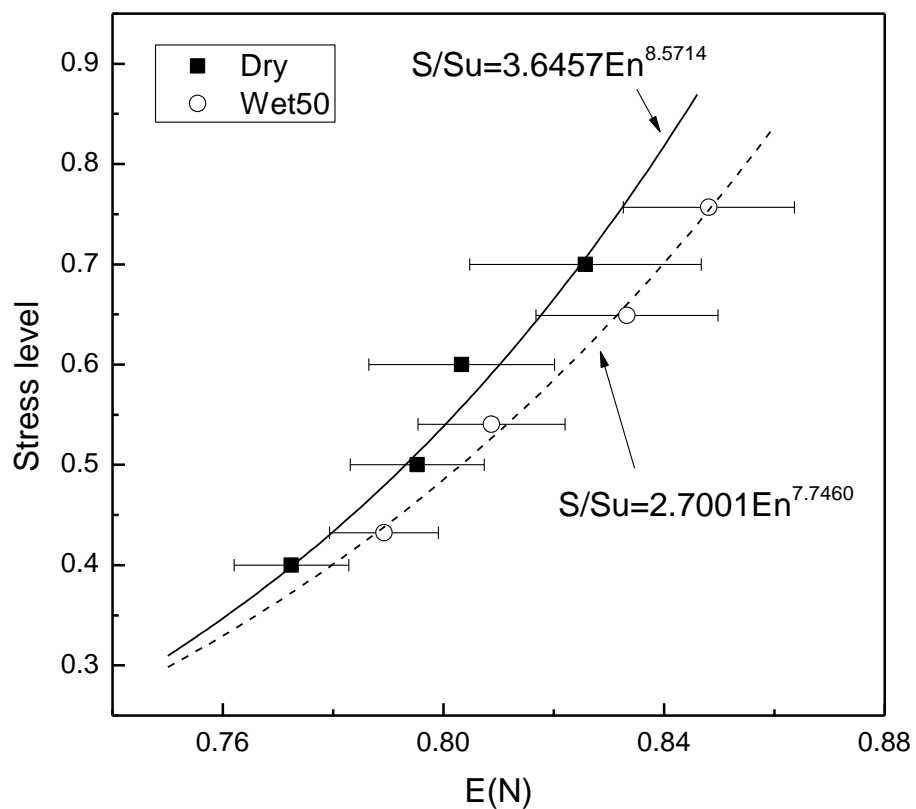


Figure 5.61. Relationship between stress level and averaged failure stiffness of dry<sup>0/90</sup> and wet<sup>0/90</sup> specimens

According to experimental data, as shown in Figure 5.62 and Figure 5.63, Eq. (4.53) gives a good prediction of the distribution of normalized failure stiffness with respect to the maximum applied cyclic stress in the fatigue test. The results presented in these figures are then used as the failure stiffness criteria to predict the material's fatigue life based on the stiffness degradation model.

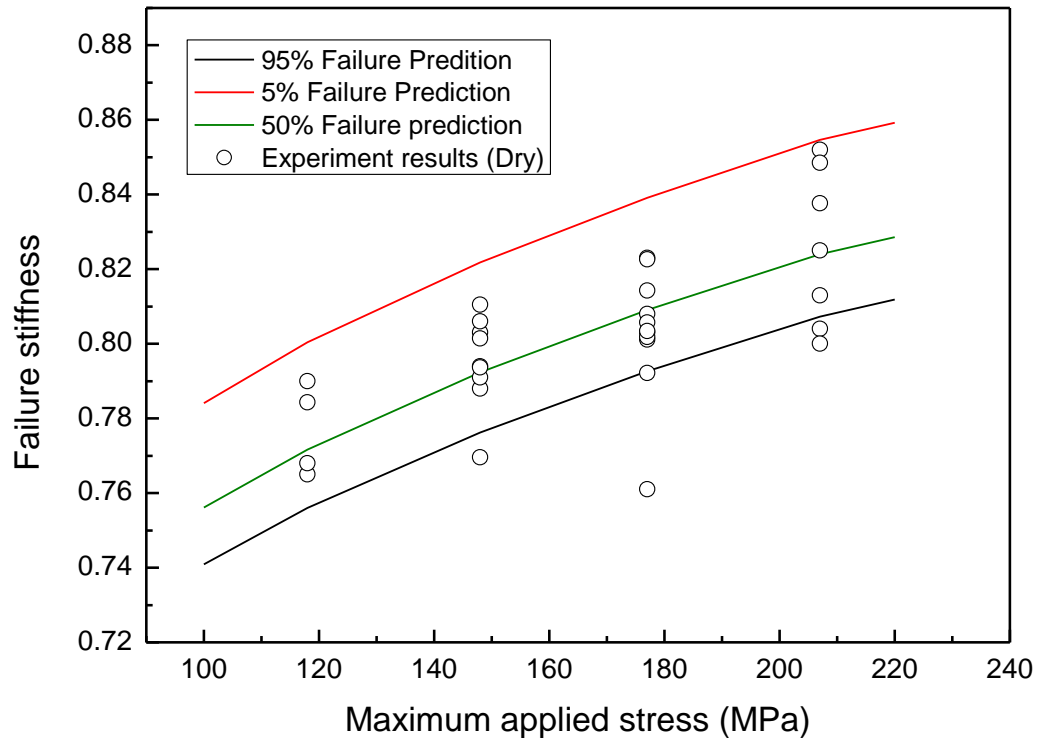


Figure 5.62. Experimental and predicted failure stiffness for dry<sup>0/90</sup> specimen

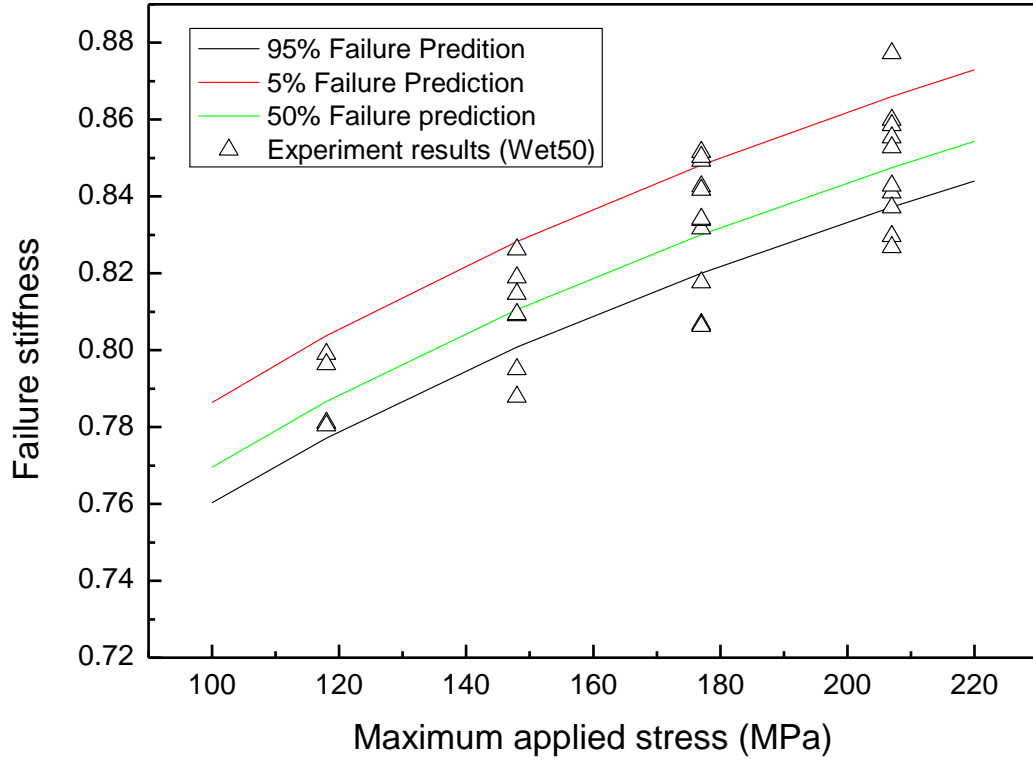


Figure 5.63. Experimental and predicted failure stiffness for wet50<sup>0/90</sup> specimen

#### 5.7.4.3 Stiffness degradation model

The experimental results of stiffness degradation curves at different stress levels are presented in Figure 5.64 to Figure 5.67 for both dry<sup>0/90</sup> and wet50<sup>0/90</sup> specimens as dotted lines. At each stress level, the experimental results are fitted with the proposed stiffness degradation model using Eq. (4.50), and the stress related parameters  $m$  and  $h$  are determined by applying nonlinear regression analysis of the results of all tested specimens. The failure stiffness of 50% possibility prediction were used all the models. The predictions of stiffness degradation were also given in those figures as the solid lines. It can be seen that the modeled solid lines are good representatives for the stiffness degradation curves at each stress level. This particular probability curve is used for predicting the fatigue life of the composite laminate by applying the range of failure stiffness given in Figure 5.68 and Figure 5.69.



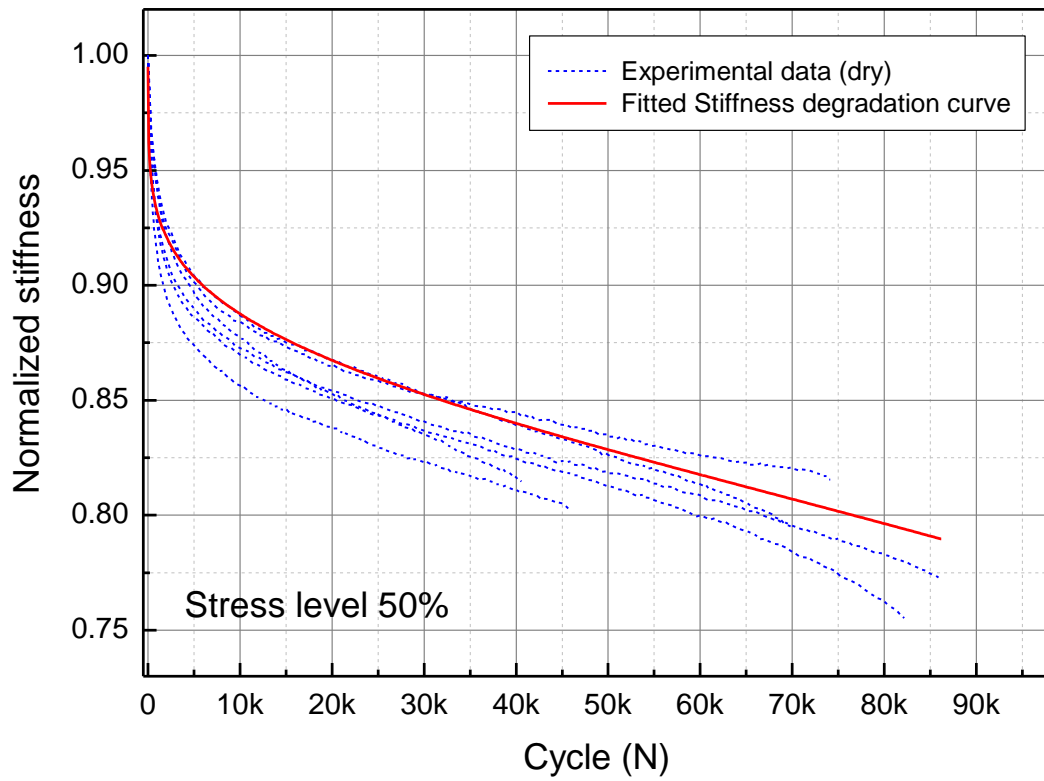


Figure 5.64. Experimental results and predicted curves at 50% stress level for  $\text{dry}^{0/90}$  specimen

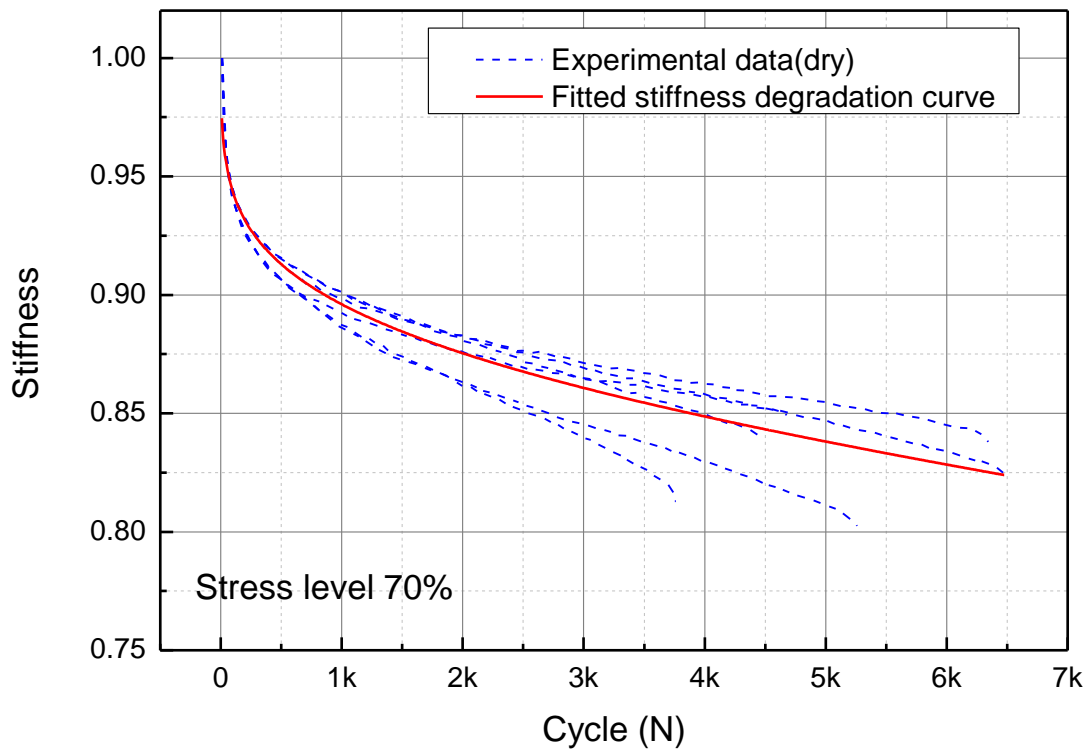


Figure 5.65. Experimental results and predicted curves at 70% stress level for  $\text{dry}^{0/90}$  specimen

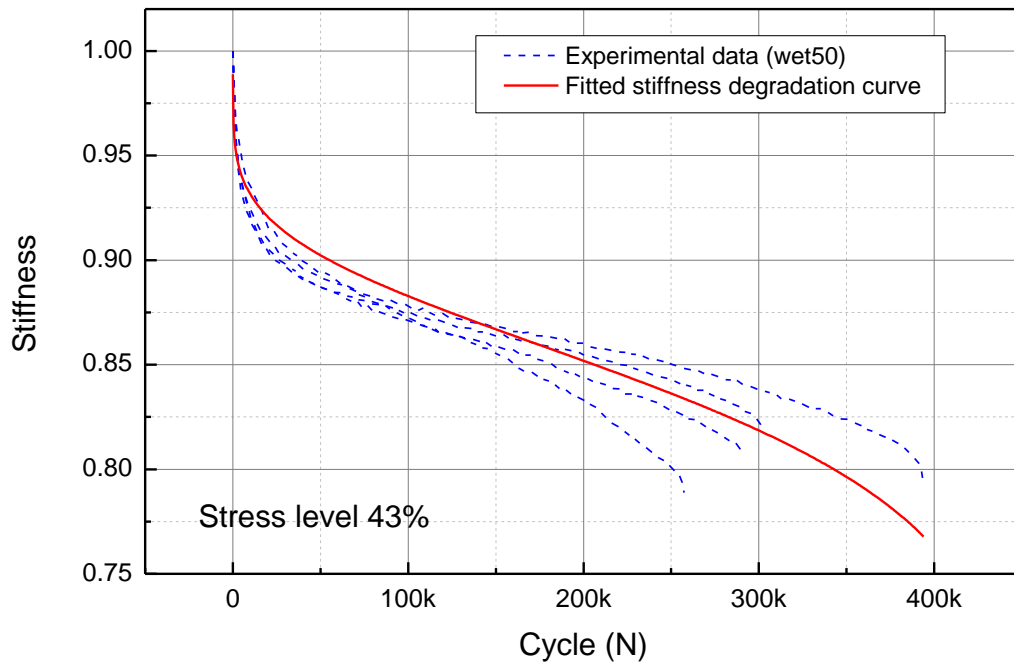


Figure 5.66. Experimental results and predicted curves at 43% stress level for wet50<sup>0/90</sup> specimen

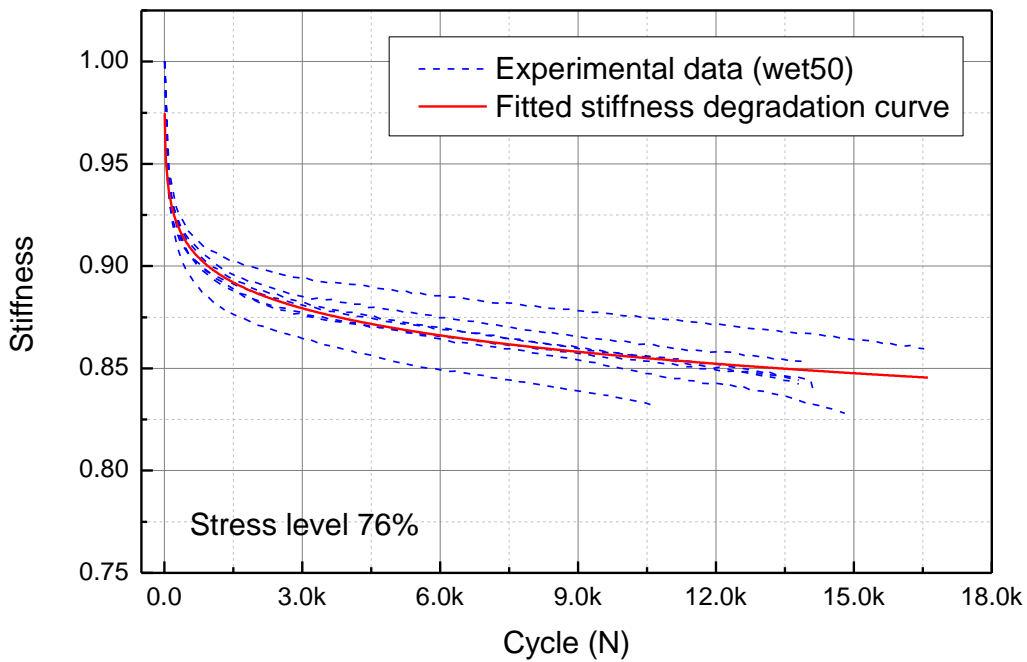


Figure 5.67. Experimental results and predicted curves at 76% stress level for wet50<sup>0/90</sup> specimen

The comparison between the predictions made by statistical analysis of S-N curve and the stiffness degradation model for both dry<sup>0/90</sup> and wet50<sup>0/90</sup> specimens are presented in Figure 5.68 and Figure 5.69. It can be seen that the

results of both methods are very close, which means that the stiffness degradation approach is able to obtain the survival probability and the damage accumulation as well. However, the prediction based on S-N curves is generally more conservative.

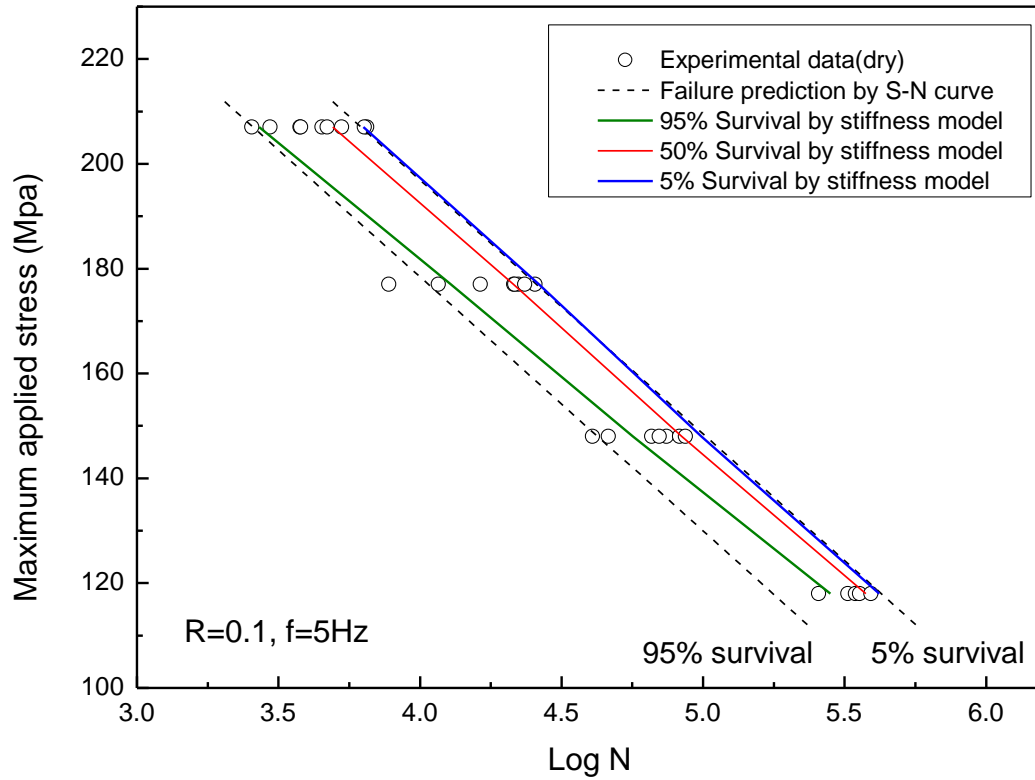


Figure 5.68. Statistical predictions by S-N curve and stiffness degradation model for dry<sup>0/90</sup> specimens

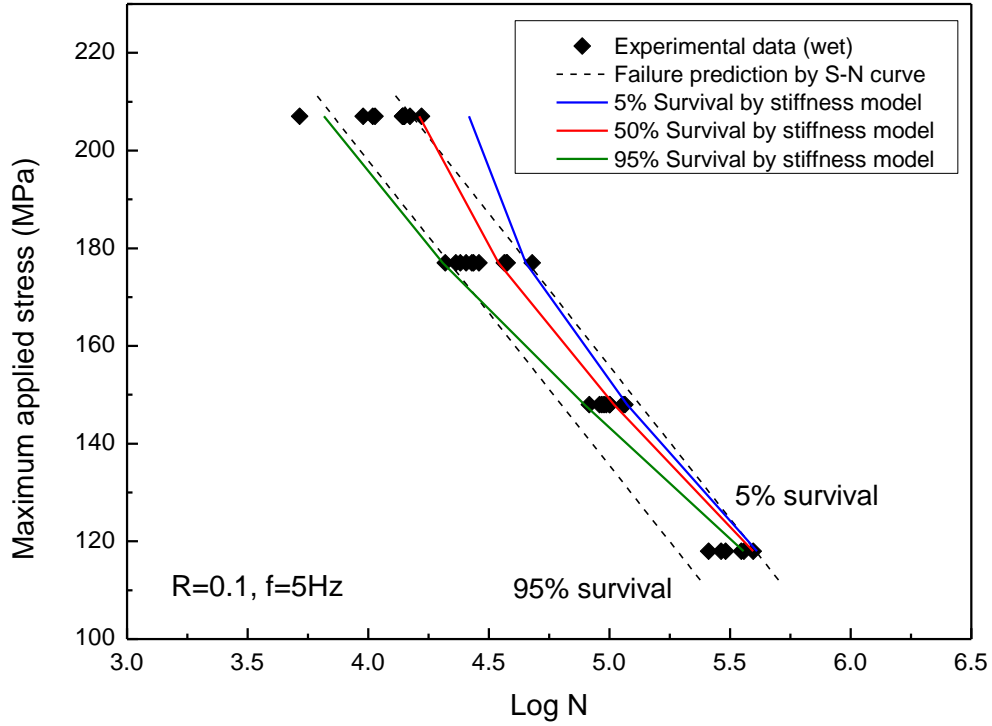


Figure 5.69. Statistical predictions by S-N curve and stiffness degradation model for wet50<sup>0/90</sup> specimens

So far, all the predictions are made at individual stress levels and the parameters  $h$  and  $m$  are actually stress dependent variables. The relationship of the parameters and applied stress is also investigated in this study. The degradation rate of the residual stiffness is assumed to be expressed by [119]

$$\frac{dE^*(N)}{dN} = \frac{-a}{(N+1)E^*(N)^{m-1}} \quad (5.18)$$

$$E^*(N) = \frac{E(N)}{E_n} \quad (5.19)$$

In this model, the parameter  $h$  is given as  $h = a \times m$ , where  $a$  and  $m$  are stress dependent. According to the fitting results, both  $m$  and  $a$  can be related as simple linear relationships with applied stress levels. The fitted curves of the parameters and constants in the proposed model are presented in Figure 5.70 and Table 5.12.

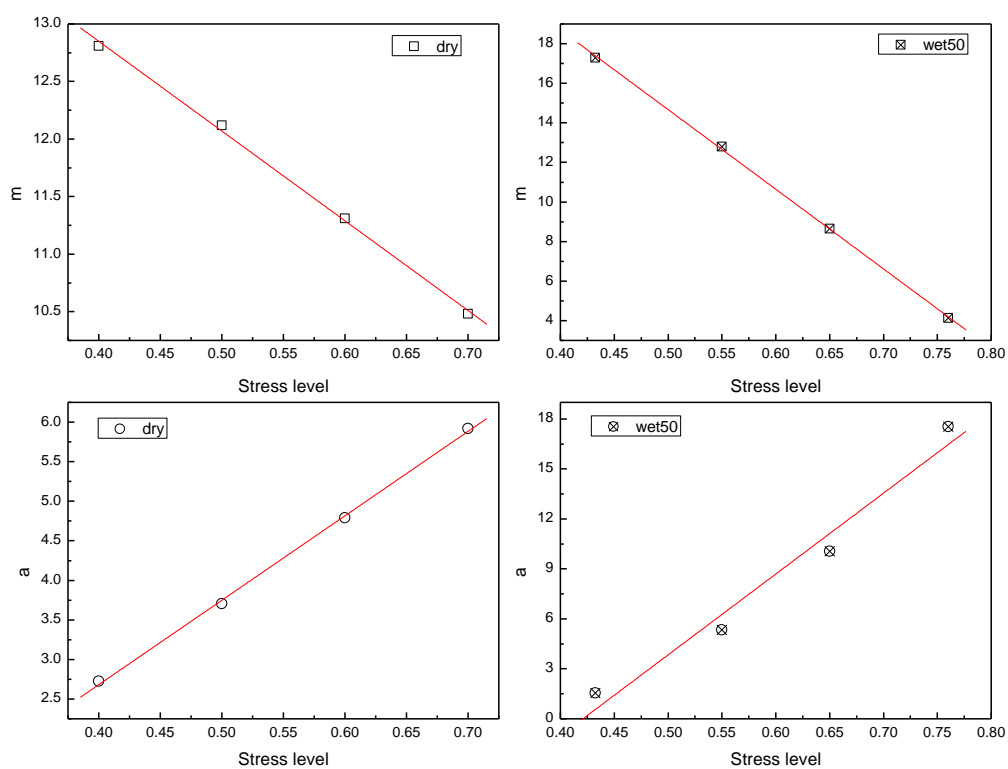


Figure 5.70. Determination of parameters of stiffness degradation model for dry<sup>0/90</sup> and wet50<sup>0/90</sup> specimens

Table 5.12. Fitted parameters for the stiffness degradation model

Stress level	dry <sup>0/90</sup>		Stress level	wet50 <sup>0/90</sup>	
	m	a		m	a
0.7	10.48	5.92	0.76	4.14	17.54
0.6	11.31	4.79	0.65	8.65	10.06
0.5	12.12	3.71	0.55	12.8	5.33
0.4	12.81	2.73	0.43	17.3	1.55

## **Chapter 6 Conclusion and Future work**

### **6.1 Conclusions**

This study investigates the long-term durability of glass fiber reinforced bismaleimide composites in seawater environments. BMI, as a relatively new thermosetting resin, its retention of excellent mechanical properties at elevated temperature is a huge natural advantage placing it as a strong candidate in marine and offshore applications. However, the effect of exposure to marine environments at wide range of service temperature on the composite material is still not clear, and there is a strong need of developing methods for long-term durability prediction. As a result, theoretical and experimental studies were conducted in this study to investigate these issues. Furthermore, the long-term life prediction methods were also reviewed and applied for static, creep and fatigue behaviors of BMI composite. As presented in the introduction, the motivation of this study is to investigate the long-term behavior of bismaleimide composites for applications such as risers and pipelines in offshore drilling industry.

The diffusion of seawater in the BMI composite at different temperatures was investigated. The water absorption by BMI composite was found to be a two-stage process. A fast first stage Fickian diffusion followed by a slow second stage water absorption due to polymer relaxation. As the Fickian model is insufficient, in this study, the water absorption of BMI composite was described by two-stage models. A two-stage diffusion model and the Langmuir model in this study. Increasing temperature largely accelerates the first stage diffusion, and the obtained diffusion coefficients follow the Arrhenius equation. This supports the assumption that the process is thermally activated. However, it has no clear relationship with the maximum water absorption. The seawater intakes for BMI composites up to 6000 hours of seawater immersion at 30°C, 50°C and 80°C were measured to be around 1.4%, 1.5% and 1.3% respectively. However, saturation was not achieved in this study except the case of 80°C immersion.

The long-term seawater effects on the tensile, flexural and shear properties of the materials were studied. Those material properties suffered 10-30% of loss after long-term exposure with seawater. In general, longer period of immersion and higher seawater temperature results in larger degradation. Although the flexural strength of wet specimen was measured around 23.6% lower than that of the dry specimen, the flexural strength of both dry and wet specimens were consistent up to 195°C, which is very close to the onset temperature, before it decreases with increased temperature. The flexural strength of dry specimens was reduced by 23.6% from 195°C to 260°C. The glass transition temperature ( $T_g$ ) of the composite with seawater absorption is considerably lowered due to the plasticization effect. At the initial stage of absorption,  $T_g$  falls sharply as the water content in the specimen increased at a very fast rate. When the diffusion rate slowed down, it remains nearly constant. After 6000 hours of immersion, the glass transition temperature reduced about 60°C and 70°C for the specimens immersed in 50°C and 80°C seawater respectively. The effect of water absorption below 50 °C was found to be reversible after drying process, which implies no chemical changes took place at this condition.

An accelerated testing method for long-term life prediction of the BMI composites was applied for viscoelastic, static, creep behaviors of the based on time-temperature superposition principle (TTSP). Master curves of static and creep strength were constructed. A simple and effective automated shifting program was developed for applying time-temperature superposition principle on the dynamic mechanical tests results. The shift factors are formulated as a function of temperature. A theoretical model of time dependent viscoelastic response is proposed based on fixed frequency storage modulus model and time-temperature superposition principle. The estimation of the proposed model is in good agreement with experimental results and the proposed model was also shown to be effective in predicting the long-term viscoelastic properties of the material under the influence of seawater absorption. Based on the prediction, in a period of 50 years, the modulus of BMI material with seawater exposure is expected to degrade by as high as 18.4 % in 50 years compared with 10.9 % for dry condition at 200°C service temperature. In fact, the proposed model is not restricted to BMI composites. Since the approach is based on time-temperature

superposition principle, the proposed formulation can be applied to other thermorheologically simple materials for predicting their long-term viscoelastic response with or without seawater exposure.

Thirdly, the effect of seawater immersion at different temperatures on the delamination behavior of the composite is studied under mode I, mode II and mixed-mode I/II loadings. The fracture toughness was found to decrease monotonically with seawater exposure and increasing temperature except for pure mode II results, where it surged up nearly 20% over the dry specimen results. However, most specimens with seawater absorption exhibited increasing resistance curves with the delamination growth. This is mainly due to the plasticization of the matrix and higher ductility of the specimen after immersion. However, it is worth pointing out that seawater also weakens the matrix and fiber/matrix interface in the long run. Hence, the influence of seawater on the interlaminar fracture behavior is a result of these two competing effects. The experimental results were correlated with existing delamination criteria to determine the parameters for cohesive zone models.

The use of an experimental procedure based on J-integral was explored for accurately evaluating the fracture toughness of composites with environmental effects, and the result was compared with that of well-established ASTM methods. The dry specimen results obtained by the J-integral method and the ASTM standard methods are generally in good agreement. However, discrepancies were found from the wet specimens results, as the LEFM assumption of small FPZ in ASTM standards is not applicable to this case. The J-integral method is suitable for more materials, and no elastic properties and system compliances need to be measured. The J-integral method also avoids the ambiguity in visual measurements of delamination length required by the standard methods. An image-processing program was developed to measure the rotation angles of the specimen automatically, allowing the interlaminar fracture toughness to be monitored with lower requirements for image resolution, light and material surface compared to previous methods.

The delamination growth of the laminate under Mode II fatigue loading was also investigated by end-notched flexure tests. A practical model using the Paris



law is proposed and proven accurate in modeling stable delamination growth for both dry and wet specimens. Immersion in seawater also has significant effects on the Mode II fatigue delamination behavior of the material. At a given normalized strain energy release rate, the crack growth is found to be much slower in wet specimens than in dry specimens.

Finally, tension-tension fatigue tests were conducted to study stiffness degradation and fatigue life of the material under cyclic loading with the influence of seawater diffusion. Both on-axis and off-axis fatigue tests with various stress ratios were performed with tension-tension loading, and the results were presented in terms of statistical S-LogN curves. It was found that the fatigue behavior of wet specimens was slightly enhanced at high stress level. However, in general, the fatigue life has been significantly shortened with seawater exposure and elevated immersion temperature. The stiffness degradation curves show that the seawater-aged specimens had higher stiffness reduction in the first stage while slower degradation rate within the linear region (second stage). Overall, the wet specimens tend to have higher final stiffness at failure than the dry specimens. A stiffness degradation model incorporating the strain failure criterion was used to describe the damage accumulation of the composite laminate statistically. The model is capable of predicting the statistical distribution of stiffness degradation curve. The life prediction agrees well with the result of statistical S-N curves and experimental data. The proposed model is attractive as it predicts not only the failure probability but also reflects damage accumulation in the material.

In conclusion, BMI composites showed very good retention in physical properties with long-term seawater exposure compared to alternative composite systems. As a consequence, the BMI matrix composite material, though mainly used on aircrafts, is considered as a promising material for offshore drilling and other marine applications with its good long-term durability in marine environment with a wide service temperature range. Considering the advantages offered by the BMI composites, we can expect a wider use of the material system in offshore and marine industry as the price goes down. In design approaches, the numerical models can be implemented with the predicted degradation of the BMI composites to account for complex environmental

effects in marine environments. The stiffness degradation model for fatigue life may be extended to apply for full-scale tests in order to reduce the large safety factors used in current applications. Although BMI composites show excellent retention of mechanical properties at elevated temperature, this study also shows that the performance is largely reduced with seawater exposure at over 80°C. Irreversible damage due to chemical changes was found at very early stage of immersion and hence the service life of the material is significantly shorten based on the predictions. Therefore, it requires the protective layer to be carefully designed for these applications and the in-service monitoring for leakage should be implemented. The delamination is also a major concern in composite structure design using BMI composite laminates due to their low interlaminar fracture toughness. In addition, the delamination behavior is very susceptible to seawater exposure. Various techniques, such as adding interleaf, stitching, z-pin and fillers, have been developed and can be used to toughen the interlaminar strength.

## **6.2 Summary of major contributions**

The major contributions of this study are listed below

- Understanding and modeling of the non-Fickian diffusion behavior of BMI composites subjected to seawater immersion at different temperatures
- Understanding the effect of seawater environments and temperature on the mechanical properties of BMI composites
- Established an empirical expressions for construction of shift factors and master curves of storage modulus to account for seawater effects in durability prediction based on Time-temperature superposition
- Studying the use of experimental procedure based on J-integral for measuring delamination properties of composites compared with the well-established ASTM methods
- Modified and improved the J-integral experimental designs and procedures with weight correction expressions, and developed an image processing program to ease the determination of experimental data.

- Understanding the seawater and temperature effects on delamination behaviors under Mode I, Mode II and Mixed Mode loadings
- Understanding the seawater effects on Mode II fatigue delamination and established an empirical model for delamination growth using Paris Law.
- Understanding the effects of seawater immersion at different temperatures on the on-axis and 45° off-axis tension-tension fatigue behavior of BMI composites.
- Established a statistical life prediction for both dry and wet BMI composites based on stiffness degradation method.

## **6.3 Future work plan**

### 6.3.1 Water absorption tests

Firstly, as revealed in the present results, the water absorption mechanism may change with temperatures. Fourier transform infrared spectroscopy is able to detect the chemical degradation during water absorption. The chemical compositions of BMI composites can be characterized by this technique, and the peak shifting or appearing on the spectra will reveal if there is any chemical reaction with seawater water. Secondly, many oil drilling applications including risers and pipelines are stressed in the water, which enhances the water penetration mechanism. Therefore, the influence of the stress on the water absorption in BMI composite also needs to be investigated. The effect of stress on water absorption may be modeled using the expansion of free volume fraction of the matrix proposed by [30]. Modifications should be made for the BMI composite since the method was only based on polymers. In addition, to get a better insight of the diffusion problem, diffusion tests on pure BMI resin need to be conducted since the effects of water absorption on the composite is mainly because of the plasticization of matrix. The saturated BMI resin can be used in DMA and mechanical tests for further investigations as well.

### 6.3.2 Long-term durability prediction

The accelerated testing method using TTSP is not the only approach to predict the creep rupture of composite material. As mentioned in the literature review, creep rupture model can also be derived based on energy method. The time related response of the material is combined with the laminated theory to model the creep behavior of the material, which can be applied in finite element models. It will be very useful if the water absorption effect can be properly implemented to the Finite element model.

### 6.3.3 Fatigue life prediction

It would be interesting to investigate the fatigue tests under immersion, as it simulates more realistic environment for marine application. The fatigue behavior of the composite will be influence by the seawater absorbed during the cyclic loading. Different constant life diagram formulations should also be analyzed to represent the fatigue life of BMI composite at arbitrary stress ratio. In terms of the stiffness degradation model, the model can be further developed with different governing equations for different stages, as the fatigue mechanism of each stage would be different.

## Reference

1. Gibson, R.F., *Principles of composite material mechanics*. 2011: CRC press.
2. Bunsell, A.R. and J. Renard, *Fundamentals of fibre reinforced composite materials*. 2005: CRC Press.
3. Davies, P. and Y.D. Rajapakse, *Durability of composites in a marine environment*. 2014: Springer.
4. Laboratory, N.E.S.R., *Sea Surface Temperature*. 2016.
5. Šturm, R., et al., *Destructive and nondestructive evaluations of the effect of moisture absorption on the mechanical properties of polyester-based composites*. *Composites Part B: Engineering*, 2015. **71**: p. 10-16.
6. Kajorncheappunngam, S., R.K. Gupta, and H.V. GangaRao, *Effect of aging environment on degradation of glass-reinforced epoxy*. *Journal of composites for construction*, 2002.
7. Ray, B.C. and D. Rathore, *Environmental damage and degradation of FRP composites: A review report*. *Polymer Composites*, 2015. **36**(3): p. 410-423.
8. Tsai, Y., et al., *Influence of hygrothermal environment on thermal and mechanical properties of carbon fiber/fiberglass hybrid composites*. *Composites Science and Technology*, 2009. **69**(3): p. 432-437.
9. Gellert, E. and D. Turley, *Seawater immersion ageing of glass-fibre reinforced polymer laminates for marine applications*. *Composites Part A: Applied Science and Manufacturing*, 1999. **30**(11): p. 1259-1265.
10. Nardone, F., et al., *Tensile behavior of epoxy based FRP composites under extreme service conditions*. *Composites Part B: Engineering*, 2012. **43**(3): p. 1468-1474.
11. Zafar, A., et al., *Investigation of the long term effects of moisture on carbon fibre and epoxy matrix composites*. *Composites Science and Technology*, 2012. **72**(6): p. 656-666.
12. Zhang, S., et al., *Evaluation of property retention in E-glass/vinylester composites after exposure to salt solution and natural weathering*. *J. Reinf. Plast. Compos.*, 2000. **19**(9): p. 704-731.
13. Prian, L. and A. Barkatt, *Degradation mechanism of fiber-reinforced plastics and its implications to prediction of long-term behavior*. *Journal of materials science*, 1999. **34**(16): p. 3977-3989.
14. Kootsookos, A. and A. Mouritz, *Seawater durability of glass-and carbon-polymer composites*. *Composites Science and Technology*, 2004. **64**(10): p. 1503-1511.
15. Li, Y., J. Miranda, and H.-J. Sue, *Hygrothermal diffusion behavior in bismaleimide resin*. *Polymer*, 2001. **42**(18): p. 7791-7799.
16. Wikipedia, *Seawater*, in <https://en.wikipedia.org/wiki/Seawater>. 2016.
17. Thomason, J., *The interface region in glass fibre-reinforced epoxy resin composites: 2. Water absorption, voids and the interface*. *Composites*, 1995. **26**(7): p. 477-485.
18. Kotsikos, G., A. Gibson, and J. Mawella, *Assessment of moisture absorption in marine GRP laminates with aid of nuclear magnetic resonance imaging*. *Plastics, Rubber and Composites*, 2007. **36**(9): p. 413-418.
19. Weitsman, Y. and M. Elahi, *Effects of fluids on the deformation, strength and durability of polymeric composites—an overview*. *Mechanics of Time-Dependent Materials*, 2000. **4**(2): p. 107-126.

20. Miyano, Y., M. Nakada, and N. Sekine, *Accelerated testing for long-term durability of FRP laminates for marine use*. Journal of composite materials, 2005. **39**(1): p. 5-20.
21. Landry, B., G. LaPlante, and L.R. LeBlanc, *Environmental effects on mode II fatigue delamination growth in an aerospace grade carbon/epoxy composite*. Composites Part A: Applied Science and Manufacturing, 2012. **43**(3): p. 475-485.
22. Yao, J. and G. Ziegmann, *Water absorption behavior and its influence on properties of GRP pipe*. Journal of composite materials, 2007. **41**(8): p. 993-1008.
23. Roy, S., et al., *Anomalous moisture diffusion in viscoelastic polymers: modeling and testing*. Journal of Applied Mechanics, 2000. **67**(2): p. 391-396.
24. Ellyin, F. and R. Maser, *Environmental effects on the mechanical properties of glass-fiber epoxy composite tubular specimens*. Composites science and technology, 2004. **64**(12): p. 1863-1874.
25. Tucker, W.C. and R. Brown, *Moisture absorption of graphite/polymer composites under 2000 feet of seawater*. Journal of composite materials, 1989. **23**(8): p. 787-797.
26. Visco, A., N. Campo, and P. Cianciafara, *Comparison of seawater absorption properties of thermoset resins based composites*. Composites Part A: Applied Science and Manufacturing, 2011. **42**(2): p. 123-130.
27. Ishisaka, A. and M. Kawagoe, *Examination of the time–water content superposition on the dynamic viscoelasticity of moistened polyamide 6 and epoxy*. Journal of applied polymer science, 2004. **93**(2): p. 560-567.
28. Neumann, S. and G. Marom, *Prediction of moisture diffusion parameters in composite materials under stress*. Journal of composite materials, 1987. **21**(1): p. 68-80.
29. Kafodya, I., G. Xian, and H. Li, *Durability study of pultruded CFRP plates immersed in water and seawater under sustained bending: Water uptake and effects on the mechanical properties*. Composites Part B: Engineering, 2015. **70**: p. 138-148 %@ 1359-8368.
30. Fahmy, A. and J. Hurt, *Stress dependence of water diffusion in epoxy resin*. Polymer Composites, 1980. **1**(2): p. 77-80.
31. Neumann, S. and G. Marom, *Stress dependence of the coefficient of moisture diffusion in composite materials*. Polymer Composites, 1985. **6**(1): p. 9-12.
32. Youssef, G., S. Fréour, and F. Jacquemin, *Stress-dependent moisture diffusion in composite materials*. Journal of Composite Materials %@ 0021-9983, 2009.
33. Pomies, F., L. Carlsson, and J. Gillespie, *Marine environmental effects on polymer matrix composites*, in *Composite Materials: Fatigue and Fracture: Fifth Volume*. 1995, ASTM International.
34. Shen, C.-H. and G.S. Springer, *Moisture absorption and desorption of composite materials*. Journal of Composite Materials, 1976. **10**(1): p. 2-20.
35. Paplham, W., et al., *Absorption of water in polyimide resins and composites*. Journal of applied polymer science, 1995. **57**(2): p. 133-137.
36. Bao, L.-R. and A.F. Yee, *Effect of temperature on moisture absorption in a bismaleimide resin and its carbon fiber composites*. Polymer, 2002. **43**(14): p. 3987-3997.
37. Bao, L.-R., A.F. Yee, and C.Y.-C. Lee, *Moisture absorption and hygrothermal aging in a bismaleimide resin*. Polymer, 2001. **42**(17): p. 7327-7333.

38. Berens, A. and H. Hopfenberg, *Diffusion and relaxation in glassy polymer powders: 2. Separation of diffusion and relaxation parameters*. Polymer, 1978. **19**(5): p. 489-496.
39. Jiang, X., et al., *Effects of hygrothermal aging on glass-fibre reinforced polymer laminates and adhesive of FRP composite bridge: Moisture diffusion characteristics*. Composites Part A: Applied Science and Manufacturing, 2014. **57**: p. 49-58.
40. Carter, H.G. and K.G. Kibler, *Langmuir-type model for anomalous moisture diffusion in composite resins*. Journal of Composite Materials, 1978. **12**(2): p. 118-131.
41. Bao, L.-R. and A.F. Yee, *Moisture diffusion and hygrothermal aging in bismaleimide matrix carbon fiber composites: part II—woven and hybrid composites*. Compos. Sci. Technol. , 2002. **62**(16): p. 2111-2119.
42. Hammami, A. and N. Al - Ghulani, *Durability and environmental degradation of glass - vinylester composites*. Polymer composites, 2004. **25**(6): p. 609-616.
43. Böer, P., L. Holliday, and T.H.-K. Kang, *Independent environmental effects on durability of fiber-reinforced polymer wraps in civil applications: A review*. Construction and Building Materials, 2013. **48**: p. 360-370.
44. Bergeret, A., et al., *The hygrothermal behaviour of glass-fibre-reinforced thermoplastic composites: a prediction of the composite lifetime*. Polymer testing, 2001. **20**(7): p. 753-763.
45. Costa, M.L., M.C. Rezende, and S.F.M. De Almeida, *Strength of hygrothermally conditioned polymer composites with voids*. Journal of composite materials, 2005. **39**(21): p. 1943-1961.
46. Fraga, A.N., et al., *Relationship between dynamic mechanical properties and water absorption of unsaturated polyester and vinyl ester glass fiber composites*. Journal of Composite Materials, 2003. **37**(17): p. 1553-1574.
47. Xu, L.R., et al., *A seawater tank approach to evaluate the dynamic failure and durability of E-glass/vinyl ester marine composites*. Composites Part B: Engineering, 2012. **43**(5): p. 2480-2486.
48. Gu, H., *Behaviours of glass fibre/unsaturated polyester composites under seawater environment*. Materials & Design, 2009. **30**(4): p. 1337-1340.
49. Poodts, E., G. Minak, and A. Zucchelli, *Impact of sea-water on the quasi static and fatigue flexural properties of GFRP*. Composite Structures, 2013. **97**: p. 222-230.
50. Roylance, D., *Engineering viscoelasticity*. Department of Materials Science and Engineering—Massachusetts Institute of Technology, Cambridge MA, 2001. **2139**: p. 1-37.
51. Taktak, R., et al., *Effect of hygrothermal aging on the mechanical properties and ductile fracture of polyamide 6: Experimental and numerical approaches*. Engineering Fracture Mechanics, 2015. **148**: p. 122-133.
52. Mahieux, C. and K. Reifsnider, *Property modeling across transition temperatures in polymers: a robust stiffness–temperature model*. Polymer, 2001. **42**(7): p. 3281-3291.
53. Barbero, E.J. and K.J. Ford, *Equivalent time temperature model for physical aging and temperature effects on polymer creep and relaxation*. TRANSACTIONS-AMERICAN SOCIETY OF MECHANICAL ENGINEERS JOURNAL OF ENGINEERING MATERIALS AND TECHNOLOGY, 2004. **126**(4): p. 413-419.
54. Goertzen, W. and M. Kessler, *Creep behavior of carbon fiber/epoxy matrix composites*. Materials Science and Engineering: A, 2006. **421**(1): p. 217-225.

55. Reeder, J.R., *Prediction of long-term strength of thermoplastic composites using time-temperature superposition*. 2013: Citeseer.
56. Honerkamp, J. and J. Weese, *A note on estimating mastercurves*. *Rheologica acta*, 1993. **32**(1): p. 57-64.
57. Williams, M.L., R.F. Landel, and J.D. Ferry, *The temperature dependence of relaxation mechanisms in amorphous polymers and other glass-forming liquids*. *Journal of the American Chemical Society*, 1955. **77**(14): p. 3701-3707.
58. Koyanagi, J., M. Nakada, and Y. Miyano, *Prediction of long-term durability of unidirectional CFRP*. *Journal of Reinforced Plastics and Composites*, 2011: p. 0731684411420314.
59. Ward, I.M. and D. Hadley, *An introduction to the mechanical properties of solid polymers*. 1993: John Wiley & Sons Ltd.; John Wiley & Sons, Inc.
60. Ding, H.Z. and Z. Wang, *Time-temperature superposition method for predicting the permanence of paper by extrapolating accelerated ageing data to ambient conditions*. *Cellulose*, 2007. **14**(3): p. 171-181.
61. Brown, R.P., T. Butler, and S.W. Hawley, *Ageing of Rubber: Accelerated Heat Ageing Test Results*. 2001: Smithers Rapra Technology.
62. Ferry, J.D. and R.A. Stratton, *The free volume interpretation of the dependence of viscosities and viscoelastic relaxation times on concentration, pressure, and tensile strain*. *Kolloid-Zeitschrift*, 1960. **171**(2): p. 107-111.
63. Angell, C., *Why  $C_1 = 16-17$  in the WLF equation is physical—and the fragility of polymers*. *Polymer*, 1997. **38**(26): p. 6261-6266.
64. Sullivan, J., *Creep and physical aging of composites*. *Composites science and technology*, 1990. **39**(3): p. 207-232.
65. Fukushima, K., et al., *Determination of time-temperature shift factor for long-term life prediction of polymer composites*.
66. Dealy, J. and D. Plazek, *Time-temperature superposition—a users guide*. *Rheol. Bull*, 2009. **78**(2): p. 16-31.
67. Hermida, É.B. and F. Povo, *Analytical-numerical procedure to determine if a set of experimental curves can be superimposed to form a master curve*. *Polymer journal*, 1994. **26**(9): p. 981-992.
68. Cho, K.S., *Geometric interpretation of time-temperature superposition*. *Korea-Australia Rheology Journal*, 2009. **21**(1): p. 13-16.
69. Gergesova, M., et al., *The closed form tTP shifting (CFS) algorithm*. *Journal of Rheology*, 2010. **55**(1): p. 1-16.
70. Sih, S. and S.W. Tsai, *Automated shift for time-temperature superposition*. in *The 12th International Conference on Composite Materials*. 1999.
71. Alwis, K.G.N.C. and C. Burgoyne, *Time-temperature superposition to determine the stress-rupture of aramid fibres*. *Applied Composite Materials*, 2006. **13**(4): p. 249-264.
72. Miyano, Y., et al., *Prediction of flexural fatigue strength of CRFP composites under arbitrary frequency, stress ratio and temperature*. *Journal of Composite Materials*, 1997. **31**(6): p. 619-638.
73. Miyano, Y., M. Nakada, and N. Sekine, *Accelerated testing for long-term durability of GFRP laminates for marine use*. *Composites Part B: Engineering*, 2004. **35**(6): p. 497-502.
74. Miyano, Y., M. Nakada, and H. Cai, *Formulation of long-term creep and fatigue strengths of polymer composites based on accelerated testing methodology*. *J. Compos. Mater.*, 2008.



75. Nakada, M. and Y. Miyano, *Accelerated testing for long-term fatigue strength of various FRP laminates for marine use*. Composites science and technology, 2009. **69**(6): p. 805-813.
76. Nakada, M. and Y. Miyano, *Advanced accelerated testing methodology for long-term life prediction of CFRP laminates*. Journal of Composite Materials, 2015. **49**(2): p. 163-175.
77. Nakada, M. and Y. Miyano, *Formulation of time-and temperature-dependent strength of unidirectional carbon fiber reinforced plastics*. J. Compos. Mater., 2012. **47**: p. 1897-1906.
78. Nakada, M. and Y. Miyano, *Effect of Water Absorption on Time–Temperature Dependent Strength of Unidirectional CFRP*, in *Durability of Composites in a Marine Environment*. 2014, Springer. p. 155-164.
79. Noda, J., M. Nakada, and Y. Miyano, *Statistical formulation for time-temperature dependent flexural strength of CFRP laminates*. J. Reinf. Plast. Compos., 2007.
80. Christensen, R.M., *An evaluation of linear cumulative damage (Miner's Law) using kinetic crack growth theory*. Mechanics of Time-Dependent Materials, 2002. **6**(4): p. 363-377.
81. Christensen, R.M., *A probabilistic treatment of creep rupture behavior for polymers and other materials*. Mechanics of Time-Dependent Materials, 2004. **8**(1): p. 1-15.
82. Christensen, R. and Y. Miyano, *Stress intensity controlled kinetic crack growth and stress history dependent life prediction with statistical variability*. International journal of fracture, 2006. **137**(1): p. 77-87.
83. Christensen, R. and Y. Miyano, *Deterministic and probabilistic lifetimes from kinetic crack growth—generalized forms*. International journal of fracture, 2007. **143**(1): p. 35-39.
84. Christensen, R.M., *A physically based cumulative damage formalism*. International Journal of Fatigue, 2008. **30**(4): p. 595-602.
85. Noda, J., M. Nakada, and Y. Miyano, *Statistical Scatter of Creep and Fatigue Failure Times for CFRP Laminates*. Journal of Reinforced Plastics and Composites, 2008.
86. Cai, H., et al., *Master Curves of Residual Creep and Fatigue Strengths for Damaged CFRP Composites*. Journal of Reinforced Plastics and Composites, 2010. **29**(7): p. 1009-1019.
87. Rajaneesh, A., et al., *Long-term life prediction of woven CFRP laminates under three point flexural fatigue*. Composites Part B: Engineering, 2016. **91**: p. 539-547.
88. Guedes, R.M., A. Sá, and H. Faria, *Influence of moisture absorption on creep of GRP composite pipes*. Polymer testing, 2007. **26**(5): p. 595-605.
89. Yao, J. and G. Ziegmann, *Equivalence of moisture and temperature in accelerated test method and its application in prediction of long-term properties of glass-fiber reinforced epoxy pipe specimen*. Polymer testing, 2006. **25**(2): p. 149-157.
90. Hu, H. and C. Sun, *The equivalence of moisture and temperature in physical aging of polymeric composites*. J. Compos. Mater., 2003. **37**(10): p. 913-928.
91. Beyene, A.T. and G. Belingardi, *Bending fatigue failure mechanisms of twill fabric E-Glass/Epoxy composite*. Composite Structures, 2015. **122**: p. 250-259.
92. Degrieck, J. and W. Van Paepegem, *Fatigue damage modeling of fibre-reinforced composite materials: review*. Applied Mechanics Reviews, 2001. **54**(4): p. 279-300.

93. Fawaz, Z. and F. Ellyin, *Fatigue failure model for fibre-reinforced materials under general loading conditions*. Journal of composite materials, 1994. **28**(15): p. 1432-1451.
94. Sutherland, H.J. and J.F. Mandell. *Optimised Goodman diagram for the analysis of fiberglass composites used in wind turbine blades*. in *A Collection of the 2005 ASME Wind Energy Symposium: Technical Papers Presented at the 43rd AIAA Aerospace Sciences Meeting and Exhibit, Reno, Nevada 10*. 2005.
95. Adam, T., et al., *A power law fatigue damage model for fibre-reinforced plastic laminates*. Proceedings of the Institution of Mechanical Engineers, Part C: Journal of Mechanical Engineering Science, 1986. **200**(3): p. 155-166.
96. Harris, B., *Fatigue behaviour of polymer-based composites and life prediction methods*. Durability Analysis of Structural Composite Systems, AH Cardon (Ed.), Balkema, Rotterdam, 1996: p. 49-84.
97. Wu, F. and W. Yao, *A fatigue damage model of composite materials*. International Journal of Fatigue, 2010. **32**(1): p. 134-138.
98. Taheri-Behrooz, F., M.M. Shokrieh, and L.B. Lessard, *Residual stiffness in cross-ply laminates subjected to cyclic loading*. Composite Structures, 2008. **85**(3): p. 205-212.
99. Kang, K.-W., D.-M. Lim, and J.-K. Kim, *Probabilistic analysis for the fatigue life of carbon/epoxy laminates*. Composite Structures, 2008. **85**(3): p. 258-264.
100. Mao, H. and S. Mahadevan, *Fatigue damage modelling of composite materials*. Composite Structures, 2002. **58**(4): p. 405-410.
101. Yang, J., L. Lee, and D. Sheu, *Modulus reduction and fatigue damage of matrix dominated composite laminates*. Composite Structures, 1992. **21**(2): p. 91-100.
102. Whitworth, H., *Evaluation of the residual strength degradation in composite laminates under fatigue loading*. Composite Structures, 2000. **48**(4): p. 261-264.
103. Zhang, W., et al., *A phenomenological fatigue life prediction model of glass fiber reinforced polymer composites*. Materials & Design, 2015. **66**: p. 77-81.
104. Daggumati, S., et al., *Fatigue and post-fatigue stress-strain analysis of a 5-harness satin weave carbon fibre reinforced composite*. Composites Science and Technology, 2013. **74**: p. 20-27.
105. Vassilopoulos, A.P. and T. Keller, *Fatigue of fiber-reinforced composites*. 2011: Springer Science & Business Media.
106. Van Paepegem, W. and J. Degrieck, *Coupled residual stiffness and strength model for fatigue of fibre-reinforced composite materials*. Composites Science and Technology, 2002. **62**(5): p. 687-696.
107. Van Paepegem, W., J. Degrieck, and P. De Baets, *Finite element approach for modelling fatigue damage in fibre-reinforced composite materials*. Composites Part B: Engineering, 2001. **32**(7): p. 575-588.
108. Van Paepegem, W. and J. Degrieck, *A new coupled approach of residual stiffness and strength for fatigue of fibre-reinforced composites*. International Journal of Fatigue, 2002. **24**(7): p. 747-762.
109. Van Paepegem, W., R. Dechaene, and J. Degrieck, *Nonlinear correction to the bending stiffness of a damaged composite beam*. Composite structures, 2005. **67**(3): p. 359-364.
110. Vassilopoulos, A.P., *Fatigue life prediction of composites and composite structures*. 2010: Elsevier.
111. Whitney, J., *Fatigue characterization of composite materials*. Fatigue of fibrous composite materials, ASTM STP, 1981. **723**: p. 133-151.

112. Philippidis, T. and A. Vassilopoulos, *Fatigue design allowables for GRP laminates based on stiffness degradation measurements*. Composites Science and Technology, 2000. **60**(15): p. 2819-2828.
113. Bond, I., *Fatigue life prediction for GRP subjected to variable amplitude loading*. Composites Part A: Applied Science and Manufacturing, 1999. **30**(8): p. 961-970.
114. Philippidis, T.P. and A.P. Vassilopoulos, *Life prediction methodology for GFRP laminates under spectrum loading*. Composites Part A: applied science and manufacturing, 2004. **35**(6): p. 657-666.
115. Boerstra, G., *The Multislope model: A new description for the fatigue strength of glass fibre reinforced plastic*. International journal of fatigue, 2007. **29**(8): p. 1571-1576.
116. Beheshty, M., B. Harris, and T. Adam, *An empirical fatigue-life model for high-performance fibre composites with and without impact damage*. Composites Part A: Applied Science and Manufacturing, 1999. **30**(8): p. 971-987.
117. Gathercole, N., et al., *Life prediction for fatigue of T800/5245 carbon-fibre composites: I. Constant-amplitude loading*. international Journal of Fatigue, 1994. **16**(8): p. 523-532.
118. Vassilopoulos, A.P., B.D. Manshadi, and T. Keller, *Influence of the constant life diagram formulation on the fatigue life prediction of composite materials*. International journal of fatigue, 2010. **32**(4): p. 659-669.
119. Whitworth, H., *A stiffness degradation model for composite laminates under fatigue loading*. Composite Structures, 1997. **40**(2): p. 95-101.
120. Montesano, J., et al., *Fatigue damage characterization and modeling of a triaxially braided polymer matrix composite at elevated temperatures*. Composite Structures, 2013. **101**: p. 129-137.
121. Selzer, R. and K. Friedrich, *Mechanical properties and failure behaviour of carbon fibre-reinforced polymer composites under the influence of moisture*. Composites Part A: Applied Science and Manufacturing, 1997. **28**(6): p. 595-604.
122. McBagonluri, F., et al., *Characterization of fatigue and combined environment on durability performance of glass/vinyl ester composite for infrastructure applications*. International journal of fatigue, 2000. **22**(1): p. 53-64.
123. Smith, L. and Y. Weitsman, *The immersed fatigue response of polymer composites*. International journal of fracture, 1996. **82**(1): p. 31-42.
124. Ellis, B. and M. Found, *The effects of water absorption on a polyester/chopped strand mat laminate*. Composites, 1983. **14**(3): p. 237-243.
125. Roylance, M.E., *The effect of moisture on the fatigue resistance of an aramid/epoxy composite*. Polymer Engineering & Science, 1982. **22**(15): p. 988-993.
126. Shan, Y., et al., *Static and dynamic fatigue of glass-carbon hybrid composites in fluid environment*. Journal of composite materials, 2002. **36**(2): p. 159-172.
127. Shan, Y. and K. Liao, *Environmental fatigue behavior and life prediction of unidirectional glass-carbon/epoxy hybrid composites*. International journal of fatigue, 2002. **24**(8): p. 847-859.
128. Siriruk, A. and D. Penumadu, *Degradation in fatigue behavior of carbon fiber-vinyl ester based composites due to sea environment*. Composites Part B: Engineering, 2014. **61**: p. 94-98.
129. Blake, S.P., K.A. Berube, and R.A. Lopez-Anido, *Interlaminar fracture toughness of woven E-glass fabric composites*. Journal of Composite Materials, 2011: p. 0021998311421221.

130. Selzer, R. and K. Friedrich, *Influence of water up-take on interlaminar fracture properties of carbon fibre-reinforced polymer composites*. Journal of Materials Science, 1995. **30**(2): p. 334-338.
131. Argüelles, A., et al., *Fatigue delamination, initiation, and growth, under mode I and II of fracture in a carbon - fiber epoxy composite*. Polymer Composites, 2010. **31**(4): p. 700-706.
132. Hojo, M., et al., *Modes I and II interlaminar fracture toughness and fatigue delamination of CF/epoxy laminates with self-same epoxy interleaf*. International journal of fatigue, 2006. **28**(10): p. 1154-1165.
133. Stigh, U., K.S. Alfredsson, and A. Biel. *Measurement of cohesive laws and related problems*. in *ASME 2009 International Mechanical Engineering Congress and Exposition*. 2009. American Society of Mechanical Engineers.
134. ASTM, *Standard Test Method for Determination of the Mode II Interlaminar Fracture Toughness of Unidirectional Fiber-Reinforced Polymer Matrix Composites*, in *D7905/D7905M-14*. 2014, American Society for Testing and Materials International: West Conshohocken, PA.
135. ASTM, *Standard Test Method for Mode I Interlaminar Fracture Toughness of Unidirectional Fiber-Reinforced Polymer Matrix Composites*, in *D5528-13*. 2013, American Society for Testing and Materials International: West Conshohocken, PA.
136. ASTM, *Standard Test Method for Mixed Model-Mode II Interlaminar Fracture Toughness of Unidirectional Fiber-Reinforced Polymer Matrix Composites*, in *D6671/D6671M-13*. 2013, American Society for Testing and Materials International: West Conshohocken, PA.
137. Gunderson, J.D., J.F. Brueck, and A.J. Paris, *Alternative test method for interlaminar fracture toughness of composites*. International journal of fracture, 2007. **143**(3): p. 273-276.
138. Rice, J.R., *A path independent integral and the approximate analysis of strain concentration by notches and cracks*. Journal of applied mechanics, 1968. **35**(2): p. 379-386.
139. Nilsson, F., *Large displacement aspects on fracture testing with double cantilever beam specimens*. International journal of fracture, 2006. **139**(2): p. 305-311.
140. Sarrado, C., et al., *An experimental data reduction method for the Mixed Mode Bending test based on the J-integral approach*. Composites Science and Technology, 2015. **117**: p. 85-91.
141. Anthony, J. and P.C. Paris, *Instantaneous evaluation of J and C*. International Journal of Fracture, 1988. **38**(1): p. R19-R21.
142. Bradley, W., C. Corleto, and D. Goetz, *Studies of Mode I and Mode II Delamination Using a J-Integral Analysis and In-Situ Observations of Fracture in the SEM*. 1990, DTIC Document.
143. Walander, T., *System for measurement of cohesive laws*, in *School of Technology and Society*. 2009, University of Skövde. p. 37
144. Stigh, U. *Cohesive Laws for Delamination of CFRP: Experiments and Model*. in *ASME 2010 International Mechanical Engineering Congress and Exposition*. 2010. American Society of Mechanical Engineers.
145. Sarrado, C., et al., *On the validity of linear elastic fracture mechanics methods to measure the fracture toughness of adhesive joints*. International Journal of Solids and Structures, 2015.

146. Turon, A., et al., *A damage model for the simulation of delamination in advanced composites under variable-mode loading*. Mechanics of Materials, 2006. **38**(11): p. 1072-1089.
147. Wu, E.M. and R. Reuter Jr, *Crack extension in fiberglass reinforced plastics*. 1965, DTIC Document.
148. Kinloch, A., et al., *The mixed-mode delamination of fibre composite materials*. Composites Science and Technology, 1993. **47**(3): p. 225-237.
149. Benzeggagh, M. and M. Kenane, *Measurement of mixed-mode delamination fracture toughness of unidirectional glass/epoxy composites with mixed-mode bending apparatus*. Composites science and technology, 1996. **56**(4): p. 439-449.
150. Camanho, P.P., C. Davila, and M. De Moura, *Numerical simulation of mixed-mode progressive delamination in composite materials*. Journal of composite materials, 2003. **37**(16): p. 1415-1438.
151. Camanho, P.P. and C.G. Dávila, *Mixed-mode decohesion finite elements for the simulation of delamination in composite materials*. NASA-Technical paper, 2002. **211737**(1): p. 33.
152. Turon, A., et al., *An engineering solution for mesh size effects in the simulation of delamination using cohesive zone models*. Engineering fracture mechanics, 2007. **74**(10): p. 1665-1682.
153. Jiang, W.G., et al., *A concise interface constitutive law for analysis of delamination and splitting in composite materials and its application to scaled notched tensile specimens*. International journal for numerical methods in engineering, 2007. **69**(9): p. 1982-1995.
154. Harper, P.W. and S.R. Hallett, *Cohesive zone length in numerical simulations of composite delamination*. Engineering fracture mechanics, 2008. **75**(16): p. 4774-4792.
155. Harper, P.W., L. Sun, and S.R. Hallett, *A study on the influence of cohesive zone interface element strength parameters on mixed mode behaviour*. Composites Part A: Applied Science and Manufacturing, 2012. **43**(4): p. 722-734.
156. Jacques, S., I. De Baere, and W. Van Paepegem, *Analysis of the Numerical and Geometrical Parameters Influencing the Simulation of Mode I and Mode II Delamination Growth in Unidirectional and Textile Composites*. Applied Composite Materials, 2014: p. 1-32.
157. Zhao, L., et al., *Simulation of delamination growth in multidirectional laminates under mode I and mixed mode I/II loadings using cohesive elements*. Composite Structures, 2014. **116**: p. 509-522.
158. Russell, A.J. and K.N. Street, *Moisture and temperature effects on the mixed-mode delamination fracture of unidirectional graphite/epoxy*. Delamination and debonding of materials, ASTM STP, 1985. **876**: p. 349-370.
159. Asp, L., *The effects of moisture and temperature on the interlaminar delamination toughness of a carbon/epoxy composite*. Composites Science and Technology, 1998. **58**(6): p. 967-977.
160. Davidson, B., M. Kumar, and M. Soffa, *Influence of mode ratio and hygrothermal condition on the delamination toughness of a thermoplastic particulate interlayered carbon/epoxy composite*. Composites Part A: Applied Science and Manufacturing, 2009. **40**(1): p. 67-79.
161. LeBlanc, L.R. and G. LaPlante, *Experimental investigation and finite element modeling of mixed-mode delamination in a moisture-exposed carbon/epoxy*

- composite. Composites Part A: Applied Science and Manufacturing, 2016. **81**: p. 202-213.
162. Sloan, F.E. and R.J. Seymour, *The effect of seawater exposure on mode I interlaminar fracture and crack growth in graphite/epoxy*. Journal of composite materials, 1992. **26**(18): p. 2655-2673.
  163. Alessi, S., G. Pitarresi, and G. Spadaro, *Effect of hydrothermal ageing on the thermal and delamination fracture behaviour of CFRP composites*. Composites Part B: Engineering, 2014. **67**: p. 145-153.
  164. Mahmood, A.H., et al., *Effect of hygrothermal conditioning on the fracture toughness of carbon/epoxy composites cured in autoclave/Quickstep*. Journal of Reinforced Plastics and Composites, 2013: p. 0731684413486367.
  165. Srivastava, V. and P. Hogg, *Moisture effects on the toughness, mode-I and mode-II of particles filled quasi-isotropic glass-fibre reinforced polyester resin composites*. Journal of Materials Science, 1998. **33**(5): p. 1129-1136.
  166. Garg, A. and O. Ishai, *Hygrothermal influence on delamination behavior of graphite/epoxy laminates*. Engineering fracture mechanics, 1985. **22**(3): p. 413-427.
  167. Greenhalgh, E. and S. Singh, *The effect of moisture, matrix and ply orientation on delamination resistance, failure criteria and fracture morphology in CFRP*, in *Composite Materials: Testing, Design, and Acceptance Criteria*. 2002, ASTM International.
  168. Meziere, Y., L. Michel, and D. Carronnier, *Mixed-mode delamination failure criteria in carbon fibre/composite under quasi-static and cyclic loading*. European Structural Integrity Society, 2000. **27**: p. 97-110.
  169. Gong, X., K. Wong, and M. Tamin, *Moisture Absorption Effects on the Resistance to Interlaminar Fracture of Woven Glass/Epoxy Composite Laminates*, in *Damage and Fracture of Composite Materials and Structures*. 2012, Springer. p. 107-127.
  170. Hintikka, P., M. Wallin, and O. Saarela, *THE EFFECT OF MOISTURE ON THE INTERLAMINAR FRACTURE TOUGHNESS OF CFRP LAMINATE*.
  171. Chou, I., *Effect of fiber orientation and moisture absorption on the interlaminar fracture toughness of CFRP laminates*. Advanced Composite Materials, 1998. **7**(4): p. 377-394.
  172. Todo, M., T. Nakamura, and K. Takahashi, *Effects of moisture absorption on the dynamic interlaminar fracture toughness of carbon/epoxy composites*. Journal of Composite Materials, 2000. **34**(8): p. 630-648.
  173. Yian, Z., S.L. Keey, and C.G. Boay, *Effects of seawater exposure on mode II fatigue delamination growth of a woven E-glass/bismaleimide composite*. Journal of Reinforced Plastics and Composites, 2016. **35**(2): p. 138-150.
  174. Hexcel, *Hexply F655 Product data*. 2005.
  175. ASTM, *Standard Test Method for Tensile Properties of Polymer Matrix Composite Materials*, in *ASTM D3039 / D3039M - 14*. 2014, American Society for Testing and Materials International: West Conshohocken, PA.
  176. ASTM, *Standard Test Methods for Flexural Properties of Unreinforced and Reinforced Plastics and Electrical Insulating Materials*, in *ASTM D790 - 15e2*. 2015, American Society for Testing and Materials International: West Conshohocken, PA.
  177. Seah, L.K., et al. *Flexural behavior of epoxy-carbon composite with diffusion effect*. in *International Conference on Experimental Mechanics 2014*. 2015. International Society for Optics and Photonics.

178. ASTM, *Standard Test Method for Shear Properties of Composite Materials by V-Notched Rail Shear Method*, in ASTM D7078 / D7078M - 12. 2012, American Society for Testing and Materials International: West Conshohocken, PA.
179. ASTM, *Standard Test Method for In-Plane Shear Response of Polymer Matrix Composite Materials by Tensile Test of a  $\pm 45^\circ$  Laminate*, in ASTM D3518 / D3518M - 13. 2013, American Society for Testing and Materials International: West Conshohocken, PA.
180. Yian, Z., S.L. Keey, and C.G. Boay, *Measurement of interlaminar fracture properties of composites using the J-integral method*. Journal of Reinforced Plastics and Composites, 2016: p. Publish ahead of print.
181. Yun, X., J. Xiong, and R. Shenoi, *Fatigue-driven model for mode II interlaminar delamination propagation of fibre/epoxy-reinforced composite laminates under three-point end-notched flexure*. Journal of Composite Materials, 2014: p. DOI: 10.1177/002199831455.
182. Russell, A. and K. Street, *Factors affecting the interlaminar fracture energy of graphite/epoxy laminates*. Progress in science and Engineering of Composites, 1982: p. 279-286.
183. Fan, C., P.-Y. Ben Jar, and J.-J. Roger Cheng, *Revisit the analysis of end-notched-flexure (ENF) specimen*. Composites Science and Technology, 2006. **66**(10): p. 1497-1498.
184. Blackman, B., A. Brunner, and J. Williams, *Mode II fracture testing of composites: a new look at an old problem*. Engineering fracture mechanics, 2006. **73**(16): p. 2443-2455.
185. Ebeling, T., et al., *Delamination failure of a woven glass fiber composite*. Journal of Composite Materials, 1997. **31**(13): p. 1318-1333.
186. Kim, J.-K. and M.-L. Sham, *Impact and delamination failure of woven-fabric composites*. Composites Science and Technology, 2000. **60**(5): p. 745-761.
187. Nakai, Y. and C. Hiwa, *Effects of loading frequency and environment on delamination fatigue crack growth of CFRP*. International journal of fatigue, 2002. **24**(2): p. 161-170.
188. Trethewey, B.R., J.W. Gillespie, and L.A. Carlsson, *Mode II cyclic delamination growth*. Journal of Composite Materials, 1988. **22**(5): p. 459-483.
189. O'Brien, T.K., W.M. Johnston, and G.J. Toland, *Mode II interlaminar fracture toughness and fatigue characterization of a graphite epoxy composite material*. NASA/TM-2010-216838, 2010.
190. Bureau, M., et al., *Interlaminar fatigue crack propagation in continuous glass fiber/polypropylene composites*. International journal of fatigue, 2002. **24**(2): p. 99-108.
191. Brunner, A., et al., *Mode II fatigue delamination resistance of advanced fiber-reinforced polymer-matrix laminates: Towards the development of a standardized test procedure*. International journal of fatigue, 2013. **50**: p. 57-62.
192. Deshpande, A.P., *Techniques in oscillatory shear rheology*.
193. Wang, Z., Y.a. Zhao, and L.K. Seah. *Life prediction of composite materials in off-shore application*. in *Composite Materials & Renewable Energy Applications (ICCMREA), 2014 International Conference on*. 2014. IEEE.
194. Richeton, J., et al., *A unified model for stiffness modulus of amorphous polymers across transition temperatures and strain rates*. Polymer, 2005. **46**(19): p. 8194-8201.

195. Yian, Z., et al., *Long-Term Viscoelastic Response of E-glass/Bismaleimide Composite in Seawater Environment*. Applied Composite Materials, 2015. **22**(6): p. 693-709.
196. Sihh, S. and S.W. Tsai, *Automated shift for time-temperature superposition*. ICCM-12, Proc., CD-disk, paper, 1999. **462**.
197. Vassilopoulos, A.P., *Fatigue Stiffness*. Wiley Encyclopedia of Composites, 2012.
198. Sutherland, L. and C.G. Soares, *Review of probabilistic models of the strength of composite materials*. Reliability Engineering & System Safety, 1997. **56**(3): p. 183-196.
199. Yian, Z., et al., *Long-Term Viscoelastic Response of E-glass/Bismaleimide Composite in Seawater Environment*. Applied Composite Materials, 2015: p. Epub ahead of Print. 22 Jan 2015. DOI:10.1007/s10443-014-9431-2.
200. Fothergill, J., *Estimating the cumulative probability of failure data points to be plotted on Weibull and other probability paper*. Electrical Insulation, IEEE Transactions on, 1990. **25**(3): p. 489-492.
201. da Silva, L. and R. Adams, *Measurement of the mechanical properties of a carbon reinforced bismaleimide over a wide range of temperatures* Revista da Associação Portuguesa de Análise Experimental de Tensões ISSN. **1646**: p. 7078.
202. Nakada, M. and Y. Miyano, *Accelerated testing for long-term fatigue strength of various FRP laminates for marine use*. Compos. Sci. Technol. , 2009. **69**(6): p. 805-813.
203. Rault, J., *Origin of the Vogel–Fulcher–Tammann law in glass-forming materials: the  $\alpha$ – $\beta$  bifurcation*. J. Non-Cryst. Solids, 2000. **271**(3): p. 177-217.
204. Yian, Z., S.L. Keey, and C.G. Boay, *Effects of seawater exposure on mode II fatigue delamination growth of a woven E-glass/bismaleimide composite*. Journal of Reinforced Plastics and Composites, 2015: p. 0731684415609139.
205. Hintikka, P., M. Wallin, and O. Saarela, *The effect of moisture on the interlaminar fracture toughness of CFRP laminate*, in *27th Congress of International Council of the Aeronautical Sciences*. 19-24 September 2010, paper no. ICAS2010-8.3ST1: Nice, France, .
206. Jacques, S., I. De Baere, and W. Van Paepegem, *Analysis of the Numerical and Geometrical Parameters Influencing the Simulation of Mode I and Mode II Delamination Growth in Unidirectional and Textile Composites*. Applied Composite Materials: p. 1-32.
207. Brunner, A., B. Blackman, and P. Davies, *A status report on delamination resistance testing of polymer–matrix composites*. Engineering fracture mechanics, 2008. **75**(9): p. 2779-2794.
208. Marom, G., *Environmental effects on fracture mechanical properties of polymer composites*. Elsevier Science Publishers, Applications of Fracture Mechanics to Composite Materials, 1989: p. 397-424.
209. Weitsman, Y.J., *Fluid effects in polymers and polymeric composites*. 2011, New York: Springer Science & Business Media.
210. Hibbs, M.F. and W.L. Bradley, *Correlations between micromechanical failure processes and the delamination toughness of graphite/epoxy systems*. Fractography of modern engineering materials: composites and metals, ASTM STP, 1987. **948**: p. 68-97.
211. Franco, L., M. Graça, and F. Silva, *Fractography analysis and fatigue of thermoplastic composite laminates at different environmental conditions*. Materials Science and Engineering: A, 2008. **488**(1): p. 505-513.



212. Lee, S.M., *Mode II delamination failure mechanisms of polymer matrix composites*. Journal of materials science, 1997. **32**(5): p. 1287-1295.